Department Electrical and Electronics Engineering

PHD THESIS

---

# Investigation on the improvement of corrosion monitor reliability, calibration, and coverage

---

*Author:*
Rukhshinda Wasif

*Supervisors:*
Professor Mohammad Osman Tokhi
Dr. John Rudlin
Dr Fang Duan
Dr. Gholamhossein Shirkoohi
Dr. Zhangfang Zhao

Submitted on
December 3, 2023

Study program:
Electrical and Electronics Engineering

# Imprint

| | |
|---|---|
| *Project:* | PHD Thesis |
| *Title*: | Investigation on the improvement of corrosion monitor reliability, calibration, and coverage |
| *Author*: | Rukhshinda Wasif |
| *Date*: | December 3, 2023 |
| *Keywords*: | Corrosion monitoring, Magnetic Flux leakage, Magnetic eddy current, Permeability measurement, Reliability |
| *Copyright*: | London South Bank University |

*Study program:*
Electrical and Electronics Engineering
London South Bank University

*Supervisor 1: Mohammad Osman Tokhi* *Supervisor 2: John Rudlin*

# Declaration of Authorship

I, Rukhshinda Wasif, declare that this thesis titled, Investigations on the improvement of corrosion monitor reliability, calibration and coverage, and the work presented in it are my own. I confirm that:

- This work was done wholly or mainly while in candidature for a research degree at the London South Bank University/TWI Ltd.
- Where any part of this thesis has previously been submitted for a degree or any other qualification at this university or any other institution, this has been clearly stated.
- Where I have consulted the published work of others, this is always clearly attributed.
- Where I have quoted from the work of others, the source is always given. With the exception of such quotations, this thesis is entirely my own work.
- I have acknowledged all main sources of help.
- Where the thesis is based on work done by myself jointly with others, I have made clear exactly what was done by others and what I have contributed myself.

Signed:

Date: 30-12-2023

# Abstract

Thickness loss due to internal corrosion and erosion is a critical issue in ferromagnetic steel structures that can cause catastrophic failures. Ultrasonic thickness gauges are widely used for the detection of wall thickness. Recently permanently installed ultrasonic sensors have become popular for the inspection of areas suspected to undergo wall thickness loss. However, these are limited by the high cost and requirement of coupling agents. To address these problems, a novel cost-effective, and smart corrosion monitor based on the magnetic eddy current technique is developed in this research. The performance and reliability of the monitor to track internal wall thickness loss is tested successfully through accelerated and real-life aging corrosion tests.

Due to the handling and safety issues associated with the powerful magnets in magnetic techniques, a particle swarm-based optimisation method is proposed and validated through two test cases. The results indicate that the area of the magnetic excitation circuit could be reduced by 38% without compromising the sensitivity.

The reliability of the corrosion monitor is improved by utilising the active redundancy approach to identify and isolate faults in sensors. A real-life aging test is conducted for eight months in an ambient environment through an accelerated corrosion setup. The results obtained from the two corrosion monitors confirm that the proposed corrosion monitor is reliable for tracking the thickness loss. The corrosion monitor is found to be stable against environmental variations.

A new in-situ calibration method based on zero-crossing frequency feature is introduced to evaluate the in-situ relative permeability. The thickness of the test specimen could be estimated with an accuracy of ± 0.6 mm.

The series of studies conducted in the project reveal that the magnetic corrosion monitor has the capability to detect and quantify uniform wall thickness loss reliably.

# Acknowledgements

First and foremost, I am extremely grateful to my supervisors, Prof. Mohammad Osman Tokhi, Dr. John Rudlin, Dr. Fang Duan, Dr. Shiva Majidnia, and Dr. Gholamhossein Shirkoohi for their invaluable advice, continuous support, and patience during my PhD study. Their immense knowledge and plentiful experience have encouraged me in all the time of my academic research and daily life. I would also like to thank Dr. John Rudlin and Dr. Shiva Majidnia for their technical support in my study. I would like to thank all the members in the NSIRC and TWI. I am grateful to my sponsor Lloyds register foundation to providing the financial support. It is their kind help and support that has made my study in the UK a wonderful time. Finally, I would like to express my gratitude to my family especially my parents, husband and children. Without their tremendous understanding and encouragement over the past few years, it would be impossible for me to complete my study.

# Contents

# List of Figures

# List of Tables

# List of Abbreviations

| | |
|---|---|
| **ABC** | **A**rtificial **B**ee **C**olony |
| **AC** | **A**lternating **C**urrent |
| **ADC** | **A**nalog to **D**igital **C**onverter |
| **ALT** | **A**ccelerated **L**ife **T**esting |
| **AMR** | **A**nisotropic **M**agneto **R**esistance |
| **API** | **A**merican **P**etroleum **I**nstitute |
| **DC** | **D**irect **C**urrent |
| **DE** | **D**ifferential **E**valuation |
| **ECA** | **E**ddy **C**urrent **A**rray |
| **EIS** | **E**lectrochemical **I**mpedance **S**pectroscopy |
| **EMAT** | **E**lectro**m**agnetic **A**coustic **T**ransducer |
| **FEA** | **F**inite **E**lement **A**nalysis |
| **FEM** | **F**inite **E**lement **M**odelling |
| **FFS** | **F**itness **F**or **S**ervice |
| **GA** | **G**enetic **A**lgorithm |
| **GDP** | **G**ross **D**omestic **P**roduct |
| **GMR** | **G**iant **M**agneto **R**esistance |
| **LFD** | **L**eakage **F**lux **D**ensity |
| **MCU** | **M**icro **C**ontroller **U**nit |
| **MEC** | **M**agnetic **E**ddy **C**urrent |
| **MFL** | **M**agnetic **F**lux **L**eakage |
| **NDT** | **N**on **D**estructive **T**esting |
| **OECD** | **O**rganisation for **E**conomic **C**ooperation and **D**evelopment |
| **PSO** | **P**article **S**warm **O**ptimisation |
| **RBI** | **R**isk **B**ased **I**nspection |
| **RFID** | **R**adio **F**requency **Id**entification |
| **RWT** | **R**emaining **W**all **T**hickness |

| | |
|---|---|
| **SAW** | **S**urface **A**coustic **W**ave |
| **TMR** | **T**unnel **M**agneto **R**esistance |
| **UT** | **U**ltrasonic **T**hickness |

*Dedicated to my teachers and family especially my mother (Ammi) and father (Abbu) who believed in empowering their daughters through education*

# Chapter 1

# Introduction

## 1.1 Background

Natural gas and oil are the key energy sources that benefit the general public, industry, agriculture, and the defence sector [1]. Oil is the lifeline of industrialised nations and has become the most important source of energy since the mid-1950s [2]. In UK 97% of the transport sector demand is fulfilled by oil [3]. Gas is a prime source for heating and electricity generation. Both oil and gas account for one-third of the United Kingdom's primary energy needs [4]. The transportation, refining, and distribution of these key energy sources are mostly carried out by pipes. The pipes are considered to be one of the safest, eco-friendly, and most reliable modes of transportation of petroleum products and crude oil [5]. Oil and gas transportation pipelines and pipework are vital to a country's energy sector. According to the organisation for economic cooperation and development (OECD), UK is the second-largest producer of oil and the third-largest producer of gas in Europe [6]. It has a huge network of pipes that extend from North Sea platforms to coastal terminals in Scotland and Northern England. The total length of six major pipelines, apart from smaller lines, is 943 miles [6]. However, pipes and pipework are subjected to different types of defects such as wall loss, fatigue cracks, stress corrosion cracking, and dents [7, 8].

The failure in the detection and mitigation of these defects may result in leakages, spills, and fire. The leakages and eventual failure in pipes lead to huge losses to the economy, environment, and human lives. Since many pipes are laid in public spaces, they pose safety hazards.

There are many causes for the introduction and propagation of these defects in the pipes. The main factors include external impacts, corrosion, erosion, material failures, and earthquakes [9]. Among these factors corrosion, especially internal corrosion has been reported to be responsible for 18 percent of major incidents in pipes both onshore and offshore in the period 1988 to 2008 [10].

Corrosion is defined as the deterioration of the metal or its properties as a result of the chemical reaction between metal and surrounding environments [11]. At every stage of the oil and gas industry, from casing strings to production platforms, drilling to transmission lines, corrosion attacks each component. Corrosion occurs in pipes because firstly, a large proportion is made of mild carbon steel which is highly susceptible to corrosion attack. Secondly, they carry corrosive products, such as water, hydrogen sulphide, and carbon dioxide [12]. It is also aggravated by microbiological activities and extreme operating environments especially high temperature and marine applications [13, 14].

A major disadvantage of corrosion is the wall thickness loss that leads to leakage and eventual failure of pipes. Furthermore, erosion also causes rapid degradation of pipe material due to inclusions in the products such as sand. Both corrosion and erosion are inevitable and can cause serious threats due to the wall thickness loss of the assets. Thus, it is crucial to detect, monitor, maintain, and mitigate wall thickness loss. Early-stage detection and monitoring of wall thickness loss can lead to huge savings on the costs associated with shutdowns, repairs, and failures. This is the reason that currently, thickness monitoring is an issue under extensive research [15–17]. Risk-based Inspection (RBI) programs mention the components in a facility that need to be inspected fully such as storage tank floors. Other components such as pressure vessels and pipes can be limited to critical areas [18]. The plant operators know the location of these critical areas in the plant. The increasing knowledge of risks, failure mechanisms, and erosion and corrosion propagation has led to the smart use of NDT techniques for economical and time-saving procedures to improve the safety of the assets.

## 1.2 Research drive

According to the National association for corrosion engineers (NACE) report, the global cost of corrosion is estimated to be 2.5 trillion US dollars [19]. Corrosion costs almost (3-4) % of the GDP of each nation. In US alone the oil and gas exploration and production industry spend a staggering amount of 1.4 billion US dollars a year on corrosion [20]. Corrosion especially internal corrosion is a major threat to the assets in the oil and gas industry leading to catastrophic failures.

European gas pipeline incident data group (EGIG) collected data for causes of accidents from 17 gas distribution companies. Their group study about the causes of damages in the gas pipelines between 2004 and 2013 [21] is shown in Figure 1.1.

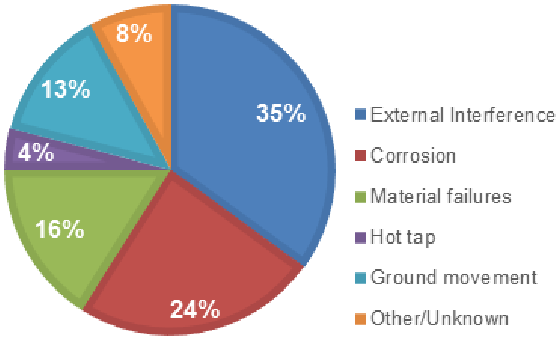

FIGURE 1.1: The main causes of damage to gas pipelines reported by EGIG during the period 2004-2013 [21].

As evident from Figure 1.1, corrosion was the second major factor responsible for the damage in gas pipelines. The US department of transportation, pipeline, and hazardous safety material (PHSMA) report indicated a three-fold increase in the internal corrosion incidents in oil pipelines during the period of 1970 to 2013 [22]. Similar trends were observed for gas pipelines. In a report published by the Canadian association for petroleum production (CAPP), internal corrosion incidents for sweet gas-gathering pipelines in Alberta increased from 25 in 1985 to 125 in 2008, while for oil effluent pipelines they increased from 75 in 1985 to 175 in 2008 [23]. Many incidents have resulted in financial, environmental, and human losses due to inadequate monitoring and mitigation of corrosion [24]. They can also result in regulatory actions and litigation against pipeline operators. A few of them along with their consequences are mentioned in Table 1.1:

TABLE 1.1: Major oil and gas pipes incidents due to corrosion in last two decades [25–28].

| S.No | Description | Year | Consequences |
|---|---|---|---|
| 1 | SINOPEC gas pipeline explosion, China | 2013 | Fatalities = 62<br>Injuries = 136<br>Financial damages = $100 million<br>Environmental damages = Benzene oil spills in sea |
| 2 | William gas pipeline, United States | 2010, 2012 | Financial damages = $295000 and $57084 |
| 3 | Enbridge pipeline, United States | 2013 | Financial damages = $13,844,274<br>Environmental damages = Impacts to vegetation, animals and ponds |
| 4 | Humber refinery explosion, United Kingdom | 2001 | Injuries = 3<br>Financial damages = £895000 + £200000 for claims<br>Environmental damages = Tonnes of toxic gases such as Hydrogen sulphide released in air |
| 5 | Natural gas pipeline rupture and fire, New Mexico | 2000 | Fatalities = 12<br>Financial damages = $998,296 |

Figures 1.2-1.4 show the extent of destruction caused by pipes failures due to corrosion.

FIGURE 1.2: SINOPEC pipeline explosion in China that killed 62 people and injured 136 [25].

FIGURE 1.3: Humber refinery, United Kingdom, gas plant damage by fire and explosion [27].

FIGURE 1.4: Fire caused by the explosion in sweet gas pipeline explosion New Mexico killing 12 people [28].

### 1.2.1 Lessons learned from past

The information presented in Table1.1 shows the extreme consequences on the economy, environment, and human lives associated with pipeline and pipework failures due to corrosion defects. The primary cause of these failures was either the lack of inspection procedures or the incapability of the inspection techniques employed to detect and monitor corrosion defects [27, 28]. Most of the pipes were monitored through visual inspection or pigging. Visual inspections and pigging cannot cover the areas of the pipes especially pipework in refineries that are inaccessible due to sharp bends or hazardous environments. These failures could be avoided by adopting a sophisticated and robust integrity management plan. The assumption that the integrity management plans can keep the pipes and pipework safe is naive [29]. The aim of integrity management is to ensure that the pipe and pipework are safe and secure under operating conditions for the given time. The process of integrity management involves inspection or monitoring, mitigation, and maintenance. An effective corrosion monitoring plan can help asset owners avoid these catastrophic failures through early-stage detection, continuous monitoring, and mitigation. If corrosion is left unattended it can lead to the eventual failure of an asset, and even explosions, posing safety risks to personnel, huge equipment costs, and subsequent environmental damage.

Due to the huge costs involved with the shutdown and failures, a great deal of research has been focused on developing corrosion monitoring systems in the last decade. Some of the important corrosion monitoring techniques that are applied in the industry are discussed here.

Electromagnetic methods such as magnetic flux leakage (MFL) and magnetic eddy current (MEC) have advantages over UT that they do not require couplants and can be applied over coatings and paints. With the development of powerful rare earth magnets, sensors with low power consumption are possible for long-term applications. Magnetic techniques have the drawback of the requirement of extremely heavy magnets and bulky setups that pose health and safety hazards. In addition, the technique is qualitative and requires calibration blocks to estimate the depth of corrosion defects from signals. It is also paramount to maintain high reliability for long-term thickness loss monitoring in permanent installations. The sensor must have a stable variation with corrosion defects without being influenced by other physical parameters.

In order to address the issues discussed above, research is necessary to develop cost-effective, and smart magnetic sensors. Magnetic sensors have been widely used in industry for the inspection of corrosion using in-line or on-line setups. The research on their application for an extended period is limited. Furthermore, there is also a need to investigate methods for improvement of the monitor's reliability, calibration, and through-thickness coverage.

## 1.3 Aim of the project

The aim of the research is to develop a low-cost smart permanently installed magnetic transducer for long-term monitoring of corrosion in ferromagnetic structures, especially oil and gas pipes, and pipework. The project was further aimed to investigate methods for improvement of reliability, calibration, and through-thickness coverage of permanently installed corrosion monitoring transducers working on the MEC principle.

## 1.4 Research objectives

The research sought to achieve the following objectives:

- Development of a wireless MEC sensor for wall thickness loss monitoring with low power consumption for the long-term applications.

  During the project, a cost-effective corrosion monitor based on the MEC principle was developed for remote thickness loss monitoring. The performance of the monitor was successfully tested using accelerated corrosion tests.

- Investigations on the critical test parameters such as induced magnetic flux density in the test sample and excitation frequency of MEC sensor to achieve maximum sensitivity.

  FE modeling and experimental studies were carried out to evaluate the effect of different parameters on the sensitivity of the sensor. It was found that excitation frequency is a critical parameter and it is crucial to avoid zero crossing frequency (ZCF) to avoid the missed signals.

- Optimisation of the design parameters of the sensor to ensure complete through-thickness coverage with the minimum size that will involve achieving the required magnetic flux density for different test sample configurations.

  An artificial intelligence (AI)-based approach was developed to avoid the time consuming and iterative procedure for the design of the magnetic excitation circuit.

- Studies on the improvement of the reliability of the sensor. Identification of critical failure modes and enhanced design based on the active redundancy principle to avoid inaccuracies. Additionally, this will enable the transducer to detect failures and continue to operate even when one of the sensors isn't working.

The reliability of the corrosion monitor was improved by employing coupled MFL and MEC sensors in the design. The active redundancy approach used in the design proved to be effective for identification of the faulty sensors through real life aging tests.

- Developing an easy and effective in-situ calibration method to estimate the remaining wall thickness of the pipe at the installation location.

  A technique based on the ZCF feature evaluated from the multi-frequency eddy current spectrum was developed for the calibration. The approach was found to be successful in the estimation of the wall thickness loss without the need of the cumbersome calibration procedure.

- Evaluate the reliability and stability of the sensor for long-term thickness loss monitoring of assets. Designing and conducting experiments to check the stability of the sensor in real environments for an extended time period against variations in environmental factors.

  A real-life aging test was conducted for eight months by inducing corrosion at two different rates to simulate wall thickness loss. The corrosion monitor was found to be stable against variations in environmental conditions.

## 1.5 Novelty statement

- There is limited work on the development of permanently installed electromagnetic sensors for long-term corrosion monitoring. The research work conducted on MEC sensors indicated that frequency is a critical parameter that needs to be optimised for the detection of corrosion defects.
- A particle swarm optimisation (PSO) algorithm is developed to optimise the size of the excitation circuit which is a new approach considering other methods in the literature are time-consuming and complicated.

- Long-term reliability of the sensor is evaluated by testing the sensor in the ambient environment. An aging test with two different corrosion rates is designed and conducted to assess the performance and stability of the magnetic monitor over an extended time period.

- The active redundancy approach is proposed in this research to improve the reliability of the sensor for fault diagnosis and continued operation.

- Estimation of remaining thickness using the ZCF feature. The calibration is carried out using calibration blocks, but a simplistic approach is proposed by evaluating the in-situ permeability by solving the inverse problem.

### 1.5.1 Publications

Wasif, R., Tokhi, M.O., Shirkoohi, G., Marks, R. and Rudlin, J., 2022. Development of Permanently Installed Magnetic Eddy Current Sensor for Corrosion Monitoring of Ferromagnetic Pipelines. Applied Sciences, 12(3), p.1037.

Wasif, R., Tokhi, M.O., Rudlin, J., Marks, R., Shirkoohi, G., Zhao, Z. and Duan, F., 2022, May. Particle swarm optimization of excitation system design of magnetic eddy current sensor. In 2022 Prognostics and Health Management Conference (PHM-2022 London) (pp. 182-187). IEEE.

Wasif, R., Tokhi, M.O., Rudlin, J., Shirkoohi, G. and Duan, F., 2023. Reliability Improvement of Magnetic Corrosion Monitor for Long-Term Applications. Sensors, 23(4), p.2212.

## 1.6 Organisation of thesis

This chapter discussed the background and objectives of the research project. The rest of the report is structured into 7 chapters.

Chapter 2 presents a background and literature review relevant to the topic. An overview of corrosion monitoring techniques used in the industry is provided, along with their merits and demerits. An in-depth explanation of electromagnetic techniques for corrosion monitoring is presented. A review of current literature on long-term remote applications utilising electromagnetic techniques is followed by an evaluation of the outstanding research questions. The chapter also discusses the methodology developed to address these research questions.

Chapter 3 discusses the work carried out on the design and development of the transducer. FE modelling conducted for the design optimisation and investigation of critical design parameters of the corrosion monitor is discussed in detail. The findings are supported by experimental work. The review of commercial products to select the appropriate electronics components for power and cost efficiency is presented. The results of the accelerated corrosion test conducted to evaluate the performance of the magnetic corrosion monitor are reported in the chapter.

A detailed overview of the studies on the through-thickness coverage of the transducer is presented in Chapter 4. The development and implementation of the PSO based approach to optimise the size of the magnetic excitation circuit are discussed. The experimental studies conducted to validate the proposed approach are also reported in detail in the chapter.

A description of the improvements and evaluation of long-term reliability is provided in Chapter 5. Studies on the improvement of the corrosion monitor using coupled MFL and MEC sensors are presented. The correlation techniques used for the identification of faulty sensors for improved reliability are investigated. The design of a real-life aging test for the assessment of the stability and performance of the corrosion monitor is outlined and the post-processing and analysis of the results obtained from the real-life aging test to support the proposed approach are also detailed.

Investigations on the calibration procedure are covered in Chapter 6. The possibility of using the in-situ magnetic permeability of the test specimen instead of the ***B-H*** curve is explored. The approach based on the differential evaluation (DE) algorithm to estimate the in-situ permeability using the ZCF feature on the multi-frequency EC spectrum is presented. A description of experimental findings supporting the proposed approach is included as well.

Concluding remarks and future work are summarised in Chapter 7.

# Chapter 2

# Background and Theory

## 2.1 Introduction

This chapter outlines the literature review on the widely employed corrosion monitoring techniques in the industry. An overview of the merits and demerits of the corrosion monitoring techniques is presented to support the selection of the MEC method for the development of a wireless corrosion monitor for the research project.

An in-depth description of the working principle of the MEC technique and the current work on the employment of the technique for remote corrosion monitoring is provided.

The limitations of the MEC for monitoring wall thickness and the methodology developed in the project to overcome these limitations are also detailed.

## 2.2 Corrosion monitoring

There is a wide range of definitions of corrosion monitoring in the industry, especially in the petrochemical and process industries. A simple definition would be as follows: "Corrosion monitoring is the process of tracking the change in thickness of a material over time" [30]. Corrosion monitoring may cover a broad range of processes, that involve measuring, controlling, and mitigating. However, the essential task is collecting, processing, and analysing data about the estimation of material loss with time using different testing methods [31]. It is worthwhile to mention here that the term corrosion monitoring is often confused with inspection. Inspections are performed less frequently, usually once a year or longer. Pipeline inspection gauges

(PIGs) or on-line tools are employed for conducting corrosion inspections for pipes and other equipment. In comparison to inspection, monitoring involves continuously observing the facility or pipes to detect any changes in thickness over time to control and manage corrosion through early detection and identification. Through corrosion monitoring, the safety, strength, integrity, and performance of a structure are monitored via sensors. The data acquired from sensors is used for making critical decisions on maintenance and shutdown, therefore, the reliability of the monitoring system is of prime importance.

There are many factors to be considered while choosing the most suitable corrosion monitoring strategy for pipes. The measurements of corrosion have to be often made in hostile environments which may involve high temperatures, hazardous products, and difficult access. Therefore, an effective corrosion monitoring system should meet the following criteria:

- It can be applied remotely. Most of the pipelines are buried and have thick insulation. They are difficult to access and a huge amount of labour cost is incurred for direct inspections of these pipelines. There is also a safety hazard involved since they carry very dangerous products.
- It can guarantee accurate, repeatable, and reliable results. It can generate results with high quality that need no specialist interpretation.
- It is simple and cost-effective.
- It is stable over an extended period of time for long-term application.

A number of systems are developed and employed for monitoring corrosion in oil and gas pipes. These can broadly be classified into two categories:

## 2.3 Intrusive techniques

The intrusive corrosion measurement methods involve measurement of the rate of corrosion due to process stream conditions by exposing the coupons or probes to the flow conditions. The intrusive monitoring devices usually involve fitting or mounting into access points. These access or fitting points are either installed during initial facility commissioning or retrofitted during their service life [32]. The intrusive methods for measurement of corrosion rates in the petrochemical industry range from simple and effective weight loss coupons to highly sensitive electrical resistance (ER) probes and linear polarisation resistance (LPR) probes. Some other intrusive methods include electrochemical impedance spectroscopy (EIS) and galvanic probes. The two commonly used monitoring systems available commercially are discussed in this section.

### 2.3.1 Weight loss coupons

Weight loss coupons are the original and longest-used intrusive methods for corrosion monitoring in oil and gas pipes [33–35]. They are the versatile, simplest, and easiest method for estimating corrosion rates in oil and gas plant equipment and pipes.

#### Working principle

Coupons (Metal beams) have the same chemical composition as the pipe material. These coupons are installed in the pipe at various strategic locations and angles [36].

The entire surface area of the coupon is immersed in the corrosive environment in the pipe. They are removed after a reasonable interval of time which can be weeks or months [30]. The coupons are then cleaned of all corrosion products and reweighed. The weight loss is converted into corrosion rate or metal loss. The coupon installed for corrosion monitoring and the corroded coupon removed for estimation of thickness loss are shown in Figures 2.1 and 2.2.

FIGURE 2.1: The installation system for weight loss coupons on pipeline [36].

FIGURE 2.2: The corroded coupon that is reweighed to estimate corrosion damage.

**Commercial products**

Cosasco, SMARTCORR, Q-Panel.

**Merits**

Weight loss coupons are cost-effective and simple tools that do not require skilled interpretation. They are versatile and can be applied to all environments [30]. They provide a quantitative estimate of the rate of corrosion within a system in operation. They are reliable methods as they provide physical evidence. This technique provides information on average material loss, corrosion rate, extent, distribution of localised corrosion, and nature of corrosion [37].

**Demerits**

Although the mechanism of the weight loss coupon method is relatively simple and data interpretation does not require specialised equipment and software, it is an intrusive method. It requires system shutdown during installation and removal of coupons which means a loss in production during shutdown time [38]. It is inexpensive in terms of the cost of coupons but has high requirements of labour, the hassle of field rounds, and costs associated with removal and insertion. It is also hazardous because of the exposure of operators/ labourers to chemicals and gases [30]. The data is acquired offline manually which restricts the measurement to a few data points which limits the ability to track corrosion versus process change. It also causes delayed information to the user [37].

### 2.3.2 Electrical resistance (ER) probes

ER probes are effective for remote monitoring of internal corrosion if installed in the proper location and correct orientation [39, 40]. It is an on-line measurement technique which means that the data is acquired constantly and the corrosion measurement data can be correlated with process changes. It can measure the effects of both electrochemical and mechanical components of corrosion such as erosion and cavitation [41]. ER probes are versatile and can be applied virtually to all types of environments [30].

#### Working principle

In this technique, an element of known cross-sectional area, in the head of the probe is exposed to the corrosive fluids in the pipelines. The element has the same chemical composition as the pipeline material. The electrical resistance of the probe is given by Equation 2.1:

$$R = \rho(L/A) \tag{2.1}$$

where, $R$ is the resistance, $\rho$ is the resistivity, $L$ is length, and $A$ is the cross-sectional area. The expression above shows that the resistance is inversely proportional to the cross-sectional area. The loss in the metal will result in a reduced cross-sectional area and in turn a proportionate increase in the electrical resistance. A schematic representation of the ER probe is shown in Figure 2.3.

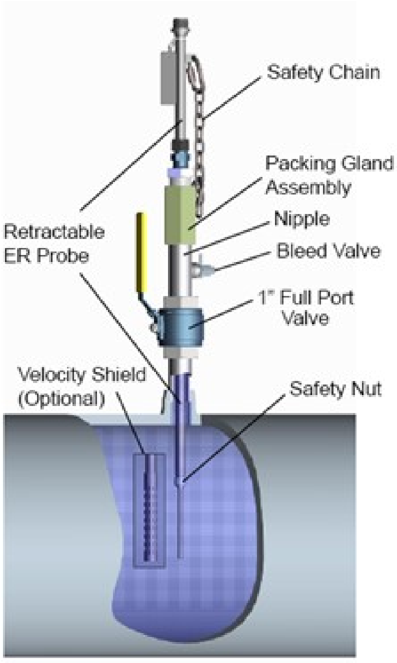

FIGURE 2.3: A common retrievable ER probe that can be installed without shutdown at specified pressure [42].

**Commercial Products**

Emersons Roxar Retractable Electrical Resistance (ER) Probe, Cosasco, EuropCORR, SmartCORR.

**Merits**

Compared to coupons, the ER method can give an on-line and continuous measurement of corrosion rates [43]. It does not have the requirement of huge labour, shutdown associated costs, and hassle of insertion and removal systems [41].

**Demerits**

The ER probe method is considered invasive because it requires direct insertion of the probe into the pipeline to expose it to the corrosive media. An access fitting hole is drilled into the pipe with a specific diameter to accommodate the device plus special mounting flanges that have to be bored and welded to ensure a seamless fit after installation [42, 44]. The probes have a lifespan of only 3 years and their re-installation poses a high risk due to the high-pressure working environments [30]. Although there are retrievable probes available that allow insertion without shutdown [43].

Intrusive methods for corrosion measurement are simple and easy to obtain qualitative results with less specialised interpretation. But they require shutdowns and intensive labour. It is difficult to inspect the buried pipelines. Therefore, the industry has focused on employing online non-intrusive monitoring sensors.

## 2.4 Non-Intrusive techniques

Non-intrusive sensors are installed on-line to monitor corrosion with time. UT gauges, optical fibre, guided waves, acoustic waves, and electromagnetic sensors are being developed for corrosion monitoring.

### 2.4.1 UT gauges

Permanently installed UT gauges have become a popular tool for real-time wall thickness monitoring of operating plants [45–47]. The ultrasonic tools are commonly used in oil and gas pipes due to the high resolution of quantitative measurement [48]. They can detect buried corrosion defects, and the confidence level of UT tools is around 95% [49].

**Working principle**

The sensors are arranged perpendicular to the wall for thickness measurement employing pulsed echo mode [50]. The same transducer emits and receives the signal. The transducer is excited by a transient high voltage to emit a short ultrasound pulse. A portion of the pulse enters the front wall. The pulse travels into the material at a certain velocity depending on the material's properties. When it reaches the boundary of the back wall and air, due to the difference in the refractive index of the two media it is reflected. The electronic tools at the receiver of the transducer measure the time of flight. The distance travelled by the ultrasonic pulse in the material is given by the expression:

$$L = t \times (\mathbf{v}/2) \tag{2.2}$$

where, $L$ = distance travelled by the pulse,
$t$ = time of flight, and
$\mathbf{v}$ = shear velocity of the pulse.

The shear velocity of the wave in the steel and products is already known and time can be calculated from the received signal. The distance of the sensor from the inner wall can be calculated which gives the thickness measurement. In typical pulsed echo UT transducers, the ultrasonic signal travels in different wave paths as shown in Figure 2.4. These are received in the signal as distinct wave packets or echoes. The time difference between echoes is calculated from the signal and multiplied by the shear velocity to get the thickness value.

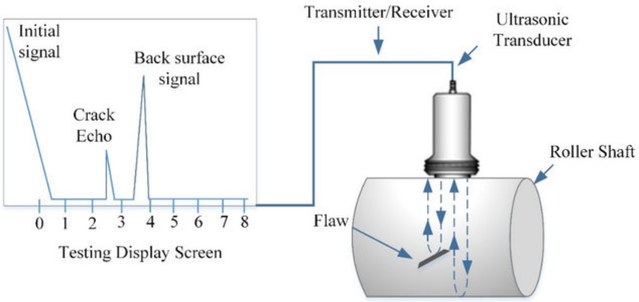

FIGURE 2.4: Schematic representation of the working principle of UT measurement [51].

### Commercial products

Rosemount™ Wireless Permasense, SMS, Wi-Corr, Inductosense WAND System.

### Merits

Ultrasonic tools are more accurate than MFL tools [32, 52]. UT tools can detect corrosion depths around ±0.3 mm to ±0.06 mm [52]. The resolution for longitudinal and circumferential wall thickness measurement is about 3 mm and 8 mm respectively [48]. The confidence level for the UT tool is around 95% which is more than MFL [49]. The calibration method is easy and simple and can directly be related to defect sizes and quantity [53].

### Demerits

The major limitation of UT tools is the requirement of a homogeneous liquid coupling agent between the pipe and the transducer due to which it cannot be used in gas pipelines [54]. This method has poor detection and sizing capability for sizing short or narrow features such as corrosion pits, pinholes, and axial and circumferential slotting [55]. The accuracy of the measurement by the UT tool is highly affected by the surface roughness and therefore, the pipe needs to be cleaned before inspection [56]. It is highly sensitive to variations in original wall thickness, bulk modulus of pipeline material, and temperature [57].

### 2.4.2 Guided waves

The guided wave ultrasonic method is a useful method for the inspection of pipe sections that cannot be accessed by PIGs or other NDE methods, such as road crossings [58]. The technique involves sending long-range acoustic waves into the pipe wall and receiving the echo signals reflected by corrosion and welds. The transducers are mounted on the pipe along the circumference.

#### Working principle

Piezoelectric crystals are used to generate ultrasonic stress waves that can travel through pipelines [59]. As there is a difference in the refractive index at the boundary between pipe and air the waves are reflected back in the pipe. Thus, the boundary of the pipe acts as a waveguide, and therefore these are called guided waves. As shown in Figure 2.5, there is constructive and destructive interference between the incident and reflected sound waves which result in a non-uniform sound intensity in the near field region. There is a critical distance beyond which the field becomes uniform. This region is called the far-field region. Therefore, flaw detection in the far-field region is more reliable.

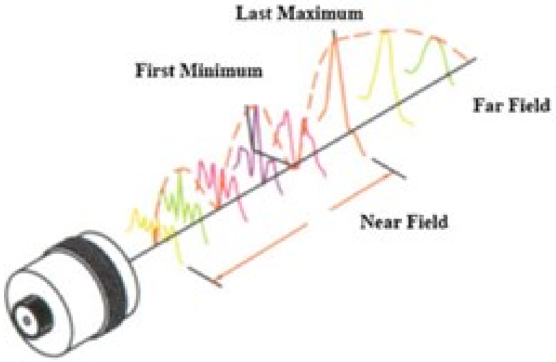

FIGURE 2.5: The UT guided wave transduction system showing near and far field [60].

Piezoelectric transducers are used to capture the waveform from the pipeline. Any defect such as cracks, pits, or corrosion results in distortion of the waveforms which can be detected by the piezoelectric sensors. A 3-D image of the internal pipe wall can be obtained by the series of consecutive axial views. This image is later analysed by an expert or an automated diagnostic system.

#### Commercial system

gPIMS

#### Merits

The guided wave transducer can detect wall loss as low as 5% of wall thickness [61]. This technique offers the possibility of rapid screening of long lengths of pipelines for corrosion and other types of defects with a typical test length being 50 m [62]. Another advantage of this method is that it can cover 360°of the pipe circumference as compared to the point thickness measurement by UT gauges [63].

#### Demerits

The ultrasonic guided wave method requires effective coupling between the transducer array and the pipe [64]. It is limited in its ability to determine the exact location and quantity of the wall loss. The application of this method is simple for straight pipes, it becomes complex for bent pipe sections. It cannot distinguish between external and internal corrosion [65]. Tests conducted on the stability of the permanently installed sensors have revealed that the signals of the sensors are highly affected by variations in temperature [66].

In addition to the non-intrusive techniques mentioned above, radio frequency identifier (RFID), inter digitated capacitance-based, surface acoustic wave (SAW), and electromagnetic guided radar are also discussed [67–70]. They need access to both sides of the pipe and have an indirect mechanism for corrosion detection [68, 71, 72]. Some commercial sensors such as corrosion radar are for the detection of corrosion under insulation that is a form of external corrosion only [70].

The discussion above shows that currently, the most viable and effective solution for remote corrosion (thickness loss) monitoring is UT transducers. However, the major drawback is the requirement of coupling agents or special mechanical devices for installation. Another major disadvantage is that they are very expensive. There is a need in the industry for a cost-effective wall thickness loss monitoring system that can overcome the limitations associated with permanently installed UT sensors.

Electromagnetic methods such as MFL, saturated low-frequency eddy current, and MEC techniques are found to be promising for the detection of both external and internal defects due to corrosion and erosion in magnetic steel components [73, 74]. Compared to UT, no coupling agent is required for these methods. They can be installed directly on surfaces with paints, and coatings. Less surface preparation is required as compared to the UT technique. The signal interpretation is relatively easy and has a high sensitivity to volumetric defects due to corrosion and erosion [75]. This is the reason electromagnetic techniques are the most popular and widely used methods for the inspection of oil and gas pipelines and storage tanks [53, 76].

In recent years, researchers have worked on the development of electromagnetic corrosion monitoring devices for tracking wall loss in mild steel structures. Zhang et al [77] developed a micromagnetic sensor to monitor corrosion from the changes in self-leakage magnetic flux. Zhang et al [78] proposed a simple MFL transducer using permanent magnet and hall effect sensor assembly to monitor corrosion in steel re-bars embedded in concrete. They found that the variations in hall sensor voltage were directly proportional to the corrosion on the steel. The results were validated through acoustic emission sensors. Li et al [79, 80] designed a corrosion monitoring device using an electromagnet and an array of hall sensors set up to monitor corrosion in steel re-bars. Ha, Seung, and Lee [81] developed a wireless pulsed eddy current (PEC) sensor for corrosion monitoring of steel framed structures.

The corrosion monitoring devices mentioned above have been designed for monitoring external corrosion only. Corrosion monitoring of oil and gas pipes requires keeping track of both internal and external wall thickness loss due to corrosion. Limited work has been done on the development of smart corrosion monitoring devices for tracking internal and buried thickness loss due to corrosion. Tsukada et al [82, 83] developed an MFL sensor for the detection of internal corrosion in steel structures using the magnetic permeability parameter. However, a major limitation of the MFL technique is the inability to distinguish between internal and external corrosion [84]. Long et al [84] have, therefore, proposed a MEC sensor that can work along with MFL sensors in the PIG to distinguish between internal and external corrosion.

The MEC technique is an adaptation of the MFL. It requires less magnetic induction as compared to the MFL technique [85, 86]. It can also distinguish between external and internal defects due to corrosion [84]. Furthermore, the signals received from MEC sensors have three features compared to only one feature (amplitude) in MFL. These include:

- Signal phase to differentiate between internal and external or buried corrosion.
- Signal amplitude to estimate the depth and size of corrosion.
- Signal shape to estimate the size/shape of corrosion.

Another major advantage of MEC is that it can be used for high-temperature applications. MFL technique relies on active magnetic sensors such as hall sensors that need to be installed close to the surface of the test specimen. Hall sensors being semiconductors have high drifts at extreme temperatures. Compared to MFL, MEC transducers are based on passive coil sensors. Coils are made of copper that has been tested at operating temperatures as high as 200°C [87]. In addition to this, the electronic system for MEC transducers can be installed at a distance from the component to avoid drift and damage due to extreme temperatures.

It is evident from the above discussion that the MEC technique outperforms MFL. Therefore, in order to design a smart MEC monitoring device, current literature on the working principle of MEC technique and advancements in the field is reviewed. The gaps in the current literature are identified and the methodology to conduct the research is also discussed in this chapter.

## 2.5 Working principle of MEC

The basic principle of the MEC technique is based on the nonlinear relationship between the magnetic field $\boldsymbol{H}$ and the induced magnetic flux density $\boldsymbol{B}$ in ferromagnetic materials. The $\boldsymbol{B}$-$\boldsymbol{H}$ curve of mild carbon steel 1002 from the materials library of Comsol Multiphysics 5.4 is shown in Figure 2.6.

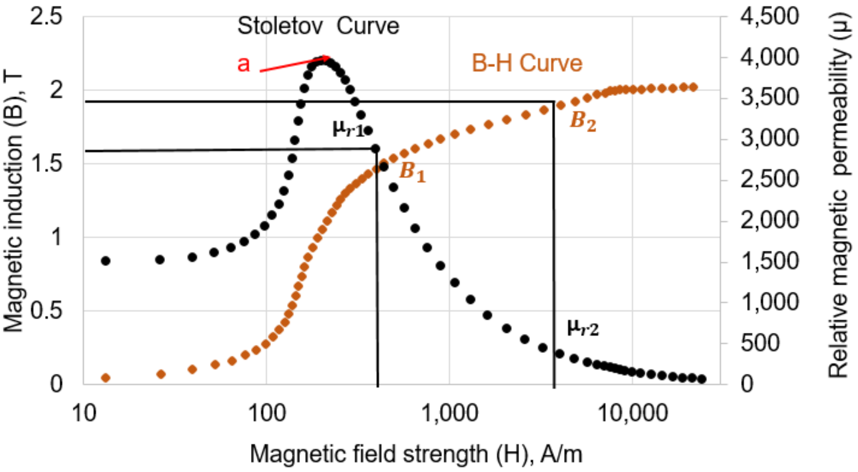

FIGURE 2.6: ***B-H*** curve for mild carbon 1002 steel from Comsol Multiphysics 5.4 material library.

When a direct current (DC) magnetic field is imposed on a mild steel sample, the increase in the induced magnetic field is higher than the applied field **H** due to the presence of unpaired electrons. Initially, there is an increase in the relative magnetic permeability $\mu_r$. However, beyond a certain point (a) in the curve, magnetic induction **B** does not increase at the same level as ***H***. This is due to the alignment of the maximum unpaired electrons in the direction of the applied magnetic field. Consequently, there is a distinct decline in relative magnetic permeability until the magnetic induction is close to saturation. The magnetic permeability of a material is its tendency to support the formation of the magnetic field inside it.

The magnetic permeability is the ratio between ***B*** and ***H*** and is expressed as:

$$\mathbf{B} = \mu_0 \left(\mathbf{H} + \mathbf{H}_m\right) \tag{2.3}$$

$$\mathbf{B} = \mu_0 \mathbf{H} \left(1 + \chi_m\right) \tag{2.4}$$

$$\mathbf{B} = \mu \mathbf{H} \tag{2.5}$$

where, $\chi_m$ is the magnetic susceptibility, $\mu_0$ is the permeability of free space, and $\mu$ is the permeability of the material under test.

Equation 2.5 shows that magnetic permeability is not a constant quantity. It is dependent on the intensity of the applied magnetic field and the induced magnetic flux density. The material properties and thickness of the test piece affect the induced magnetic flux density. When there is a wall thickness loss in the material, the induced magnetic flux density will decrease if the material is magnetised beyond a point (a), where the permeability is declining sharply. Consequently, the permeability will change. The magnetic field lines are not confined to the specimen. The magnetic flux also escapes into the surrounding air, referred to as leakage magnetic flux $\phi_{LMF}$. When there is a wall loss there will be a decrease in the magnetic permeability of the material and an increase in the leakage flux. The variation of the magnetic permeability can be detected by perturbation in the impedance of the harmonically excited coil above the sample. A schematic representation of the working principle of MEC is presented in Figure 2.7.

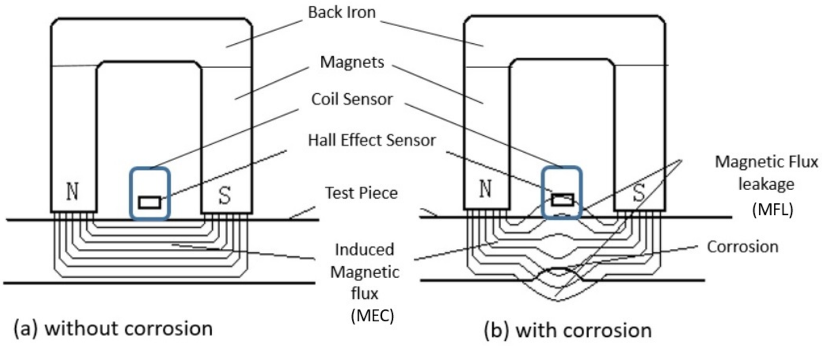

FIGURE 2.7: The schematic representation of the MEC and MFL working principle.

When a coil with sinusoidal excitation is placed above the magnetised steel sample, the magnetic field will affect the eddy current coil signal in two ways. Firstly, the depth of penetration ($\delta$) of the eddy current is increased by a few millimetres, as expressed by:

$$\delta = \sqrt{\frac{1}{\pi f \mu \sigma}} \tag{2.6}$$

where, $f$ is the excitation frequency, $\sigma$ is the electrical conductivity, and $\mu$ is the magnetic permeability of the sample. The depth of penetration of eddy current is limited to a fraction of a millimetre of mild steel owing to its high permeability. However, magnetising the sample can increase it by a few millimetres due to reduced magnetic permeability.

Secondly, the eddy current field, set up in the sample due to the time-harmonic magnetic field of the coil, will be affected by perturbations in the permeability caused by the corrosion defects. Consequently, a variation in the impedance of the coil will be experienced due to the wall thickness loss in the sample. The impedance of the coil is expressed as:

$$\mathbf{Z} = R + jX_L \tag{2.7}$$

where, $\mathbf{Z}$ is the impedance, $R$ is the resistance to the flow of the alternating current in the coil, and $X_L$ is the inductive reactance. The resistance of the coil is a function of the electric field set up by the eddy current and is sensitive to the variation in the conductivity ($\sigma$) of the sample. The imaginary part of the impedance, called reactance ($X_L$), is the opposition due to magnetic fields induced by the time-varying current and is affected by the permeability changes of the test sample.

Theoretically, the expression for calculating the perturbation in the coil impedance ($\Delta\mathbf{Z}$) placed above the sample with different metallic composition [88, 89] is given by:

$$\Delta\mathbf{Z} = Kj\omega \int_0^\infty \frac{\left(P^2\left(r_2, r_1\right)\right)}{\alpha^6} A\left(\alpha\right) \left[\phi\left(\alpha\right) - \frac{\alpha\mu_2 - \alpha\mu_0}{\alpha\mu_2 + \alpha\mu_0}\right] \tag{2.8}$$

where, $K$ and $P$ are the constants related to the coil parameters, $A(\alpha)$ and $\phi(\alpha)$ are the magnetic scalar potential and flux set up by the coil, respectively, and are a function of $\alpha$, which is related to both conductivity and permeability of the test sample. Under DC biased magnetic field, the conductivity effect is found to be negligible and the real part of the impedance can, therefore, be ignored for the sensor design optimisation [85, 90].

In summary, if the test specimen is magnetised beyond the declining point of the permeability in the ***B-H*** curve, the change in the wall thickness of the test specimen results in a sharp decrease in the magnetic permeability. This variation in the magnetic permeability is detected by the changes in the voltage or reactance of the eddy current coil.

MEC has become a proactive field of research in recent years. Most of the work is focused on the optimisation of the design of magnetisation circuits, and sizing of defects. A detailed literature review of the research work carried out on the MEC technique is presented in section 2.6.

## 2.6 Literature on MEC

Sukhikhkh and Sagalov [91] conducted experimental studies on the inspection of spent fuel elements with austenitic and ferritic steel cladding using the saturated eddy current technique. They developed a transducer with an electromagnetic magnetisation system and a differential eddy current coil sensor. Pulsed excitation with a frequency of 40 kHz was used to inspect the fuel cells. The study revealed that buried defects could only be detected with the test specimen magnetised close to saturation. The design of their MEC transducer is shown in Figure 2.8

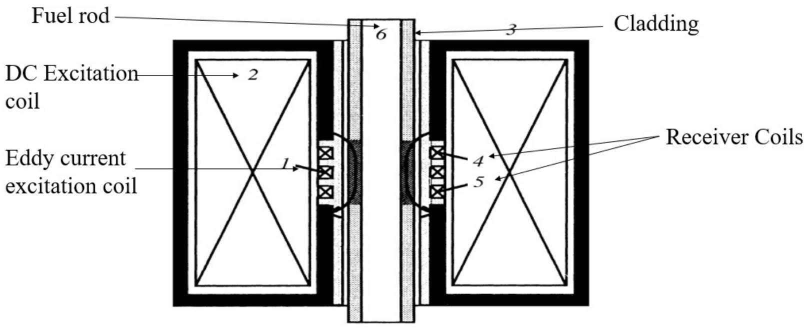

FIGURE 2.8: Design of saturated eddy current transducer for inspection of spent fuel elements [91].

Deng et al [73] proposed differential pick-up coils set up for measuring the distortion of surface magnetic permeability caused by cracks. Magnetisation of the test specimen is achieved by an encircling electromagnet. An operating frequency of 20 kHz was used for the excitation of the eddy current coil. The magnetisation current was found to have a significant impact on the detection of cracks. The research findings revealed that MEC can be used for the detection of cracks in components with thicknesses up to 15 mm. The test setup is shown in Figure 2.9.

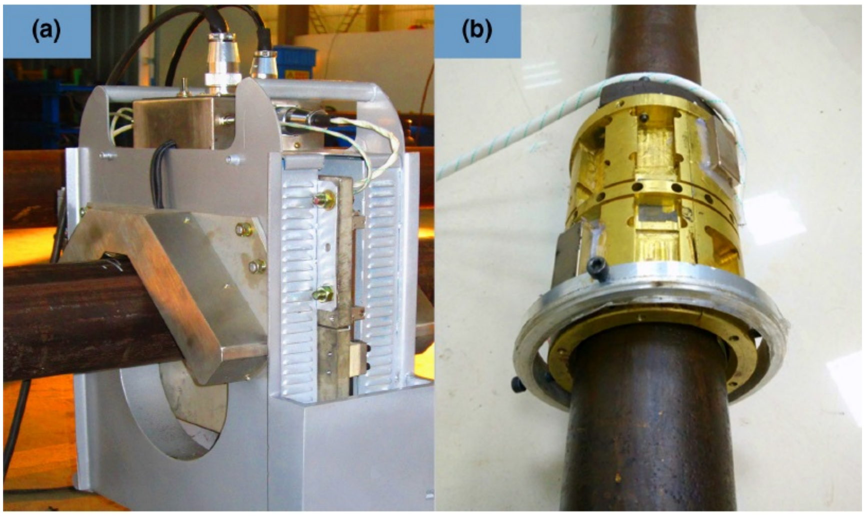

FIGURE 2.9: The permeability measuring device based on MEC technique [73].

Li et al [85] developed a DC magnetisation biased eddy current array (ECA) testing system for the quantification of buried defects. The received signal features such as width, peak amplitude, and contour orientation were related to the defect profiles using the least regression technique. The design of their MBECAT system is shown in Figure 2.10.

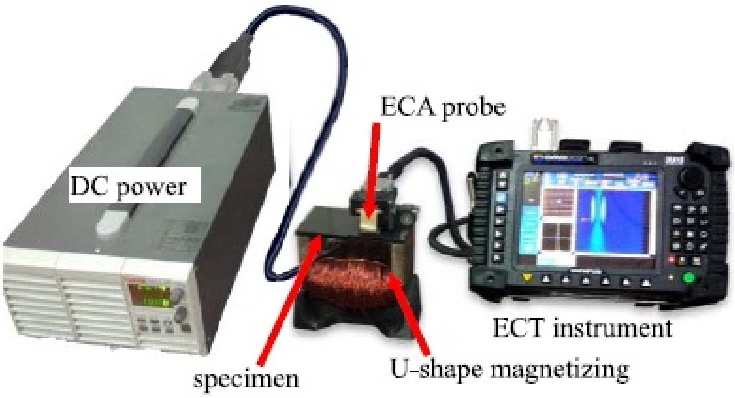

FIGURE 2.10: Magnetisation biased ECA system developed for quantification of buried defects [85].

Chikami and Fukuoka [92] utilised AC magnetisation to overcome the limitation of the test thickness using DC current. A coil with 410 turns and an operating frequency of 50 kHz for excitation were used. Their results show that the detection was different for each synchronous position. The suggested technique can, therefore, be applied for niche applications where the thicknesses of components are beyond 15 mm.

Long et al [84] proposed a MEC sensor that can work along with MFL sensors in PIG inspection to distinguish between internal and external defects. The excitation frequency of 62.5 kHz was used as the test frequency. Their research findings showed that the MEC technique has higher sensitivity and capability to distinguish between internal and external corrosion.

Studies have also been conducted to evaluate the effect of test parameters on the detection capability of the MEC technique. Ren et al [93] reported the effect of excitation frequency and magnetising current on the detection sensitivity of MEC sensors. They concluded that the excitation frequency and the amplitude of magnetising current have a strong influence on the detection sensitivity. Therefore, studies are required to find the optimal frequency and magnetic field strength.

The research works presented above reveal that the MEC transducers discussed in the literature are only intended for inspection. There is no information on the design of wireless MEC monitoring devices. The following gaps are identified in the current literature.

- The design of a power-efficient magnetisation circuit to achieve the required magnetic flux density.
- A range of test frequencies are used by the researchers for the detection of defects. From the literature review, it is evident that the excitation frequency is a crucial parameter and needs further investigation to improve the sensitivity of the corrosion monitoring device.
- The development of MEC sensors is primarily focused on inspection. Detailed research is needed to develop low-cost smart MEC monitor. Corrosion monitors should be capable of transmitting data remotely via multiple communication protocols based on the location and accessibility of the site.

### 2.6.1 Methodology for the design of smart MEC monitor

The development of the smart MEC monitor requires the design of the following essential components.

- Excitation circuit.
- Coil sensor.
- Data acquisition and processing system.
- Signal communication system.

To develop the excitation circuit and coil sensor, the critical parameters are the magnetic field intensity, induced magnetic flux density, and excitation frequency as discussed in Section 2.6. The magnetic flux induced in the test piece must produce a sharp decline in the magnetic permeability with wall thickness loss. This will ensure the detection of perturbations in the magnetic permeability with the coil sensor. Therefore, it is imperative to compute the magnetic permeability of the specimen. The computation of magnetic permeability in ferromagnetic materials requires solving the problems involving the interaction of the electric and magnetic fields. The solution to electromagnetic problems is obtained by using the Maxwell equations of electromagnetism [94].

The objective for the sensitivity of the MEC monitor is set to detect a 1 mm uniform wall thickness loss on an 8 mm thick mild steel plate. This involves the solution of magnetostatic and AC fields. As the magnetostatic and AC fields are governed by different sets of equations, a two-step approach can be used.

- Magnetostatic field involves the evaluation of the magnetic field produced by permanent magnets and the induced magnetic flux density in the material. The variation in magnetic permeability is then evaluated from the ***B*-*H*** curve. Magnetic permeability is used for the design of the excitation circuit.
- AC field is used to compute the response of the harmonically excited coil due to changes in the magnetic permeability obtained from the first step. This is utilised for the optimisation of the coil parameters and excitation frequency.

### 2.6.2 Design of excitation circuit

The magnetic field produced by permanent magnets is a field with no currents or steady current fields. This problem is solved by employing Ampere Maxwell law and Gauss law for magnetic fields [95].

#### Ampere Maxwell law

It states that "Stationary currents (not changing with time) through a surface produce a circulating magnetic field around any path that bounds that surface".

The differential form of Ampere Maxwell is written as:

$$\nabla \times \mathbf{H} = \mathbf{J} + \frac{\partial \mathbf{D}}{\partial t} \tag{2.9}$$

The above equation states that the curl of the magnetic field $\nabla \times \boldsymbol{H}$, that is, the tendency of the magnetic field to circulate is produced either by the stationary current density $\boldsymbol{J}$ or the displacement current density $\boldsymbol{D}$ or by both sources. In steady current fields, the displacement current density term is not used.

#### Gauss law for magnetic fields

Gauss' law for magnetic fields states that the magnetic flux passing through any closed surface is zero.

The law can be written in differential form as follows:

$$\nabla . \mathbf{B} = 0 \tag{2.10}$$

The divergence of the magnetic field, that is, the tendency of the magnetic field to flow away from it than towards it is zero which is analogous to the fact that magnetic field lines will always travel from the north pole to the south pole (the poles cannot be separated) and magnetic charge density must be zero everywhere [94].

The induced magnetic field in the specimen is deduced by computing the magnetic scalar potential by utilising Ampere Maxwell and Gauss laws.

Magnetic scalar potential $\Psi$ is used to determine the $\boldsymbol{H}$-field in steady or no current fields, similar to using the electric potential to determine the electric field in electrostatics. One key use of $\Psi$ is to determine the magnetic field due to permanent magnets when their magnetisation is known. In the current free fields,

$$\nabla \times \mathbf{H} = 0 \tag{2.11}$$

The magnetic scalar potential is defined as [96]:

$$\mathbf{H} = -\nabla \psi \tag{2.12}$$

Using Ampere and Gauss law:

$$\nabla.\mathbf{B} = \mu_0 \nabla.(\mathbf{H} + \mathbf{M}) \tag{2.13}$$

This can be written as:

$$\nabla^2 \psi = -\nabla.\mathbf{H} = \nabla.\mathbf{M} \tag{2.14}$$

where, $\nabla.\boldsymbol{M}$ represents the source of field due to magnets. The magnetic charge density $\rho_m$ due to the permanent magnets can thus be calculated as:

$$\rho_m = \nabla.\mathbf{M} \tag{2.15}$$

### 2.6.3 Design of EC coil sensor

The design of the coil sensor requires the solution of AC fields for optimisation of the coil parameters and excitation frequency. The coil is sinusoidally excited and the problem is solved by Faraday's Law of induction:

### 2.6.4 Faraday's law

Faraday's law demonstrates that "A changing magnetic flux in a circuit can induce an electromotive force (voltage) in any boundary path of that surface". However, these induced electric fields are very different from the fields produced by electric charge and Faraday's law gives the understanding of this phenomenon [97].

The differential form of Faraday's law is generally written as:

$$\nabla \times \mathbf{E} = -\frac{\partial \mathbf{B}}{\partial t} \tag{2.16}$$

This shows that the variation in the magnetic field with time produces a circulating electric field ***E***.

The Maxwell equations can only be applied to a medium. The medium affects the electromagnetic field through three phenomena, that is, electric polarisation, magnetisation, and electric conduction [94].

The problem for the design of the magnetising circuit and EC coil can be solved by either analytical methods or FE modelling. Analytical models are good for understanding the physical phenomena [98]. However, they are time-consuming and less accurate as they need assumptions to simplify the problem. They are not applicable to complex geometries. FE models are computationally efficient and accurate [99].

The methodology used in this research to develop the novel smart MEC corrosion monitor based on the existing literature review is presented in Figure 2.11.

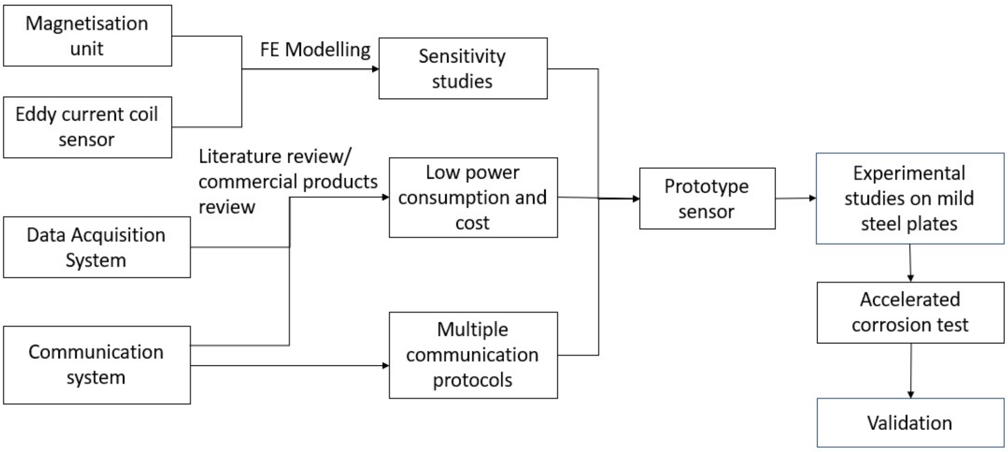

FIGURE 2.11: Flowchart presenting the methodology for the development of smart MEC monitor based on literature review.

## 2.7 Optimisation of the MEC excitation circuit

The detection capability of the MEC technique depends on the attainment of the required magnetic flux density in the test specimen. The research conducted on the design of MEC transducers has reported that the magnetising current or field is a critical factor for detecting wall loss due to corrosion [73, 93]. However, to the author's knowledge, there is no information on the optimum operating point in the ***B*-*H*** curve for MEC testing in the literature. If the sample is not magnetised beyond the point in the ***B*-*H*** curve where magnetic permeability is decreasing sharply, defects will produce a poor or no signal. Magnetising the sample beyond saturation increases the background noise and makes it difficult to distinguish signals from noise.

Furthermore, high magnetisation fields require bulky equipment with huge and powerful magnets resulting in complex handling and posing health and safety hazards. The size of the MEC transducer is crucial, especially for monitoring applications. The size of the monitoring device should be small to avoid handling and installation issues, but at the same time, it should achieve through-thickness coverage to avoid missed or poor signals.

To ensure through-thickness coverage, the induced magnetic field test component should be the same as the operating point of MEC on the ***B*-*H*** curve. The induced magnetic field in the test component is dependent on a number of factors such as thickness, liftoff, and magnetic permeability [100–102]. For different pipe diameters and thicknesses, there will be different liftoffs. This will lead to a variation in the induced magnetic flux density. Therefore, it is important to optimise the magnetising circuit parameters to achieve a high sensitivity to defects while keeping yoke sizes as small as possible for various test component configurations. The research work carried out on the optimisation of the MEC and MFL techniques has indicated that the excitation systems with optimised parameters outperform the non-optimised setups [103, 104].

The permanent magnet-based excitation yoke consists of a magnet bridge with two magnets, separated by a distance, and a metal with high magnetic permeability to close the bridge [105]. The magnetic field produced by the system depends on the dimensions of the magnets, the separation distance between the magnets, and the height of the metal bar [102, 106]. The design of the sensor requires optimisation of all these parameters to achieve a high signal-to-noise ratio with a minimum yoke size.

There are two approaches employed for the design optimisation of the magnetic excitation circuit discussed in the literature:

- Analytical approaches
- FE modelling

An analytical approach based on lumped parameter model has been proposed for multi-parametric optimisation of the excitation yoke in [106, 107]. The lumped parameter model assumes the magnetising circuit analogous to a simplified electric circuit [108]. The leakage flux is evaluated by formulating equations using Kirchoff and Ohm's law. Both researchers have implemented a genetic algorithm (GA) to achieve maximum leakage flux with a yoke of minimum size. The GA was further modified in [107] to decrease the weight of the MFL sensor without compromising its sensitivity. However, the approach is time-consuming as it requires the calibration of the lumped parameter model for each test case before implementing the optimisation algorithm.

The analytical models are complex and time-consuming. They need assumptions to form close equations, therefore, cannot be applied to complex geometries. FE modelling is the most popular method for designing MEC and MFL yokes. It is considered a reliable and efficient technique to optimise the parameters of the magnetic circuit. In most cases, the FE models are created with software packages such as Comsol Multiphysics, and Ansys [90, 109, 110].

FE packages have limited functionality for optimising multiple-parameter systems. Since they require many iterations to reach an optimum solution, they are time-consuming and computationally expensive. An efficient, less time-consuming, and easy-to-implement multi-parametric optimisation method is needed to address this problem.

A number of studies on MFL have investigated the problem of developing AI-based solutions for designing the magnetising yoke for different pipe configurations and properties. As the magnetising yoke is identical for both MFL and MEC methods, the only difference being the induced magnetic flux density in the test sample, the literature pertinent to the design of the MFL setup is discussed here.

A novel strategy based on a neuro-fuzzy model was developed by Ravanbod and Norouzi to numerically reduce the time consumed for modelling the yokes in [111]. FE models were used to create training data sets as experimental data was not available. The technique can only be employed for a rough estimation of the yoke dimensions.

A more accurate and practical approach proposed by Chang et al [103] is the implementation of a GA using the Java scripted Comsol model in MATLAB. However, it has certain limitations. GA requires many iterations to reach the optimal solution; therefore, it is tedious and computationally costly [112].

The following gaps are identified in the current literature:

- The induced magnetic flux density required to achieve a high signal-to-noise ratio for the MEC technique. Limited work is done in this context on evaluating the operating point on the ***B-H*** curve for MEC testing.
- An efficient and time-saving methodology based on AI tools to optimise the size of the excitation circuit for different test configurations while achieving maximum sensitivity (through thickness coverage).

### 2.7.1 Methodology for optimisation

The discussion above reveals that for the optimisation of the excitation system using AI, there are two techniques discussed in the literature:

- Machine learning tools
- Meta-heuristic algorithms

Machine learning tools are accurate and efficient [113] but the major limitation is the requirement of large training data sets. This means a huge computation cost and time are incurred for generating data sets using either FE modelling or experimental results.

In contrast to machine learning models, meta-heuristic algorithms do not require historical data. The algorithms generate random solutions and use them to find an optimum solution. They are not very accurate at finding the optimum solution, however, they can reach a suitable solution in situations with time and cost constraints and where historical data is unavailable.

There is a large number of meta-heuristic algorithms developed and employed for multi-parametric optimisation problems such as GA, PSO, bats echolocation, ant colony, bee colony, and DE. GA has been employed in [103] for the optimisation of yoke parameters. GA is the most popular method used for electromagnetic problems [114].

PSO algorithm similar to the GA is a population-based stochastic search method. It is superior to GA in terms of convergence and computational cost due to fewer function evaluations [114–116] . Additionally, the probability of obtaining the optimal solution for systems with an increasing number of variables is less with a decreased accuracy with GA in comparison to PSO [117]. This is the reason PSO is widely used for multi-parametric optimisation problems in electrical and electromagnetic fields [117–119]. PSO is simple, computationally efficient, and robust for multi-objective, dynamic, and fuzzy problems [120, 121].

As the design of a magnetic circuit requires multi-parameter optimisation, the PSO algorithm can produce an efficient and fast solution. Considering that the magnetisation setup for MFL is similar to MEC, the only difference being the magnetic flux density; the methodology suggested can also be used to design MFL tools.

The methodology to conduct the research on the development of PSO of the excitation system design of the MEC monitor is shown in Figure 2.12.

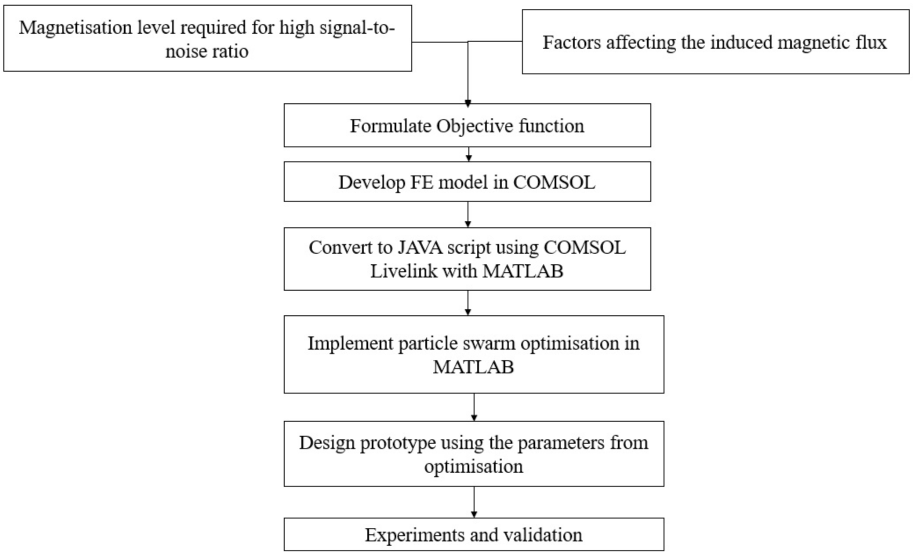

FIGURE 2.12: Flowchart presenting the methodology to develop AI based optimisation technique for MEC excitation circuit.

## 2.8 Improvement in reliability for long-term application

It is challenging to assess the long-term performance and reliability of transducers/sensors for permanent installation [122]. They cannot be calibrated and cross-checked frequently as compared to manually operated or temporary sensors [123]. Moreover, regardless of the specialised design and sophisticated maintenance procedures, the sensors will be subject to failures due to degradation introduced by aging. The failure rate of sensor systems follows a bathtub curve during their life cycle. When detailed knowledge of failure modes for an application is available, reliability can be evaluated by estimating the remaining life by conducting accelerated life tests [124–127]. Accelerated life tests (ALT) are based on critical failure modes, and by improving design against these critical failure modes, reliability can be enhanced [128–131]. ALT is widely employed by researchers to evaluate and improve the reliability of sensors and electronic devices [127, 132–136].

Some researchers have proposed a combination of ALT and real-life aging tests in the service environment to evaluate the reliability and identify critical failure modes for re-design [137, 138]. In the case of newly developed sensors whose past history is unknown, the stability and reliability of the application are evaluated by real-life aging tests [139, 140].

The long-term reliability and failure modes of sensors can be estimated by identifying the failure modes from ALT and real-life aging tests. The wear period of the sensor can then be extended by design improvements; however, it cannot be avoided. The reliability of the sensor will eventually decrease with time due to degradation caused by material aging, wear, and corrosion [122]. It can also lead to imprecise data due to drift with time. Degradation of sensors can lead to either false positive or missed signals. The sensors/ transducers will eventually fail, therefore, new approaches have been proposed in the literature to improve the long-term reliability and stability of monitoring devices over an extended period of time.

### 2.8.1 Methodology

As the aging process is inevitable, advances have been made in the prediction of long-term reliable performance via predictive maintenance [141], and predictive fail-safe [142, 143].

The predictive fail-safe technique is used more frequently for fault detection in sensors either through analytical [144, 145] or hardware approaches [146]. Guan et al [122] proposed an analytical active redundancy approach that can help in the identification of faulty sensors for sensor systems in downhole applications [147, 148]. Analytical approaches require prior knowledge about the sensor behaviour, and the service environment to identify and isolate the anomaly of the sensor from the application. This is not always possible, especially, for newly developed sensors.

The hardware approach involves using active or passive redundancy to measure the same physical quantity [122]. Multiple sensors either similar or dissimilar, are installed at the same location for recording measurements. Active redundancy has the benefits of diagnosis of sensor faults such as degradation and/or drift and isolation to ensure reliable performance for long-term applications. The faulty sensor diagnosis is carried out by specialised algorithm [149–151] or correlation analysis [152, 153] on time series data received from these sensors. Algorithms based on AI are more accurate and efficient for complex sensor networks. But compared to correlation tools, they are complicated and require extensive data from previous experiences for training and learning.

The hardware-based approach is employed for the improvement of reliability of corrosion monitoring devices in [151, 154].

The above discussion reveals that there is very limited work carried out on the development and reliability evaluation of electromagnetic corrosion monitoring devices for both internal and external corrosion. Based on the literature review presented above, the following gaps are identified in the current literature:

- There is limited work on the evaluation of long-term stability and performance of corrosion monitoring devices for tracking wall thickness loss due to internal and buried corrosion and erosion. Design of an experiment to simulate corrosion in service environments for assessing the sensitivity of corrosion monitors to wall loss is required.
- Investigations on the design of the corrosion monitoring device based on the active redundancy principle to ensure reliable operation over an extended time period.
- Development of methodology to identify and isolate the faulty sensor for the continued operation of the monitoring device.

The approach used in this research to improve and evaluate the reliability of the corrosion monitor is presented in Figure 2.13.

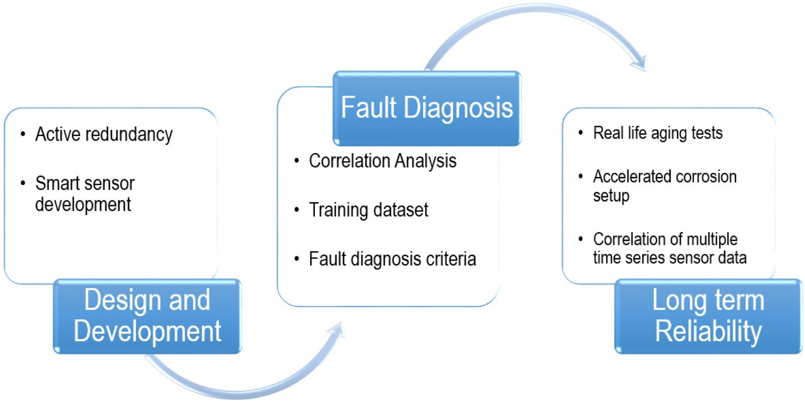

FIGURE 2.13: The methodology for evaluation and improvement of long-term reliability and stability of MEC corrosion monitor.

## 2.9 Estimation of remaining wall thickness

The objective of thickness loss due to corrosion monitoring is to produce data to assess the state of the asset for safe operation. According to API 579, an essential parameter to conduct fitness for service (FFS) for components with thickness loss is the remaining wall thickness to make decisions on the safety, repair, or shutdown [18]. Therefore, it is pertinent that the corrosion monitoring technique should be capable of indicating the changes in the remaining wall thickness of the component. Data from the monitoring devices can be used to provide warnings when wall thicknesses decrease beyond a certain point.

As the corrosion monitoring device developed in this research has both MFL and MEC sensors, literature on the sizing studies conducted for both techniques is presented in this section.

A major limitation of the MEC and MFL techniques is that they are qualitative [53]. To quantify the wall loss from MFL and MEC methods, currently, a calibration procedure is adopted in the industry. A reference block with artificially machined defects of 20%, 40%, 60%, and 80% wall loss is prepared [155, 156]. The field signals are correlated with the calibration block to roughly estimate the depth of corrosion. However, both MFL and MEC signals are sensitive to variations in lift-off, and magnetic permeability. Since the magnetic permeability of mild steel varies with the material properties, temperature, and the presence of stress, the size of the defect obtained for calibration is not accurate [86]. This is the reason magnetic methods are used as screening tools and need to be followed by UT for accurate wall thickness profiling [53].

To avoid the complex calibration procedure for quantification of corrosion depth, research is conducted to develop methods for the reconstruction of the remaining wall thickness profile. These procedures involve solving an inverse problem using analytical [98, 157] or FE forward models [158, 159] and/or machine learning/neural networks. The signals from the field tests are correlated with the modelling results using mathematical or machine learning tools to construct the thickness profile of the test component [158]. The methods also involve the implication of AI tools to estimate the defect profile based on signal features from the site test results [160].

The magnetic dipole model is widely employed for the analytical modelling of MFL fields due to defects [98, 161–164].

Though analytical models are computationally less expensive as compared to FE model [165], the accuracy is compromised due to the assumptions made for simplifications. The corrosion defect is assumed to be relatively small compared to the radius of the pipe, so the magnetic field around the corrosion defect can be viewed as uniform. The major disadvantage of the dipole model is that the amplitudes of the magnetic flux are not correctly modelled. The normalisation of the signals is required to estimate the intensity of the leakage field [98]. Therefore, it is not possible to assess the uncertainty in the depth grading of MFL measurements using the dipole model [166]. Furthermore, the lift-off is found to have a crucial effect on the sizing capability of analytical models, and a compensation technique is required [167].

FE models are more accurate as compared to analytical models [99, 168, 169] and FE modelling is a better option for complex defects geometries [170]. FE modelling is also employed for developing linear or non-linear forward models for the prediction of defect shape and size depths in MFL testing [158, 159, 171–174]. Inverse models such as GA [175], PSO [176–178], cuckoo search [179], and neural networks [171, 180–182] are suggested in the literature.

A hybrid approach for saving computational time using the analytical model as coarse and FEM as fine has also been proposed in [183–185].

Machine learning methods have also been employed to estimate the defect size, depth, and orientation from the MFL signals obtained from the experimental field results [113, 186–190].

Li et al [85] used the MEC signal features such as signal width, peak voltage, and contour orientation to estimate the depth, width, and orientation of the defects. Compared to MFL, there is limited work on the remaining wall thickness estimation using MEC.

Machine learning models require a large amount of data to train the model and estimate the parameters for the estimation of defect profile. The data set for training to estimate the learning parameters is either obtained from finite element models

[113] or experiments [171]. The achievement of test data using experimental setup is not considered feasible due to the vast variation in test configurations and steel grades involved [86]. A large computational cost is incurred to generate training data sets using FE models.

The iterative approaches mentioned above are not accurate and a calibration procedure is required for accurate estimation of thickness profiles [170]. The calibration procedure involves updating the estimated thickness profile with the thickness profile obtained from the field using other NDT techniques. This is time consuming and cumbersome procedure. An in-situ calibration procedure is, therefore, required for avoiding the complex calibration process.

There are two unknown parameters that are interdependent for the estimation of the remaining wall thickness.

- Magnetic permeability of the material under test.
- Thickness of the component.

The leakage magnetic field from the FE model is correlated with the lab test results to compute the magnetic permeability iteratively [113, 159, 171, 190, 191]. In practice, the material of the reference sample for calibration and the test sample may have different magnetic permeability. The magnetic permeability is not constant and is dependent on stress, temperature, and other factors [86, 162]. As a result, even after calibration with the reference sample, the defect profile may not be accurate. Consequently, the identified defect often needs to be determined or tested by an alternative NDT technique, for example by ultrasound testing, since the relative permeability of the pipe is usually not known [86]. Often this is not a viable option and even when available it is time-consuming and expensive.

A solution to avoid this calibration procedure is proposed by the patented Innospection's partial saturated eddy current sensor [86]. The sensor comprises the magnetic field sensor to compute the apparent magnetic permeability at the location of the sensor and ensure the required level of magnetic field is induced in the test specimen, and an EC sensor to evaluate the defect sizes.

However, magnetic sensors such as hall effect sensors indirectly measure the magnetic permeability from the leakage magnetic fields. Furthermore, due to the magnetic compression effect at high background magnetic fields, the volume of the leakage magnetic field is less than actual [192]. Therefore, for samples magnetised close to saturation, this could lead to inaccuracies.

The following gaps are identified in the existing literature from the discussions presented above:

- The calibration procedure for estimating the thickness profile of the corroded sample is cumbersome and inaccurate. An in-situ accurate and computationally efficient calibration procedure is required for the evaluation of the magnetic permeability to develop the forward FE model based on actual material properties and test configurations.
- A fast and computationally efficient inverse model to evaluate the remaining wall thickness.

### 2.9.1 Methodology

Compared to hall effect sensors, EC testing is widely used for evaluating the magnetic permeability of mild carbon and metallic steel [193–199].

Since the permeability of low carbon steel is complex and frequency-dependent [200], multi-frequency eddy current data is used to extract signals' features sensitive to relative magnetic permeability [201–204]. Efforts are also being made to separate the effect of conductivity and liftoff from magnetic permeability [205]. Researchers have found that the relative permeability of mild carbon steel samples could be derived with a small error of 0.61% [201].

Phase signature has been used for the determination of permeability in metallic steel in [206]. The studies conducted by Zhu et al [207] have revealed a linear relationship between relative permeability and ZCF. A number of researchers have reported ZCF feature invariant to liftoff and sensitive to variation in magnetic permeability [208–210].

It is evident from the discussion that for mild carbon steel ZCF feature is sensitive to relative magnetic permeability. Liftoff invariant compensation techniques are also being developed in the literature, but as this research is focused on the permanently installed corrosion monitoring device, variations in the liftoff can be ignored.

Based on the literature presented in this section, the methodology to estimate the remaining wall thickness is presented in Figure 2.14. A DE algorithm is developed to formulate the inverse problem as it has better performance in solving problems with low dimensions [211].

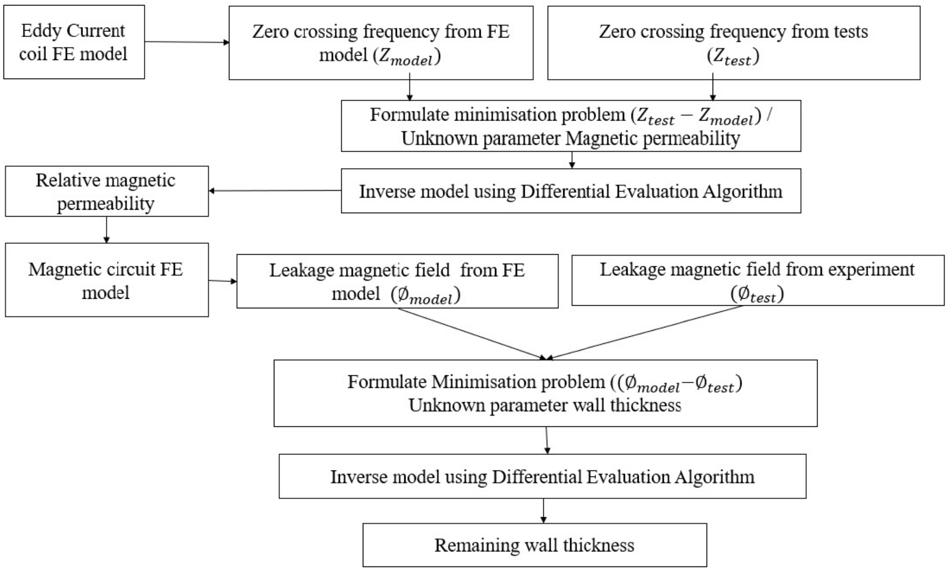

FIGURE 2.14: The methodology for estimating the remaining wall thickness from the corrosion monitor.

A detailed literature review of the prospects of the MEC technique for remote corrosion monitoring was presented in this chapter. The aim of the review was to identify the gaps in the current literature on the through thickness coverage, reliability, and calibration of the magnetic corrosion monitor. Furthermore, this chapter also established the methodology to conduct the research project to address these gaps.

In the review, it was found that while a number of studies are conducted on developing MEC sensors, they are mostly related to inspection purposes. There is little work on the design of MEC sensors for remote corrosion monitoring. The significant factors that need to be considered for the design of a permanently installed corrosion monitor are sensitivity, cost, and power efficiency. Therefore, a methodology was proposed to consider these in the development of the magnetic corrosion monitor.

A major drawback of the MEC technique is the bulky and heavy magnetic excitation circuits that can be optimised using analytical and FE modelling approaches as discussed in this chapter. However, these are iterative in nature and time-consuming. To reduce computational time and cost, a PSO-based technique is proposed for reducing the size of the magnetic excitation circuit without compromising sensitivity.

To improve the reliability a magnetic corrosion monitor based on the active redundancy principle will be developed in the project. The concept of coupled sensors discussed in the literature was presented in this chapter. This will be extended further for devising a method for the identification and isolation of faulty sensors to avoid false alarms and missed signals.

In order to avoid calibration using reference blocks, a calibration procedure based on in-situ magnetic permeability estimation is proposed. This will address errors in the evaluation of wall thickness loss due to changes in material properties or test configurations.

The work carried out on the design and development of the smart corrosion monitor is discussed in Chapter 3.

## Chapter 3

# Development of smart MEC Transducer

### 3.1 Introduction

This chapter presents the work carried out on the development of a low-cost and power-efficient smart MEC corrosion monitoring device. The experiments designed and conducted to evaluate the performance of the monitor for detecting uniform wall thickness loss are also discussed. The essential components that need to be designed for the development of the wireless MEC monitor are as follows:

- MEC transducer with the excitation circuit and EC coil sensor.
- Data acquisition unit to acquire, convert and store the signals from the coil sensor.
- Signal communication system to send data through wireless protocols.

### 3.2 Design of MEC transducer

The excitation circuit of MEC consists of permanent magnets and a back iron bridge with high magnetic permeability to complete the magnetic circuit and focus the magnetic field in the test specimen. The MEC technique requires powerful magnets to achieve a high magnetic flux density in the test specimen. The magnetic induction in the material should be at the point where the change in wall thickness leads to a sharp decline in magnetic permeability. The ***B-H*** curve of mild carbon steel reveals that this can be achieved by magnetising the test component to and beyond 1.4 T [212].

To design the magnetisation unit, therefore, it is imperative to ensure that the magnetic field induced in the test specimen is above 1.4 T. The magnetic field produced by permanent magnets is determined by the working point/operation point in their demagnetisation curve. The demagnetisation curve of commercially available permanent magnets is shown in Figure 3.1.

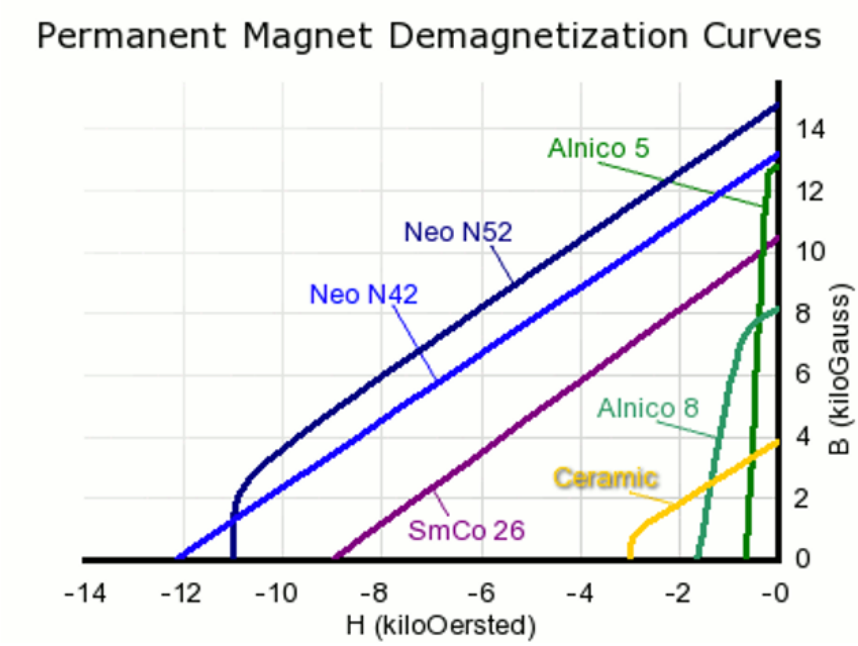

FIGURE 3.1: Demagnetisation curve of commercially available magnets [213].

The comparison of different properties of the demagnetisation curves of the commercially available magnets are listed in Table 3.1.

TABLE 3.1: Properties of commercially available permanent magnets [214, 215].

| | Ferrite | Alnico | Samarium Cobalt | | Neodymium | |
|---|---|---|---|---|---|---|
| Property | Ceramic 8 | Alnico5 | 1:5 | 2:17 | Bonded | Sintered |
| ***Br*** (T) | 0.38-0.42 | 1.1-1.25 | 0.8-0.96 | 0.95-1.10 | 0.6-0.7 | 1.0-1.4 |
| ***Hci*** (kA/m) | 242-236 | 50 | 1100-2000 | 600-2000 | 600-1200 | 950-2700 |
| Tc (Curie Temp) | 460°C | 890°C | 727°C | 825°C | 360°C | 310 °C |

The parameters such as remnant flux density and/or the coercive magnetic field strength (magnetic field required for the demagnetisation) are used for the computation of the magnetic field produced by them. Remnant flux density is the intrinsic property of the magnets. The coercivity defines the magnetic field intensity produced by the magnets. Though alnico magnets can operate at high temperatures, their demagnetisation field is very low (50 kA/m) as compared to ferrite and neodymium magnets. Samarium cobalt magnets are very brittle [216], and require special care during installation to avoid breakage. Therefore, ferrite and neodymium magnets were used for modelling the excitation system.

The coil sensor and the excitation circuit were modelled using FE to evaluate their design parameters.

### 3.2.1 FE Modelling

The numerical modelling of the MEC transducer in Comsol Multiphysics 5.4 was performed using a two-step approach. Initially, the magnetic excitation circuit was modelled in magnetic fields without currents in order to optimise the yoke design parameters. An optimisation study was then performed in the frequency domain of the magnetic fields module for the eddy current coil sensor. The aim of FEA was to:

- Determine the size of the excitation unit for commercially available magnets to detect a 1mm uniform thickness loss in an 8mm thick plate.
- Calculate the size parameters of the probe (magnets, coils, and the back iron).
- Acquire the optimal excitation frequency for the coil sensor.

#### Geometry and material properties

A three-dimensional parametrised model of the magnetic circuit was built in the steady magnetic fields module. The length, width, and height of the magnet were defined as the parameters for achieving the magnetic induction of 1.4 T in the test specimen. A liftoff of 1 mm was introduced between the excitation circuit and the test specimen to accommodate for the distance between the MEC probe and the test specimen.

An 8 mm thick plate was used as the test specimen and the thickness of the plate was decreased in increments of 1 mm to simulate uniform wall thickness loss. A spherical air domain was defined around the magnetic excitation circuit to truncate the model at a reasonable distance where the effect of magnetic field is considered to be negligible. The magnetic insulation boundary condition was applied to compute the flux densities in the truncated region. The geometry of the magnetic excitation circuit built in Comsol Multiphysics and the parameters defined for computing the yoke sizes are presented in Figure 3.2.

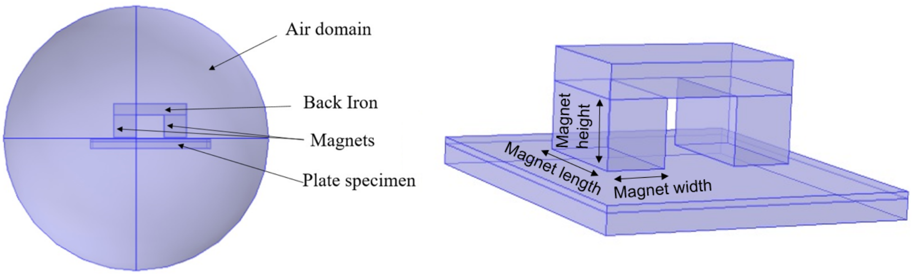

(a) (b)

FIGURE 3.2: (a) The geometry of the excitation circuit, and (b) The parameters computed from the FE model to achieve magnetic induction of 1.4 T in the test specimen.

The material properties defined for the different components of the model are presented in Table 3.2 [217, 218].

TABLE 3.2: Material properties defined in the FE model.

| **Description** | **Material** | **Properties** | |
|---|---|---|---|
| Magnet No.1 | Neodymium | Magnetisation | 835 kA/m |
| | | Relative Permeability | 1.05 |
| | | Electrical conductivity | 1x10$^6$ S/m |
| Magnet No.2 | Ferrite | Magnetisation | 240 kA/m |
| | | Relative permeability | 1 |
| | | Electrical conductivity | 1x10$^7$ S/m |
| Plate specimen | Mild carbon steel | Relative permeability | ***B-H*** curve |
| | | Initial permeability | 150 |
| | | Electrical conductivity | 10$^6$ S/m |

### Meshing

The mesh convergence study was conducted to reduce the difference between the approximate FE and the actual solution. Though mesh refinement results in decreasing the difference between the approximate and actual solution, computational time and cost are increased. Therefore, an iterative approach is adopted to find the optimum mesh size for the convergence of the solution. An adaptive mesh technique with free tetrahedral mesh was used. The mesh parameters were refined until no more variations in the flux values were observed after further refinement. The magnetic flux density was computed at three different locations. Figure 3.3 shows the locations where the flux densities were calculated and the convergence results for one of these locations.

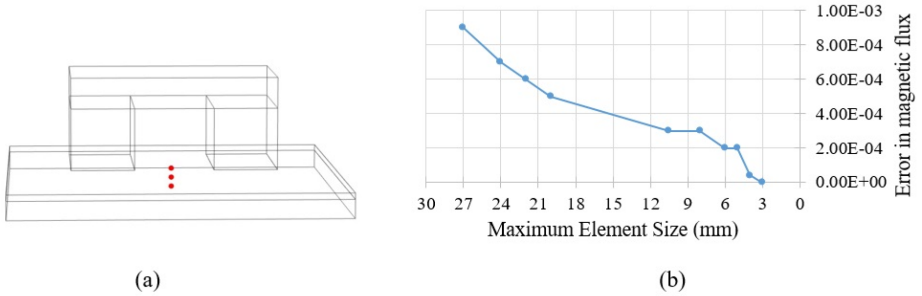

(a) (b)

FIGURE 3.3: (a) The locations for the points at which the magnetic flux was computed for mesh convergence study, and (b) The graph showing the decrease in the error between the flux values with improved mesh refinement.

It is evident from the Figure 3.3 that the error does not change proportionately with the variation in the mesh size. This is because for large mesh sizes, the computed magnetic flux density changes randomly after each iteration. The mesh parameters at which the results were found to converge are listed in Table 3.3.

TABLE 3.3: The parameters of the mesh deduced from the mesh convergence study.

| Element size parameters | Values |
|---|---|
| Maximum element size | 3 mm |
| Minimum element size | 0.05 mm |
| Maximum element growth rate | 1.3 |
| Resolution of narrow regions | 1 |

### 3.2.2 Results

A stationary parametric study was carried out to evaluate the optimum size of the yokes required for ferrite and neodymium magnets to achieve a magnetic induction of 1.4 T in the plate specimen. The results are shown in Figure 3.4 and listed in Table 3.4.

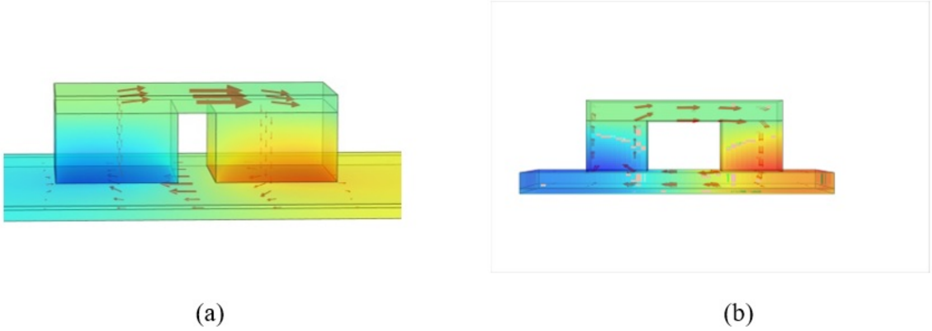
(a) (b)

FIGURE 3.4: (a) FE model of the excitation circuit with ferrite magnets' yoke, and (b) FE model for the excitation circuit with neodymium magnets' yoke.

TABLE 3.4: The dimensions of the ferrite and neodymium magnets computed from the FE model of the excitation system.

| **Parameter** | **Ferrite (mm)** | **Neodymium (mm)** |
|---|---|---|
| Pole width | 80 | 20 |
| Length | 80 | 40 |
| Height | 50 | 20 |
| Distance between magnets | 25 | 25 |

The results indicate that for ferrite magnets, the comparative size of the excitation circuit is almost three folds. Though the temperature performance of neodymium magnets is poor as compared to alnico and ferrite magnets, these are a more suitable choice for applications at temperatures of 60°C or below. Furthermore, the size of the transducer also affects the estimation of the wall thickness loss as the technique averages the area covered by the transducer. The signals obtained for deep and narrow defects are similar to those of wide and shallow defects. The large size yoke also limits the installation of the monitor on small diameter pipes with limited access. Therefore, the neodymium magnet excitation system with dimensions of 65x40x40 mm was chosen for further study.

Since the EC coil sensor requires the solution of the AC field, this cannot be modelled using the magnetostatic module. Due to the limited depth of penetration of eddy current, the thickness loss cannot be simulated as the change in plate thicknesses. The wall thickness loss is simulated as the variation in the relative magnetic permeability caused by the static field. To compute the changes in the relative magnetic permeability of the plate specimen due to uniform wall thickness loss, the thickness of the simulated plate was decreased from 8 mm to 4 mm with the increment steps of 1 mm. The FE model illustrating the increase in the flux density due to 50% uniform wall loss in an 8 mm thick plate specimen is shown in Figure 3.5.

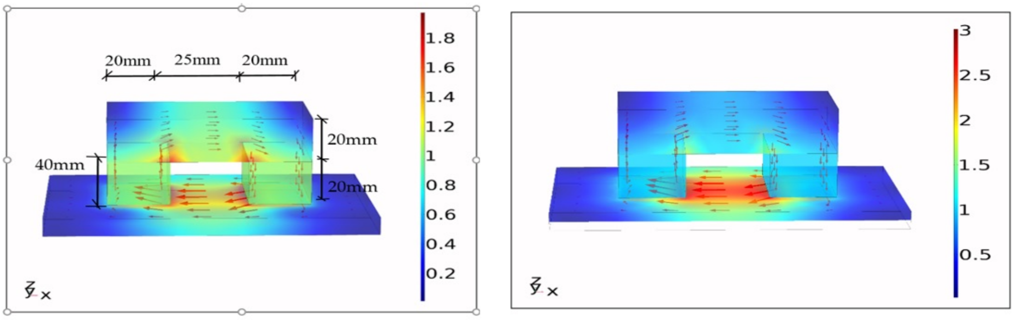

(a) (b)

FIGURE 3.5: The FE model for magnetostatic study; (a) The flux density distribution in an 8 mm thick sample, and (b) The comparative increase in the flux density distribution in a 4 mm thick plate.

The magnetic flux densities were computed at 1 mm equidistant points on the area covered by the coil sensor (i.e. the separation distance between the magnets). The ***B-H*** curve of mild carbon steel 1002 from the Comsol Multiphysics library was used for calculating the relative magnetic permeability. The variation in the relative magnetic permeability due to uniform wall thickness losses of 1 mm, 2 mm, 3 mm, and 4 mm in an 8 mm thick plate were computed. The variation in the magnetic flux densities and relative magnetic permeability due to uniform wall thickness loss in the 8 mm plate is shown in Figure 3.6.

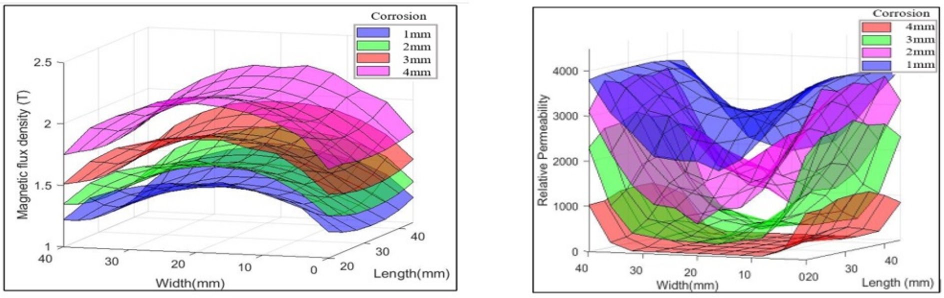

(a) (b)

FIGURE 3.6: (a) The values of the magnetic flux densities in plates with different thicknesses from the FE model, and (b) The permeability evaluated from the flux densities for the uniform wall loss of 1 mm up to 4 mm for the 8 mm thick plate.

The surface plot representing the flux densities in Figure 3.6 is not smooth due to the uneven variation in the flux. Since mild carbon steel is a non-linear magnetic material, the variation in the magnetic flux due to the wall thickness loss is not linear or constant at different locations between the magnets.

### 3.2.3 Design of coil sensor

The optimisation of the excitation frequency was carried out in the frequency domain of the magnetic fields module. For frequency-dependent studies, a fine mesh is needed for convergence. To save computation cost and time, a 2-D axis-symmetric model was built. The dimension and number of turns in the coil cannot be increased because of the limited space between the magnets. The increase in the number of turns and size of the coil sensor will increase the sensitivity but lead to a need for increasing the separation distance between the magnets. This will eventually decrease the magnetic field thus decreasing the magnetic induction. The coil parameters used for the modelling studies are listed in Table 3.5.

TABLE 3.5: The coil parameters used for modelling the EC coil sensor.

| Coil parameter | Values (mm) |
|---|---|
| Internal diameter (ID) | 10 |
| Outer diameter (OD) | 18 |
| Height | 15 |
| No. of turns | 350 |

### Mesh convergence study

Since the frequency domain study involves the solution to the electromagnetic wave propagation problem, mesh convergence is difficult to achieve. Therefore, a quasi-static approach is used to solve the frequency domain problems. The assumption is made that the speed of propagation of electromagnetic waves is finite and the fields can be calculated from the stationary currents at every instant. This means that to capture the propagation of the waves, the size of the mesh element should be smaller than the wavelength [219]. Therefore, for the convergence of results, a very fine mesh is required for computing fields at higher frequencies.

Furthermore, for modelling eddy current, the skin effect has a significant impact on the convergence of results. During the mesh convergence study, it was observed that the results did not converge even when the element size was reduced to 0.1 mm. In order to solve this problem, for the boundaries near the sites of eddy current coils, an adaptive mesh was defined. The resolution of boundary regions perpendicular to the eddy currents was increased to achieve convergence as shown in Figure 3.7.

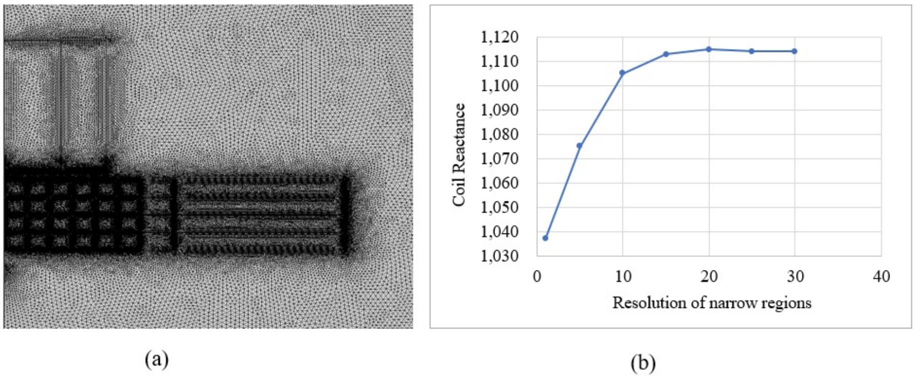

(a)

(b)

FIGURE 3.7: (a) The adaptive mesh used for modelling the coil, and (b) the convergence of coil reactance with increasing resolution of narrow regions.

### Results

A parametric study was conducted where the frequency was swept from 1 kHz to 300 kHz with an increment of 10 kHz. The relative magnetic permeability computed from the first step was assigned to the plate specimen in the coil model. The solved FE coil model and the solution for the parameters at 100 kHz are presented in Figure 3.8.

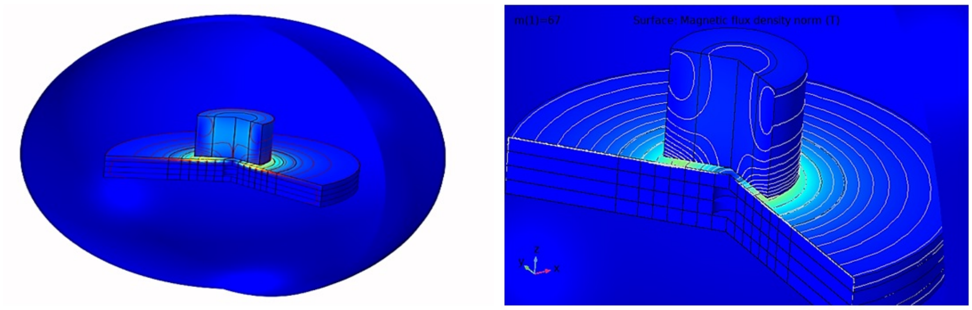

(a) (b)

FIGURE 3.8: (a) The 2-D axis-symmetric FE model, and (b) the solution for coil parameters at 100 kHz frequency.

The reactance computed for different frequencies has values in a wide range. The reactance values were normalised to show the comparison. The inductive reactance of the 8 mm thick plate was considered as the reference for normalisation. The response of the coil sensor for the range of frequencies obtained from the FE model is shown in Figure 3.9.

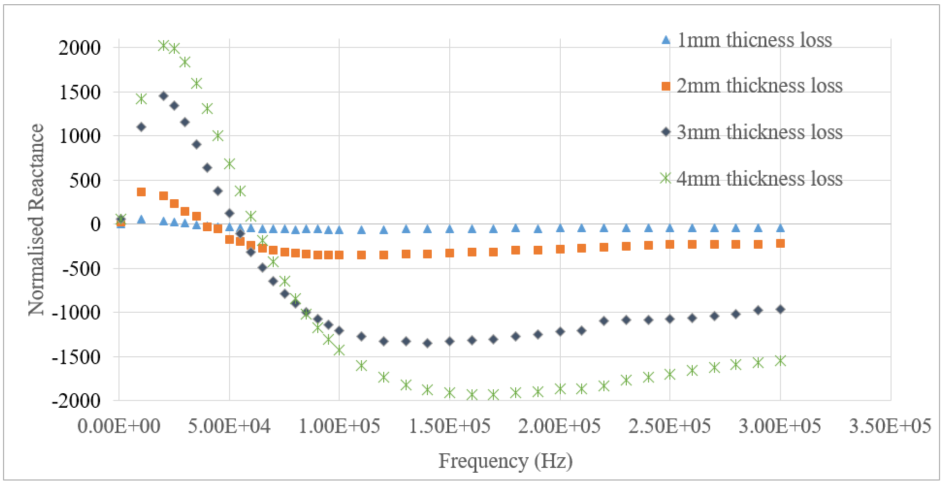

FIGURE 3.9: The normalised reactance values for test plate specimens at different thicknesses.

It is evident from Figure 3.9, that the variation in the inductive reactance due to changes in the thickness is frequency dependent. The sensitivity of the eddy current coil sensor has two peaks in the multi-frequency spectrum. There is an increase in sensitivity at lower frequencies until a certain frequency is reached. It starts to decrease and becomes zero at the frequency called the zero crossing frequency. At higher frequencies, it starts to become increasingly negative. A second optimal frequency is observed at higher frequencies where the variation in the reactance values is highest due to the change in thicknesses. A very small variation in sensitivity occurs after this point. The FE model Comsol file is attached in Appendix A.

The modelling results seem to align with the literature findings cited in the previous chapter i.e. there are two operating frequencies at which the sensitivity of the coil sensor is maximised. It is significant to consider the optimisation of the frequency to achieve maximum sensitivity. This needs to be validated by experiments.

## 3.3 Design of data acquisition system

To measure the complex impedance, the ADC should be capable of sampling the analog signals at a faster rate for the measurement of complex impedance. AD5933 impedance converter and network analyser is developed by analog devices for the measurement of complex impedance in electrochemical, bioelectric impedance, impedance spectroscopy, and corrosion monitoring [220–222]. It is a high precision impedance analyser chip with a sampling rate of 1 MHz samples per second [223]. It has an onboard frequency generator for exciting the device under test (DUT) at a certain frequency. The onboard digital signal processing (DSP) engine carries out the discrete Fourier transform (DFT). The DFT algorithm returns the value of the real and imaginary parts of the impedance. The block diagram of AD5933 and the Pmodia board based on AD5933 used in the study is shown in Figure 3.10.

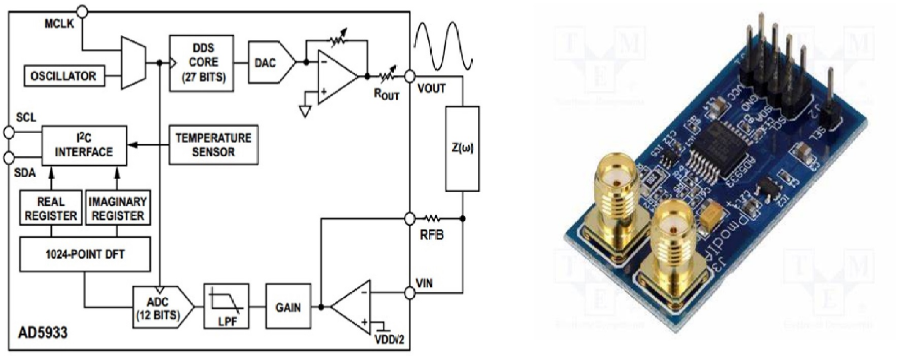

(a)

(b)

FIGURE 3.10: (a) The block diagram of AD5933, and (b) Pmodia board based on AD5933 for I2C interface

The frequency range for performing the frequency sweep is 1 kHz to 100 kHz. However, the impedance at higher frequencies can also be computed with a small error [224].

To measure the unknown impedance using AD5933, the system needs to be calibrated using a simple inverting amplifier (resistor of known impedance). The value of the inverting amplifier should be related to the range of the unknown impedance by the following relationship:

$$R_{fb} = \frac{\mathbf{Z}_{min} + \mathbf{Z}_{max}}{3} \tag{3.1}$$

where, $\mathbf{Z}_{min}$ is the minimum unknown impedance value and $\mathbf{Z}_{max}$ is the maximum unknown impedance value.

The inverting amplifier senses the current in the unknown impedance and converts it into voltage [224, 225]. The gain factor is calculated by the formula:

$$GainFactor = \frac{\left[\frac{1}{Impedance}\right]}{Magnitude} \tag{3.2}$$

When the DUT is connected to the board, the measurements are multiplied by the gain factor evaluated in the calibration step and then the impedance is calculated.

Both the imaginary and real parts of the impedance, along with the phase, are computed.

AD5933 requires a 3.3 V DC power supply and has the option to excite the DUT at four different voltage ranges. It is recommended to use the highest voltage range for less noise in the signal. Therefore, 2 Vp-p was used as the excitation voltage.

AD5933 based Pmodia board has an I2C interface to connect it with the microcontroller to program frequency sweep and store the data before transmission.

ATmega328P was used as the microcontroller because of the following advantages over other commercially available products.

- Compared to the advanced microcontrollers (STM32, and RP2040) that are 32-bit, they are 8/16-bit and easier to program. They do not have complex hardware and do not need core programming. For applications where advanced functions with multi-peripheral applications are not required, Atmega328P is a good choice.
- Atmega328p based boards are compact and are ideal for applications with limited space.
- Atmega328P is power economical compared to Atmega328 and STM32 [226].
- Compared to the Atmega328 and STM32 they are cheaper and simple to use [227].
- Because of their popularity and wide usage, they are easily available.

The codes for programming the microcontrollers were written in C++ using the Arduino IDE interface. The code is attached to Appendix B.

## 3.4 Design of communication system

For the design of the communication system, it is important to consider the communication constraints at the location of the installation of the corrosion monitor. The communication system was developed on three different communication protocols as discussed below:

### Wi-Fi

Wi-Fi is the most commonly used data transmission technique where there is access to the wireless area network. ESP8266 is a widely used Wi-Fi module for wireless sensors [228, 229]. ESP8266 is a low-cost Wi-Fi microchip, with built-in TCP/IP networking software, and microcontroller capability [230]. It has GPIO pins for the I2C interface with AD 5933 and 10-bit microcontroller. It is widely used for IoT applications and its reliability is well established for permanent monitoring applications. The ESP8266 microcontroller was programmed to perform the frequency sweep and send the data to the data cloud through Wi-Fi. The setup is discussed in C hapter 4.

### Radio frequency transceiver and Wi-Fi

At places where the Wi-Fi network is not close or the signals are weak, radio frequency transceivers can be attached to the sensor. NRF24L01 is attached to the Atmega328p microcontroller to transmit the signals. NRF24L01 is low-cost and easily programmable with Atmega328p [231]. It has a communication range of 100 m and works on a frequency band of 2.4 GHz. A gateway was designed with NRF24L01 connected to Node MCU ESP8266. The transceiver was programmed with ESP8266 MCU to receive the signals. The signals were sent to the data cloud using the Wi-Fi module. The block diagram is shown in Figure 3.11.

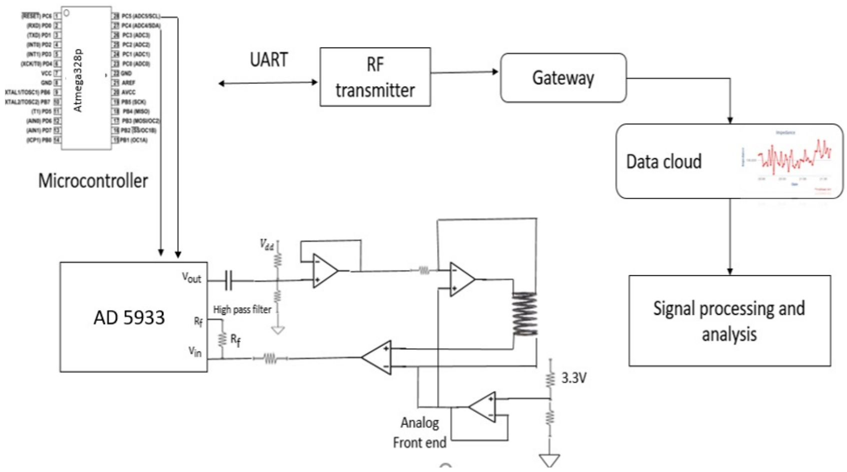

FIGURE 3.11: (a) The block diagram of the data acquisition and RF transceiver-based communication system.

**Cellular network**

The cellular network is the best option for long-range communication. They are the most widely used options for IoT applications. Though they are reliable and have high data quality, they are power-hungry and expensive. But they are good at locations where there are no nearby routers. TTGO T-Call is a new ESP32 development board that combines a SIM800L GSM/GPRS module that was programmed to send the data from the MEC sensor through sim data.

The programs written for the corrosion monitors are attached in Appendix B.

## 3.5 Experimental studies

### 3.5.1 Frequency optimisation

To validate the results obtained from the FE model and evaluate the optimal frequency for the MEC corrosion monitor, experiments were conducted.

The prototype transducer built using the dimensions evaluated from the magnetostatic FE model is shown in Figure 3.12.

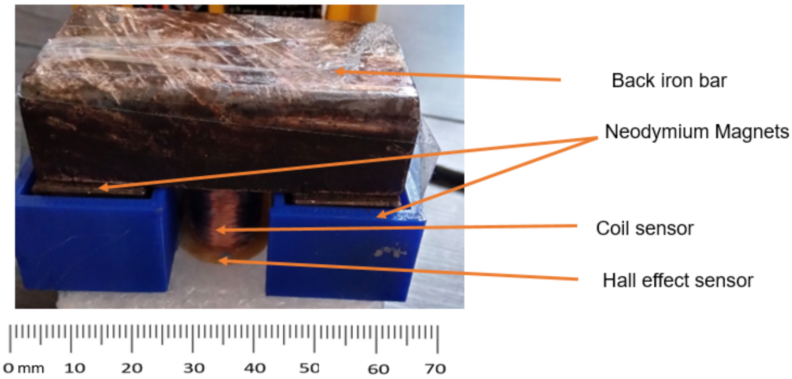

FIGURE 3.12: The prototype MEC transducer.

Mild steel plates of thicknesses 4, 5, 6, 7, and 8 mm were tested. The reactance value obtained for the 8 mm thick plate was considered the reference value. The results were normalised by subtracting the coil sensor reactance from the reference value. The results are illustrated in Figure 3.13.

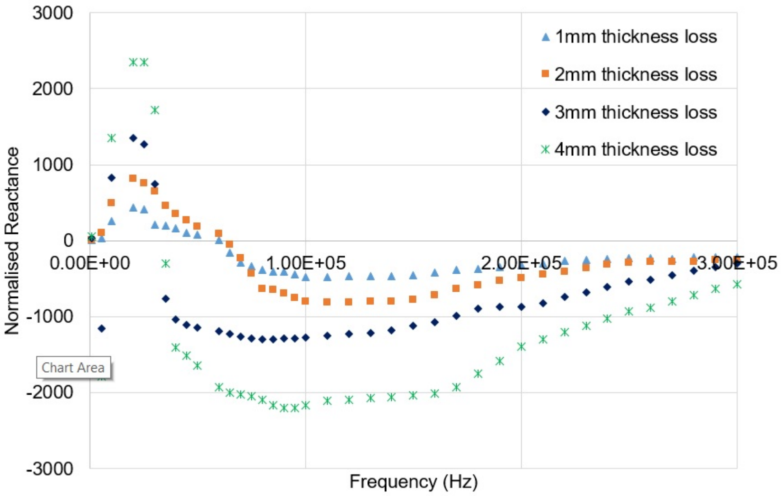

FIGURE 3.13: The normalised reactance values for test plate specimens at different thicknesses.

Figure 3.13 validates the FE modelling results. The sensitivity of the eddy current coil sensor is frequency-dependent. There is a significant effect of the excitation frequency on the detection capability of the sensor. It is clear that there are two optimal frequencies (20 kHz and 100 kHz) that can be used as operating frequencies for sensor design.

Though the trends in the change in sensitivity were found to be identical with the frequency for both the FE model and the experiment results there were some disagreements.

- The ZCF for the FE model moved from 35 kHz to 54 kHz when there was 50% wall thickness loss in the 8 mm thick plate. However, the same shift in the ZCF was not observed from the experimental results.
- The optimal frequency for the detection of 1 mm uniform thickness loss in the 8 mm thick plate was 100 kHz in experiments. This was predicted in the modelling results to be about (140 kHz).

These differences in the modelling and experimental results are expected to be due to the limitations of modelling magnetic materials close to saturation. For non-linear magnetic materials such as mild carbon steel, it is not always possible to evaluate and assign the actual magnetic properties on a point-to-point basis in the FE model

[232]. The magnetic properties are dependent on a number of factors such as temperature, presence of stress, and applied magnetisation field. It is, therefore, impossible to evaluate these accurately. Moreover, detailed information is not available from the manufacturers. FE models can give an indication of the trends and results but they are not definitive. The comparison of the FE model and experimental results shows that the disagreement was more obvious for low-thickness plates where the magnetic induction is close to saturation. This is because of the limited capability of the software to solve magnetic saturation phenomena.

For 1 mm uniform wall loss in the 8 mm thick plate, both FE models and experimental results were found to be in agreement as shown in Figures 3.14 and 3.15.

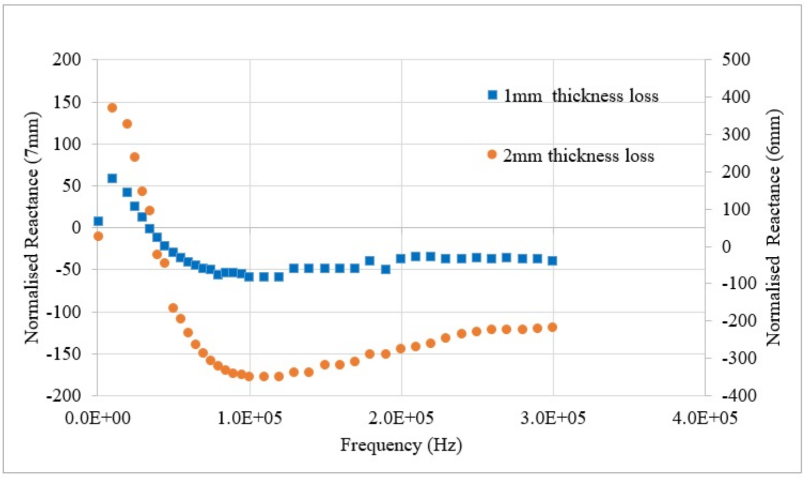

FIGURE 3.14: The normalised reactance values computed from the FE model for 7 mm and 6 mm thick plates.

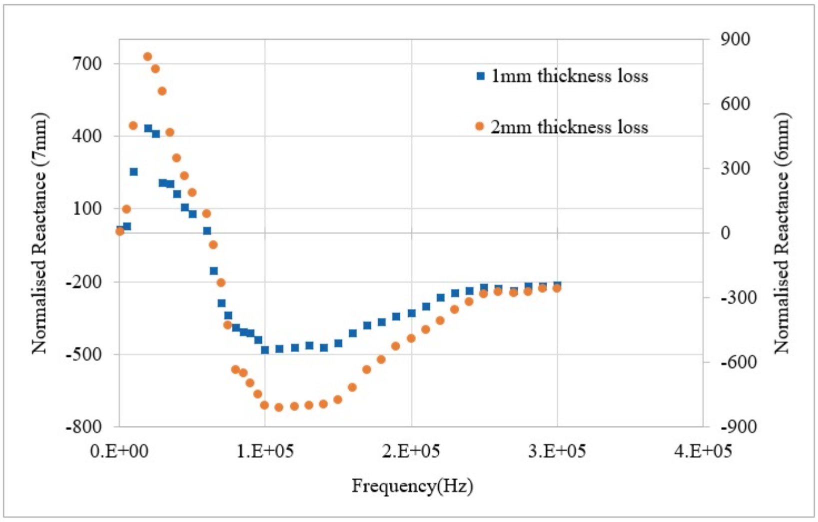

FIGURE 3.15: The normalised reactance values obtained from experiments for 7 mm and 6 mm thick plates.

The differences in the reactance values from the FE model and experiments can be explained by the calibration procedure adopted for measuring complex impedance from AD5933. At low frequencies, a resistor with high resistance was used as an inverted amplifier for the amplification of the reactance. Therefore, the reactance values obtained from the experiments are higher than the FE model. However, there is a limitation on the range of amplification that can be used at higher frequencies to avoid saturation of the impedance measurement circuit.

The results for the uniform corrosion of 1 mm and 2 mm in the 8 mm thick plate are comparable for both the FE model and the experiments as depicted in Figures 3.14 and 3.15. Based on these results, 100 kHz was used to design the wireless MEC sensor as it was found to be more sensitive to wall loss.

### 3.5.2 Experiments in simulated corrosion environment

To evaluate the performance of the corrosion monitor for detecting the wall thickness loss, an accelerated corrosion test was designed. There are a number of techniques that are used for conducting accelerated corrosion tests, such as impressed current and immersion in salt water or corrosive acid solution [233]. A technique that can induce uniform corrosion at a high rate was required to evaluate the performance of the smart corrosion monitor in a reasonable time.

Diluted sulphuric acid is found to be very corrosive to mild carbon steel [234]. At room temperature, carbon steel samples soaked in 10% v/v sulphuric acid for 24 hours achieved a corrosion rate of as high as 110 $gm/dm^2/day$ [235]. This means that the corrosion rate of 1.3 mm per day can be achieved using this concentration of sulphuric acid. The dilution of concentrated sulphuric acid results in an increase in the corrosion rate of carbon steel. This is because of an increase in the solubility of the ferrous sulphate protective layer formed by the acid on the steel surface [236].

To capture the variation in the signals of corrosion sensor, a 20% v/v sulphuric acid solution was used to carry out the test. An 8 mm thick S275 mild steel plate sample was kept in a cell containing acid for 72 hours. A temperature and humidity sensor (AM2302) was also installed at the test site to record the environmental data and controlled through Atmega328P microcontroller.

The laboratory where the experiment was conducted did not have Wi-Fi router nearby. Therefore, radio frequency transmitter NRF24L01 was attached to the microcontroller via UART port to send the signals to the gateway. The gateway was designed using Node MCU0.9 Wi-Fi module and NRF24L01 transceiver. The signals received from the transceiver were sent to the data cloud ThingSpeak through Node MCU Wi-Fi module.

The setup for the accelerated corrosion test and the prototype sensor is shown in Figures 3.16.

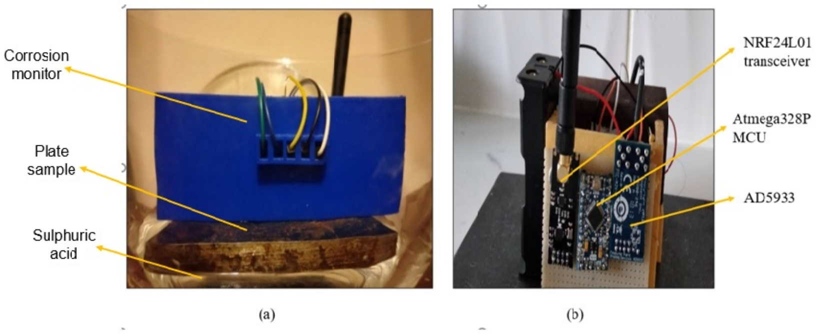

FIGURE 3.16: (a) Experimental setup for the accelerated corrosion test, and (b) The prototype smart corrosion monitor

The sensor was programmed to record the inductive reactance every minute and transmit it to the data cloud. To reduce power consumption, the sensor was put to sleep after recording the reactance, temperature, and humidity. The sensor only used 80 $\mu A$ during operation and 13 $\mu A$ in deep sleep mode.

The results from the corrosion monitor and AM2302 sensors for 72 hours are shown in Figures 3.17 and 3.18, respectively.

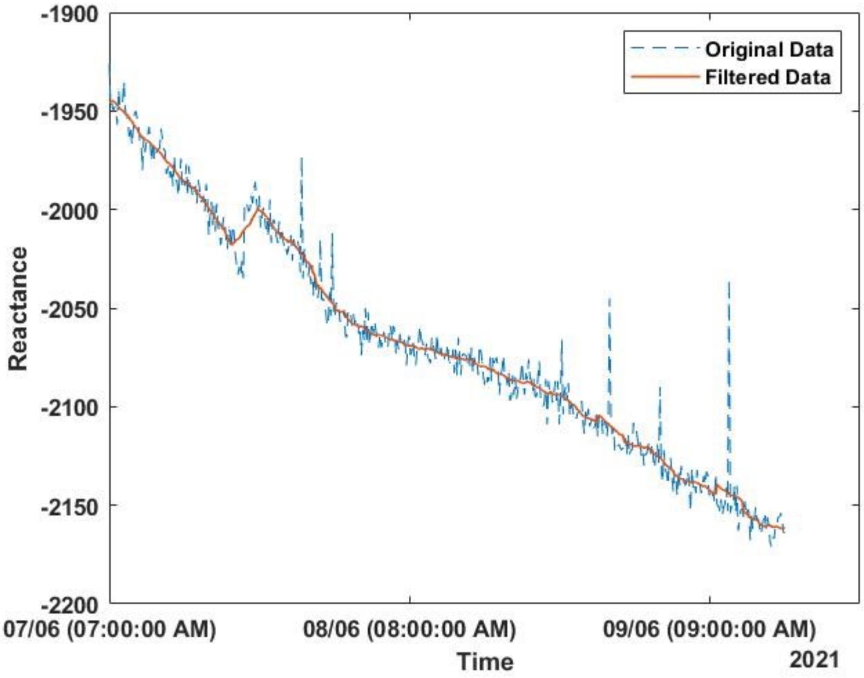

FIGURE 3.17: The MEC monitor signals recorded for 72 hours.

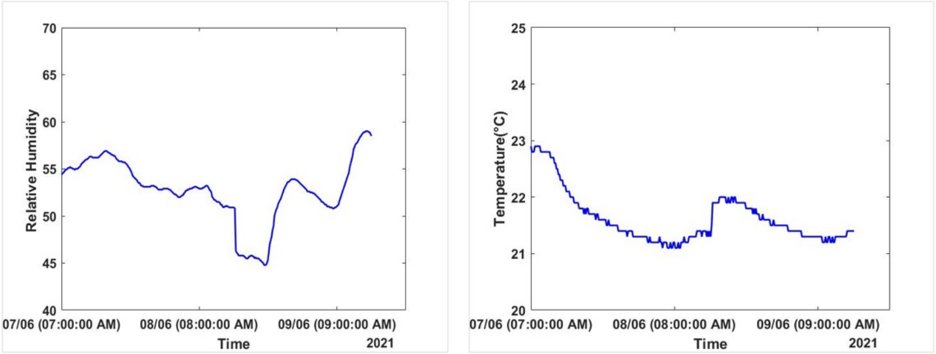

(a)

(b)

FIGURE 3.18: (a) The relative humidity (% RH) values and, (b) Temperature (°C) recorded throughout the procedure

Figure 3.17 demonstrates that white noise due to the electronics was observed in the measurements. To filter the signals, a 10-point moving average filter was employed.

It can be seen from Figures 3.18, there was a slight variation in the temperature and humidity at the test site. However, the trend in the reactance signals from the monitor does not show huge variations due to these changes. The sensor was found to be sensitive to thickness loss and withstood fluctuations in temperature and humidity in ambient environments. The slight jump in the signals on 07 June 2022 was due to the movement of the specimen while cleaning the corrosion products from the plate.

The graph of the rate of change of reactance with respect to time in hours is shown in Figure 3.19. It is evident from the Figure that the corrosion rate was high at the start of the test. This is due to the absence of corrosion products that form a protective layer around the sample.

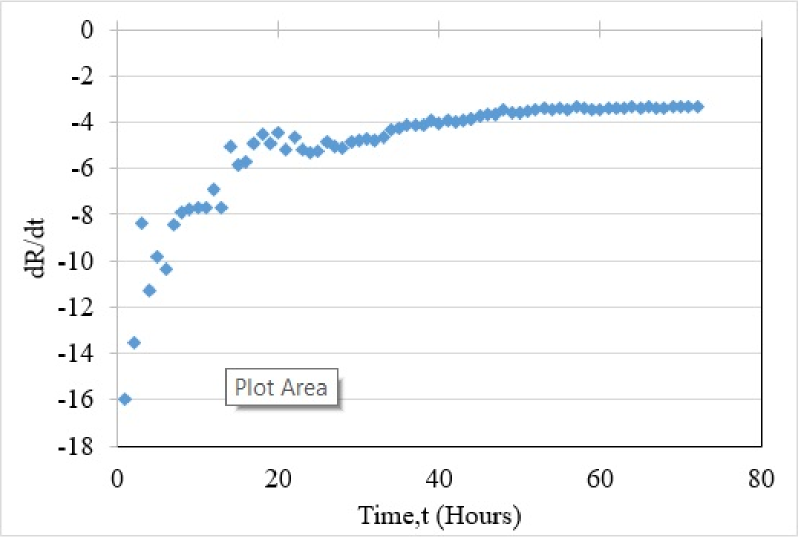

FIGURE 3.19: The graph showing the rate of change in uniform corrosion per hour throughout the test.

## 3.6 Discussions

A novel smart corrosion monitoring device based on the MEC technique was developed for the permanent monitoring of thickness loss due to corrosion and erosion in ferromagnetic structures. This study aimed to develop a device that is small, low-cost, and energy-efficient. This was achieved through FE modelling and experimental studies.

A two-step approach was employed for FE modelling to evaluate the parameters for the design of the excitation circuit and eddy current coil sensor. The optimisation studies on the excitation circuit revealed that neodymium magnets were suitable for this application due to their high magnetic fields and small size. The simulation of thickness loss was conducted by defining the variation in the magnetic permeability in the eddy current coil model. The modelling results revealed that the sensitivity of the sensor is frequency dependent. There were two optimal frequencies at which high sensitivity was observed.

The behaviour of the reactance as a function of frequency when a coil is placed above a ferromagnetic sample can be explained as follows:

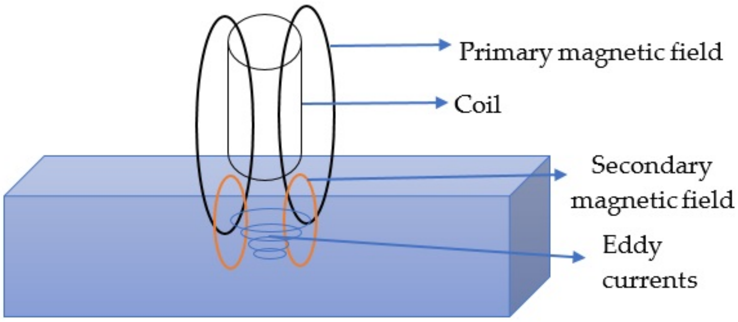

FIGURE 3.20: The schematic representation of the MEC principle

Figure 3.20 depicts that when a coil with sinusoidal excitation is placed over a ferromagnetic material, there are two sets of magnetic fields produced in the test component. One is the primary magnetic field generated by the applied excitation current. Due to this time-varying primary magnetic field, eddy currents are induced in the test material that leads to a secondary magnetic field. Being opposite in direction, the secondary magnetic field opposes the primary magnetic field.

The primary magnetic field is increased with increasing frequency. It is also amplified due to the high magnetic permeability of the ferromagnetic material. Similarly, the secondary magnetic field also increases due to an increase in the intensity of the eddy current. However, eddy current have a low depth of penetration in carbon steel due to high permeability. Therefore, a DC-biased magnetic field is applied to reduce the permeability and increase the depth of penetration of the eddy current. At low frequencies, the effect of the secondary field is less due to the low intensity of induced eddy currents. Therefore, the primary magnetic field intensity increases and the variation in magnetic permeability due to loss of thickness is likewise magnified.

This results in an increase in sensitivity as the frequency is increased. However, at the same time as the frequency is further increased, the intensity of the secondary magnetic field starts to increase cancelling the primary magnetic field. Thus the sensitivity starts to decrease until it reaches a minimum at zero crossing frequency (ZCF) as both fields cancel each other. Beyond ZCF, the secondary field overpowers the primary field and the reactance becomes increasingly until saturation of eddy currents. This is why the rate of change in reactance becomes negative.

These results were validated through experiments. Similar trends were observed in the reactance versus frequency plot. However, there were some disagreements about the ZCF. The differences were more prominent for plates with low thicknesses as they had high magnetic induction. This is due to the limited information available on the magnetic properties of the material.

For this study, 100 kHz was used as the test frequency to design the corrosion monitor because:

- For thick plates (7 mm and 6 mm) FE model and test results were found to be in agreement
- Compared to the optimal frequency values on the lower frequency side, the sensitivity showed no sharp decline and there were fewer fluctuations

The data acquisition system was designed by interfacing AD5933 with the Atmega-328P microcontroller unit. Based on the data communication service available at the test location, a radio frequency transceiver with a Wi Fi gateway was used. This gateway was designed to send the data wirelessly to the data cloud. To test the corrosion monitoring device for detection of thickness loss, accelerated corrosion tests with dilute sulphuric acid were conducted. The effect of environmental factors was also recorded. The comparison of the signals proved that the sensor was sensitive to thickness loss due to corrosion and the signals were not affected by temperature or humidity level changes.

The sensor was designed to optimise the cost and power consumption. The breakdown of the cost of the MEC corrosion monitor is listed in Table 3.6.

TABLE 3.6: Breakdown of the cost of MEC corrosion monitor.

| **Description** | **Cost (£)** |
|---|---|
| Neodymium magnets | 41 |
| Atmega328p MCU | 6.8 |
| AD5933 board | 83.89 |
| Back iron | 21 |
| Node MCU Esp8266 | 5.15 |
| NRF24L01 transceiver | 5 |
| Esp32 with GSM module | 22.94 |
| **Total** | **185.87** |

Table 3.6 shows that compared to UT corrosion monitors which can cost thousands of pounds, the MEC corrosion monitor costs considerably less. The power efficiency of the monitor was accomplished by choosing a microcontroller with low power consumption, and available easily in the market. In addition, the microcontroller was programmed to be put into deep sleep mode to further reduce power consumption.

## 3.7 Summary

The study presented in this chapter has the following conclusions:

- The MEC corrosion monitoring device offers the possibility of detecting thickness wall loss in magnetic materials at ambient temperatures. The monitor is found to be unaffected by small variations in temperature and humidity levels.
- The sensitivity of the sensor is related to the magnetic induction and excitation frequency of the coil sensor. The magnetic induction can be improved by the use of powerful rare earth magnets. The FE modelling and experimental results revealed that excitation frequency is a critical parameter. In terms of sensitivity, there are two optimal frequencies. It is important to avoid the ZCF. Therefore, careful consideration is required to obtain the multi-frequency spectrum on calibration samples to design the test frequency.
- Three different communication protocols are being developed for the corrosion monitor that give the flexibility to install them on a wide range of sites

It is possible to extend the study to quantify corrosion defects using different signal parameters. A multi-frequency sensor may be developed in the future as frequency is highly related to the permeability of samples under test and may be useful for characterising defects.

Defect detection requires an understanding of how frequency affects the sensor's sensitivity. This can be further studied in the future to correlate the optimal frequency with the magnetic properties of the material and the nature of defects. Different approaches for simulating the magnetic saturation model can be introduced to minimise the discrepancies between the FE model and the experimental results to reduce error. This could be done by modelling the non-linear magnetic material by defining the magnetic permeability instead of the $\boldsymbol{B}$-$\boldsymbol{H}$ curve. Different methods to evaluate the in-situ magnetic permeability are proposed by researchers in the literature that can be used to model the ferromagnetic materials close to saturation. This is discussed in chapter 6 in detail.

During the study of the design and development of magnetic corrosion monitors, the magnetic excitation circuit and excitation frequency were found to significantly affect the monitor's sensitivity. An analysis of the excitation frequency optimisation was presented in this chapter. The studies performed on the magnetic excitation circuit optimisation to enhance the monitor's detection capability are discussed in the next chapter.

# Chapter 4

# Optimisation of the Magnetic Excitation Circuit

## 4.1 Introduction

This chapter presents the work carried out on the optimisation of the magnetic excitation circuit of the MEC corrosion monitor to achieve through thickness coverage. As discussed in Chapter 3, the sensitivity of the MEC corrosion monitor is dependent on the magnetic flux density induced in the test specimen. For the detection of buried and internal volumetric defects, it is vital to ensure that the required magnetic flux density is induced throughout the thickness. Moreover, due to the powerful rare earth magnets used in the excitation circuit, size, and weight optimisation is imperative to avoid handling and health and safety hazards.

The current techniques of magnetic excitation circuit optimisation are complex and time-consuming. Therefore, research was conducted on the development of an artificial intelligence (AI) based methodology for fast and efficient optimisation of the magnetic excitation system of the MEC corrosion monitor. The studies conducted as part of the research presented are as follows:

- Evaluation of the relationship between the MEC sensor's sensitivity and the induced magnetic flux density in the test specimen. This is required to determine the minimum magnetic flux density to ensure through-thickness coverage to detect defects.

- Determine the factors that affect the magnetic field strength created by the magnetic excitation circuit.
- Design of an optimised magnetic excitation circuit using the PSO algorithm.
- Validation of the approach through experimental studies on two different test cases.
- Comparison of the performance of PSO against two stochastic algorithms.

## 4.2 Sensitivity of the corrosion monitor

As discussed in Chapter 2, the sensitivity of MEC and MFL sensors depends on the intensity of magnetic flux density in the test specimen. The study of the minimum magnetic induction required to achieve a high signal-to-noise ratio was conducted through numerical modelling.

### 4.2.1 FE modelling

To evaluate the relationship between sensitivity and induced magnetic flux density $\boldsymbol{B}$, a parametric study was performed. The intensity of the induced flux density in the test specimen was increased by increasing the dimensions of the magnets. A defect of size (5x5x1) mm was introduced in a plate of 8 mm thickness. The defect size was considered based on the threshold size that can be easily detected by the MEC transducer.

The details on the approach, material properties, and meshing have already been discussed in Chapter 3. The geometry of the plate specimen with the defect is presented in Figure 4.1.

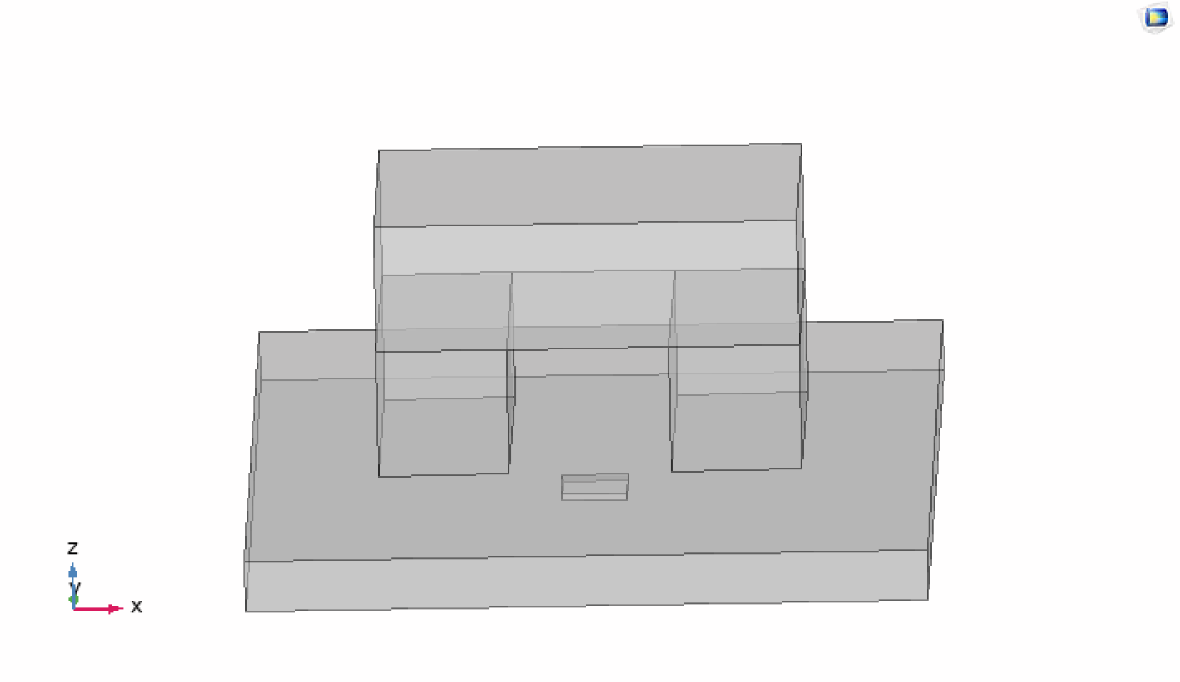

FIGURE 4.1: The geometry of the plate specimen with the defect used for FE modelling.

The coil sensor was excited at a frequency of 100 kHz. The sensitivity (S) of the coil sensor was calculated at different induced magnetic flux densities using the expression:

$$S = \frac{r_1 - r_2}{r_1} \times 1000 \tag{4.1}$$

where, $r_1$ is the reactance of the coil sensor above the test plate with no defect, and $r_2$ is the reactance of the sensor above the test plate with the defect.

The relationship between the sensitivity and the induced magnetic field density in the test specimen is presented in Figure 4.2.

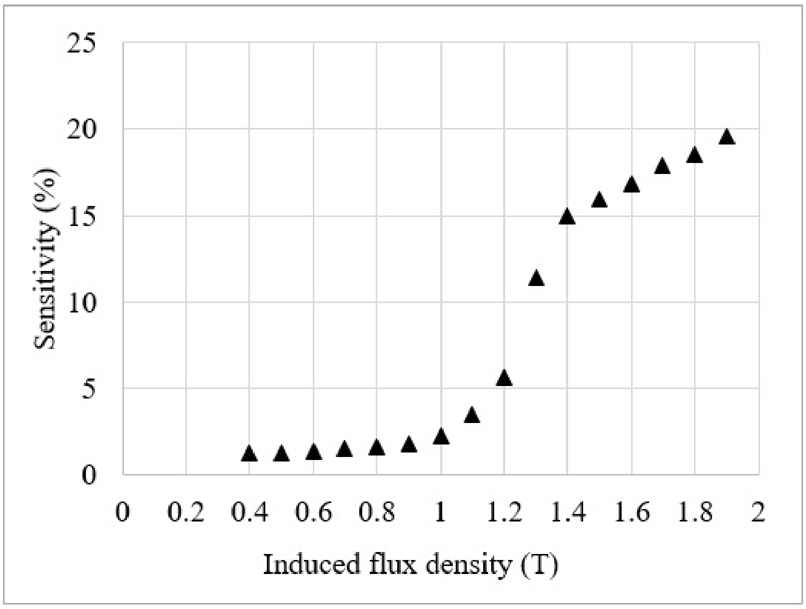

FIGURE 4.2: The relationship between induced magnetic flux density and the sensitivity of the MEC sensor.

Figure 4.2 depicts a sharp increase in the sensitivity beyond a field of 1.2 T. It increases as there is an increase in the magnetic field induction, however, above 1.4 T there is not a significant increase. The increase in the induced flux density leads to a considerable increase in the size of the excitation circuit and the power of the magnets. Therefore, a compromise is required to achieve a reasonable signal-to-noise ratio while keeping the size of the yoke as small as possible. A 10% change in the base or reference signal is obtained at 1.2 T which can easily be detected. Since ferromagnetic materials have varied magnetic properties, assessing the actual magnetic flux density induced in the test specimen is difficult. Therefore, a conservative value of 1.4 T was defined as the required induced magnetic flux density.

## 4.3 Factors affecting the magnetic induction

To define the input variables required for the optimisation of the excitation circuit, it is pertinent to determine the yoke parameters that affect the induced magnetic field intensity. The excitation yoke parameters are;

- Pole width of the magnets (PW).
- Length of magnets (ML).

- Height of magnets (MH).
- Height of the back iron piece (YH).
- Separation distance between magnets (SD).

All these parameters were defined in the FE model to evaluate the effect of these factors on the induced magnetic flux density in the test specimen. As the induced magnetic flux density is not uniform throughout the thickness of the test plate, therefore, the flux density was plotted along the line at the centre of the plate where the MEC sensor is located. Figure 4.3 shows the location where the flux density was computed.

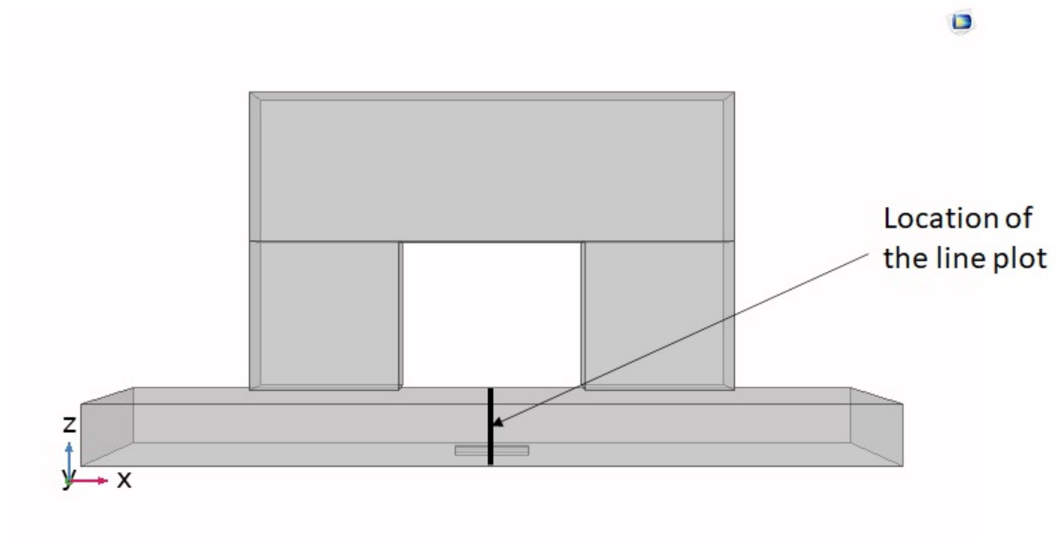

FIGURE 4.3: The line along which magnetic flux density was computed.

The results for the variation in the induced magnetic flux density due to the changes in the parameters of the excitation yoke are shown in Figures 4.5 to 4.8.

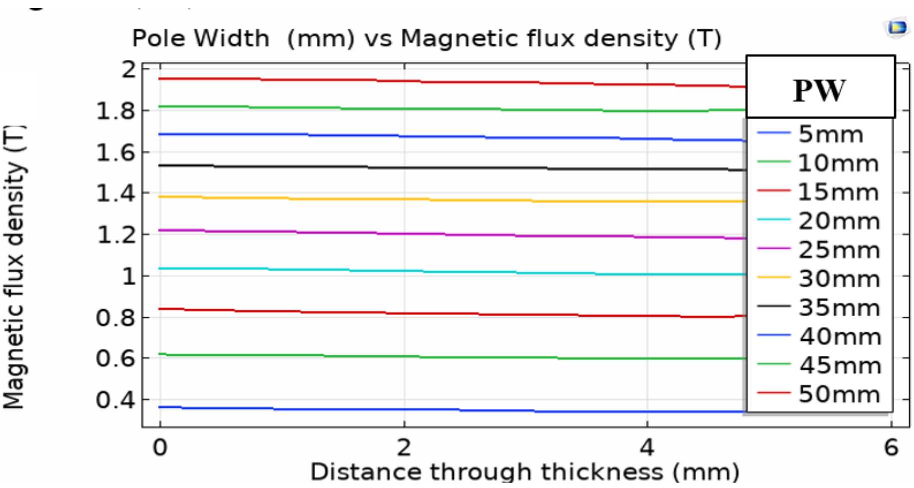

FIGURE 4.4: Variation in induced magnetic flux density for different pole widths of the magnet.

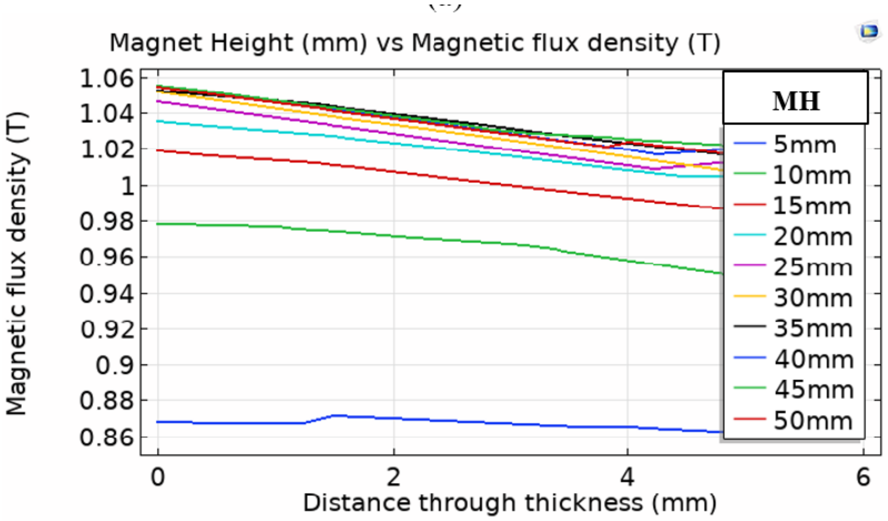

FIGURE 4.5: Variation in induced magnetic flux density for different heights of the magnet.

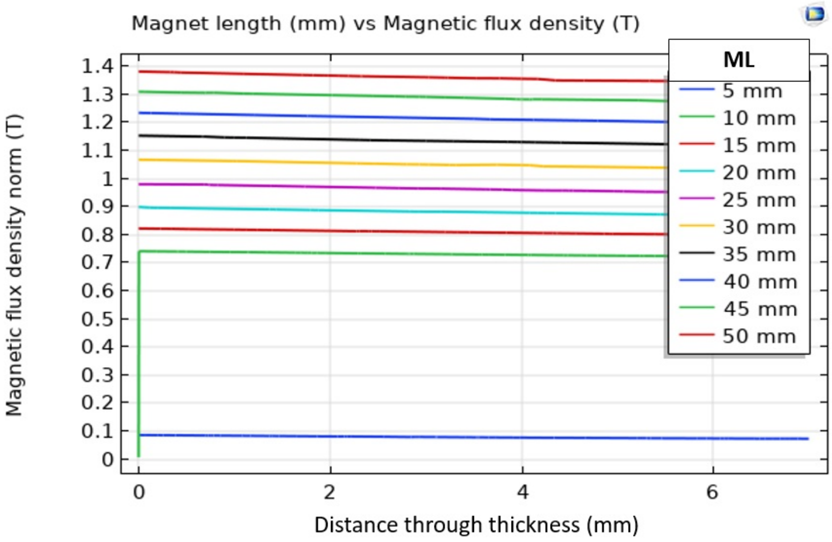

FIGURE 4.6: Variation in induced magnetic flux density for different lengths of the magnet.

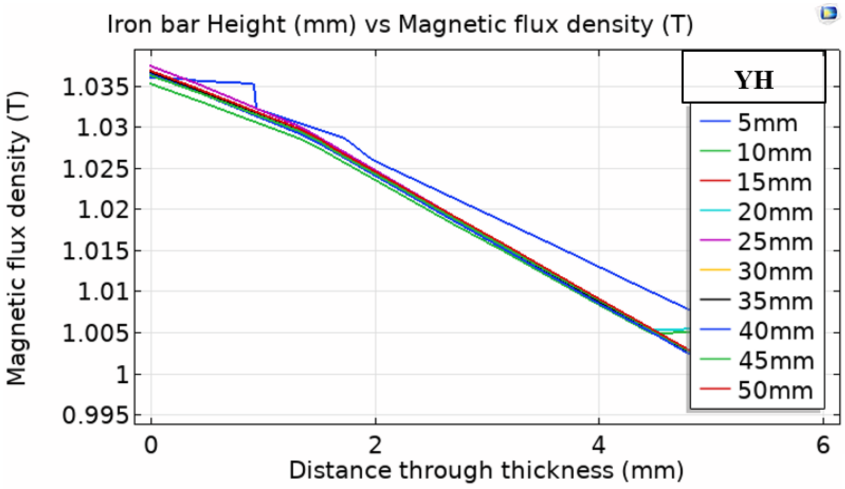

FIGURE 4.7: Variation in induced magnetic flux density for different heights of back iron.

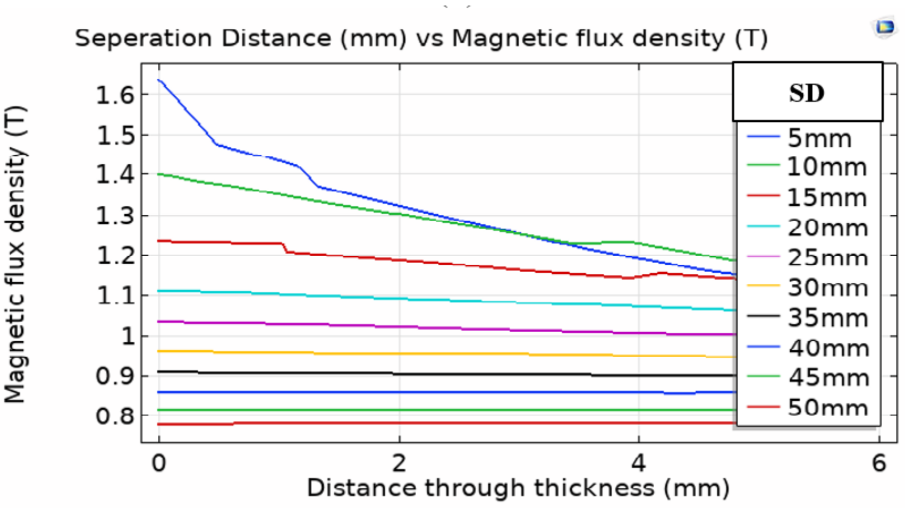

FIGURE 4.8: Variation in induced magnetic flux density for different separation distances between magnets.

Figures 4.5 and 4.8 indicate that the factors such as magnet pole width and separation distance between the magnets have a significant impact on the induced magnetic flux density. The height of the magnet has less effect as the dimensions are increased beyond a certain value. This can help in defining the limits for the input variables for the parametric optimisation to reduce computational costs.

The size of the back iron piece was found to have not much influence on the induced magnetic flux density after the yoke height is increased beyond 10 mm. This can be explained by the high magnetic permeability of iron. For thin iron yokes, the induced flux density is close to saturation, the capacity of the iron plate to carry the magnetic flux is less, and a lot of flux escapes into the surrounding air. This results in a decrease in focusing the induced flux density in the test specimen. To avoid the computational cost, the yoke height parameter can be avoided. A constant yoke height of 20 mm is used for the optimisation study to ensure that the magnetic flux density in the back iron piece is not close to saturation.

### 4.3.1 Problem formulation

The FE modelling results are used to formulate the optimisation problem. The objective function is defined as the minimisation problem and expressed as:

$$Objective function = min\,|(1.4 - \mathbf{B}_1)| \tag{4.2}$$

where $\mathbf{B}_1$ is the flux density induced in the plate specimen.

As evident from the modelling studies the induced magnetic flux density in the test specimen is not uniform through the thickness, therefore, $\mathbf{B}_1$ is defined as the minimum flux at the centre.

The limits of the input parameters that need to be optimised are listed in Table 4.1.

TABLE 4.1: Maximum and minimum limits for yoke parameters for optimisation study

| **Parameter** | **Minimum limit (mm)** | **Maximum limit (mm)** |
|---|---|---|
| PW | 10 | 150 |
| ML | 10 | 200 |
| MH | 10 | 60 |
| SD | 20 | 50 |

In order to optimise the design of the magnetic excitation circuit an algorithm based on PSO was developed. As a metaheuristic, PSO is a form of artificial intelligence that can provide solutions to unknown functions based on no or few assumptions.

## 4.4 Particle swarm optimisation

PSO algorithm works by initialising a swarm or population of candidate solutions called particles in a search space randomly. Each particle has a position $X_i$ and velocity $\mathbf{V}_i$ at iteration i. The particles are moved around in the search space using simple formulae based on the particle's position and velocity. The objective function or fitness value is computed at each iteration. The most optimal particle position $p_{best}$ and the best swarm solution $g_{best}$ are stored in memory. The particle's movement is guided by $p_{best}$, and $g_{best}$, and after each iteration t, the position and velocities are updated by the formula:

$$X_i^{t+1} = X_i^t + \mathbf{V}_i^{t+1} \tag{4.3}$$

where,

$$V_i^{t+1} = w\mathbf{V}_i^t + c_1 r_1 (p_{best} - X_i^t) + c_2 r_2 (g_{best} - X_i^t) \tag{4.4}$$

The velocity of the particle is determined by three hyperparameters;

Cognitive $w\mathbf{V}_i^t$, personal learning coefficient $c_1 r_1 (p_{best} - X_i^t)$, and $c_2 r_2 (g_{best} - X_i^t)$ is the social learning coefficient. The cognitive term involves the inertial weight $w$ parameter that decides the direction of the velocity of the particles. If $w > 1$, it means that the particle will travel in the same direction in the search space as the previous particle position. This is called diversification or exploitation. If the parameter value is between 0 and 1, the direction of the particle is changed to refine the global search. This is called exploration. To improve the exploration a small value of $w$ is recommended to increase the chances of obtaining global optimum as the particles' look for the solution in a number of directions. However, the time for computation increases. A higher value will increase exploitation and the likelihood of premature convergence to a solution that may not be the global optimum. It is, therefore, recommended to use a dynamic value of inertial weight to narrow down the search initially. This will decrease exploitation and increase exploration after each iteration to save computational time and obtain a global optimum solution.

The personal learning and global learning terms update the particle search stochastically based on the particle's individual learning experience and the swarm's neighbourhood experience, respectively. The coefficients $r_1$ and $r_2$ are numbers in the range [0 - 1], generated randomly, and are unique for each iteration. The coefficient $c_1$ allows the particles to adjust their velocity by learning from their own best experiences whereas, $c_2$ is the social parameter that guides them according to the best global solution.

The pseudo-code for the PSO algorithm is:

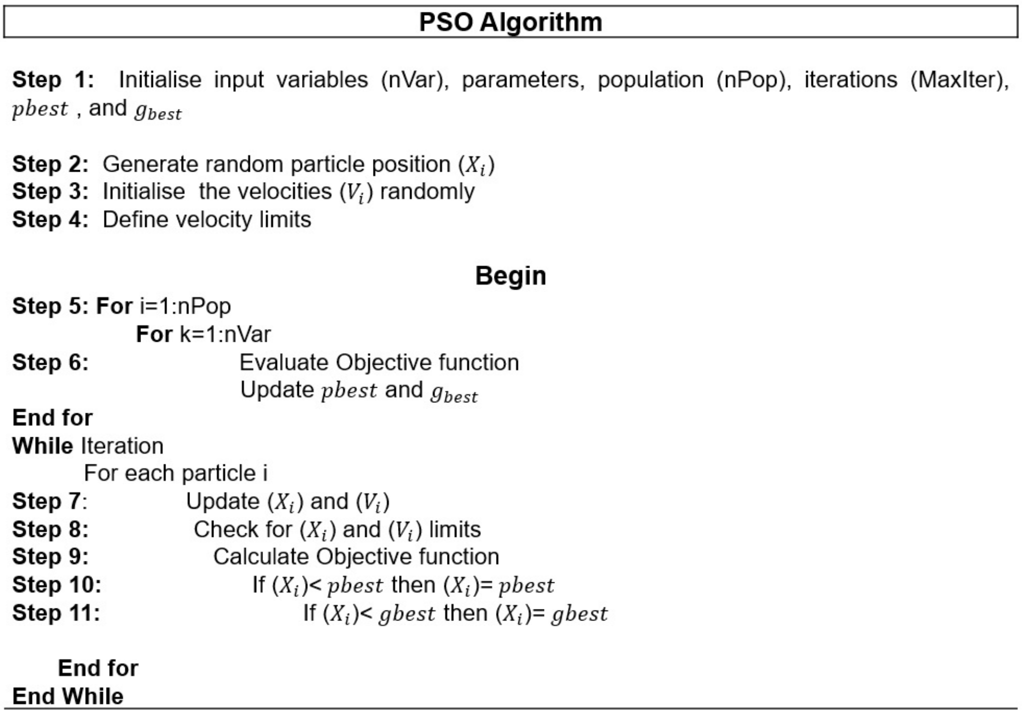

```
PSO Algorithm

Step 1: Initialise input variables (nVar), parameters, population (nPop), iterations (MaxIter), $pbest$ , and $g_{best}$

Step 2: Generate random particle position ($X_i$)
Step 3: Initialise the velocities ($V_i$) randomly
Step 4: Define velocity limits

                                Begin
Step 5: For i=1:nPop
            For k=1:nVar
Step 6:             Evaluate Objective function
                    Update $pbest$ and $g_{best}$
End for
While Iteration
        For each particle i
Step 7:         Update ($X_i$) and ($V_i$)
Step 8:          Check for ($X_i$) and ($V_i$) limits
Step 9:            Calculate Objective function
Step 10:               If ($X_i$)< $pbest$ then ($X_i$)= $pbest$
Step 11:                    If ($X_i$)< $gbest$ then ($X_i$)= $gbest$

    End for
End While
```

### 4.4.1 Implementation in MATLAB

To implement the PSO algorithm in MATLAB, a model was built in Comsol. The model was converted to Java script using Comsol Livelink. The PSO algorithm script was developed in MATLAB. A dynamic inertial weight parameter was defined to improve the computational efficiency of the algorithm.

The inertial parameter $w$ was defined by the expression;

$$w = (w_{max} - \frac{j}{MaxIter}) \times (w_{max} - w_{min}) \tag{4.5}$$

where, $w_{max}$ is the maximum value of inertia, $w_{min}$ is the minimum value of inertia, $j$ is the current iteration number, and $MaxIter$ is the maximum number of iterations.

The parameters defined for implementation of the algorithm are listed in Table 4.2.

TABLE 4.2: The values selected for parameters for the PSO algorithm.

| **Parameter** | **Value** |
|---|---|
| nPop | 12 |
| MaxIter | 50 |
| $c_1$ | 2 |
| $c_2$ | 2 |
| $w_{max}$ | 0.9 |
| $w_{min}$ | 0.4 |

The yoke parameters were optimised for two different test cases:

- Detection of 5x5x1 mm and 5x5x2 mm machined defects on an 8 mm thick mild carbon S275JR plate.
- Detection of 1mm wall thickness loss in 12 mm thick plate with 2 mm liftoff.

The results of the optimisation study implemented on an 8 mm thick steel plate with a minimum defect size of 5x5x1 mm are presented here:

The input variables were initialised randomly and the fitness function was calculated. After each iteration, the particle position was updated based on personal and global learning. The algorithm converged at $37^{th}$ iteration at the fitness function value of $10^{-4}$, the convergence graph is shown in Figure 4.9.

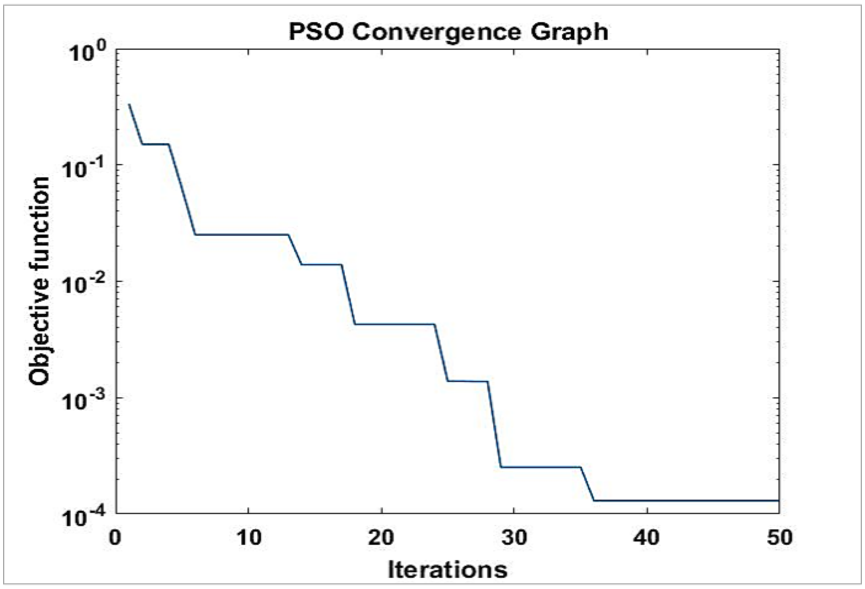

FIGURE 4.9: PSO convergence graph for the solution of test case 1.

The movement of the swarm towards the optimal magnet dimensions is depicted in Figure 4.10.

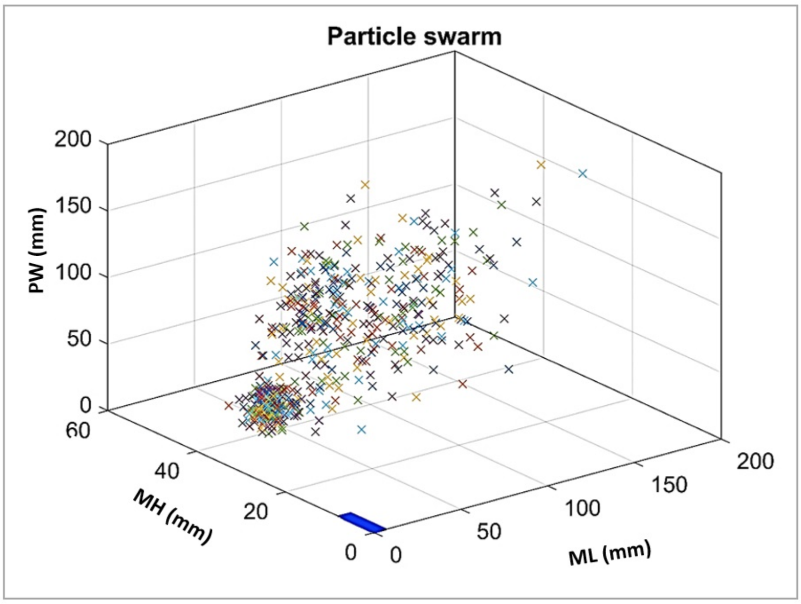

FIGURE 4.10: The movement of swarm towards the optimal solution

The magnetic circuit obtained by the implementation of PSO on different test configurations is presented in Table 4.3.

#### Magnetic excitation circuits due to different plate thicknesses

TABLE 4.3: The magnetic excitation circuit parameters obtained from the PSO algorithm.

| Plate height (mm) | PW (mm) | ML (mm) | MH (mm) | SD (mm) |
|---|---|---|---|---|
| 6 | 18 | 25 | 36.5 | 25 |
| 8 | 19.8 | 40 | 19.5 | 25 |
| 10 | 24.6 | 43.9 | 25.5 | 20.1 |
| 12 | 33.2 | 45 | 29.5 | 22 |

#### Magnetic excitation circuits with different liftoffs

To evaluate the effect of liftoff on the size of the excitation circuit, the liftoff was varied from 1mm to 4mm with an increment of 1 mm for a 12 mm thick plate. The results are presented in Table 4.4.

TABLE 4.4: Dimension of the magnetic excitation circuit for different lift-offs for 12 mm thick plate.

| Liftoff (mm) | PW (mm) | ML (mm) | MH (mm) | SD (mm) |
|---|---|---|---|---|
| 1 | 22 | 38 | 26 | 26 |
| 2 | 20 | 39 | 40 | 24 |
| 3 | 18 | 48 | 42 | 25 |
| 4 | 25 | 45 | 48 | 24 |

### 4.4.2 PSO comparison with other algorithms

To evaluate the performance of the PSO algorithm, a comparative study was conducted. The minimisation problem was solved using genetic (GA), and artificial colony bee (ABC) algorithms. Two parameters were used to evaluate the performance i.e. number of iterations to reach the optimal solution and the time required per iteration. The results are illustrated in Figures 4.11 and 4.12.

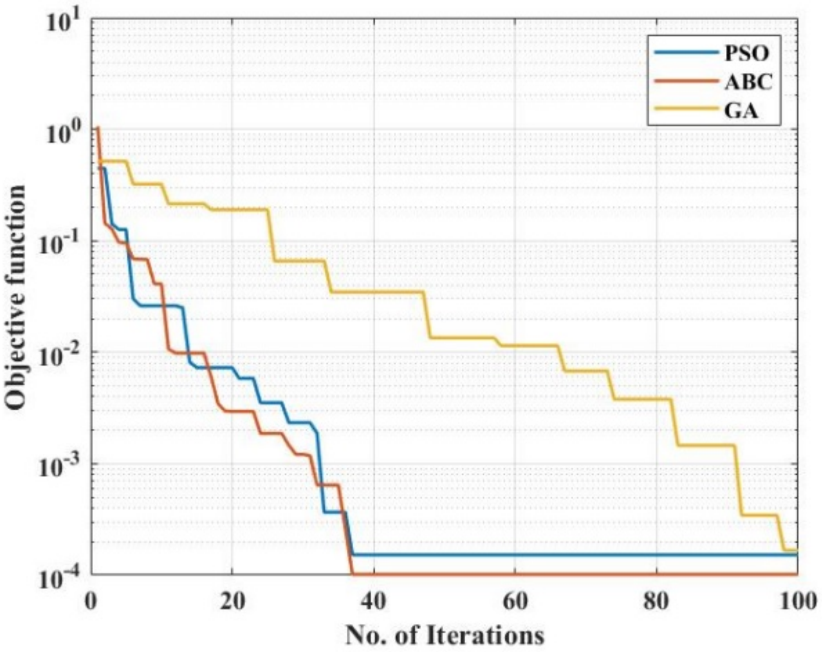

FIGURE 4.11: Convergence graph for GA, ABC, and PSO algorithm.

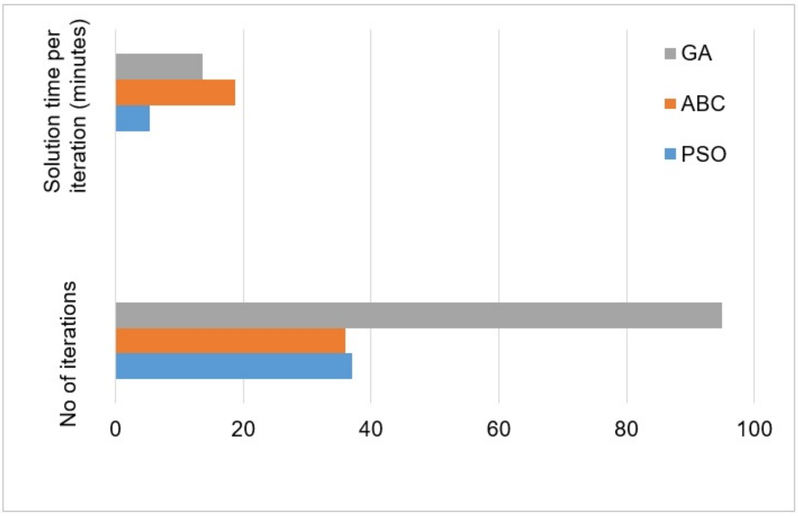

FIGURE 4.12: Comparison of PSO with ABC and GA.

The convergence graph reveals that GA requires a large number of iterations compared to ABC and PSO. ABC and PSO converged at the $37^{th}$ iteration to the global optimum solution. Since the ABC algorithm requires more FE models to be solved per iteration than PSO, the solution time per iteration is higher as evident from Figure 4.12. Therefore, ABC was found to be computationally less efficient than PSO in terms of solution time.

Consequently, for the solution of the optimisation of magnetic excitation circuit parameters, the PSO algorithm was found to be computationally efficient.

## 4.5 Experimental studies and results

The results obtained from the implementation of PSO were validated through a series of experimental studies. Two different test configurations were tested with the MEC transducer built using the parameters obtained from the PSO algorithm. The test setup and results are explained in detail as follows:

### 4.5.1 Test case 1

Defects D1 (5x5x2 mm) and D2 (5x5x1 mm) were machined on an 8 mm thick mild carbon steel plate. The test plate with defect dimension and the prototype sensor are shown in Figures 4.13 and 4.14.

FIGURE 4.13: The mild steel plate with machined defects.

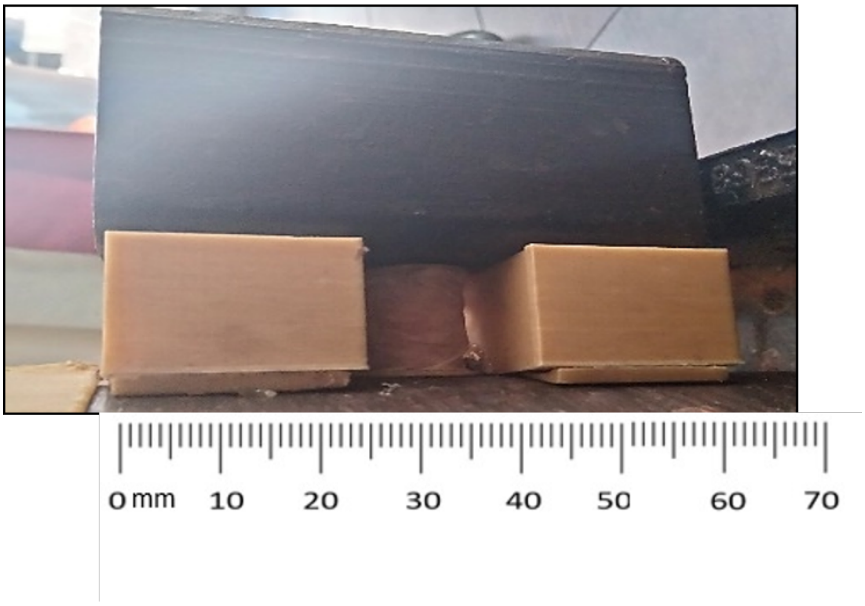

FIGURE 4.14: Prototype sensor developed for test case 1.

It is difficult to handle the neodymium magnets as they can leap and slam together from a distance of several inches. They can severely pinch or even break fingers if trapped between them [237]. Therefore, to avoid damage, the magnetic corrosion monitor was constructed by putting the individual magnets first on the test plate in the holder. This is helpful in handling the magnets as the test plate shields the magnetic field of the individual magnet and placing them close to each other is relatively easy and safe.

The construction of the MEC transducer was carried out in the following steps:

- Step 1: Mark the poles of the magnets. It is important that the opposite poles of the magnets should be facing in the same direction.

FIGURE 4.15: The opposite pole of the magnets marked to ensure that the direction of the magnets is correct.

- Step 2: One magnet is placed in the holder on the test specimen or keeper with high magnetic permeability. This is done to shield the magnetic field, this reduces the chances of snapping and sticking of the two magnets when they are brought close to each other.

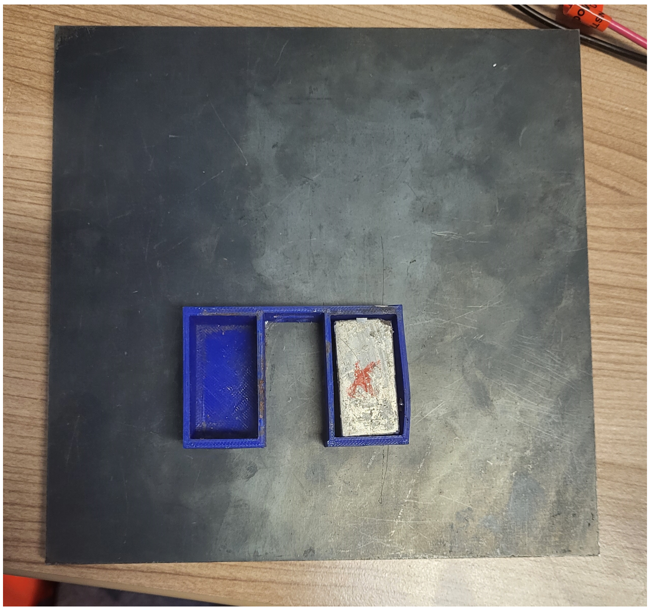

FIGURE 4.16: First magnet placed on the test specimen/catcher.

- Step 3: Keep a thick wooden or plastic piece in the space between the magnets.

FIGURE 4.17: Wooden piece placed in the space between the magnets to avoid snapping.

- Step 4: Place the second magnet in the holder making sure that the marked pole is facing in the same direction.

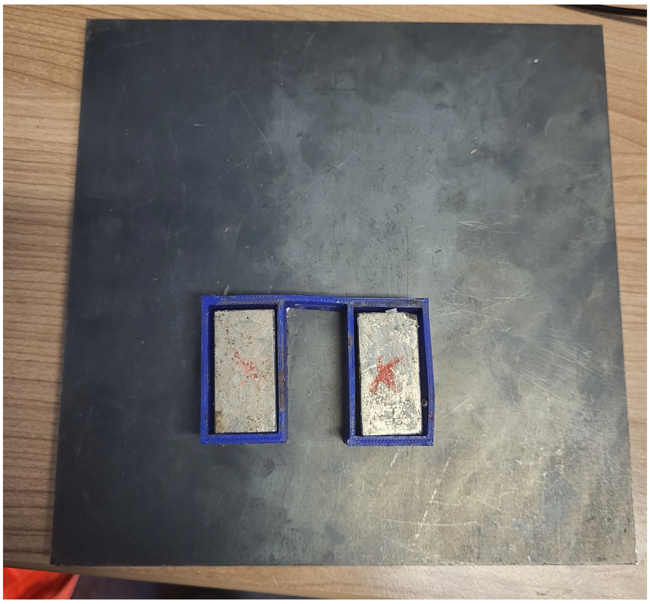

FIGURE 4.18: Magnets placed in the holder.

- Step 5: When the transducer is not in use, it can be kept on a keeper made of mu metal to shield the field and avoid accidents.

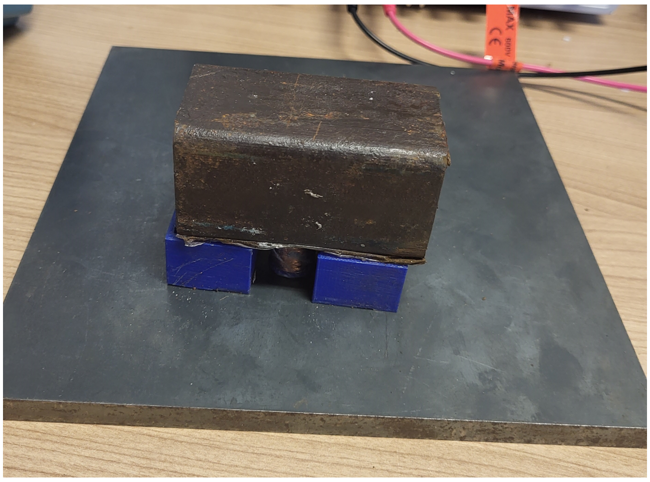

FIGURE 4.19: The magnetic excitation circuit.

The test results from the prototype sensor are presented in Figure 4.20.

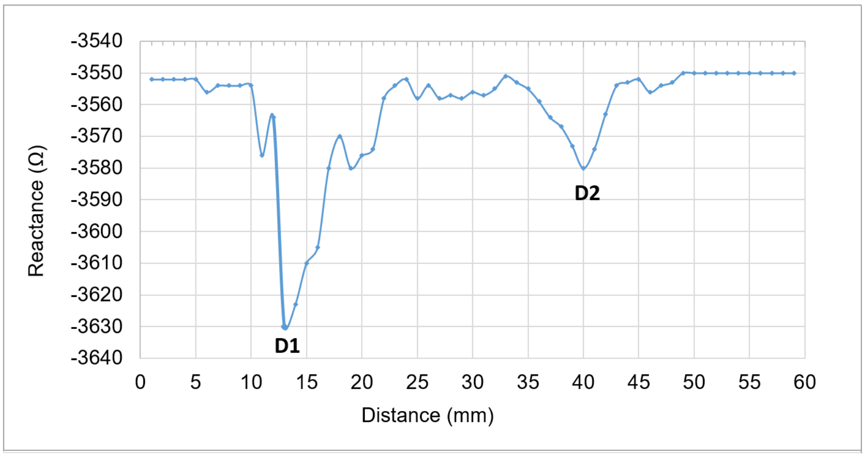

FIGURE 4.20: Signals for the defects D1 and D2 obtained from the prototype sensor.

### 4.5.2 Test case 2

For test case 2, an 11 mm thick plate with 2 mm liftoff was tested to detect a uniform wall thickness loss of 1 mm. The magnetic excitation circuit was developed with the size 40x40x20 mm. Handling neodymium magnets of this size is very difficult and poses health and safety hazards. Therefore, instead of moving the corrosion monitor on the test specimen, a plate of 1 mm was stacked and removed from the 10 mm thick plate to test the wall thickness loss. The test setup is shown in Figures 4.21.

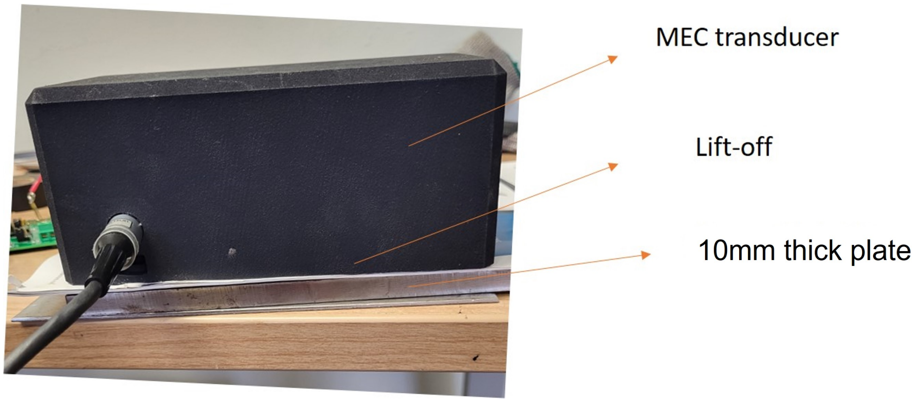

FIGURE 4.21: Experimental setup for test case 2.

The plate thickness loss was also tested using the first prototype with the magnetic excitation circuit dimensions 20x40x20 mm. The results for the normalised percentage variation in the signals for both prototypes presented in Figure 4.22.

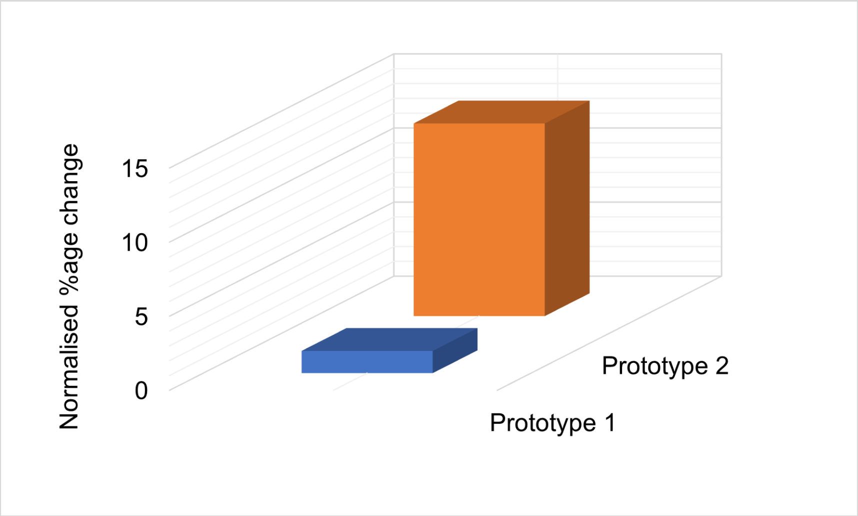

FIGURE 4.22: Normalised %age variation in the signals obtained from the two prototype monitors for test case 2.

It is evident from Figure 4.22 that there was a very small variation in the signals with the first transducer due to the small size. However, when the same was tested with the increased magnetic circuit size, the change in the wall thickness loss could be detected.

## 4.6 Summary

An AI-based methodology was proposed to optimise the design parameters for the magnetic excitation circuit. Numerical modelling was conducted to formulate the objective function as the minimisation problem. From FEA it was found that a reasonable signal-to-noise ratio can be achieved when the magnetic flux density induced in the test specimen is 1.4 T. Furthermore, the input parameters for the optimisation problem were identified and the limits were determined. The magnetic induction was not significantly affected by the back iron height beyond a certain thickness. Since the objective of the back iron piece is to shield and focus the magnetic field, therefore for future study a thickness of 20 mm was used to avoid the escape of magnetic flux in the surrounding air.

A parametric model was developed in Comsol Multiphysics and converted to Javascript which can be solved using MATLAB. The magnetic flux density induced in the test specimen is not uniform throughout the thickness. Therefore, the magnetic flux density was computed along a line through the centre to calculate the minimum flux throughout the plate. The PSO algorithm was developed in MATLAB and the parameters for inertial weight and acceleration constant were defined. The performance of PSO was compared with two famous stochastic algorithms, GA and ABC. Based on the number of iterations required for convergence, and the time required for each iteration, PSO was found to outperform GA and ABC in the optimisation of the magnetic circuit.

Two different test cases were developed to evaluate and validate the performance of PSO for the design optimisation. The magnetic excitation circuit was optimised for test specimens with different thicknesses and liftoffs. The results obtained from the PSO implementation were used to build two different MEC transducers and tested on two test cases. The handling of the neodymium magnets is very difficult and can cause injuries. Therefore, to build the yokes magnets are individually placed on the test specimen in the 3D-printed holder. The magnets stick to the plate that shields the magnetic field produced by them. This reduced the danger of slamming and leaping of the magnets. The results revealed that yoke size is a crucial parameter for the detection of volumetric defects. The magnetic excitation circuit for an 8 mm thick plate was not able to detect defects in an 11 mm specimen. This was due to the fact that the 11 mm plate was under saturated. The liftoff had a significant impact on the detection capability and large magnetic induction is required for detection of the wall thickness loss.

The studies show that magnetic flux density induced in the test specimen is a crucial factor for the detection of wall thickness loss defects from the MEC transducer. As the pipes have different diameters and thicknesses and surface conditions, the same magnetic excitation circuit is not suitable for different test specimens. Therefore, it is pertinent to optimise the design of the magnetic excitation circuit to achieve through thickness coverage to avoid missed signals.

## Chapter 5

# Reliability Improvement of Corrosion Monitor

### 5.1 Introduction

The development of the MEC corrosion monitor was discussed in detail in chapter 3. The coil sensor was used in the MEC monitor for sensing the changes in the wall thicknesses due to its advantages over magnetic sensors. Coil sensors are passive components and can be used in hostile operating environments since the electronic components can be placed away from the coil sensor where the temperature is high. This is the reason MEC sensors were the primary choice for the development of the magnetic corrosion monitor. However, increased reliability is required for monitoring devices developed for remote and long-term applications. It is imperative to identify and isolate faulty sensors for continued operation over an extended time period. The studies presented in this chapter on the improvement and assessment of the long-term reliability of MEC magnetic corrosion monitors are as follows:

- Design of corrosion monitor based on dissimilar active redundancy principle. Feasibility studies through FE modelling and experiments were carried out to analyse the possibility of using the MFL sensor with the magnetic excitation circuit of MEC monitor. Experiments were conducted on the newly developed prototype corrosion monitor to validate the FE modelling results.

- Design and execution of real-life aging tests in the ambient environment with different corrosion rates to evaluate the performance and stability of the corrosion monitor over an extended time period.

- Development of a simple methodology to identify faulty sensors using correlation analysis on time series data received from the sensors.

## 5.2 Design of MFL transducer

For the MFL technique the test specimen is required to be magnetised close to saturation to avoid missed signals [238, 239]. The need for high magnetic induction is essential for MFL inspection tools that operate on-line and in-line. Due to the movement of the transducers in these tools, noise is introduced because of velocity and surface roughness [239–241]. Therefore, the signal-to-noise ratio is reduced, and buried defects are difficult to detect.

The magnetic excitation circuit developed for the MEC corrosion monitor discussed in Chapter 4, was designed to achieve an induced magnetic flux density of 1.4 T in the test specimens. Numerical modelling is used to determine the feasibility of detecting buried wall thickness loss with the MFL sensor at 1.4 T. The modelling results are further employed for the selection of commercially available magnetic sensors based on design parameters such as saturation field density, and sensitivity.

### 5.2.1 FE modelling

The magnetic excitation circuit developed for the MEC corrosion monitor discussed in Chapter 3 was used for the computation of leakage magnetic flux density due to wall thickness loss.

The variation in the leakage flux density due to a 50% uniform wall thickness loss in an 8 mm thick mild steel plate is shown in Figures 5.1 and 5.2. The increase in the flux density is represented by the number of arrows and not their size in both figures.

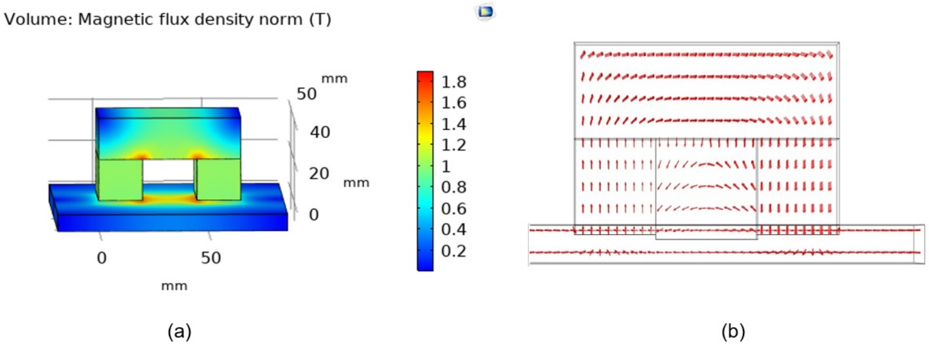

FIGURE 5.1: (a) FE model of the magnetic excitation circuit above 8 mm thick plate, and (b) the arrow plot of the magnetic flux density.

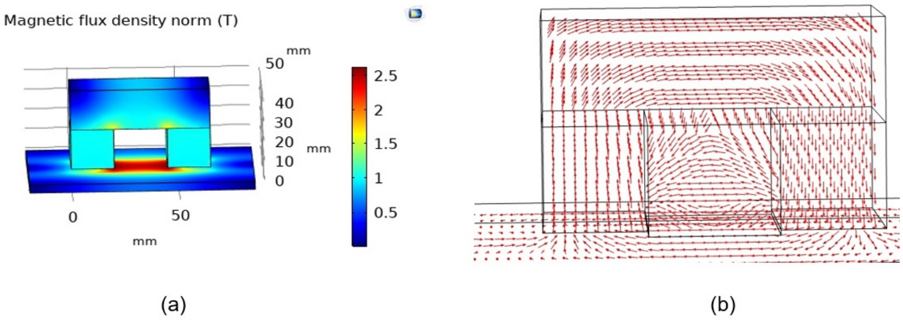

FIGURE 5.2: (a) FE model, and (b) the arrow plot illustrating increase in the magnetic flux density above 4 mm thick plate.

For the selection of magnetic sensor, the significant parameters to be considered are the saturation field and sensitivity (output voltage in mV per Gauss change in the magnetic flux density). This is computed by evaluating the background flux density (BFD) for different plate thicknesses and the minimum variation in leakage flux density (LFD) due to uniform wall thickness loss in an 8 mm thick plate. The LFD and BFD were evaluated at the centre of the excitation circuit, 1 mm above the plate specimen. The location where the BFD and LFD were evaluated is shown in Figure 5.3.

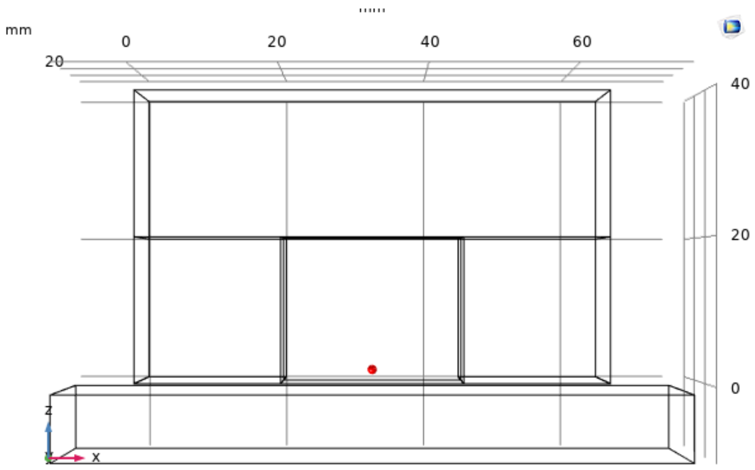

FIGURE 5.3: The location at which BFD and LFD were computed.

The results computed from the FE model are presented in Figure 5.4.

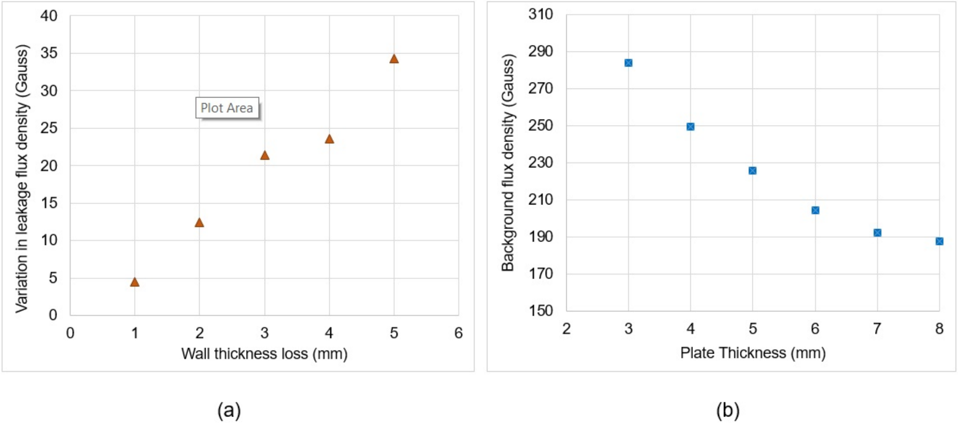

FIGURE 5.4: The plot between (a) The LFD and wall thickness, and (b) BFD for different plate thicknesses.

Figure 5.4 shows that the saturation field of the magnetic sensor for MFL application must be higher than 300 Gauss or 30 mT. The sensor should be capable of detecting a change of at least 2-3 Gauss in the magnetic flux density. The resolution and saturation field density considered for the magnetic field sensor is conservative to account for variations in material properties and liftoff.

### 5.2.2 Development of smart corrosion monitor

Magnetic field sensors commonly used in commercial applications, were reviewed for the MFL transducer. Table 5.1 presents the comparison of the properties of some common commercially available magnetic field sensors [242, 243].

TABLE 5.1: Comparison of the properties of commercially available magnetic field sensors [242, 243].

| Sensor | Sensitivity (mV/Gauss) | Saturation field (mT) | Power (mW) |
|---|---|---|---|
| Hall sensor (Allergo A-1324) | 5 | >500 | 35 |
| GMR sensor (AAH002-2E) | 72.5 | 5-10 | 100 |
| AMR (HMC-1002) | 16 | 1-5 | 45 |
| TMR (STJ-240) | 120 | 2 | 14.4 |

It is evident from Table 5.1 that the hall effect sensors have a much higher saturation field as compared to other magnetic field sensors. The sensor is likely to experience this magnitude which would saturate other magnetic sensors. Moreover, the resolution of the hall effect sensor is enough to detect changes in the magnitude of magnetic flux density due to 1 mm wall thickness loss in an 8 mm thick plate. Therefore, the Allergo A-1324 hall sensor was used for the development of the prototype corrosion monitor. The prototype MFL transducer is shown in Figure 5.5.

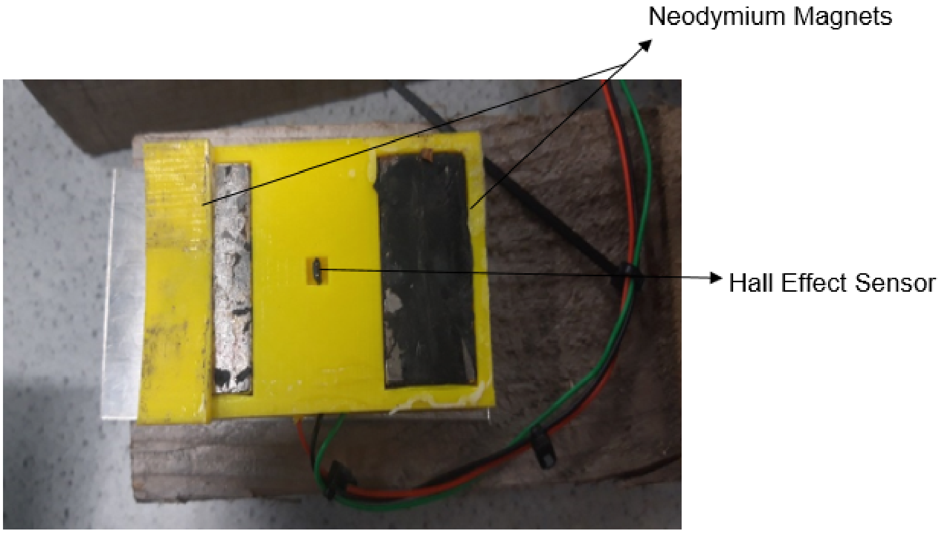

FIGURE 5.5: Prototype magnetic flux leakage transducer.

For the design of the smart magnetic monitor, the hall effect sensor was attached to the analog pin $A_0$ of the Node MCU8266. The microcontroller was programmed to acquire signals from both MEC and MFL sensors with a delay of 50 seconds between the readings to avoid interference between the signals.

A series of experiments were conducted on the prototype magnetic corrosion monitor to validate the FE modelling results. The results for the variation in the signals of MFL and MEC sensors due to uniform wall thickness loss in the 8 mm thick plate are shown in Figure 5.6.

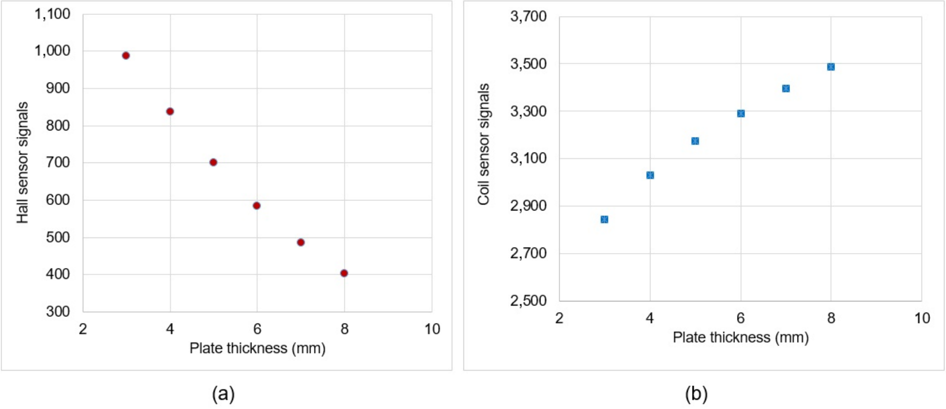

(a)

(b)

FIGURE 5.6: (a) Hall (MFL) sensor signals in bytes, (b) Coil (MEC) sensor signals for different plate thicknesses.

The corrosion monitor was also tested on a corroded pipe sample and the results obtained from both sensors were compared with UT test results. The test was conducted using zero degrees pulse-echo UT thickness probe by Olympus. The thickness measurements were taken on a 2x2 cm grid for mapping. The corroded pipe sample and the test setup and the corroded pipe sample are shown in Figures 5.7 and 5.8.

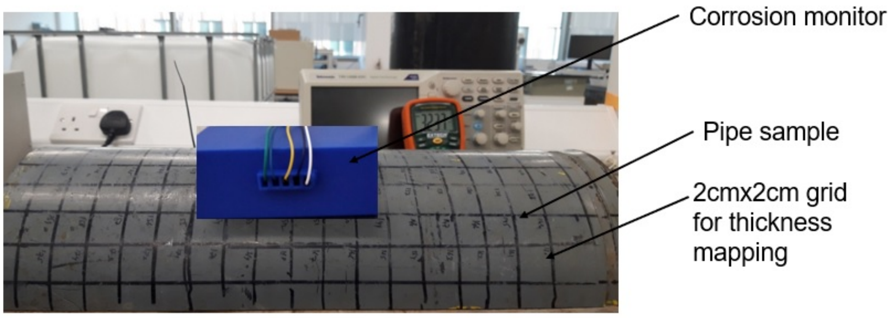

FIGURE 5.7: Test setup for the corroded pipe sample.

FIGURE 5.8: The image of corroded pipe sample showing the areas with wall thickness loss.

The results obtained from UT, MFL and MEC sensors are shown in Figures 5.9 to 5.11.

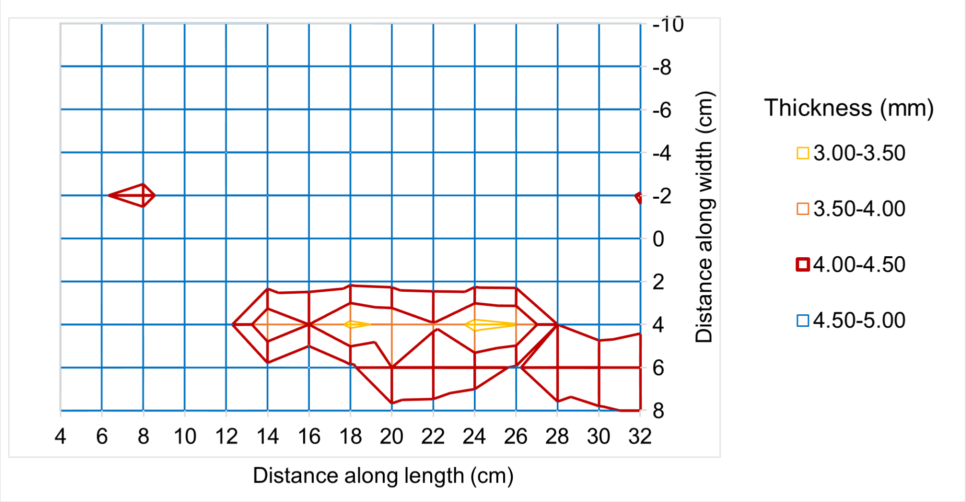

FIGURE 5.9: UT test results for corroded pipe sample.

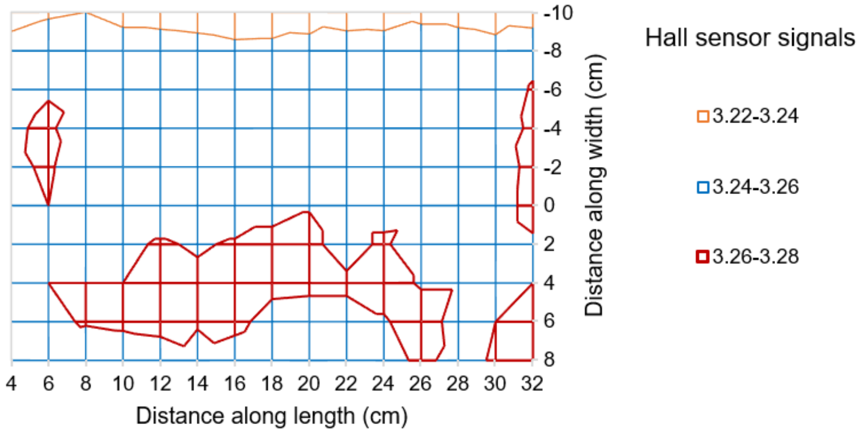

FIGURE 5.10: MFL test results for corroded pipe sample.

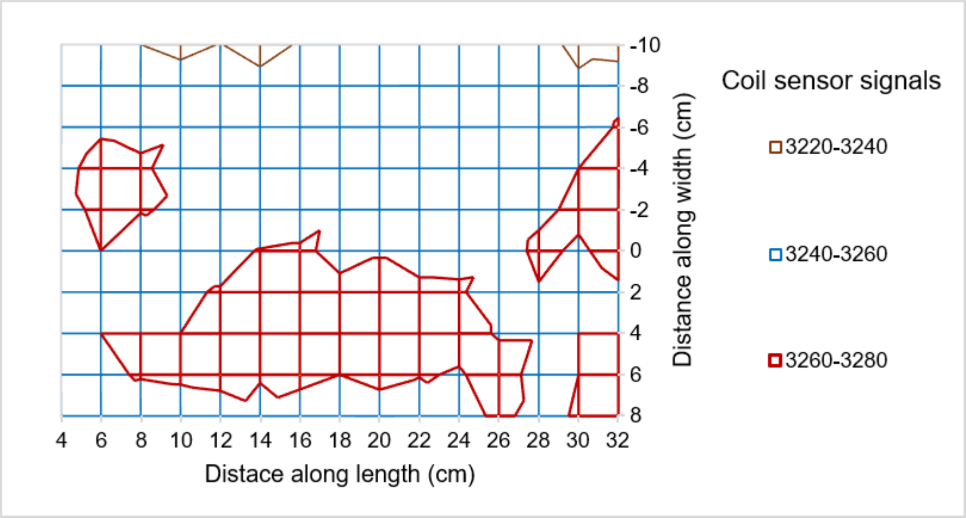

FIGURE 5.11: MEC test results for corroded pipe sample.

The results presented in Figures 5.10 and 5.11 show that both MFL and MEC sensors were capable of detecting wall thickness due to corrosion. However, both MFL and MEC sensors have a spatial resolution of the order of the area covered by the excitation circuit. This is the reason that the corroded areas appear to be larger in MEC and MFL plots compared to the UT thickness map. Unlike hall sensors, MEC sensors have a large coverage area due to the size of the sensing coil.

FE modelling and experimental results demonstrate that although MFL and MEC work differently, they can be used with the same magnetic excitation circuit. They can be utilised to monitor wall thickness loss at the identical installation point. This characteristic can be exploited for the diagnosis and isolation of faulty sensors for long-term applications. As there are very few chances of failure of both sensors at the same time, this can help in ensuring continuous operation of the corrosion monitor over an extended time period and therefore, achieve high reliability. The reliability of the newly developed magnetic corrosion monitor was tested through real-life aging test conducted for seven months.

## 5.3 Real-life aging test

Thickness loss due to corrosion in carbon steel can take years. Therefore, it is not easy to assess the performance of the magnetic corrosion monitor for the detection of wall thickness loss. A real-life aging test in the ambient environment was designed to induce corrosion at two different rates for the evaluation of the stability and detection capabilities of the corrosion monitor. The purpose of the real-life aging tests was to determine if the changes in the sensors' signals due to changes in environmental factors were less than the variation caused by wall thickness loss.

The experiments were carried out in two different stages:

- Stage 1: A saltwater circulation setup was designed to induce corrosion at a slow rate. This was done in order to test the stability of the sensors against changes in environmental conditions such as humidity and temperature.
- Stage 2: An accelerated corrosion environment was simulated using the impressed current technique to assess the capability of MFL and MEC sensors for the detection of wall loss over time.

### 5.3.1 Salt water circulation set up

Two prototype magnetic corrosion monitors were installed on a 6 mm thick mild steel pipe section. Node MCU8266 was connected to the Wi-Fi router to send the signals to the ThingSpeak data cloud. The block diagram of the smart corrosion monitor and the prototype magnetic corrosion monitor is shown in Figures 5.12 and 5.13.

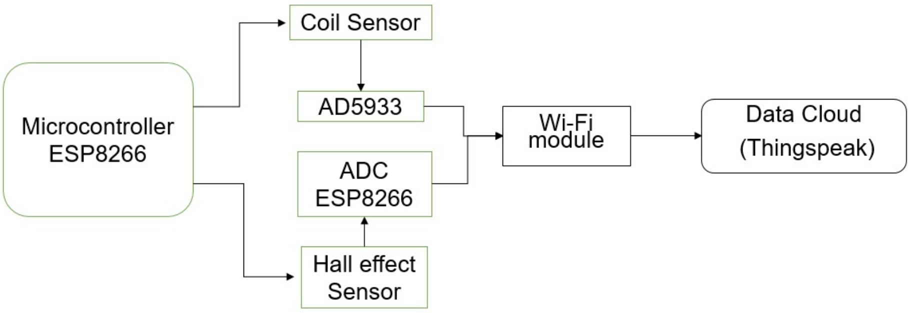

FIGURE 5.12: The block diagram of the smart corrosion monitor.

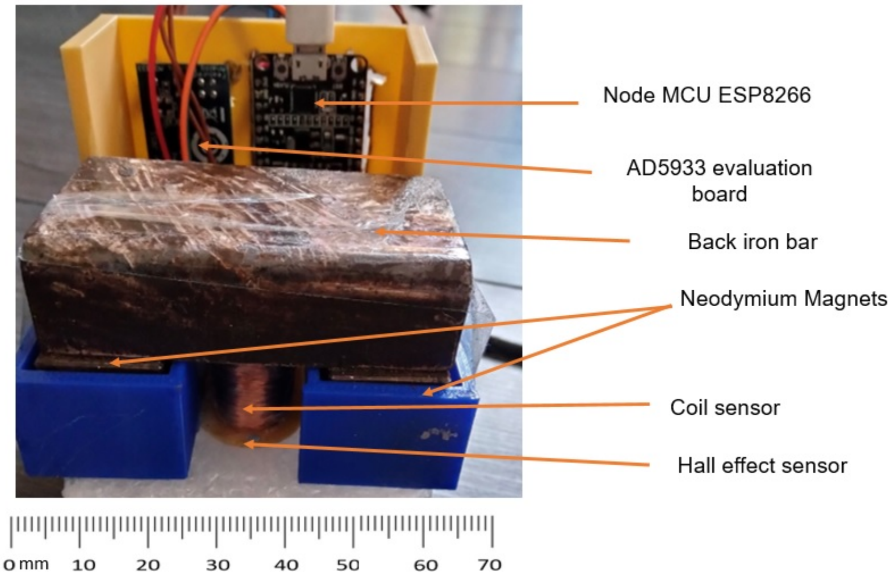

FIGURE 5.13: The prototype smart corrosion monitor.

The salt water was circulated using a solar pump assembly to induce corrosion at a slow rate. The pipe section was placed outside in the open for three months. The experimental setup is shown in Figure 5.14.

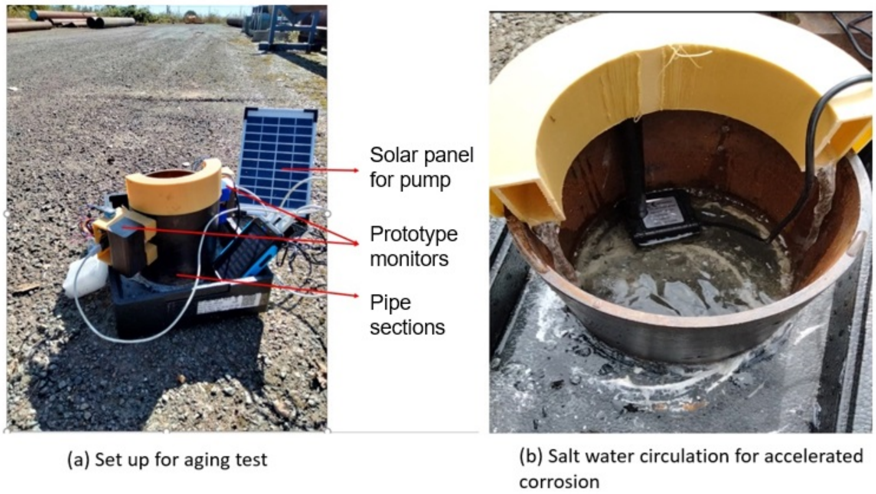

(a) Set up for aging test

(b) Salt water circulation for accelerated corrosion

FIGURE 5.14: Experimental setup for aging test in ambient environment.

A moving average filter was used to remove white noise from the signals received from MFL and MEC sensors. Figures 5.15 and 5.16 present the MFL and MEC sensor signals for corrosion monitors 1 and 2 for the period of 1st April to June 2022.

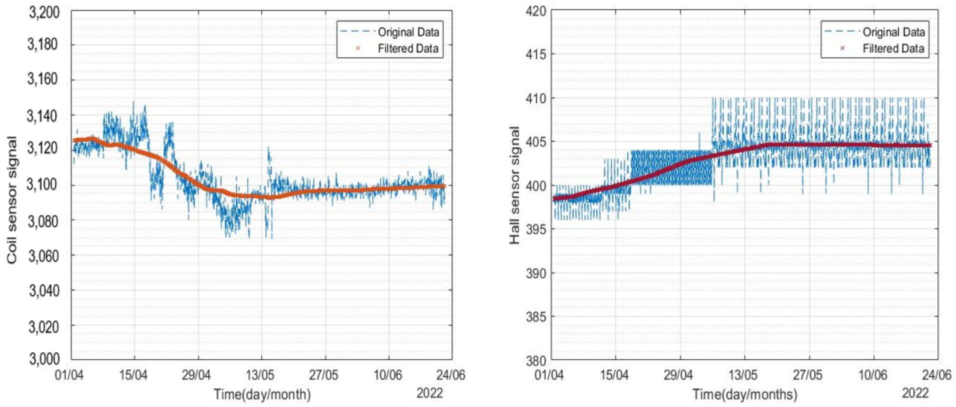

(a) MEC sensor signals (b) MFL sensor signals

FIGURE 5.15: The signals received from corrosion monitor 1 for the period of April 2022-June 2022.

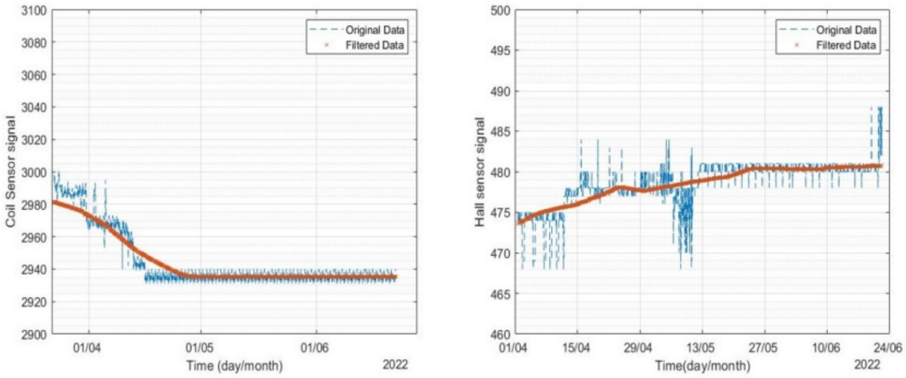

(a) MEC sensor signals (b) MFL sensor signals

FIGURE 5.16: The signals received from corrosion monitor 2 for the period of April 2022-June 2022.

It is evident from Figures 5.15 and 5.16 that there was no significant variation in the MFL and MEC signals for both corrosion monitors. Initially, at the start of the test, there were some changes observed in the signals. However, due to the frequent deposition of corrosion products on the pipe surface and inside the solar pump, there was not much thickness loss. The MFL and MEC sensors for both corrosion monitors did not show remarkable variations compared to the signals for 1 mm uniform wall loss for the plate sample. For 1 mm wall loss the signals from the MFL sensor expressed a 17% change in the base signal and approximately 6% change in the coil sensor signals. For corrosion monitor 1, the MFL sensor showed only a 1% change in the signals, and a 0.7% variation in MEC sensor signals was observed. A similar trend was expressed by corrosion monitor 2, where the MFL sensor showed 0.6% and the MEC sensor had a change of 2%. The test results demonstrated that both MFL and MEC sensors were stable against changes in temperature and humidity in the ambient environment.

### 5.3.2 Accelerated corrosion using impressed current

Impressed current is commonly employed for accelerating corrosion in steel reinforcements for achieving high corrosion rates in short time intervals [244, 245]. Using this technique, corrosion is induced by applying an electric potential between a carbon steel piece (anode) and a stainless steel bar (cathode). To enable current flow, salt water is used as an electrolyte. An illustration of the impressed current technique used to accelerate corrosion in the pipe section is presented in Figure 5.17.

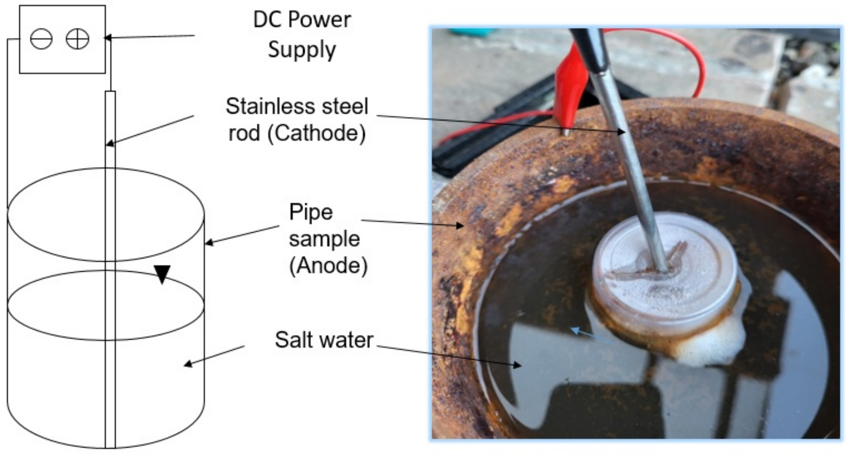

(a) Schematic representation

(b) Test setup on pipe sample

FIGURE 5.17: Experimental setup for impressed current technique to achieve high corrosion rate.

The pipe section was tested using the impressed current test setup for four months from July to October 2022. A 10 V voltage was applied using a DC power supply, and a 3%v/v NaCl solution was used as an electrolyte. To accelerate corrosion, the deposited corrosion products were cleaned regularly. The MEC and MFL signals received from corrosion monitor 1 are presented in Figure 5.18.

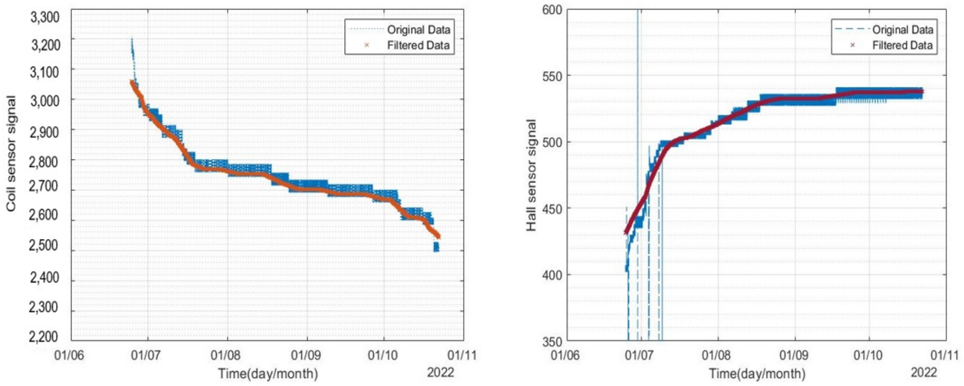

(a) MEC sensor signals

(b) MFL sensor signals

FIGURE 5.18: The signals received from corrosion monitor 1 for the period of July-October, 2022.

Signals received from MEC and MFL sensors of corrosion monitor 1 exhibited significant changes. The amplitude of the MEC sensor signals decreased by 20% while the amplitude of the MFL sensor signals increased by almost 30%. The plate sample test showed a 20% increase in MFL sensor signals and a 7% decrease in MEC sensor signals due to 1 mm wall loss. Compared to the MEC sensor signals, the amplitude of MFL sensor signals showed less variation. This is because the area covered by the MEC sensor coil was 20 mm (outer diameter of the coil) as compared to the MFL hall sensor. The slight difference in trend observed may be due to sharp pits forming outside the MFL sensor's coverage area.

The signals received from corrosion monitor 2 for the period of July to October 2022 are shown in Figure 5.19.

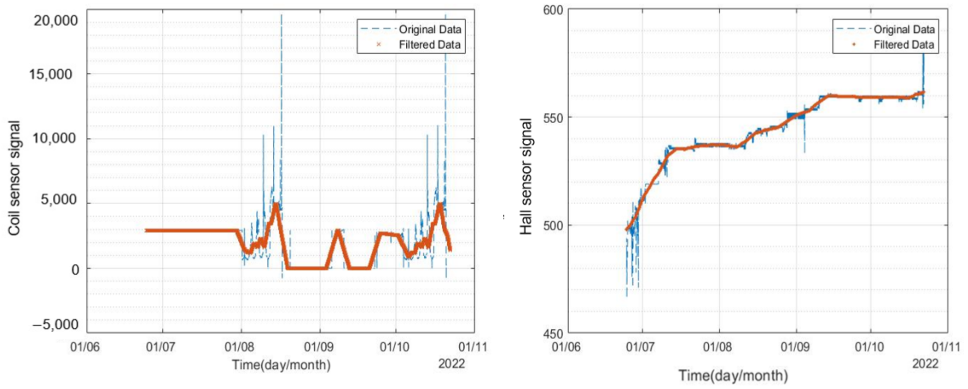

(a) MEC sensor signals

(b) MFL sensor signals

FIGURE 5.19: The signals received from corrosion monitor 2 for the period of July-October, 2022.

It can be seen from Figure 5.19 that the amplitude of the MFL sensor signals increased by 18%. The signals from MEC sensors, however, did not follow the expected pattern. The variation in the signals obtained from plate specimens and real-life aging tests are presented in Table 5.2.

TABLE 5.2: The comparison of variation in the MFL and MEC sensor signals from calibration and real-life aging tests.

| **Description** | **MEC sensor signals variation (units)** | **MFL sensor signals variation (units)** |
|---|---|---|
| 1 mm thickness loss | 113 | 76 |
| Monitor 1(April-June) | 25 | 7 |
| Monitor 2 (April-June) | 32 | 6 |
| Monitor 1 (July-Oct) | 446 | 89 |
| Monitor 2 (July-Oct) | N/A | 60 |

The comparison of the results obtained from the real-life aging test demonstrates that the variation in the signals from both sensors followed different trends. To investigate further the anomalous pattern in the time series data collected from MFL and MEC sensors and the identification of faulty sensors, a correlation study was conducted.

## 5.4 Correlation analysis

Systems based on the active redundancy principle employ multiple sensors to measure the same physical quantity. A spatial and temporal correlation exists between sensor data collected at analogous times and places. Despite the fact that individual sensor data may not show any faults, correlation analysis can reveal faults when the data from different sensors are analysed together.

Correlations between multivariate dataset from different sensors can be found using a number of techniques like principal component analysis [246], Kerner principle component analysis [247], and canonical correlation analysis [248]. Since the magnetic corrosion monitor developed in this research project involves time-series data from two sensors only, a simple and computationally efficient approach can be used for correlation. One of the techniques is Pearson's correlation coefficient or bivariate correlation for comparing two sets of data to determine the strength of the linear relationship. The Pearson correlation coefficient indicates the statistical relationship between two continuous variables [249]. Using this method, associations between variables are measured using the principle of covariance. As well as providing information about the magnitude of the association, it also gives details about its direction. Variables are measured regardless of their unit of measurement.

Pearson's correlation coefficient is computed by the expression:

$$r = \frac{n(\sum xy) - (\sum x)(\sum y)}{\sqrt{[n\sum x^2 - (\sum x)^2][n\sum y^2 - (\sum y)^2]}} \tag{5.1}$$

Where r is Pearson's coefficient, n is the number of readings/signals, x represents readings/signals from the first sensor, and y is the readings/signals from the second sensor.

Pearson's coefficient ranges between -1 and 1. The '0' coefficient value shows that there is no relationship between the variables. The higher the value of the coefficient, the stronger the correlation. A value in the range [-1,0] depicts that a negative relationship exists between the two variables indicating the movement of the variables in opposite directions. Positive correlation [0,1] shows that the variables are either increasing or decreasing.

For fault diagnosis in the sensors of the corrosion monitor, training data sets are needed to determine the relationship between the amplitudes of the MFL and MEC sensor signals due to wall thickness loss. Pearson's correlation coefficient threshold is defined using training datasets to decide if the sensors have anomalous patterns in the data. The training datasets are derived either by analysing sensor history or by testing the calibration sample with fault-free sensors. Because the corrosion monitor is a newly developed device with no prior history, five repeated measurements were taken on mild steel S275JR plates with thicknesses from 3 mm to 10 mm with an increment of 1 mm at each step. The results for the MEC and MFL sensors are presented in Figures 5.20 and 5.21 respectively.

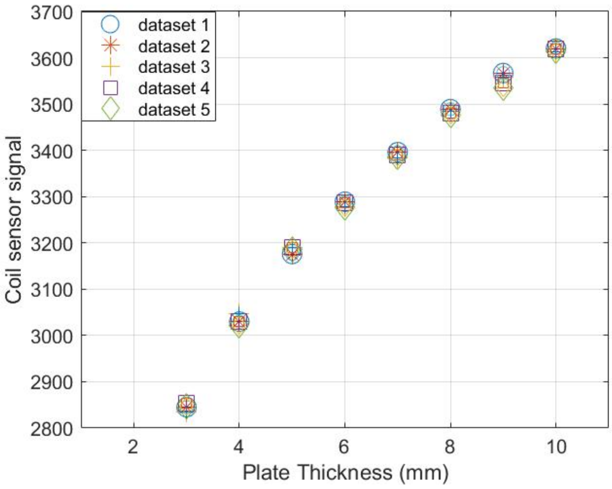

FIGURE 5.20: Training datasets for MEC sensor.

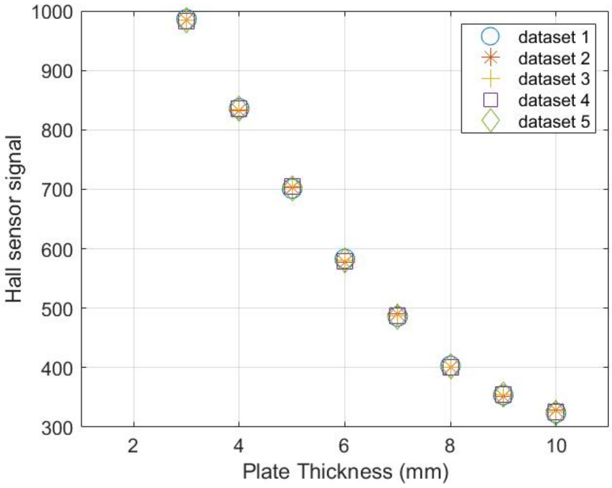

FIGURE 5.21: Training datasets for MFL sensor.

Pearson's coefficient values from the five training datasets are listed in Table 5.3.

TABLE 5.3: Pearson's correlation coefficient for MFL and MEC sensors calculated from the training datasets.

| **S.No.** | **Pearson's coefficient** |
|---|---|
| 1 | -0.90 |
| 2 | -0.92 |
| 3 | -0.93 |
| 4 | -0.95 |
| 5 | -0.89 |

It can be seen from Table 5.3 that a strong negative relationship exists between the signals of MFL and MEC sensors for uniform plate thickness. It is assumed that the wall thickness loss is uniform for computing Pearson's correlation coefficient for these datasets. This may not be true in service environments where sharp pits and localised corrosion defects may affect the results. Therefore, a wide range of thresholds [-1, -0.5] is considered for identifying anomalous patterns in the time series data from corrosion monitors 1 and 2.

### 5.4.1 Faulty sensor diagnosis

The time series data from MFL and MEC sensors can be represented as:

$$S(t, w) = x^n + \varepsilon^n \tag{5.2}$$

where $t$ denotes the current timestamp, $\omega$ is the size of the window, and $x^n(n = 1, 2, 3, .......)$ shows the column vector comprising the nth feature of the signal in the sensor data set for the interval $t$ to $t + \omega - 1$. $\varepsilon^n$ is the randomly distributed white noise associated with the signal. For the calculation of Pearson's coefficient, a time interval is defined. The time window of one month was used for calculating Pearson's correlation coefficient to evaluate the correlation between MFL and MEC sensor readings for both corrosion monitors. The results are presented in Table 5.4.

TABLE 5.4: Pearson's correlation coefficient computed from time series data of the corrosion monitors (*InF=complex square root).

| Month | Corrosion monitor 1 | Corrosion monitor 2 |
|---|---|---|
| April 2022 | -0.95 | -0.87 |
| May 2022 | -0.87 | -0.91 |
| June 2022 | -0.94 | -0.92 |
| July 2022 | -0.94 | -1 |
| August 2022 | -0.95 | InF* |
| September 2022 | -0.85 | InF* |
| October 2022 | -0.68 | InF* |

Table 5.4 shows that a strong correlation existed between MFL and MEC sensor signals of corrosion monitor 1 for the period of April to September 2022. However,

Pearson's coefficient value decreased to -0.68 in October 2022. This could be attributed to the sharp pits formed on the heavily corroded pipe. Although the value is still within the threshold limit, this needs to be investigated further.

For corrosion monitor 2 a strong negative relationship existed between both sensors for the period of April to July 2022. The value of Pearson's correlation coefficient returned an infinite value after July. This indicates the possibility of faults in the sensors of the corrosion monitor 2. At the end of the test, both corrosion monitors were examined to determine the cause of the error. The Pmodia board used for measuring reactance signals was found to be damaged. A potential cause of failure may be the absence of an onboard voltage regulator. Other components of the corrosion monitor were found to be in good working condition. Pmodia is the impedance evaluation board based on AD5933 that is available commercially. There is not much information on the reliability tests and long-term performance of the board from the manufacturers. The rest of the components, including Node MCU0.9, hall sensors, and copper coils, have been proven to perform well over the long term [250–252].

Pearson's correlation coefficients calculated from the real-life aging test varied from those calculated from the training datasets. Furthermore, considerable variation in the signals for both sensors of corrosion monitor 1 and 2 was observed during the test. Accordingly, to investigate the reasons for differences, the thickness of the areas of the pipe section under both corrosion monitors was measured using the electromagnetic acoustic thickness (EMAT) probe by Innerspec Technologies. A grid spacing of 15x15 mm was used to capture thickness changes for corrosion mapping. The test setup is presented in Figure 5.22.

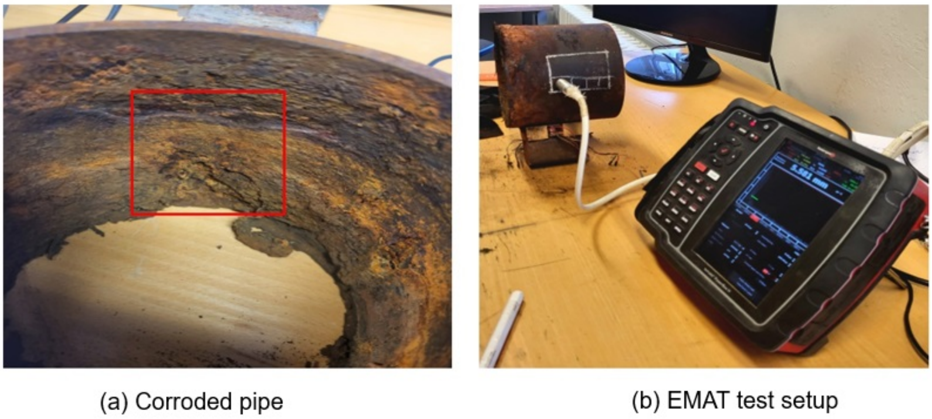
(a) Corroded pipe

(b) EMAT test setup

FIGURE 5.22: (a) The corroded pipe section, and (b) EMAT test setup for thickness measurement.

The thickness measurements obtained from the EMAT thickness test are listed in Table 5.5.

TABLE 5.5: Thickness measurements from EMAT for the areas under corrosion monitor 1 and 2.

| | **Corrosion monitor 1** | | | **Corrosion monitor 2** | | |
|---|---|---|---|---|---|---|
| **Distance (mm)** | 15 | 30 | 45 | 15 | 30 | 45 |
| 15 | 3.4 | 3.2 | 3.4 | 2.5 | 5.6 | 5.6 |
| 30 | 4.5 | 4.5 | 4.6 | 5.5 | 4.3 | 5.6 |
| 45 | 3.5 | 4.8 | 5.4 | 4 | 4 | 4.9 |
| 60 | 5.6 | 5.6 | 4.6 | 5.7 | 3.4 | 5.4 |

The thickness maps for the area covered by corrosion monitor 1 and 2 are shown in Figures 5.23 and 5.24 respectively.

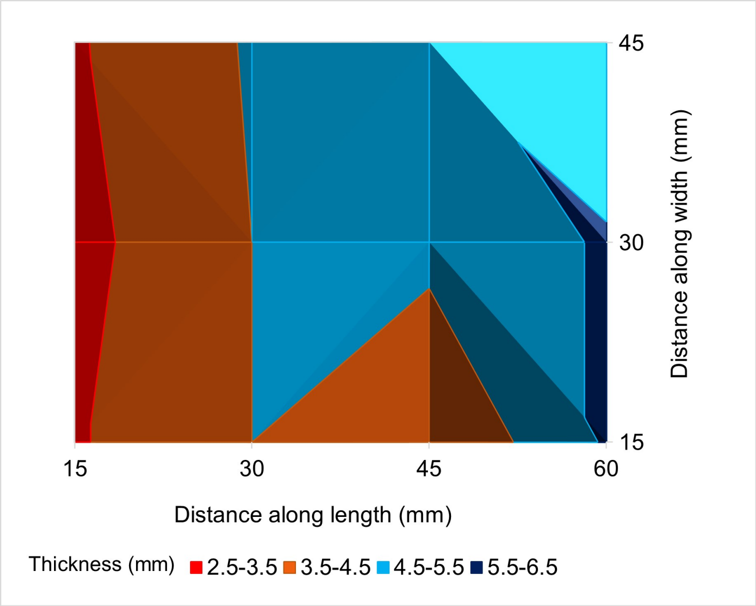

FIGURE 5.23: Thickness map of the pipe area covered by corrosion monitor 1.

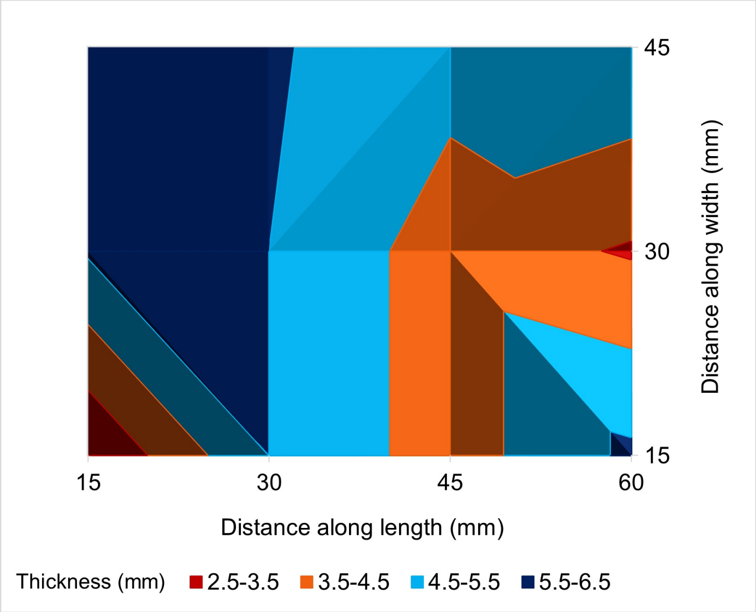

FIGURE 5.24: Thickness map of the pipe area covered by corrosion monitor 2.

The results presented in Table 5.5 confirm that the wall thickness loss was not uniform. The thickness loss was as high as 60% at some locations. MFL sensor installation point was a bit farther away from these locations. The wall thickness loss was 25% of the original pipe thickness at the location of the MFL sensor. This localised wall thickness loss resulted in the decreasing correlation between MFL and

MEC sensor signal amplitude. This issue can be resolved by utilising an array of MFL sensors to evaluate localised wall loss. Furthermore, the correlation of multiple MFL sensor data can be used to locate sharp pits and calculate wall thickness loss accurately.

## 5.5 Discussion

A novel magnetic corrosion monitor with the dissimilar active redundancy principle was proposed to improve long-term reliability. Feasibility studies conducted through FE modelling revealed that the same magnetic excitation circuit can be used for both MFL and MEC sensors. The results from the FE model suggested that the magnetic field sensor required for MFL applications should have high saturation density due to large leakage magnetic flux. Based on the review of the common commercially available magnetic sensors, the Allergo A-1324 was found to be suitable for corrosion monitor due to their high saturation fields, reasonable sensitivity, and low power consumption.

A prototype smart magnetic corrosion monitor was constructed based on the FE modelling results. Experiments were conducted on mild carbon steel plates with different thicknesses for evaluating the amplitude of MFL and MEC sensor signals due to uniform wall loss. The corrosion monitor was also used to test a sample that had been damaged by corrosion. The results were compared with the UT gauge results. It was observed that both MFL and MEC sensors could detect corroded areas successfully. One significant observation was that the corroded areas detected by MEC were larger than those detected by MFL or UT. This was due to the fact that both MFL and UT are point sensors while the coverage area of MEC sensors is of the order of the diameter of the coil sensor. The coil sensor averages the area under the coil. Therefore, sharp pits with high wall thickness loss may appear as uniform corrosion with shallow wall thickness loss. It was found that both MFL and MEC sensors were capable of detecting the thickness loss based on changes in the amplitude of the signals.

The long-term reliability of the prototype corrosion monitor was examined through a real-life aging test. The objective of testing the corrosion monitor in the ambient environment was to confirm if the variation in the signals of the sensors due to environmental factors is less than the changes due to wall thickness loss. The test was designed in two stages to evaluate the performance and stability of the developed corrosion monitor for tracking wall thickness loss over an extended time period in an open environment. In the first stage, a slat water circulation setup was used to induce corrosion at a slow rate in a pipe section for three months. Two smart prototype corrosion monitors were installed on the test pipe. No significant changes in the signals' amplitude were observed for both corrosion monitors. It was found that the sensor signals remained stable despite the fluctuations in environmental factors during this time period. The white noise in the signals of the coil (MEC) sensor was due to the electronics used for reactance measurement. The noise can be subsided by developing a data acquisition system suitable for the application.

During the second stage, an accelerated corrosion rate was achieved using the impressed current technique. There were significant changes in the signals' amplitude of both sensors for corrosion monitors 1 and 2. The results obtained for corrosion monitor 2 were found to be different than the expected trend. Studies on fault diagnosis in sensors were conducted to delve deeper into this issue. A correlation analysis based on Pearson's correlation coefficient was used to develop a methodology for the identification of faulty sensors from time series data. The training data set was obtained by repeated measurements of mild carbon steel plates of variable thickness. The thickness loss was assumed to be uniform for the calculation of Pearson's coefficient for training data sets. A strong negative correlation was found between the MFL and MEC sensor signals' amplitude due to uniform wall loss.

The comparison of Pearson's correlation coefficient with the training datasets indicated that corrosion monitor 2 had a faulty sensor. This was also confirmed when both corrosion monitors were examined at the end of the test. The impedance evaluation board Pmodia was identified as the critical component. Though the correlation coefficient for corrosion monitor 1 was found to be within the threshold range, the reason for the large variation in the value from the training data sets was investigated by thickness measurements of the pipe section.

Thickness measurements from EMAT tests showed that wall thickness loss was highly loclaised with some areas corroded as high as 60% of the original wall thickness. At the installation point of MFL sensors for corrosion monitor 1, the wall thickness loss was only 25%. Since MFL sensors have a small coverage area as compared to MEC sensors, this resulted in differences in the values of Pearson's correlation coefficient calculated from training datasets. Nonetheless, both MFL and MEC sensors were able to detect changes in wall thickness loss and withstand variations in temperature and humidity levels. The corrosion monitor developed in this project is suitable for applications where the wall thickness loss due to corrosion is expected to be uniform. Furthermore, all the NDE techniques including UT struggle with the detection and sizing of short and narrow defects such as pits [55].

The dissimilar active redundancy concept presented in this chapter for the improvement of long-term reliability of the corrosion monitor was found to be successful in identifying faulty sensors. This is crucial for remote corrosion monitoring applications, especially with accessibility issues. The sensors will eventually fail over time due to aging phenomena. The aging time period can be extended by design improvements but cannot be avoided. Identification and isolation of faulty sensors can ensure that the corrosion monitoring device can track wall loss over an extended time period. This can also help avoid false alarms and missed signals.

## 5.6 Summary

There is limited work on the design and reliability of corrosion monitoring devices for detecting buried or internal wall thickness loss. The work presented in this chapter was aimed at addressing this issue. The conclusions deduced from the investigations on the improvement of long term performance and reliability of the corrosion monitor are as follows:

1. MFL sensors are capable of detecting wall thickness loss at a magnetic flux density of 1.4 T in the test specimen for permanent installation applications. Therefore, the same magnetic excitation circuit can be used for both MFL and MEC sensors. It can be used for diagnosing malfunctions in either sensor using correlation between the time series data from both sensors.

2. Correlation analysis of the time series data from MFL and MEC sensors using the Pearson correlation coefficient reveals that MFL and MEC sensors have a strong negative relationship. Due to the differences in the coverage area of

both sensors, data from a single MFL sensor is not enough to identify the faulty sensor.

3. The corrosion monitor was stable against temperature and humidity in a real-life aging test conducted in two stages. The sensors are capable of tracking internal and buried wall thickness loss over time.

4. The impedance evaluation board Pmodia based on AD5933 is the critical component.

Pearson's correlation coefficient for the identification of faulty sensors was designed on the assumption that corrosion is uniform in the test specimen. In real-life aging tests, it was observed that the difference in the coverage range of MFL and MEC sensors adversely affects the correlation between the signals. The difference was high for defects such as sharp pits and localised corrosion. This problem can be solved by employing an array of MFL sensors and a detailed study of the correlation coefficient for fault diagnosis. The study can further be extended to distinguish between sharp pits and uniform corrosion defects using time series data from MEC and multiple MFL sensors.

For improved reliability, the impedance evaluation board needs to be redesigned. The Pmodia board used in this study was commercially available but was found to be not suitable for corrosion monitoring applications.

This study aimed to develop a magnetic corrosion monitoring system that would provide qualitative indications of wall thickness loss in test components. The experimental results concluded that the severity of corrosion defects could be estimated by evaluating the percentage loss in the base signal. UT or other NDT techniques are needed to quantify corrosion defects. This is a major limitation that needs to be addressed to improve the capabilities of the magnetic corrosion monitor. Both MFL and EC signals are affected by the magnetic permeability of the test specimen. Therefore, information on the magnetic permeability is required for quantification of corrosion defects. Further investigations into the estimation of the remaining wall thickness of the test components carried out as a part of this research project are discussed in Chapter 6.

# Chapter 6

# Estimation of Remaining Wall Thickness

## 6.1 Introduction

The estimation of remaining wall thickness (RWT) from MFL signals requires a calibration procedure to correlate the leakage flux density (LFD) with the defect depth. The calibration is carried out to estimate the leakage flux density using the ratio of the magnetic induction (***B***) at a certain applied magnetic field (***H***) i.e. the magnetic permeability of the material. Moreover, it is imperative to ensure that the relative permeability at the installation location of the corrosion monitor is in the operating region, that is, decreasing sharply to achieve high sensitivity to wall thickness loss defects. This chapter presents the methodology developed as part of this research for in-situ calibration of the test specimen. The proposed approach was developed through the following steps:

- Development of a forward FE model for computation of ZCF from the multi-frequency reactance signals of EC coil sensor.
- Design and implementation of an inverse DE algorithm for the evaluation of in-situ relative permeability of the test component. This was done by formulating the objective function to correlate the test and FE model ZCF.
- Calibration of the MFL FE model by using the in-situ relative permeability to evaluate the LFD at the sensor location.

- An inverse model for predicting the RWT from the forward calibrated MFL model and the test or reference signal.
- Validation of the proposed approach on two different test cases.

## 6.2 Problem formulation

The estimation of the RWT is obtained by solving the inverse problem to correlate the field test MFL sensor signals with the forward physical model. Researchers have used ***B*-*H*** curves from the material library of the FE package such as Comsol Multiphysics or ANSYS to compute the LFD due to certain defect profiles for correlation with the test signals. Quantitative studies on the characterisation and propagation of MFL signals in oil and gas pipes have revealed that residual stresses and heat treatments change the permeability, coercivity, and other magnetic properties of the steel and hence may alter MFL signals by more than 40% [253]. Therefore, to estimate the size of the defect accurately, it is necessary to incorporate these effects on the MFL signals.

Furthermore, the LFD obtained from the FE model by using the ***B*-*H*** curve is observed to be highly overestimated. This is because ***B*-*H*** curves are obtained by standard techniques where the bar or ring or bar sample is homogeneously magnetised from all sides. The test setup adopted for the determination of the ***B*-*H*** curve from the ring specimen is shown in Figure 6.1.

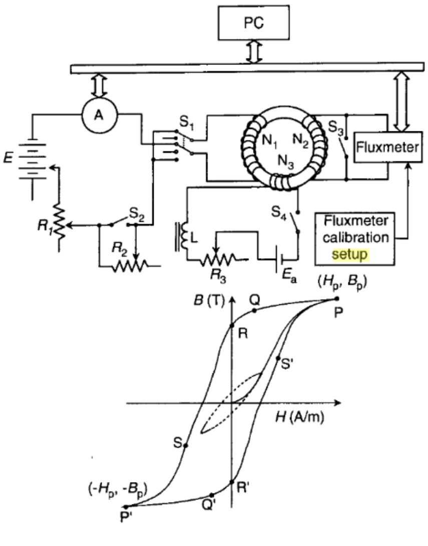

FIGURE 6.1: Experimental setup for determination of the ***B*-*H*** curve from ring specimen [254].

However, for MFL this assumption is not applicable. In the MFL technique, the magnetic excitation circuit is placed above the test specimen. The magnetic field is not applied homogeneously around the test specimen. Accordingly, the LFD calculated from the FE model is much higher than the LFD calculated from the tests.

In order to compute the LFD at the location of the installation of the magnetic corrosion monitor, therefore, a new methodology is presented in this chapter. The constitutive relation to solving the problems for ferromagnetic materials can be defined using either relative permeability or ***B*-*H*** curve.

Instead of the ***B*-*H*** curve, the materials can be modelled by defining the relative magnetic permeability, that is the ratio between the induced magnetic flux density ***B*** and applied magnetising force ***H*** at the specific excitation magnetic field.

Relative magnetic permeability is an intrinsic property of the material, however, it is indirectly dependent on the thickness of the magnetised test specimen. When the magnetic flux density in the magnetised test specimen is increased due to the wall thickness loss, the flux carrying capacity of the specimen which is the relative magnetic permeability is decreased. The LFD can be computed by estimating the magnetic permeability for a particular thickness of the specimen and vice versa. The problem can be formulated as an inverse problem when the LFD from the field tests is defined in the model to deduce the thickness. However, the in-situ relative permeability at the location of the magnetic excitation circuit is required to be defined in the model to solve the inverse problem.

The apparent relative permeability at the location of the MEC corrosion monitor can be estimated by inverting the ZCF feature measured using the multi-frequency reactance signals.

**Zero crossing frequency (ZCF)**

ZCF is defined as the point where the inductive energy stored in the EC sensor above the test specimen is the same as in the air [209].

In ferromagnetic materials, multi-frequency EC sensor's magnetic field acts on the specimen in two ways. The primary magnetic field of the coil sensor magnetises the sample. At lower frequencies the effect of the primary magnetic field is dominant and therefore, the inductance energy is high. The second effect is due to the eddy currents induced in the test specimen. This results in the secondary magnetic field that opposes the primary magnetic field. As the frequency increases the effect of eddy currents increases due to the saturation of the primary magnetic field. At a certain frequency called ZCF, they both balance each other and the inductance of the sensor is the same for both test specimen and air. Since the intensity of both primary and secondary magnetic fields are dependent on the magnetic permeability, ZCF is directly related to the magnetic permeability of the test specimen. Thus, the in-situ relative permeability can be estimated by inverting the experimental ZCF with the in-situ relative permeability of the EC coil model using the iterative approach.

As discussed in Chapter 5, the magnetic corrosion monitor utilises both MFL and MEC sensors for improved reliability. The coupled sensors can also be used to find the in-situ relative permeability, that is the permeability of the magnetised test specimen at the location of the installation of the corrosion monitor.

### 6.2.1 Test case 1

#### Calibration

To determine the apparent relative permeability for the specimen whose thickness is unknown, the ZCF feature is computed from the multi-frequency reactance signals on the test plates.

The complex part of the impedance $X$ can be represented as the reactance in free space $X_0$ and the change in reactance $\Delta X$ when the coil sensor is above the test specimen.

$$\begin{aligned} X &= X_0 + \Delta X \\ \Delta X &= X - X_0 \end{aligned} \tag{6.1}$$

The reference ZCF was obtained by performing a frequency sweep on the coil sensor using the AD5933 evaluation board. Mild steel S275JR plate samples with thicknesses of 3 to 8 mm with an increment of 1 mm at each step were tested and the ZCF

$\omega_0$ was calculated from the multi-frequency reactance data. The frequency sweep was performed from 10 kHz to 100 kHz with an increment of 1 kHz at each step.

The values of ZCF for different plate thicknesses are listed in Table 6.1.

TABLE 6.1: Test results of ZCF values for different plate thicknesses.

| **Plate thickness (mm)** | **Zero crossing frequency** |
|---|---|
| 3 | 64 |
| 4 | 82 |
| 5 | 97 |
| 6 | 110 |
| 7 | 125 |
| 8 | 133 |

The EC coil sensor model was built in Comsol Multiphysics to compute the multi-frequency reactance spectrum. The relative permeability was defined as a variable in the material properties.

A DE algorithm was developed to inverse the ZCF for the estimation of the apparent relative permeability for the test specimen at the given applied magnetic field **(H)**. The fitness function is formulated as a minimisation function to minimise the difference between the ZCF computed from the FE model and the reference ZCF obtained from the experimentation.

$$f_{calibration} = min\left|ZCF_{ref} - ZCF_{model}\right| \tag{6.2}$$

The $ZCF_{model}$ was computed by the 2-D symmetric coil model discussed in Chapter 3. The model was converted to Java script using Comsol Livelink to solve the model with the DE algorithm in MATLAB.

A frequency sweep was performed from 10 kHz to 200 kHz with an increment of 1 kHz. $\Delta X$ was computed and ZCF ($\omega_0$) was determined by the interpolation function in MATLAB.

### DE Algorithm

DE is a stochastic-based algorithm that does not require a gradient of the problem to be optimised. It can therefore be used for problems that are changing over time. There are two phases of DE optimisation.

- First step is the initialisation in which a uniformly distributed population is generated randomly.
- The next phase is the evolution that involves updating the solution by combining the current solution (mutation) which is then crossed over and the best selection is made.

This process is repeated until the stopping criteria condition is fulfilled.

The agents ($x$) in the population ($NP$) where $Np > 4$ are generated randomly in the search space using the expression;

$$x_{j,i} = unifrnd.(x_j^U - x_j^L) \tag{6.3}$$

where, $i = 1, 2, ..., NP$, $j = 1, ...D$ (variable size), $x_j^U$ is the upper bound of the variable and $x_j^L$ is the lower bound of the variable or agent.

Mutation involves choosing three vectors or agents ($a$, $b$, and $c$) randomly for each target vector $x$. The mutant vector is then computed at each iteration ($t$) by:

$$y_{j,i,t+1} = a_t + F(b_t - c_t) \tag{6.4}$$

where, $a$, $b$, and $c$ are the vectors $a \neq b \neq c \neq x$, and $F$ represents the differential weight that is a real-valued scaling vector in the range of 0 to 1. Consequently, the mutations are amplified based on the different $F$ values.

To enhance the diversity, the cross-over ($CR$) parameter is defined. The trial vector is selected based on:

$$u_{j,i,t+1} = \begin{cases} y_{j,i,t+1} & if \quad r_i < CR \quad or \quad i = R \\ x_{j,i,t} & otherwise \end{cases} \tag{6.5}$$

where, $R\varepsilon$ $1, 2, ..., n$, $n$ is the dimension of the problem solved, $r_i$ is a uniformly distributed random number, and $CR$ is the cross-over probability that is in the range of 0 to 1. It controls the likelihood that a trial vector will come from the mutant vector rather than the current one.

In the last step, the selection is made based on the greedy approach. This is the reason that the DE algorithm is faster than other evolutionary algorithms, such as genetic algorithms, at finding the optimum solution.

Selection is based on the comparison of the trial and current vector to minimise the fitness function:

$$X_{i,t+1} = \begin{cases} Y_{i,t+1} & iff(y_{i,t+1}) \leq f(x_{i,t}) \\ X_{i,t} & otherwise \end{cases} \tag{6.6}$$

The pseudo-code for the DE algorithm is given as:

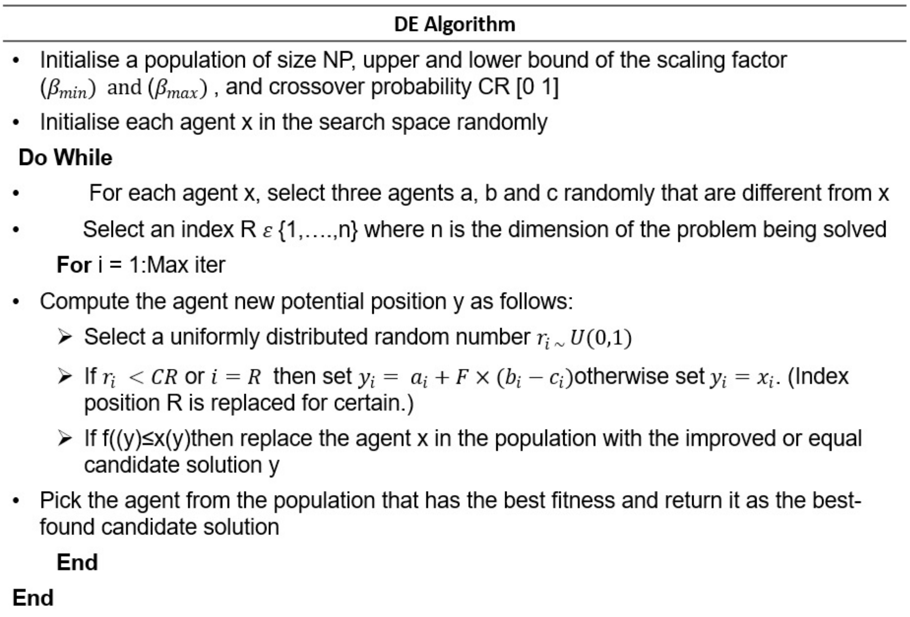

```
DE Algorithm
• Initialise a population of size NP, upper and lower bound of the scaling factor
  $(\beta_{min})$ and $(\beta_{max})$ , and crossover probability CR [0 1]
• Initialise each agent x in the search space randomly
Do While
•   For each agent x, select three agents a, b and c randomly that are different from x
•   Select an index R $\varepsilon$ {1,….,n} where n is the dimension of the problem being solved
  For i = 1:Max iter
• Compute the agent new potential position y as follows:
    ➢ Select a uniformly distributed random number $r_i \sim U(0,1)$
    ➢ If $r_i < CR$ or $i = R$ then set $y_i = a_i + F \times (b_i - c_i)$otherwise set $y_i = x_i$. (Index
      position R is replaced for certain.)
    ➢ If f((y)≤x(y)then replace the agent x in the population with the improved or equal
      candidate solution y
• Pick the agent from the population that has the best fitness and return it as the best-
  found candidate solution
  End
End
```

The apparent relative permeability was defined as the agent x and the optimum value was computed by the minimisation of the fitness function. The parameters defined in the algorithm are listed in Table 6.2.

TABLE 6.2: Parameters defined in the DE algorithm.

| **Parameters** | **Values** |
|---|---|
| NP | 15 |
| CR | 0.5 |
| Beta (max) | 0.8 |
| Beta (min) | 0.2 |
| x(min) | 60 |
| x (max) | 2000 |

The convergence graph obtained from the implementation of the DE algorithm is shown in Figure 6.2.

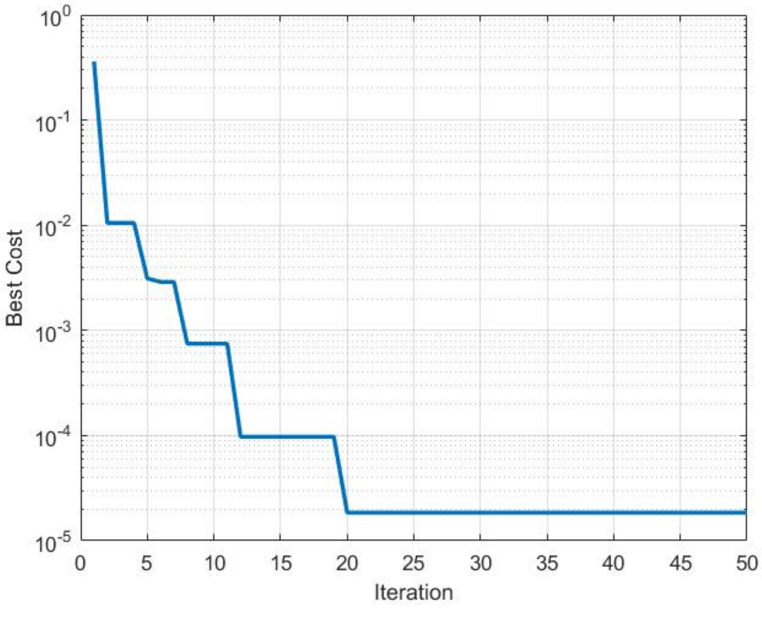

FIGURE 6.2: DE convergence graph for calibration problem.

The values of relative magnetic permeability obtained from the DE algorithm are presented in Table 6.3.

TABLE 6.3: The in-situ relative permeability computed from the DE algorithm.

| **Plate thickness (mm)** | **In-situ relative permeability** |
|---|---|
| 3 | 278 |
| 4 | 340 |
| 5 | 416 |
| 6 | 543 |
| 7 | 889 |
| 8 | 1037 |

The results from Table 6.3 show that the in-situ permeability of the plate sample decreases due to the wall thickness loss. This is because the sample is magnetised beyond a certain point in the ***B-H*** curve by the magnetic excitation circuit subsequently decreasing the flux carrying capacity. This is the reason that a small change in the thickness causes a significant change in the LFD.

### Remaining wall thickness estimation

The Allergo A-1324 Hall effect sensor was used to measure the LFD for different plate thicknesses. The test setup is discussed in Chapter 5. The results obtained from the experiments are presented in Table 6.4.

TABLE 6.4: Test results for the hall effect sensor voltage and LFD.

| Plate thickness (mm) | Hall sensor Voltage (V) | Leakage flux density (mT) |
|---|---|---|
| 3 | 1.65 | 18.3 |
| 4 | 1.79 | 14.2 |
| 5 | 1.97 | 10.8 |
| 6 | 2.07 | 8.6 |
| 7 | 2.17 | 6.6 |
| 8 | 2.18 | 6.4 |

The in-situ relative magnetic permeability obtained from the calibration step is assigned to the Java-scripted 3-D magnetic excitation circuit model. The 3-D MFL model is discussed in detail in Chapter 3 and Chapter 5. The plate thickness was defined as the variable/agent ($x$) in the DE algorithm and the LFD is evaluated for various values of plate thicknesses. This is done until the difference between the LFD obtained from the experiments, and the FE model was minimised.

The results for the estimated and actual wall thickness are shown in Table 6.5.

TABLE 6.5: Plate thickness estimated from the DE inverse algorithm.

| **Plate thickness (mm)** | **In-situ relative permeability** |
|---|---|
| 3 | 3.5 |
| 4 | 4.2 |
| 5 | 5.1 |
| 6 | 5.8 |
| 7 | 7.1 |
| 8 | 7.8 |

It can be seen from the results presented in Table 6.5 that the thickness of the plate can be estimated with a maximum error of ±0.5 mm.

The computational efficiency of the DE algorithm employed in this research was compared with the PSO algorithm. The comparison was based on the number of iterations required for convergence. The time required for each iteration was also evaluated. The comparison is shown in Figure 6.3.

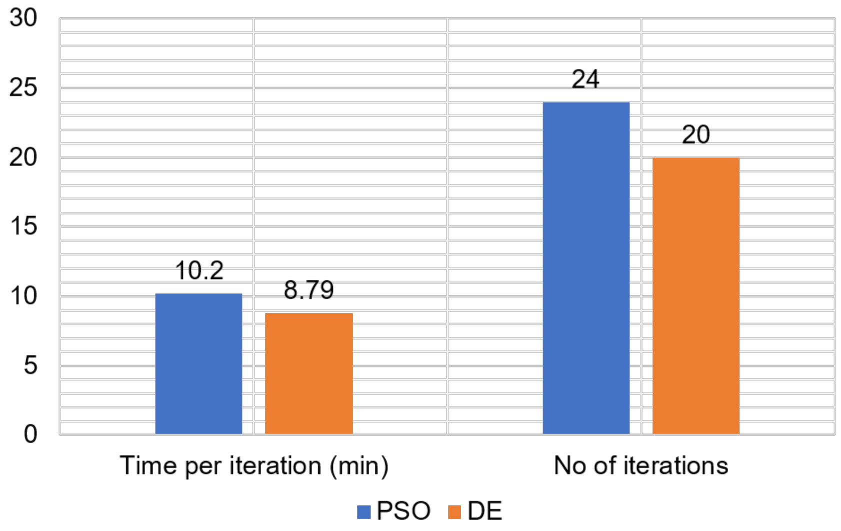

FIGURE 6.3: The comparison of the PSO and DE algorithm for the calibration problem.

It is evident from Figure 6.3 that DE has slightly better performance than PSO.

### 6.2.2 Test case 2

In order to validate the approach proposed in Section 2 an experimental study was conducted. A mild steel pipe sample was tested using the sensors. The pipe sample was machined to have thicknesses of 2.6 mm, 3.1 mm, 4.1 mm, and 5.3 mm. The pie sample is shown in Figure 6.4.

FIGURE 6.4: Pipe sample used for the test case 2.

AD5933 evaluation board was used for evaluating the multi-frequency reactance signals to find the ZCF. Hall sensor was connected to ADC ESP8266 to find the changes in the voltage due to varying LFD. The test setup is shown in Figure 6.5.

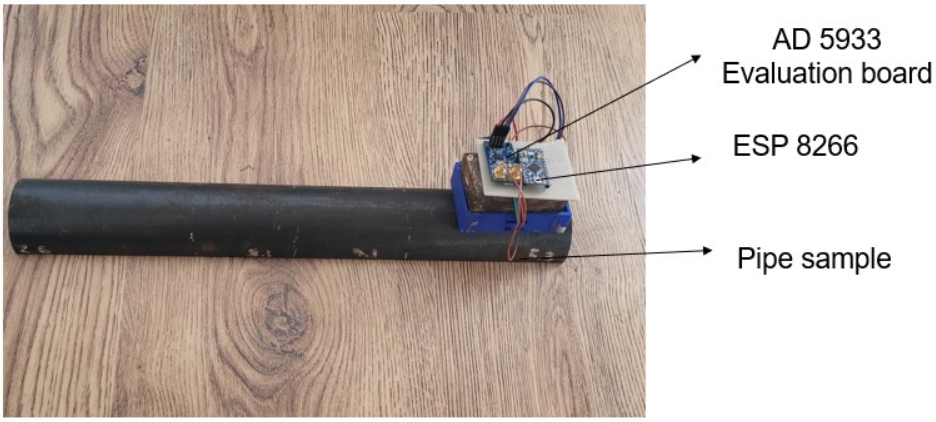

FIGURE 6.5: Experimental setup for the test case 2.

The forward coil model was built in Comsol Multiphysics to evaluate the magnetic permeability for in-situ calibration from the ZCF feature as shown in Figure 6.6.

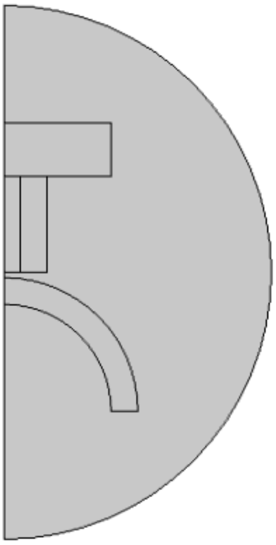

FIGURE 6.6: Geometry of the coil model for calibration of MFL model.

The results from the test are summarised in Table 6.6.

TABLE 6.6: ZCF obtained from experiment for test case 2.

| **Pipe thickness (mm)** | **Zero crossing frequency (kHz)** |
|---|---|
| 2.6 | 78 |
| 3.1 | 86 |
| 4.1 | 95 |
| 5.3 | 115 |

The 3-D MFL model was calibrated using the permeability obtained for the correlation of ZCF from the model and experiment. The geometry of the MFL model used to estimate the thickness of the pipe from MFL signals is shown in Figure 6.7.

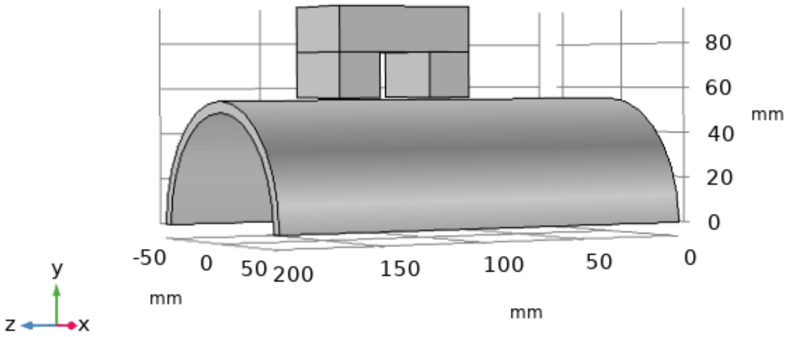

FIGURE 6.7: Geometry of the MFL model for the estimation of RWT for test case 2.

The thickness of the pipe sample estimated from the DE algorithm is presented in Table 6.7.

TABLE 6.7: Estimated pipe wall thicknesses for test case 2 from DE algorithm.

| **Actual wall thickness (mm)** | **Estimated wall thickness (mm)** |
|---|---|
| 2.6 | 2.2 |
| 3.1 | 2.5 |
| 4.1 | 4.5 |
| 5.3 | 4.8 |

The results obtained from the DE algorithm reveal that the thickness of the pipe can be estimated with an accuracy of ± 0.6 mm.

## 6.3 Summary

To determine the RWT from MFL signals, an in situ calibration approach was proposed. In addition, the study is also important to ensure that the test specimen is magnetised above the operating point where the permeability is decreasing sharply to ensure that the wall thickness loss defects can be detected from the MFL sensor. The inverse methodology involves the correlation of MFL signals from the FE model and field tests. The magnetic properties of the test specimen are required to evaluate the LFD from analytical or numerical models. ***B-H*** curves from the material library can be used for modelling ferromagnetic materials. However, the magnetic properties of ferromagnetic materials are dependent on a number of factors such as heat treatments, the presence of inclusions, residual stresses, magnetism, and defects. Therefore, the ***B-H*** curve in the material library is not representative of the test specimen properties.

In-situ relative magnetic permeability was estimated by formulating an inverse problem based on the ZCF feature. A multi-frequency reactance response spectrum was obtained for various plate specimen thicknesses using AD5933 evaluation board. The ZCF computed from the experiment was used as a reference signal. This was then defined as the fitness function for the DE algorithm. Magnetic permeability was defined as the unknown variable for the inverse problem in the coil sensor FE model. In agreement with the theory, magnetic permeability decreases as the thickness of the plate specimen is reduced.

The magnetic excitation circuit model developed in Comsol Multiphysics was calibrated using the magnetic permeability obtained. The LFD evaluated from the tests on different plate thicknesses was defined in the DE to inverse the flux density to the plate thickness. The results revealed that the plate thickness could be accurately estimated with an error of ± 0.5 mm. After that, the approach was validated on a second test case. A pipe sample with different thicknesses was tested using MEC and MFL sensors. The results revealed that the pipe sample thickness could successfully be estimated with an error of ± 0.6 mm by the calibration methodology proposed in this project.

The study was conducted on the test specimens with uniform wall thicknesses. However, in real-world circumstances, wall thickness loss can be localised and an average wall thickness can be evaluated with this setup. An array of MFL sensors can, however, be used to record the LFD at multiple locations. Since the MFL signals' amplitude is proportional to the defect depth, this can be exploited to determine the depth of the defect depth at multiple points for obtaining the thickness map.

For the calibration of the model, the assumption was made that the magnetic permeability is uniform throughout the magnetised sample thickness. The magnetic shielding effect is less pronounced under high magnetisation, so this approach can be used for samples with less thickness. There is a large magnetic shielding effect for these samples, especially above 10 mm, so the magnetic permeability may differ, especially on the far side. Therefore, the study can be extended to employ techniques such as low-frequency or pulsed eddy current sensors with high penetration depths. This will make it possible to estimate in-situ magnetic permeability in different layers of the test specimen. This can improve the calibration procedure for accurate sizing.

This chapter discussed the research work conducted on the determination of the RWT from the MFL and MEC sensor signals. This is required to develop a warning system for asset owners when the wall thickness is reduced beyond a critical value. The conclusions and future recommendations for the research project are presented in Chapter 7.

# Chapter 7

# Summary and Recommendations

## 7.1 Introduction

The research project aimed to develop a proposed wireless magnetic corrosion monitor for tracking wall thickness loss in ferromagnetic structures. Furthermore, the study investigated the methods to improve the coverage, reliability, and calibration of the corrosion monitor.

The successful outcomes of the project and the recommendations for future studies are discussed in the following sections:

## 7.2 Concluding remarks

The details of the questions explored and studies conducted in order to answer them to achieve the goals of the research study are as follows:

### 7.2.1 Development of magnetic corrosion monitor

- Is it feasible to develop a wireless, and cost-effective magnetic corrosion monitor to track buried and/or internal wall thickness loss over an extended period of time?
- How can the power consumption of the magnetic corrosion monitor be optimised so that it can run on batteries for a long period of time?
- What are the essential characteristics and limitations of the magnetic corrosion monitor?

Based on the answers to the questions, the following conclusions were drawn:

A cost-effective and small-size wireless MEC transducer has been developed and tested successfully through an accelerated corrosion test for detecting wall thickness loss in steel structures.

The reactance of the MEC sensor has been found to be sensitive to the wall thickness loss and stable against small variations in the temperature and humidity in the controlled lab environment.

The critical factors that affect the detection capabilities of the MEC monitor are the magnetic field induced in the test specimen and the excitation frequency of the harmonically excited coil sensor.

A minimum magnetic induction of 1.4 T is required in the test specimen. Optimising the parameters of the magnetic excitation circuit using FE modelling is necessary to make sure the magnetic induction is above this value.

The MEC soil sensor's sensitivity depends on excitation frequency. The sensitivity is maximum at two optimal frequencies. At ZCF, however, the sensitivity is minimal. Hence, it is crucial to avoid ZCF and its adjacent frequencies in the design of the sensor.

The power efficiency of the monitor has been improved by programming the microcontroller to turn into deep sleep mode during the intervals when the signals are not recorded.

The MEC corrosion monitor has the following main advantages over ultrasonic thickness transducers widely used in industry:

- They do not require coupling agents to install them on the surfaces to be monitored.
- They are not expensive. The cost of the components used in one monitor is around £200, which is much less than UT corrosion monitors.

The major limitation of the proposed MEC monitor is that it cannot be used for very thick components especially beyond 15 mm due to the magnetic shielding effect. Huge and powerful rare earth magnets are required for thick components that pose handling issues and health and safety hazards.

### 7.2.2 Coverage (through-thickness)

- What are the factors that affect the sensitivity of the magnetic corrosion monitor?
- How to ensure that the sensor is capable of detecting wall thickness loss in different setups?

The conclusions from the studies to address questions related to the optimisation are:

A PSO based approach has been proposed and validated on two test cases to avoid the time-consuming and iterative optimisation methods.

The sensitivity of the MEC corrosion sensor has been found to increase remarkably with the increase in the induced flux density in the test specimen. In contrast, there is no significant increase in the sensitivity of the MEC sensor when the induced flux density is above 1.2 T.

A magnetic flux density of 1.4 T induced through the thickness in the test specimen can ensure that the volumetric defect such as 10% wall thickness loss can be easily detected by the MEC sensor. A 3% change in the signals has been considered acceptable that is easily distinguishable from the white noise due to electronics (0.8%).

The factors that affect the induced magnetic flux density in the test specimen are the dimensions of the magnets, the separation distance between the magnets, and the height of the back iron piece.

The pole width, length of the magnet, and separation distance between the magnets are significant factors. It has been found that beyond a certain value, the height of the back iron and magnet height have little effect on the induced flux density.

The results have revealed that the area of the MEC corrosion monitor could be reduced by 38% for the two different test cases presented in this study without compromising sensitivity. This approach can thus considerably reduce the magnetic excitation circuit size to avoid health and safety and handling issues. This can also ensure through-thickness coverage to avoid missed signals due to wall loss.

### 7.2.3 Reliability of corrosion monitor

- How can the reliability monitor be improved for long-term applications?
- How can the performance of the magnetic corrosion monitor for the detection of wall thickness loss with time be investigated?

The main conclusions from the reliability studies are:

The reliability of the MEC monitor has been improved by the active redundancy approach to identify and isolate faulty sensors. This can assure continued operation especially where the access is difficult to check the sensors repeatedly.

The magnetic excitation circuit used for the MEC sensor has the capability to detect variations in leakage flux density using hall effect sensors at identical locations. This is possible because the corrosion monitor has been designed to be installed at one location and therefore, there is no velocity-induced noise. The MEC sensor has been designed to exhibit a 3% change in the base signal for a 1 mm uniform wall loss in an 8 mm thick specimen. This is because the base signal is high but this can be improved by normalisation or considering the base signal as 1. MFL sensors for the same configuration show a variation of almost 6%.

The correlation of the time series signals from MFL and MEC sensor signals can be established through Pearson's correlation coefficient. The faulty sensor can be identified by the variation in sensors' signals from the threshold coefficient value.

The real-life aging test carried out through two different rates of accelerated corrosion has confirmed that the corrosion monitor can detect wall thickness loss. The aim of the real-life aging test was to determine:

- Stability of the individual components in the corrosion monitor (electronics, magnets, sensors).
- Performance of the sensors to differentiate between the signals due to wall thickness loss and noise.

The signals due to wall thickness loss have been found to be distinct from the noise due to electronics and environmental factors.

The Pearson correlation coefficient computed from the time series signals of MFL and MEC sensors for one of the corrosion monitors has indicated a potential problem in either of the sensors.

In contrast to the hall effect sensor, the MEC coil sensor have shown more noise in its signals. The major reason for the noise has been the electronics in the impedance evaluation board. Furthermore, the board has also been found to be unreliable for long-term applications. One of the boards was found to be burnt at the end of the test.

A large variation in Pearson's correlation coefficient has been observed between the test datasets performed on uniform-thickness specimens and the real-life aging test. This has been due to the difference in the areas covered by the sensors.

### 7.2.4 Calibration and wall thickness estimation

- Can magnetic techniques (MFL and MEC) be used to estimate the severity of wall thickness loss with time to issue warnings or alarms to avoid catastrophic incidents?

  The MEC corrosion monitor discussed in this project can be used in two operation modes:

  - To detect wall thickness loss with time.
  - To monitor how much wall thickness is lost. This can be used to develop a warning system.

In both cases, it is paramount to estimate the in-situ relative magnetic permeability of the test specimen at the installation location of the corrosion monitor. The information on the relative permeability is needed to compute the depth of penetration of eddy currents and the magnetic induction to make sure that the detection of defects from the corrosion monitor. This is also required for the estimation of the remaining wall thickness.

A novel in-situ calibration procedure has, therefore, been developed to evaluate the local magnetic permeability using coupled MFL and MEC sensors.

The ZCF obtained from the multi-frequency spectrum has been found to be sensitive to the changes in the in-situ relative permeability.

The ZCF from the test specimen was inverted to apparent relative permeability in the FE model by the differential evaluation algorithm. This local permeability has been used to calibrate the MFL FE model for the correlation of leakage flux density with the amplitude of the hall sensor's signals to determine wall thickness.

The approach has been validated through two different test cases. The results have indicated that test specimen thickness could successfully be estimated by the approach with an accuracy of 19%. This method can be applied for the evaluation of the remaining thickness where the wall loss is uniform.

A comparative study on the computational efficiency of the DE algorithm has shown that DE takes less time per iteration as compared to PSO.

## 7.3 Future work and recommendations

It is recommended to test the smart magnetic corrosion monitor on the structures in service especially pipes and piping to evaluate the prospects of the application in the industry. The effect of the factors such as the flow and pressure of the products inside the pipes is required to see the commercial feasibility of the corrosion monitor.

The power efficiency of the corrosion monitor can further be improved by using low-energy Bluetooth devices such as Zigbee, Nordic and ARM boards.

The power consumption can further be improved by using timers that can wake up and excite the sensors remotely for data acquisition.

Energy harvesting and improve communication systems can be developed in the future for underwater applications such as sub-sea pipelines and structures.

The signal acquisition board Pmodia used in the project was found to be not best suited for the application due to noise. It is therefore imperative to design the electronic components or filters to subside the noise through better signal conditioning.

To develop a better correlation between MFL and MEC signals, the study can further be extended to design an array of MFL sensors in the space between the magnets. This can also be utilised to characterise the wall thickness loss as uniform or localised.

The accuracy achieved by the in situ calibration method was found to be ± 0.6 mm. This can be improved by using multiple features of the multi-frequency reactance spectrum to estimate the in-situ relative permeability such as peak frequency and phase signature. By developing multi-objective algorithms using two or more features from the multi-frequency reactance spectrum, the effect of the relative permeability on the accurate estimation of remaining wall thickness can be studied.

This research was focused on the detection and quantification of uniform wall thickness loss defects. However, in the field, the corrosion defects are highly localised. An in-depth and detailed study can be conducted to evaluate the prospects of characterisation and quantification of different corrosion defects such as pits using coupled MFL and MEC sensors.

The corrosion monitor was designed and tested for applications in the ambient environment. The neodymium magnets used in the study can operate at temperatures as high as 80°C with a small loss in the flux density. Future research can be done to define the maximum operating temperature for the corrosion monitor. Sustained and cyclic thermal loading tests are required to be carried out to estimate the reliability of the sensor for high temperature applications.

Accelerated life test models such as coffin mason based aging tests can be designed to evaluate the useful life of the corrosion monitor.

For high temperature applications, where neodymium magnets cannot be employed, the research can further be extended to investigate magnets with high curie temperatures. A modification in the design of the EC coil sensor could also be studied for magnets with low strength, like alnico or ferrite.

# References

[1] Werner Rott et al. "A novel pipe-cap system for corrosion protection and security." In: *Journal of Pipeline Engineering* 11.2 (2012).

[2] UKOG. *Business Outlook Report, 2022*. Available at: https : / / oeuk . org . uk / product-category/oeuk-reports/. (Accessed on: April 2022).

[3] UK Offshore Engineers. *Importance of Oil and Gas.* July 2022.

[4] Yahaya Y Yusuf et al. "The UK oil and gas supply chains: An empirical analysis of adoption of sustainable measures and performance outcomes". In: *International Journal of Production Economics* 146.2 (2013), pp. 501–514.

[5] SA Amadi. "Analysis of Corrosion Induced Failure of Oil Pipeline in the Marine Environment and Possible Control Measures". In: *I Control Pollution* 23.2 (1970), pp. 261–270.

[6] US Energy Information Administration. "Country Analysis Executive Summary United Kingdom". In: *Report* (2022), pp. 1–10.

[7] Jinghai Zhou, Li Sun, and Hongnan Li. "Study on dynamic response measurement of the submarine pipeline by full-term FBG sensors". In: *The Scientific World Journal* 2014 (2014).

[8] Xie Mingjiang and Tian Zhigang. "A review on pipeline integrity management utilizing in-line inspection data [J]". In: *Engineering Failure Analysis* 92.10 (2018), pp. 222–239.

[9] Mustafa Coramik and Yavuz Ege. "Discontinuity inspection in pipelines: A comparison review". In: *Measurement* 111 (2017), pp. 359–373.

[10] Raymond R Fessler. "Pipeline corrosion". In: *Report, US Department of Transportation Pipeline and Hazardous Materials Safety Administration, Baker, Evanston, IL* (2008).

[11] James G Speight. *Oil and gas corrosion prevention: From surface facilities to refineries*. Gulf Professional Publishing, 2014.

[12] W Sun and S Nešic. “A mechanistic model of uniform hydrogen sulfide/carbon dioxide corrosion of mild steel”. In: *Corrosion* 65.5 (2009), pp. 291–307.

[13] Muntazir Abbas and Mahmood Shafiee. “An overview of maintenance management strategies for corroded steel structures in extreme marine environments”. In: *Marine Structures* 71 (2020), p. 102718.

[14] AIM Ismail and AM El-Shamy. “Engineering behaviour of soil materials on the corrosion of mild steel”. In: *Applied clay science* 42.3-4 (2009), pp. 356–362.

[15] Kateryna Popova and Tomáš Prošek. “Corrosion Monitoring in Atmospheric Conditions: A Review”. In: *Metals* 12.2 (2022), p. 171.

[16] H Shafeek, HA Soltan, and MH Abdel-Aziz. “Corrosion monitoring in pipelines with a computerized system”. In: *Alexandria Engineering Journal* 60.6 (2021), pp. 5771–5778.

[17] M Karami. “Review of corrosion role in gas pipeline and some methods for preventing it”. In: *Journal of pressure vessel technology* 134.5 (2012).

[18] MS Attia et al. “Assessment of corrosion damage acceptance criteria in API579-ASME/1 code”. In: *International Journal of Mechanics and Materials in Design* 12.1 (2016), pp. 141–151.

[19] Baorong Hou et al. “The cost of corrosion in China”. In: *npj Materials Degradation* 1.1 (2017), p. 4.

[20] Gerhardus Koch. “Cost of corrosion”. In: *Trends in oil and gas corrosion research and technologies* (2017), pp. 3–30.

[21] Barbara Tchórzewska-Cies´lak et al. “Approaches for safety analysis of gas-pipeline functionality in terms of failure occurrence: A case study”. In: *Energies* 11.6 (2018), p. 1589.

[22] Pipeline incident 20 year trends. Available at: https://www.phmsa.dot.gov/ data-and-statistics/pipeline/pipeline-incident-20- year-trends. (Accessed on: Jan 2022).

[23] CAPP. “Mitigation of Internal Corrosion in Carbon Steel Oil Effluent Pipeline Systems”. In: *Report* (2018).

[24] B El Ibrahimi et al. “Amino acids and their derivatives as corrosion inhibitors for metals and alloys”. In: *Arabian Journal of Chemistry* 13.1 (2020), pp. 740–771.

[25] Agence France Presse. *Chinese oil giant Sinopec to pay big over pipeline blast that killed more than 60 people*. Available at: https://www.businessinsider.com/chinese-oil-giant-sinopec-to-pay-big-over-pipeline-blast-that-killed-more-than-60-people-2014-1?r=US&IR=T. (Accessed on Feb 2022)

[26] www.phmsa.dot.gov. (n.d.). *Pipeline Failure Investigation Reports* | PHMSA. [online] Available at: https://www.phmsa.dot.gov/safety-reports/pipeline-failure-investigation-reports

[27] UK Health and Safety Executive. *Public Report of The Fire and Explosion at the ConocoPhillips Humber Refinery*. 2001.

[28] Safety Board. “Natural Gas Pipeline Rupture and Fire Near Carlsbad, New Mexico August 19, 2000”. In: (2000).

[29] P Hopkins. “Pipeline integrity: some lessons learnt”. In: *International Pipeline Integrity & Repairs Conference*. Newcastle University. 2004.

[30] ES Ameh, SC Ikpeseni, and LS Lawal. “A review of field corrosion control and monitoring techniques of the upstream oil and gas pipelines”. In: *Nigerian Journal of Technological Development* 14.2 (2017), pp. 67–73.

[31] Edward Ghali, Vedula S Sastri, and Mimoun Elboujdaini. *Corrosion prevention and protection: practical solutions*. John Wiley & Sons, 2007.

[32] Facundo Varela, Mike Yongjun Tan, and Maria Forsyth. “An overview of major methods for inspecting and monitoring external corrosion of on-shore transportation pipelines”. In: *Corrosion Engineering, Science and Technology* 50.3 (2015), pp. 226–235.

[33] J-W Wu et al. “Electrochemical techniques correlation study of on-line corrosion monitoring probes”. In: *Materials and corrosion* 66.2 (2015), pp. 143–151.

[34] S Papavinasam et al. “Comparison of techniques for monitoring corrosion inhibitors in oil and gas pipelines”. In: *Corrosion* 59.12 (2003), pp. 1096–1111.

[35] Ruishu F Wright et al. “Review on corrosion sensors for structural health monitoring of oil and natural gas infrastructure”. In: *Smart Structures and NDE for Energy Systems and Industry 4.0*. Vol. 10973. SPIE. 2019, pp. 128–142.

[36] Caproco. *Coupons/Probes*. URL: http://www.caproco.com/access/coupons.htm.

[37] ScribbleTribe Studios and Omar El Sheikh. *Introduction to corrosion coupons*. Apr. 2020. URL: https://www.assetintegrityengineering.com/introduction-corrosion-coupons/.

[38] Thomas B Olsson. "Evaluation of corrosion in different parts of an oil refinery using corrosion coupons". MA thesis. 2014.

[39] Daniel E Powell. "Internal Corrosion Monitoring Using Coupons and Er Probes A Practical Focus on the Most Commonly Used, Cost-Effective Monitoring Techniques". In: *Oil and Gas Pipelines* (2015), pp. 495–514.

[40] Tom Pickthall et al. "Corrosion Monitoring Equipment, A Review of Application and Techniques". In: *CORROSION 2011* (2011).

[41] C Sean Brossia. "Electrical resistance techniques". In: *Techniques for corrosion monitoring*. Elsevier, 2021, pp. 267–284.

[42] *Electrical resistance (ER) monitoring*. URL: https://www.alspi.com/erintro.htm.

[43] L Yang and KT Chiang. "On-line and real-time corrosion monitoring techniques of metals and alloys in nuclear power plants and laboratories". In: *Understanding and Mitigating Ageing in Nuclear Power Plants*. Elsevier, 2010, pp. 417–455.

[44] Armando Jacob Espinoza and Thomas Conner Field. "Comparison of Intrusive and Non-Intrusive Methods for Corrosion Monitoring of Fuel Processing Systems". In: (2017).

[45] Frederic Cegla. "Ultrasonic monitoring of corrosion with permanently installed sensors (PIMS)". In: *Sensors, Algorithms and Applications for Structural Health Monitoring*. Springer, 2018, pp. 13–20.

[46] James Barshinger, Bruce Pellegrino, and Michael Nugent. "Permanently installed monitoring system for accurate wall thickness and corrosion rate measurement". In: *CORROSION 2016* (2016).

[47] Michael Siu Hey Leung and Joseph Corcoran. "Evaluating the probability of detection capability of permanently installed sensors using a structural integrity informed approach". In: *Journal of Nondestructive Evaluation* 40.3 (2021), pp. 1–17.

[48] Mingjiang Xie and Zhigang Tian. “A review on pipeline integrity management utilizing in-line inspection data”. In: *Engineering Failure Analysis* 92 (2018), pp. 222–239.

[49] Hartmut Goedecke. “Ultrasonic or MFL inspection: which technology is better for you”. In: *Pipeline & gas journal* 230.10 (2003), pp. 34–41.

[50] PRECISION THICKNESS GAUGE. “Operation Manual”. In: (2008).

[51] Muhammad Jamil et al. “Internal cracks and non-metallic inclusions as root causes of casting failure in sugar mill roller shafts”. In: *Materials* 12.15 (2019), p. 2474.

[52] F Caleyo et al. “Criteria for performance assessment and calibration of in-line inspections of oil and gas pipelines”. In: *Measurement Science and Technology* 18.7 (2007), p. 1787.

[53] Yan Shi et al. “Theory and application of magnetic flux leakage pipeline detection”. In: *Sensors* 15.12 (2015), pp. 31036–31055.

[54] Qiuping Ma et al. “Pipeline in-line inspection method, instrumentation and data management”. In: *Sensors* 21.11 (2021), p. 3862.

[55] HR Vanaei, Abdoulmajid Eslami, and Afolabi Egbewande. “A review on pipeline corrosion, in-line inspection (ILI), and corrosion growth rate models”. In: *International Journal of Pressure Vessels and Piping* 149 (2017), pp. 43–54.

[56] MA Rasoli et al. “Influence of ultrasonic vibrations on tube spinning process”. In: *Journal of Materials Processing Technology* 212.6 (2012), pp. 1443–1452.

[57] Hui Wang et al. “A Bayesian model framework for calibrating ultrasonic in-line inspection data and estimating actual external corrosion depth in buried pipeline utilizing a clustering technique”. In: *Structural Safety* 54 (2015), pp. 19–31.

[58] Rafael Wagner et al. “Guided wave testing performance studies: comparison with ultrasonic and magnetic flux leakage pigs”. In: *Insight-Non-Destructive Testing and Condition Monitoring* 55.4 (2013), pp. 187–196.

[59] DN Alleyne et al. “Rapid, long range inspection of chemical plant pipework using guided waves”. In: *AIP conference proceedings*. Vol. 557. 1. American Institute of Physics. 2001, pp. 180–187.

[60] Younho Cho et al. “A study on the guided wave mode conversion using self-calibrating technique”. In: *Journal of the Korean society for nondestructive testing* (2000).

[61] Peter Huthwaite et al. “Mode selection for corrosion detection in pipes and vessels via guided wave tomography”. In: *IEEE transactions on ultrasonics, ferroelectrics, and frequency control* 60.6 (2013), pp. 1165–1177.

[62] Peter Cawley et al. “Practical long range guided wave inspection-applications to pipes and rail”. In: *Mater. Eval* 61.1 (2003), pp. 66–74.

[63] Christian Willberg et al. “Simulation methods for guided wave-based structural health monitoring: a review”. In: *Applied Mechanics Reviews* 67.1 (2015).

[64] Sina Fateri et al. “Investigation of ultrasonic guided waves interacting with piezoelectric transducers”. In: *IEEE Sensors Journal* 15.8 (2015), pp. 4319–4328.

[65] Xiaojuan Wang et al. “Experimental investigation of reflection in guided wave-based inspection for the characterization of pipeline defects”. In: *NDT & e International* 43.4 (2010), pp. 365–374.

[66] Peter Cawley, Frederic Cegla, and Andrea Galvagni. “Guided waves for NDT and permanently-installed monitoring”. In: *Insight-Non-Destructive Testing and Condition Monitoring* 54.11 (2012), pp. 594–601.

[67] Arvind Deivasigamani et al. “A review of passive wireless sensors for structural health monitoring”. In: *Modern Applied Science* 7.2 (2013), pp. 57–76.

[68] Helena K Twigg and Marc Molinari. “Test results for a capacitance-based corrosion sensor”. In: *Thirteenth International Conference on Condition Monitoring and Machine Failure Prevention Technologies, 10.10. 2016-12.10. 2016, Paris.* 2016.

[69] Aamir F Malik, Zainal A Burhanudin, and Varun Jeoti. “A flexible polyimide based SAW delay line for corrosion detection”. In: *2011 National Postgraduate Conference*. IEEE. 2011, pp. 1–6.

[70] *Products*. URL: https://www.corrosionradar.com/products.

[71] Shuangxi Zhou et al. “A novel passive wireless sensing method for concrete chloride ion concentration monitoring”. In: *Sensors* 17.12 (2017), p. 2871.

[72] Khalada Perveen et al. “Corrosion potential sensor for remote monitoring of civil structure based on printed circuit board sensor”. In: *IEEE transactions on instrumentation and measurement* 63.10 (2014), pp. 2422–2431.

[73] Zhiyang Deng et al. “A permeability-measuring magnetic flux leakage method for inner surface crack in thick-walled steel pipe”. In: *Journal of Nondestructive Evaluation* 36.4 (2017), pp. 1–14.

[74] Helena G Ramos and A Lopes Ribeiro. “Present and future impact of magnetic sensors in NDE”. In: *Procedia Engineering* 86 (2014), pp. 406–419.

[75] Shiwei Liu et al. “A review of wire rope detection methods, sensors and signal processing techniques”. In: *Journal of Nondestructive Evaluation* 39.4 (2020), pp. 1–18.

[76] Ali Sophian, Gui Yun Tian, and Sofiane Zairi. “Pulsed magnetic flux leakage techniques for crack detection and characterisation”. In: *Sensors and Actuators A: Physical* 125.2 (2006), pp. 186–191.

[77] Hong Zhang et al. “The Non-Destructive Test of Steel Corrosion in Reinforced Concrete Bridges Using a Micro-Magnetic Sensor”. In: *Sensors* 16.9 (2016). ISSN: 1424-8220. DOI: 10.3390/s16091439. URL: https://www.mdpi.com/1424-8220/16/9/1439.

[78] Jinrui Zhang et al. “An innovative corrosion evaluation technique for reinforced concrete structures using magnetic sensors”. In: *Construction and Building Materials* 135 (2017), pp. 68–75.

[79] Zhe Li et al. “Use of a novel electro-magnetic apparatus to monitor corrosion of reinforced bar in concrete”. In: *Sensors and Actuators A: Physical* 286 (2019), pp. 14–27.

[80] Zhe Li et al. “Corrosion mechanism of reinforced bars inside concrete and relevant monitoring or detection apparatus: A review”. In: *Construction and Building Materials* 279 (2021), p. 122432.

[81] Namhoon Ha, Han-Seung Lee, and Songjun Lee. “Development of a Wireless Corrosion Detection System for Steel-Framed Structures Using Pulsed Eddy Currents”. In: *Sensors* 21.24 (2021), p. 8199.

[82] Keiji Tsukada et al. "A magnetic flux leakage method using a magnetoresistive sensor for nondestructive evaluation of spot welds". In: *Ndt & E International* 44.1 (2011), pp. 101–105.

[83] Keiji Tsukada et al. "Detection of inner corrosion of steel construction using magnetic resistance sensor and magnetic spectroscopy analysis". In: *IEEE Transactions on Magnetics* 52.7 (2016), pp. 1–4.

[84] Yue Long et al. "A method using magnetic eddy current testing for distinguishing ID and OD defects of pipelines under saturation magnetization". In: *The Applied Computational Electromagnetics Society Journal (ACES)* (2020), pp. 1089–1098.

[85] Erlong Li et al. "Quantitative Evaluation of Buried Defects in Ferromagnetic Steels Using DC Magnetization-Based Eddy Current Array Testing". In: *IEEE Transactions on Magnetics* 56.9 (2020), pp. 1–11.

[86] Andreas Boenisch (Schwarmstedt). "Partial saturation eddy current sensor apparatus and method of use". Current U.S. Class: Sensor Supported, Positioned, Or Moved Within Pipe (324/220) 20130234701. Nov. 12, 2010.

[87] Sungho Choi et al. "Electromagnetic acoustic transducers for robotic nondestructive inspection in harsh environments". In: *Sensors* 18.1 (2018), p. 193.

[88] Jin Xu et al. "Measuring ultrathin metallic coating properties using swept-frequency eddy-current technique". In: *IEEE Transactions on Instrumentation and Measurement* 69.8 (2020), pp. 5772–5781.

[89] Mingyang Lu et al. "Reducing the lift-off effect on permeability measurement for magnetic plates from multifrequency induction data". In: *IEEE Transactions on Instrumentation and Measurement* 67.1 (2017), pp. 167–174.

[90] Zhiyang Deng et al. "Multi-source effect in magnetizing-based eddy current testing sensor for surface crack in ferromagnetic materials". In: *Sensors and Actuators A: Physical* 271 (2018), pp. 24–36.

[91] AV Sukhikh and SS Sagalov. "Application of the magnetic saturation method for eddy-current inspection of spent fuel elements from fast reactors". In: *Atomic Energy* 102.2 (2007), pp. 139–145.

[92] Tatsuya Chikami and Katsuhiro Fukuoka. “Consideration of magnetic saturation ECT using AC magnetisation”. In: *International Journal of Applied Electromagnetics and Mechanics* 59.4 (2019), pp. 1331–1339.

[93] Xianzhi Ren, Shangkun Ren, and Qingquan Fan. “Influence of excitation current characteristics on sensor sensitivity of permeability testing technology based on constant current source”. In: *2018 7th International Conference on Energy, Environment and Sustainable Development (ICEESD 2018)*. Atlantis Press. 2018, pp. 1149–1153.

[94] Jian-Ming Jin. *Theory and computation of electromagnetic fields*. John Wiley & Sons, 2011.

[95] Yanhua Sun, Yihua Kang, and Chen Qiu. “A new NDT method based on permanent magnetic field perturbation”. In: *NDT & E International* 44.1 (2011), pp. 1–7.

[96] Oszkar Biro et al. “Voltage-driven coils in finite-element formulations using a current vector and a magnetic scalar potential”. In: *IEEE transactions on magnetics* 40.2 (2004), pp. 1286–1289.

[97] Alexandre Guterman. “Phase velocity equalization using patterned reference planes”. In: *2016 IEEE International Symposium on Electromagnetic Compatibility (EMC)*. IEEE. 2016, pp. 524–529.

[98] D Minkov et al. “Estimating the sizes of surface cracks based on Hall element measurements of the leakage magnetic field and a dipole model of a crack”. In: *Applied Physics A* 74.2 (2002), pp. 169–176.

[99] RC Ireland and CR Torres. “Finite element modelling of a circumferential magnetiser”. In: *Sensors and Actuators A: Physical* 129.1-2 (2006), pp. 197–202.

[100] Francisco Louis Valentine. *Effect of debris-induced lift-off on magnetic flux leakage inspection results*. West Virginia University, 2000.

[101] Xiao-chun Song, Song-ling Huang, and Wei Zhao. “Optimization of the magnetic circuit in the MFL inspection system for storage-tank floors”. In: *Russian journal of nondestructive testing* 43.5 (2007), pp. 326–331.

[102] Chai Xiuli, Zeng Dechang, and Liu Guixiong. “Study on simulation and experiment of the magnetizer in magnetic flux leakage testing”. In: *2007 International Conference on Mechatronics and Automation*. IEEE. 2007, pp. 3083–3087.

[103] Yu Chang et al. “Effects of excitation system on the performance of magnetic-flux-leakage-type non-destructive testing”. In: *Sensors and Actuators A: Physical* 268 (2017), pp. 201–212.

[104] Gwan Soo Park and Eun Sik Park. “Improvement of the sensor system in magnetic flux leakage-type nondestructive testing (NDT)”. In: *IEEE Transactions on magnetics* 38.2 (2002), pp. 1277–1280.

[105] ZD Wang, Y Gu, and YS Wang. “A review of three magnetic NDT technologies”. In: *Journal of Magnetism and Magnetic Materials* 324.4 (2012), pp. 382–388.

[106] Jaime A Parra-Raad and Sebastián Roa-Prada. “Multi-objective optimization of a magnetic circuit for magnetic flux leakage-type non-destructive testing”. In: *Journal of Nondestructive Evaluation* 35.1 (2016), pp. 1–12.

[107] Xingliang Jiang et al. “Optimal design of MFL sensor for detecting broken steel strands in overhead power line”. In: *Progress In Electromagnetics Research* 121 (2011), pp. 301–315.

[108] Xueyu Wang et al. “Study on the lift-off effect on MFL signals with magnetic circuit model and 3D FEM”. In: *Insight-Non-Destructive Testing and Condition Monitoring* 54.9 (2012), pp. 505–510.

[109] Gwan Soo Park and Eun Sik Park. “Improvement of the sensor system in magnetic flux leakage-type nondestructive testing (NDT)”. In: *IEEE Transactions on Magnetics* 38.2 (2002), pp. 1277–1280. DOI: *10.1109/20.996326*.

[110] Tao Zhang, Guiyun Tian, and Xianzhang Zuo. “Pulsed magnetic flux leakage sensor systems and applications”. In: *2011 IEEE International Instrumentation and Measurement Technology Conference*. IEEE. 2011, pp. 1–6.

[111] H Ravanbod and E Norouzi. “A Novel Method for Modeling the Magnetizing Yoke”. In: *Electromagnetics* 30.3 (2010), pp. 297–308.

[112] Seng Poh Lim and Habibollah Haron. “Performance comparison of genetic algorithm, differential evolution and particle swarm optimization towards benchmark functions”. In: *2013 IEEE Conference on Open Systems (ICOS)*. IEEE. 2013, pp. 41–46.

[113] Mojtaba Rostami Kandroodi et al. “Defect detection and width estimation in natural gas pipelines using MFL signals”. In: *2013 9th Asian Control Conference (ASCC)*. IEEE. 2013, pp. 1–6.

[114] Yahya Rahmat-Samii. “Genetic algorithm (GA) and particle swarm optimization (PSO) in engineering electromagnetics”. In: *17th International Conference on Applied Electromagnetics and Communications, 2003. ICECom 2003.* IEEE. 2003, pp. 1–5.

[115] Yao Duan, RG Harley, and TG Habetler. “Comparison of particle swarm optimization and genetic algorithm in the design of permanent magnet motors”. In: *2009 IEEE 6th international power electronics and motion control conference*. IEEE. 2009, pp. 822–825.

[116] Jizhong Zhu. *Optimization of power system operation*. John Wiley & Sons, 2015.

[117] Ganesh K Venayagamoorthy and Ronald G Harley. “Swarm intelligence for transmission system control”. In: *2007 IEEE Power Engineering Society General Meeting*. IEEE. 2007, pp. 1–4.

[118] DH Tungadio et al. “Particle swarm optimization for power system state estimation”. In: *Neurocomputing* 148 (2015), pp. 175–180.

[119] A Godio and A Santilano. “On the optimization of electromagnetic geophysical data: Application of the PSO algorithm”. In: *Journal of Applied Geophysics* 148 (2018), pp. 163–174.

[120] V Selvi and R Umarani. “Comparative analysis of ant colony and particle swarm optimization techniques”. In: *International Journal of Computer Applications* 5.4 (2010), pp. 1–6.

[121] Vaishali R Kulkarni and Veena Desai. “ABC and PSO: A comparative analysis”. In: *2016 IEEE International Conference on Computational Intelligence and Computing Research (ICCIC)*. IEEE. 2016, pp. 1–7.

[122] Shan Guan, Christopher Taylor, and Narasi Sridhar. “Prediction of Sensor System Reliability”. In: *International journal of COMADEM* 20.4 (2017).

[123] Amer Kajmakovic et al. “Degradation Detection in a Redundant Sensor Architecture”. In: *Sensors* 22.12 (2022), p. 4649.

[124] Yu-De Wang et al. “The reliability and lifetime distribution of SnO2-and CdSnO3-gas sensors for butane”. In: *Sensors and Actuators B: Chemical* 92.1-2 (2003), pp. 186–190.

[125] Slobodan Petrovic et al. “Reliability test methods for media-compatible pressure sensors”. In: *IEEE Transactions on Industrial Electronics* 45.6 (1998), pp. 877–885.

[126] Herbert R Shea. “Reliability of MEMS for space applications”. In: *Reliability, Packaging, Testing, and Characterization of MEMS/MOEMS V*. Vol. 6111. SPIE. 2006, pp. 84–93.

[127] Jae-Seong Jeong et al. “Lifetime and failure analysis of perovskite-based ceramic NTC thermistors by thermal cycling and abrasion combined stress”. In: *Microelectronics Reliability* 76 (2017), pp. 112–116.

[128] Dimitri Kececioglu. *Reliability and life testing handbook*. Vol. 2. DEStech Publications, Inc, 2002.

[129] VN A NAIKAN. *Reliability engineering and life testing*. PHI Learning Pvt. Ltd., 2008.

[130] Alex Porter. *Accelerated testing and validation*. Elsevier, 2004.

[131] Arun Bala Subramaniyan, Rong Pan, and Wendai Wang. “Optimal planning and inference for sequential accelerated life testing with two or more experimental factors”. In: *2019 Annual Reliability and Maintainability Symposium, RAMS 2019*. Institute of Electrical and Electronics Engineers Inc. 2019, p. 8768991.

[132] Cezary Sydlo et al. “Reliability studies on integrated GaAs power-sensor structures using pulsed electrical stress”. In: *Microelectronics Reliability* 43.9-11 (2003), pp. 1929–1933.

[133] Chandradip Patel, Patrick McCluskey, and David Lemus. “Performance and reliability of MEMS gyroscopes at high temperatures”. In: *2010 12th IEEE Intersociety Conference on Thermal and Thermomechanical Phenomena in Electronic Systems*. IEEE. 2010, pp. 1–5.

[134] Roderich Zeiser et al. “Failure mode analysis and optimization of assembled high temperature pressure sensors”. In: *2014 15th International Conference on Thermal, Mechanical and Mulit-Physics Simulation and Experiments in Microelectronics and Microsystems (EuroSimE)*. IEEE. 2014, pp. 1–6.

[135] Rahul Prajesh et al. “Development and reliability analysis of micro gas sensor platform on glass substrate”. In: *Microsystem Technologies* 25.9 (2019), pp. 3589–3597.

[136] I Marozau et al. “Reliability assessment and failure mode analysis of MEMS accelerometers for space applications”. In: *Microelectronics Reliability* 88 (2018), pp. 846–854.

[137] CA Betty, Sipra Choudhury, and KG Girija. “Reliability studies of highly sensitive and specific multi-gas sensor based on nanocrystalline SnO2 film”. In: *Sensors and Actuators B: Chemical* 193 (2014), pp. 484–491.

[138] Miklós Lenner et al. “Long-Term Reliability of Fiber-Optic Current Sensors”. In: *IEEE Sensors Journal* 20.2 (2020), pp. 823–832. DOI: `10.1109/JSEN.2019.2944346`.

[139] I Sayago et al. “Long-term reliability of sensors for detection of nitrogen oxides”. In: *Sensors and Actuators B: Chemical* 26.1-3 (1995), pp. 56–58.

[140] Subbiah Karthick et al. “Reliability and long-term evaluation of GO-MnO2 nano material as a newer corrosion monitoring sensor for reinforced concrete structures”. In: *Cement and Concrete Composites* 100 (2019), pp. 74–84.

[141] R Keith Mobley. *An introduction to predictive maintenance*. Elsevier, 2002.

[142] Amer Kajmakovic et al. “Predictive fail-safe improving the safety of industrial environments through model-based analytics on hidden data sources”. In: *2018 IEEE 13th International Symposium on Industrial Embedded Systems (SIES)*. IEEE. 2018, pp. 1–4.

[143] Donghoon Shin, Kang-moon Park, and Manbok Park. “Development of fail-safe algorithm for exteroceptive sensors of autonomous vehicles”. In: *Electronics* 9.11 (2020), p. 1774.

[144] Daoliang Li et al. “Recent advances in sensor fault diagnosis: A review”. In: *Sensors and Actuators A: Physical* 309 (2020), p. 111990.

[145] Anupam Das, J Maiti, and RN Banerjee. “Process monitoring and fault detection strategies: a review”. In: *International Journal of Quality & Reliability Management* (2012).

[146] Amer Kajmakovic et al. “Challenges in Mitigating Errors in 1oo2D Safety Architecture with COTS Micro-controllers”. In: *International Journal on Advances in Systems and Measurements* 13.3-4 (2020), pp. 250–263.

[147] Arun Agarwal et al. “Quantitative assessment of failure probability of underground natural gas storage wells using an integrated bow-tie Bayesian

network approach". In: *Journal of Failure Analysis and Prevention* 21.1 (2021), pp. 107–123.

[148] Shan Guan et al. "Internal corrosion direct assessment using Bayesian networks modeling with limited data: A case study". In: *CORROSION 2016*. OnePetro. 2016.

[149] L Jiang et al. "Sensor degradation detection in linear systems". In: *Engineering Asset Management*. Springer, 2006, pp. 1252–1260.

[150] Duo Ma et al. "Automatic defogging, deblurring, and real-time segmentation system for sewer pipeline defects". In: *Automation in Construction* 144 (2022), p. 104595.

[151] Zhe Li et al. "Coupled application of innovative electromagnetic sensors and digital image correlation technique to monitor corrosion process of reinforced bars in concrete". In: *Cement and Concrete Composites* 113 (2020), p. 103730. ISSN: 0958-9465. DOI: https://doi.org/ 10 . 1016 / j. cemconcomp. 2020 . 103730.

[152] Han Li et al. "Correlation-Based Anomaly Detection Method for Multi-sensor System". In: *Computational Intelligence and Neuroscience* 2022 (2022).

[153] Fan Jiang et al. "A fusion feature extraction method using EEMD and correlation coefficient analysis for bearing fault diagnosis". In: *Applied Sciences* 8.9 (2018), p. 1621.

[154] Zhe Li et al. "Combined application of novel electromagnetic sensors and acoustic emission apparatus to monitor corrosion process of reinforced bars in concrete". In: *Construction and Building Materials* 245 (2020), p. 118472.

[155] M Boat et al. "Factors that affect the defect sizing capabilities of the magnetic flux leakage". In: *Silverwing (UK) Ltd., Swansea, UK, Tech. Rep* ().

[156] Yaman Hamed et al. "Two steps hybrid calibration algorithm of support vector regression and K-nearest neighbors". In: *Alexandria Engineering Journal* 59.3 (2020), pp. 1181–1190.

[157] Catalin Mandache and Lynann Clapham. "A model for magnetic flux leakage signal predictions". In: *Journal of Physics D: Applied Physics* 36.20 (2003), p. 2427.

[158] BS Wijerathna et al. “Linear Approximation for Mapping Remaining Wall Thickness Using a Magnetic Flux Leakage Sensor”. In: *Australasian Conference on Robotics and Automation*. ACRA. 2016.

[159] Buddhi Wijerathna et al. “Iterative coarse to fine approach for interpretation of defect profiles using MFL measurements”. In: *2015 IEEE 10th Conference on Industrial Electronics and Applications (ICIEA)*. IEEE. 2015, pp. 1099–1104.

[160] AA Carvalho et al. “MFL signals and artificial neural networks applied to detection and classification of pipe weld defects”. In: *Ndt & E International* 39.8 (2006), pp. 661–667.

[161] Sushant M Dutta, Fathi H Ghorbel, and Roderic K Stanley. “Dipole modeling of magnetic flux leakage”. In: *IEEE Transactions on Magnetics* 45.4 (2009), pp. 1959–1965.

[162] Yujue Wang et al. “Dipole modeling of stress-dependent magnetic flux leakage”. In: *NDT & E International* 95 (2018), pp. 1–8.

[163] Bin Liu et al. “The axial crack testing model for long distance oil-gas pipeline based on magnetic flux leakage internal inspection method”. In: *Measurement* 103 (2017), pp. 275–282.

[164] Senxiang Lu et al. “An estimation method of defect size from MFL image using visual transformation convolutional neural network”. In: *IEEE Transactions on Industrial Informatics* 15.1 (2018), pp. 213–224.

[165] Yong Zhang, Zhongfu Ye, and Chong Wang. “A fast method for rectangular crack sizes reconstruction in magnetic flux leakage testing”. In: *Ndt & E International* 42.5 (2009), pp. 369–375.

[166] Gerhard Kopp and Herbert Willems. “Sizing limits of metal loss anomalies using tri-axial MFL measurements: A model study”. In: *Ndt & E International* 55 (2013), pp. 75–81.

[167] Sushant M Dutta, Fathi H Ghorbel, and Roderic K Stanley. “Simulation and analysis of 3-D magnetic flux leakage”. In: *IEEE Transactions on Magnetics* 45.4 (2009), pp. 1966–1972.

[168] Zhang Guoguang and Liu Jing. “Finite element modelling of circumferential magnetic flux leakage inspection in pipeline”. In: *2010 International Conference on Intelligent Computation Technology and Automation*. Vol. 2. IEEE. 2010, pp. 327–330.

[169] KC Hari, M Nabi, and SV Kulkarni. “Improved FEM model for defect-shape construction from MFL signal by using genetic algorithm”. In: *IET science, measurement & technology* 1.4 (2007), pp. 196–200.

[170] Xiang Peng et al. “Analysis of magnetic-flux leakage (MFL) data for pipeline corrosion assessment”. In: *IEEE Transactions on Magnetics* 56.6 (2020), pp. 1–15.

[171] Robin H Priewald et al. “Fast magnetic flux leakage signal inversion for the reconstruction of arbitrary defect profiles in steel using finite elements”. In: *IEEE Transactions on Magnetics* 49.1 (2012), pp. 506–516.

[172] S Ratnajeevan H Hoole et al. “Inverse problem methodology and finite elements in the identification of cracks, sources, materials, and their geometry in inaccessible locations”. In: *IEEE Transactions on Magnetics* 27.3 (1991), pp. 3433–3443.

[173] W Han and P Que. “An improved genetic local search algorithm for defect reconstruction from MFL signals”. In: *Russian Journal of Nondestructive Testing* 41.12 (2005), pp. 815–821.

[174] Senxiang Lu et al. “Precise inversion for the reconstruction of arbitrary defect profiles considering velocity effect in magnetic flux leakage testing”. In: *IEEE Transactions on Magnetics* 53.4 (2016), pp. 1–12.

[175] Wen-hua Han et al. “Magnetic flux leakage signal inversion of corrosive flaws based on modified genetic local search algorithm”. In: *Journal of Shanghai Jiaotong University (Science)* 14.2 (2009), pp. 168–172.

[176] Wenhua Han et al. “Defect profile estimation from magnetic flux leakage signal via efficient managing particle swarm optimization”. In: *Sensors* 14.6 (2014), pp. 10361–10380.

[177] Huixuan Fu, Yuchao Wang, and Ding Jin. “Pipeline defect reconstruction based on improved particle swarm optimization with LSSVM”. In: *2016 35th Chinese Control Conference (CCC)*. IEEE. 2016, pp. 3595–3599.

[178] Wenhua Han et al. “Magnetic flux leakage signal inversion based on improved efficient population utilization strategy for particle swarm optimization”. In: *Russian Journal of Nondestructive Testing* 53.12 (2017), pp. 862–873.

[179] Wenhua Han et al. “Cuckoo search and particle filter-based inversing approach to estimating defects via magnetic flux leakage signals”. In: *IEEE Transactions on Magnetics* 52.4 (2015), pp. 1–11.

[180] Junjie Chen, Songling Huang, and Wei Zhao. “Three-dimensional defect inversion from magnetic flux leakage signals using iterative neural network”. In: *IET Science, Measurement & Technology* 9.4 (2015), pp. 418–426.

[181] Jian Feng et al. “Fast reconstruction of defect profiles from magnetic flux leakage measurements using a RBFNN based error adjustment methodology”. In: *IET Science, Measurement & Technology* 11.3 (2017), pp. 262–269.

[182] Chao Xu et al. “Finite-element neural network-based solving 3-D differential equations in MFL”. In: *IEEE Transactions on Magnetics* 48.12 (2012), pp. 4747–4756.

[183] Junjie Chen. “3-D defect profile reconstruction from magnetic flux leakage signals in pipeline inspection using a hybrid inversion method”. In: *The Applied Computational Electromagnetics Society Journal (ACES)* (2017), pp. 826–832.

[184] Reza K Amineh et al. “A space mapping methodology for defect characterization from magnetic flux leakage measurements”. In: *IEEE Transactions on Magnetics* 44.8 (2008), pp. 2058–2065.

[185] Maryam Ravan et al. “Sizing of 3-D arbitrary defects using magnetic flux leakage measurements”. In: *IEEE transactions on magnetics* 46.4 (2009), pp. 1024–1033.

[186] Ahmad Khodayari-Rostamabad et al. “Machine learning techniques for the analysis of magnetic flux leakage images in pipeline inspection”. In: *IEEE Transactions on magnetics* 45.8 (2009), pp. 3073–3084.

[187] Pradeep Ramuhalli, Lalita Udpa, and Satish S Udpa. “Electromagnetic NDE signal inversion by function-approximation neural networks”. In: *IEEE transactions on magnetics* 38.6 (2002), pp. 3633–3642.

[188] Mohamed Layouni, Mohamed Salah Hamdi, and Sofiène Tahar. “Detection and sizing of metal-loss defects in oil and gas pipelines using pattern-adapted wavelets and machine learning”. In: *Applied Soft Computing* 52 (2017), pp. 247–261.

[189] Ameet Joshi et al. “Adaptive wavelets for characterizing magnetic flux leakage signals from pipeline inspection”. In: *IEEE transactions on magnetics* 42.10 (2006), pp. 3168–3170.

[190] Guanyu Piao et al. “Fast reconstruction of 3-D defect profile from MFL signals using key physics-based parameters and SVM”. In: *NDT & E International* 103 (2019), pp. 26–38.

[191] Jian Feng et al. “A sensor liftoff modification method of magnetic flux leakage signal for defect profile estimation”. In: *IEEE Transactions on Magnetics* 53.7 (2017), pp. 1–13.

[192] Yanhua Sun and Yihua Kang. “Magnetic compression effect in present MFL testing sensor”. In: *Sensors and Actuators A: Physical* 160.1-2 (2010), pp. 54–59.

[193] VA Syas’ ko et al. “Measuring Magnetic Permeability of Monolithic Annular Measures in Alternating Magnetic Fields”. In: *Russian Journal of Nondestructive Testing* 55 (2019), pp. 851–857.

[194] Gary G Bush. “Measurement techniques for permeability, permittivity and EMI shielding: a review”. In: *Proceedings of IEEE Symposium on Electromagnetic Compatibility*. IEEE. 1994, pp. 333–339.

[195] D Desjardins, TW Krause, and L Clapham. “Transient eddy current method for the characterization of magnetic permeability and conductivity”. In: *NDT & E International* 80 (2016), pp. 65–70.

[196] AM Beese and Dirk Mohr. “Identification of the direction-dependency of the martensitic transformation in stainless steel using in situ magnetic permeability measurements”. In: *Experimental mechanics* 51.5 (2011), pp. 667–676.

[197] Mihai Radu et al. “Continuous magnetic method for quantitative monitoring of martensitic transformation in steels containing metastable austenite”. In: *Scripta Materialia* 52.6 (2005), pp. 525–530.

[198] X Ma, AJ Peyton, and YY Zhao. “Eddy current measurements of electrical conductivity and magnetic permeability of porous metals”. In: *Ndt & E International* 39.7 (2006), pp. 562–568.

[199] M-E Kouli and M Giannakis. “Stress state evaluation in low carbon and TRIP steels by magnetic permeability”. In: *IOP Conference Series: Materials Science and Engineering*. Vol. 108. 1. IOP Publishing. 2016, p. 012013.

[200] Nicola Bowler. “Frequency-Dependence of Relative Permeability in Steel”. In: *AIP Conference Proceedings*. Vol. 820. 1. American Institute of Physics. 2006, pp. 1269–1276.

[201] Mingyang Lu et al. “Lift-off invariant inductance of steels in multi-frequency eddy-current testing”. In: *NDT & E International* 121 (2021), p. 102458.

[202] Mingyang Lu, Anthony Peyton, and Wuliang Yin. “Acceleration of frequency sweeping in eddy-current computation”. In: *IEEE Transactions on Magnetics* 53.7 (2017), pp. 1–8.

[203] Wuliang Yin and AJ Peyton. “Thickness measurement of non-magnetic plates using multi-frequency eddy current sensors”. In: *Ndt & E International* 40.1 (2007), pp. 43–48.

[204] W. Yin, S.J. Dickinson, and A.J. Peyton. “Evaluating the Permeability Distribution of a Layered Conductor by Inductance Spectroscopy”. In: *IEEE Transactions on Magnetics* 42.11 (2006), pp. 3645–3651. DOI: `10.1109/TMAG.2006.880992`.

[205] Yating Yu et al. “Investigation on conductivity invariance in eddy current NDT and its application on magnetic permeability measurement”. In: *2015 IEEE Far East NDT New Technology & Application Forum (FENDT)*. IEEE. 2015, pp. 257–262.

[206] Mingyang Lu et al. “Measurement of permeability for ferrous metallic plates using a novel lift-off compensation technique on phase signature”. In: *IEEE Sensors Journal* 19.17 (2019), pp. 7440–7446.

[207] W. Zhu et al. “Modelling and experimental study of magnetic induction spectroscopy for rail decarburisation measurement”. In: *2014 IEEE Far East Forum on Nondestructive Evaluation/Testing*. 2014, pp. 345–348. DOI: `10.1109/FENDT.2014.6928293`.

[208] W Zhu et al. “Development and deployment of online multifrequency electromagnetic system to monitor steel hot transformation on runout table of hot strip mill”. In: *Ironmaking & Steelmaking* 41.9 (2014), pp. 685–693.

[209] Mingyang Lu et al. “Reducing the Lift-Off Effect on Permeability Measurement for Magnetic Plates From Multifrequency Induction Data”.

In: *IEEE Transactions on Instrumentation and Measurement* 67.1 (2018), pp. 167–174. DOI: 10.1109/TIM.2017.2728338.

[210] AJ Peyton et al. “Monitoring microstructure changes in rod online by using induction spectroscopy”. In: *Ironmaking & Steelmaking* 37.2 (2010), pp. 135–139.

[211] Abdullah Al-Dujaili, Muhammad Rizwan Tanweer, and Suresh Sundaram. “DE vs. PSO: A Performance Assessment for Expensive Problems.” In: *SSCI*. 2015, pp. 1711–1718.

[212] *Comparison of MFL and MEC*. URL: *https://www.innospection.com/images/PDF/Technology_-_Comparison_of_MEC MFL_for_Tank_Floor_Inspection-min.pdf/%20Accessed%20on% 2010-11-2022.*

[213] K Magnetics. “KJ Magnetics-Neodymium Magnet Specifications”. In: *Neodymium Magnet Physical Properties* (2011).

[214] SR Trout. “Material selection of permanent magnets, considering thermal properties correctly”. In: *Proceedings: Electrical Insulation Conference and Electrical Manufacturing and Coil Winding Conference (Cat. No. 01CH37264)*. IEEE. 2001, pp. 365–370.

[215] Jan Svoboda. *Magnetic techniques for the treatment of materials*. Springer Science & Business Media, 2004.

[216] Zhen Zhao et al. “Mechanical properties of samarium cobalt: A molecular dynamics study”. In: *Materials Today Communications* 31 (2022), p. 103676.

[217] *Ferrite Magnets/Ceramic Magnets Datasheet*. URL: https://www.eclipsemagnetics.com/site/assets/files/19602/ferrite_ceramic_datasheet.pdf%20/Accessed%20on%2010-11-2022.

[218] *NEODYMIUM IRON BORON MAGNETS*. URL: https://www.arnoldmagnetics.com/products/neodymium-iron-boron-magnets/%20/Accessed% 20on%2010-11-2022.

[219] COMSOL Multiphysics. “Comsol user’s Guide, Version 5.3”. In: *COMSOL AB, Stockholm, Sweden* (2018).

[220] Javier Ferreira, Fernando Seoane, and Kaj Lindecrantz. “AD5933-based electrical bioimpedance spectrometer. Towards textile-enabled applications”. In: *2011 Annual International Conference of the IEEE Engineering in Medicine and Biology Society*. IEEE. 2011, pp. 3282–3285.

[221] Sean Brennan. “Measuring a grounded impedance profile using the AD5933”. In: *Analog Devices: Application Note* (2006), pp. 1–12.

[222] Liviu Breniuc, Valeriu David, and Cristian-Győző Haba. “Wearable impedance analyzer based on AD5933”. In: *2014 International Conference and Exposition on Electrical and Power Engineering (EPE)*. IEEE. 2014, pp. 585–590.

[223] Rohan Munjal, Frank Wendler, and Olfa Kanoun. “Embedded wideband measurement system for fast impedance spectroscopy using undersampling”. In: *IEEE Transactions on Instrumentation and Measurement* 69.6 (2019), pp. 3461–3469.

[224] Konrad Chabowski et al. “Simple wide frequency range impedance meter based on AD5933 integrated circuit”. In: *Metrology and Measurement Systems* 22.1 (2015).

[225] Rudy Tawie and Embam Da’ud. “Low-cost impedance approach using AD5933 for sensing and monitoring applications”. In: *IOP Conference Series: Materials Science and Engineering*. Vol. 429. 1. IOP Publishing. 2018, p. 012104.

[226] Folasade M Dahunsi et al. “Selected Microcontrollers and Sensors Analysis for Electrical Energy Metering Circuits”. In: *2022 IEEE Nigeria 4th International Conference on Disruptive Technologies for Sustainable Development (NIGERCON)*. IEEE. 2022, pp. 1–5.

[227] M Caruso et al. “A low-cost, real-time monitoring system for PV plants based on ATmega 328P-PU microcontroller”. In: *2015 IEEE International Telecommunications Energy Conference (INTELEC)*. IEEE. 2015, pp. 1–5.

[228] Tejas Thaker. “ESP8266 based implementation of wireless sensor network with Linux based web-server”. In: *2016 Symposium on Colossal Data Analysis and Networking (CDAN)*. IEEE. 2016, pp. 1–5.

[229] Manushri Gowda et al. “Power consumption optimization in iot based wireless sensor node using esp8266”. In: *ITM Web of Conferences*. Vol. 32. EDP Sciences. 2020, p. 03048.

[230] Ali Al Dahoud and Mohamed Fezari. “NodeMCU V3 for fast IoT application Development”. In: *Notes* 5 (2018).

[231] Nestor Michael Tiglao et al. “Agrinex: A low-cost wireless mesh-based smart irrigation system”. In: *Measurement* 161 (2020), p. 107874.

[232] Murat Yilmaz and Philip T Krein. “Capabilities of finite element analysis and magnetic equivalent circuits for electrical machine analysis and design”. In: *2008 IEEE Power Electronics Specialists Conference*. IEEE. 2008, pp. 4027–4033.

[233] Goitseone Malumbela, Pilate Moyo, and Mark Alexander. “A step towards standardising accelerated corrosion tests on laboratory reinforced concrete specimens”. In: *Journal of the South African Institution of Civil Engineering= Joernaal van die Suid-Afrikaanse Instituut van Siviele Ingenieurswese* 54.2 (2012), pp. 78–85.

[234] Zehbour Panossian et al. “Corrosion of carbon steel pipes and tanks by concentrated sulfuric acid: a review”. In: *Corrosion Science* 58 (2012), pp. 1–11.

[235] Glenn H Damon. “Acid corrosion of steel”. In: *Industrial & Engineering Chemistry* 33.1 (1941), pp. 67–69.

[236] SW Dean Jr and GD Grab. “Corrosion of carbon steel tanks in concentrated sulfuric acid service”. In: *Materials performance* 25.7 (1986), pp. 48–52.

[237] Sung Eun Kim et al. “Caution warnings are required for the sale of neodymium magnets in Korea”. In: *Journal of The Korean Society of Emergency Medicine* 30.6 (2019), pp. 603–607.

[238] Gang Wang et al. “Optimal frequency of AC magnetic flux leakage testing for detecting defect size and orientation in thick steel plates”. In: *IEEE Transactions on Magnetics* 57.9 (2021), pp. 1–8.

[239] Bo Feng et al. “A Review of Magnetic Flux Leakage Nondestructive Testing”. In: *Materials* 15.20 (2022), p. 7362.

[240] Zhiyang Deng et al. “Effects of surface roughness on magnetic flux leakage testing of micro-cracks”. In: *Measurement Science and Technology* 28.4 (2017), p. 045003.

[241] Erlong Li et al. “Spatial-spectrum-based measurement of the surface roughness of ferromagnetic components using magnetic flux leakage method”. In: *IEEE Transactions on Instrumentation and Measurement* 70 (2020), pp. 1–10.

[242] Mohammed Asadullah Khan et al. “Magnetic sensors-A review and recent technologies”. In: *Engineering Research Express* 3.2 (2021), p. 022005.

[243] Nor Afandi Sharif et al. "Theory and development of magnetic flux leakage sensor for flaws detection: A review". In: *J. Kejuruter* 32 (2020), pp. 385–395.

[244] Shuxian Hong et al. "Determination of impressed current efficiency during accelerated corrosion of reinforcement". In: *Cement and Concrete Composites* 108 (2020), p. 103536.

[245] G Nossoni and R Harichandran. "Current efficiency in accelerated corrosion testing of concrete". In: *Corrosion* 68.9 (2012), pp. 801–809.

[246] Hai-Bin Huang, Ting-Hua Yi, and Hong-Nan Li. "Bayesian combination of weighted principal-component analysis for diagnosing sensor faults in structural monitoring systems". In: *Journal of Engineering Mechanics* 143.9 (2017), p. 04017088.

[247] Yuanqing Wang and Fan Deng. "A sensor fault diagnosis method based on KPCA and contribution graph". In: *Vibroengineering Procedia* 33 (2020), pp. 6–10.

[248] Hai-Bin Huang, Ting-Hua Yi, and Hong-Nan Li. "Canonical correlation analysis based fault diagnosis method for structural monitoring sensor networks". In: *Smart Struct. Syst* 17.6 (2016), pp. 1031–1053.

[249] Nian Shong Chok. "Pearson's versus Spearman's and Kendall's correlation coefficients for continuous data". PhD thesis. University of Pittsburgh, 2010.

[250] Sarmad Mahmood et al. "Esp 8266 node mcu based weather monitoring system". In: (2020).

[251] K Jyostsna Vanaja et al. "IOT based agriculture system using node MCU". In: *International Research Journal of Engineering and Technology* 5.3 (2018), pp. 3025–3028.

[252] Naohiro Kuze and Ichiro Shibasaki. "MBE research and production of Hall sensors". In: *III-Vs Review* 10.1 (1997), pp. 28–32.

[253] Bin Liu et al. "Quantitative study on the propagation characteristics of MFL signals of outer surface defects in long-distance oil and gas pipelines". In: *NDT & E International* (2023), p. 102861.

[254] Fausto Fiorillo. *Characterization and measurement of magnetic materials*. Academic Press, 2004.

## Appendix A

# Magnetic excitation circuit model

## Contents

# A.1. Global Definitions

| | |
|---|---|
| Date | May 18, 2021 10:30:31 AM |

### GLOBAL SETTINGS

| | |
|---|---|
| Name | Optimisation.mph |
| Path | C:\Users\wasifr\Documents\Comsol files\Optimisation.mph |
| Version | COMSOL Multiphysics 5.5 (Build: 359) |

### USED PRODUCTS

| |
|---|
| COMSOL Multiphysics |
| AC/DC Module |

## A.1.1 PARAMETERS

### PARAMETERS 1

| Name | Expression | Value | Description |
|---|---|---|---|
| ML | 40[mm] | 0.04 m | |
| PH | 4 [mm] | 0.004 m | |
| SD | 25[mm] | 0.025 m | |
| MH | 20 [mm] | 0.02 m | |
| YH | 20 [mm] | 0.02 m | |
| PW | 20[mm] | 0.02 m | |
| LOff | 1 [mm] | 0.01 m | |

## A.2 Component 1

SETTINGS

| Description | Value |
|---|---|
| Unit system | Same as global system |
| Avoid inverted elements by curving interior domain elements | Off |

### A.2.1 DEFINITIONS

#### 2.1.1 Coordinate Systems

**Boundary System 1**

| | |
|---|---|
| Coordinate system type | Boundary system |
| Tag | sys1 |

COORDINATE NAMES

| First | Second | Third |
|---|---|---|
| t1 | t2 | n |

### A.2.2 MATLAB OPTIMISATION

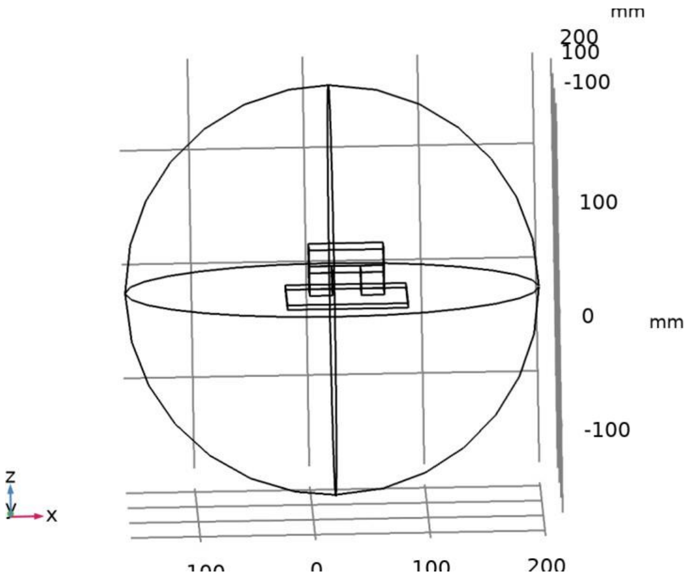

*Matlab Optimisation*

UNITS

| | |
|---|---|
| Length unit | mm |
| Angular unit | deg |

GEOMETRY STATISTICS

| Description | Value |
|---|---|
| Space dimension | 3 |
| Number of domains | 5 |
| Number of boundaries | 32 |
| Number of edges | 58 |
| Number of vertices | 34 |

### 2.2.1 Magnet1 (blk1)

POSITION

| Description | Value |
|---|---|
| Position | {0, 0, LOff} |

AXIS

| Description | Value |
|---|---|
| Axis type | z - axis |

SIZE AND SHAPE

| Description | Value |
|---|---|
| Width | PW |
| Depth | ML |
| Height | MH |

### 2.2.2 Magnet2 (blk2)

POSITION

| Description | Value |
|---|---|
| Position | {PW + SD, 0, LOff} |

AXIS

| Description | Value |
|---|---|
| Axis type | z - axis |

SIZE AND SHAPE

| Description | Value |
|---|---|
| Width | PW |
| Depth | ML |
| Height | MH |

### 2.2.3 Ironbar (blk3)

POSITION

| Description | Value |
|---|---|
| Position | {0, 0, MH + LOff} |

AXIS

| Description | Value |
|---|---|
| Axis type | z - axis |

SIZE AND SHAPE

| Description | Value |
|---|---|
| Width | (2*PW + SD) |
| Depth | ML |
| Height | YH |

### 2.2.4 Steelplate (blk4)

POSITION

| Description | Value |
|---|---|
| Position | {-PW, -ML, -5} |

AXIS

| Description | Value |
|---|---|
| Axis type | z - axis |

SIZE AND SHAPE

| Description | Value |
|---|---|
| Width | (4*PW) + SD |
| Depth | 3*ML |
| Height | 4 |

### 2.2.5 Air (sph1)

POSITION

| Description | Value |
|---|---|
| Position | {PW, ML, 0} |

AXIS

| Description | Value |
|---|---|
| Axis type | z - axis |

SIZE

| Description | Value |
|---|---|

| Description | Value |
|---|---|
| Radius | 4*ML |

### 2.2.6 Plate 2 (blk5)

POSITION

| Description | Value |
|---|---|
| Position | {20, 0, 0} |

AXIS

| Description | Value |
|---|---|
| Axis type | z - axis |

SIZE AND SHAPE

| Description | Value |
|---|---|
| Width | 25 |
| Depth | 40 |
| Height | 21 |

### 2.2.7 Corrrosion (blk6)

POSITION

| Description | Value |
|---|---|
| Position | {-PW, -ML, -7} |

AXIS

| Description | Value |
|---|---|
| Axis type | z - axis |

SIZE AND SHAPE

| Description | Value |
|---|---|
| Width | (4*PW) + SD |
| Depth | 3*ML |
| Height | 2 |

### 2.2.8 corrosion2 (blk7)

POSITION

| Description | Value |
|---|---|
| Position | {-PW, -ML, -9} |

AXIS

| Description | Value |
|---|---|
| Axis type | z - axis |

SIZE AND SHAPE

| Description | Value |
|---|---|
| Width | (4*PW) + SD |
| Depth | 3*ML |
| Height | 2 |

### 2.2.9 corrosion 3 (blk8)

POSITION

| Description | Value |
|---|---|
| Position | {-PW, -ML, -11} |

AXIS

| Description | Value |
|---|---|
| Axis type | z - axis |

SIZE AND SHAPE

| Description | Value |
|---|---|
| Width | (4*PW) + SD |
| Depth | 3*ML |
| Height | 2 |

## A.2.3 MATERIALS

### 2.3.1 Air

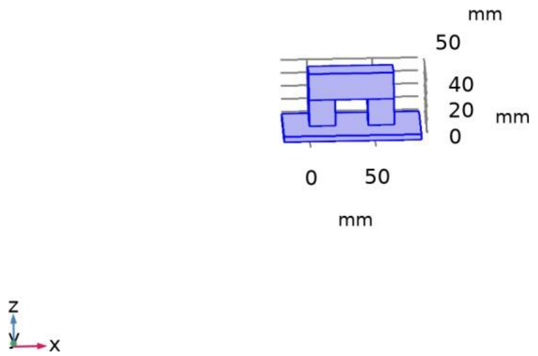

*Air*

#### SELECTION

| | |
|---|---|
| Geometric entity level | Domain |
| Selection | Geometry geom1: Dimension 3: Domain 1 |

#### MATERIAL PARAMETERS

| Name | Value | Unit |
|---|---|---|
| Relative permeability | 1 | 1 |

#### BASIC SETTINGS

| Description | Value |
|---|---|
| Coefficient of thermal expansion | {{alpha_p(pA, T), 0, 0}, {0, alpha_p(pA, T), 0}, {0, 0, alpha_p(pA, T)}} |
| Mean molar mass | 0.02897 |
| Bulk viscosity | muB(T) |
| Relative permeability | {{1, 0, 0}, {0, 1, 0}, {0, 0, 1}} |
| Relative permittivity | {{1, 0, 0}, {0, 1, 0}, {0, 0, 1}} |
| Dynamic viscosity | eta(T) |
| Ratio of specific heats | 1.4 |
| Electrical conductivity | {{0[S/m], 0, 0}, {0, 0[S/m], 0}, {0, 0, 0[S/m]}} |
| Heat capacity at constant pressure | Cp(T) |
| Density | rho(pA, T) |

| Description | Value |
|---|---|
| Thermal conductivity | {{k(T), 0, 0}, {0, k(T), 0}, {0, 0, k(T)}} |
| Speed of sound | cs(T) |

REFRACTIVE INDEX SETTINGS

| Description | Value |
|---|---|
| Refractive index, real part | {{1, 0, 0}, {0, 1, 0}, {0, 0, 1}} |
| Refractive index, imaginary part | {{0, 0, 0}, {0, 0, 0}, {0, 0, 0}} |

NONLINEAR MODEL SETTINGS

| Description | Value |
|---|---|
| Parameter of nonlinearity | (def.gamma + 1)/2 |

### 2.3.2 Iron

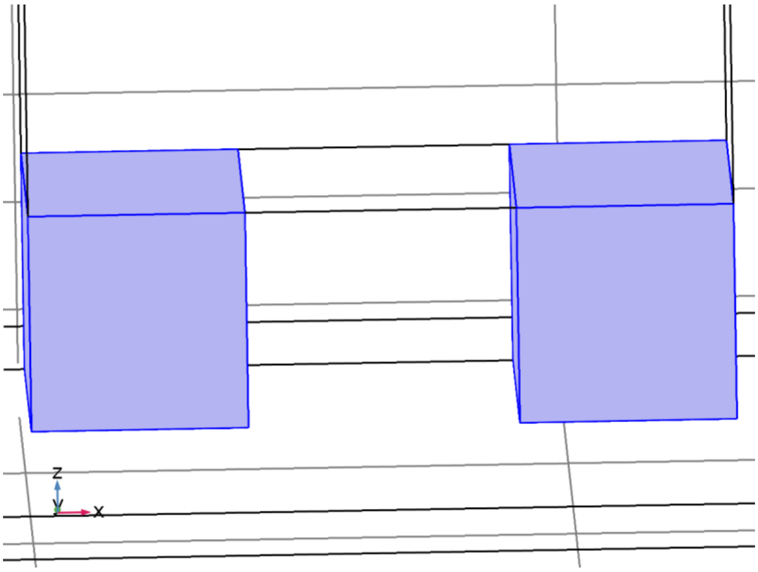

*Iron*

SELECTION

| | |
|---|---|
| Geometric entity level | Domain |
| Selection | Geometry geom1: Dimension 3: Domains 3, 5 |

BASIC SETTINGS

| Description | Value |
|---|---|
| Relative permeability | {{1.05, 0, 0}, {0, 1.05, 0}, {0, 0, 1.05}} |
| Electrical conductivity | {{1.12e7[S/m], 0, 0}, {0, 1.12e7[S/m], 0}, {0, 0, 1.12e7[S/m]}} |
| Coefficient of thermal expansion | {{12.2e-6[1/K], 0, 0}, {0, 12.2e-6[1/K], 0}, {0, 0, 12.2e-6[1/K]}} |

| Description | Value |
|---|---|
| Heat capacity at constant pressure | 440[J/(kg*K)] |
| Relative permittivity | {{1, 0, 0}, {0, 1, 0}, {0, 0, 1}} |
| Density | 7870[kg/m^3] |
| Thermal conductivity | {{76.2[W/(m*K)], 0, 0}, {0, 76.2[W/(m*K)], 0}, {0, 0, 76.2[W/(m*K)]}} |

YOUNG'S MODULUS AND POISSON'S RATIO SETTINGS

| Description | Value |
|---|---|
| Young's modulus | 200e9[Pa] |
| Poisson's ratio | 0.29 |

### 2.3.4 Iron 1

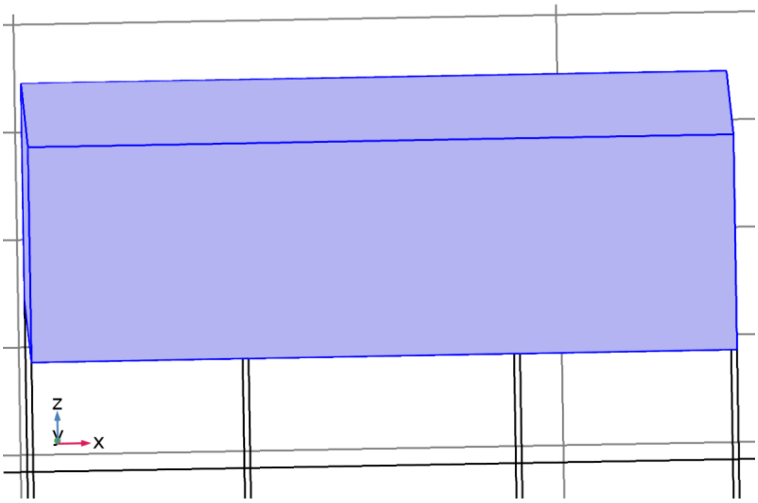

*Iron 1*

SELECTION

| | |
|---|---|
| Geometric entity level | Domain |
| Selection | Geometry geom1: Dimension 3: Domain 4 |

MATERIAL PARAMETERS

| Name | Value | Unit |
|---|---|---|
| Relative permeability | 4000 | 1 |

BASIC SETTINGS

| Description | Value |
|---|---|
| Relative permeability | {{4000, 0, 0}, {0, 4000, 0}, {0, 0, 4000}} |

| Description | Value |
|---|---|
| Electrical conductivity | {{1.12e7[S/m], 0, 0}, {0, 1.12e7[S/m], 0}, {0, 0, 1.12e7[S/m]}} |
| Coefficient of thermal expansion | {{12.2e-6[1/K], 0, 0}, {0, 12.2e-6[1/K], 0}, {0, 0, 12.2e-6[1/K]}} |
| Heat capacity at constant pressure | 440[J/(kg*K)] |
| Relative permittivity | {{1, 0, 0}, {0, 1, 0}, {0, 0, 1}} |
| Density | 7870[kg/m^3] |
| Thermal conductivity | {{76.2[W/(m*K)], 0, 0}, {0, 76.2[W/(m*K)], 0}, {0, 0, 76.2[W/(m*K)]}} |

### YOUNG'S MODULUS AND POISSON'S RATIO SETTINGS

| Description | Value |
|---|---|
| Young's modulus | 200e9[Pa] |
| Poisson's ratio | 0.29 |

## 2.3.5 Low Carbon Steel 1002

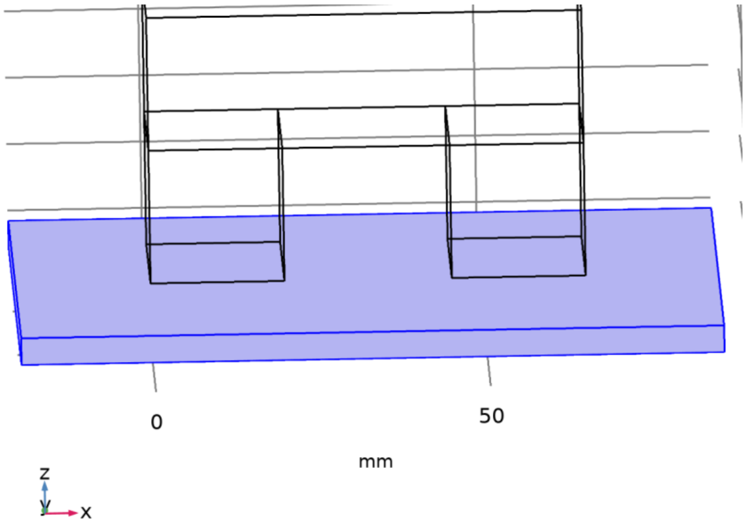

*Low Carbon Steel 1002*

### SELECTION

| | |
|---|---|
| Geometric entity level | Domain |
| Selection | Geometry geom1: Dimension 3: Domain 2 |

### MATERIAL PARAMETERS

| Name | Value | Unit |
|---|---|---|
| Relative permeability | 150 | 1 |

#### BASIC SETTINGS

| Description | Value |
|---|---|
| Electrical conductivity | {{8.41[MS/m], 0, 0}, {0, 8.41[MS/m], 0}, {0, 0, 8.41[MS/m]}} |
| Relative permittivity | {{1[1], 0, 0}, {0, 1[1], 0}, {0, 0, 1[1]}} |
| Relative permeability | {{150, 0, 0}, {0, 150, 0}, {0, 0, 150}} |
| relpermeability_symmetry | 0 |

#### B-H CURVE SETTINGS

| Description | Value |
|---|---|
| Magnetic flux density norm | BH(normHin) |
| Magnetic field norm | BH_inv(normBin) |
| Magnetic coenergy density | BH_prim(normHin) |
| Magnetic field norm | sqrt(H1^2 + H2^2 + H3^2 + eps) |
| Magnetic flux density norm | sqrt(B1^2 + B2^2 + B3^2 + eps) |

### A.2.4 MAGNETIC FIELDS, NO CURRENTS

#### USED PRODUCTS

| |
|---|
| COMSOL Multiphysics |
| AC/DC Module |

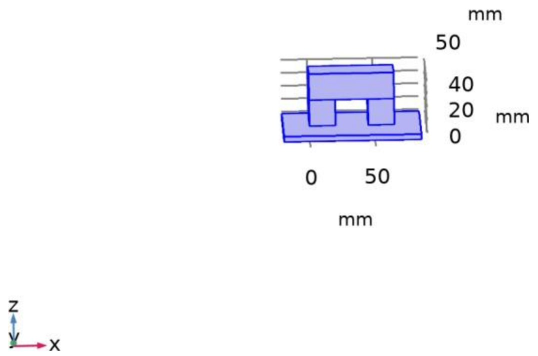

*Magnetic Fields, No Currents*

#### SELECTION

| | |
|---|---|
| Geometric entity level | Domain |
| Selection | Geometry geom1: Dimension 3: All domains |

EQUATIONS

$$\mathbf{H} = -\nabla V_{\mathrm{m}}$$

$$\nabla \cdot \mathbf{B} = 0$$

### 2.4.1 Interface settings

**Discretization**

SETTINGS

| Description | Value |
|---|---|
| Magnetic scalar potential | Quadratic |

### 2.4.2 Variables

| Name | Expression | Unit | Description | Selection |
|---|---|---|---|---|
| mfnc.tHX | -VmTX | A/m | Tangential magnetic field, material frame, X component | Boundaries 1–32 |
| mfnc.tHY | -VmTY | A/m | Tangential magnetic field, material frame, Y component | Boundaries 1–32 |
| mfnc.tHZ | -VmTZ | A/m | Tangential magnetic field, material frame, Z component | Boundaries 1–32 |
| mfnc.tHx | -VmTx | A/m | Tangential magnetic field, x component | Boundaries 1–32 |
| mfnc.tHy | -VmTy | A/m | Tangential magnetic field, y component | Boundaries 1–32 |
| mfnc.tHz | -VmTz | A/m | Tangential magnetic field, z component | Boundaries 1–32 |
| mfnc.Bbx | 0 | T | Background magnetic flux density, x component | Domains 1–5 |
| mfnc.Bby | 0 | T | Background magnetic flux density, y component | Domains 1–5 |
| mfnc.Bbz | 0 | T | Background magnetic flux density, z component | Domains 1–5 |
| mfnc.Hbx | 0 | A/m | Background magnetic field, x component | Domains 1–5 |
| mfnc.Hby | 0 | A/m | Background magnetic field, y component | Domains 1–5 |
| mfnc.Hbz | 0 | A/m | Background magnetic | Domains 1–5 |

| Name | Expression | Unit | Description | Selection |
|---|---|---|---|---|
| | | | field, z component | |
| mfnc.nx | nx | | Normal vector, x component | Boundaries 5–18, 21–22, 25–32 |
| mfnc.ny | ny | | Normal vector, y component | Boundaries 5–18, 21–22, 25–32 |
| mfnc.nz | nz | | Normal vector, z component | Boundaries 5–18, 21–22, 25–32 |
| mfnc.nx | dnx | | Normal vector, x component | Boundaries 1–4, 19–20, 23–24 |
| mfnc.ny | dny | | Normal vector, y component | Boundaries 1–4, 19–20, 23–24 |
| mfnc.nz | dnz | | Normal vector, z component | Boundaries 1–4, 19–20, 23–24 |
| mfnc.nmeshx | nxmesh | | Mesh normal vector, x component | Boundaries 5–18, 21–22, 25–32 |
| mfnc.nmeshy | nymesh | | Mesh normal vector, y component | Boundaries 5–18, 21–22, 25–32 |
| mfnc.nmeshz | nzmesh | | Mesh normal vector, z component | Boundaries 5–18, 21–22, 25–32 |
| mfnc.nmeshx | dnxmesh | | Mesh normal vector, x component | Boundaries 1–4, 19–20, 23–24 |
| mfnc.nmeshy | dnymesh | | Mesh normal vector, y component | Boundaries 1–4, 19–20, 23–24 |
| mfnc.nmeshz | dnzmesh | | Mesh normal vector, z component | Boundaries 1–4, 19–20, 23–24 |
| mfnc.unmeshx | unxmesh | | Mesh normal vector, upside, x component | Boundaries 1–32 |
| mfnc.unmeshy | unymesh | | Mesh normal vector, upside, y component | Boundaries 1–32 |
| mfnc.unmeshz | unzmesh | | Mesh normal vector, | Boundaries 1– |

| Name | Expression | Unit | Description | Selection |
|---|---|---|---|---|
|  |  |  | upside, z component | 32 |
| mfnc.dnmeshx | dnxmesh |  | Mesh normal vector, downside, x component | Boundaries 1–32 |
| mfnc.dnmeshy | dnymesh |  | Mesh normal vector, downside, y component | Boundaries 1–32 |
| mfnc.dnmeshz | dnzmesh |  | Mesh normal vector, downside, z component | Boundaries 1–32 |
| mfnc.I_sXX | (spatial.invF11*(spatial.invF11*mfnc.I_sxx+spatial.invF21*mfnc.I_syx+spatial.invF31*mfnc.I_szx)+spatial.invF21*(spatial.invF11*mfnc.I_sxy+spatial.invF21*mfnc.I_syy+spatial.invF31*mfnc.I_szy)+spatial.invF31*(spatial.invF11*mfnc.I_sxz+spatial.invF21*mfnc.I_syz+spatial.invF31*mfnc.I_szz))*spatial.detF | 1 | Spatial identity matrix, material frame, XX component | Domains 1–5 |
| mfnc.I_sYX | (spatial.invF11*(spatial.invF12*mfnc.I_sxx+spatial.invF22*mfnc.I_syx+spatial.invF32*mfnc.I_szx)+spatial.invF21*(spatial.invF12*mfnc.I_sxy+spatial.invF22*mfnc.I_syy+spatial.invF32*mfnc.I_szy)+spatial.invF31*(spatial.invF12*mfnc.I_sxz+spatial.invF22*mfnc.I_syz+spatial.invF32*mfnc.I_szz))*spatial.detF | 1 | Spatial identity matrix, material frame, YX component | Domains 1–5 |
| mfnc.I_sZX | (spatial.invF11*(spatial.invF13*mfnc.I_sxx+spatial.invF23*mfnc.I_syx+spatial.invF33*mfnc.I_szx)+spatial.invF21*(spatial.invF13*mfnc.I_sxy+spatial.invF23*mfnc.I_syy+spatial.invF33*mfnc.I_szy)+spatial.invF31*(spatial.invF13*mfnc.I_sxz+spatial.invF23*mfnc.I_syz+spatial.invF33*mfnc.I_szz))*spatial.detF | 1 | Spatial identity matrix, material frame, ZX component | Domains 1–5 |
| mfnc.I_sXY | (spatial.invF12*(spatial.invF11*mfnc.I_sxx+spatial.invF21*mfnc.I_syx+spatial.invF31*mfnc.I_szx)+spatial.invF22*(spatial.invF11*mfnc.I_sxy+spatial.invF21*mfnc.I_syy+s | 1 | Spatial identity matrix, material frame, XY component | Domains 1–5 |

| Name | Expression | Unit | Description | Selection |
|---|---|---|---|---|
| | patial.invF31*mfnc.I_szy)+spatial.invF32*(spatial.invF11*mfnc.I_sxz+spatial.invF21*mfnc.I_syz+spatial.invF31*mfnc.I_szz))*spatial.detF | | | |
| mfnc.I_sYY | (spatial.invF12*(spatial.invF12*mfnc.I_sxx+spatial.invF22*mfnc.I_syx+spatial.invF32*mfnc.I_szx)+spatial.invF22*(spatial.invF12*mfnc.I_sxy+spatial.invF22*mfnc.I_syy+spatial.invF32*mfnc.I_szy)+spatial.invF32*(spatial.invF12*mfnc.I_sxz+spatial.invF22*mfnc.I_syz+spatial.invF32*mfnc.I_szz))*spatial.detF | 1 | Spatial identity matrix, material frame, YY component | Domains 1–5 |
| mfnc.I_sZY | (spatial.invF12*(spatial.invF13*mfnc.I_sxx+spatial.invF23*mfnc.I_syx+spatial.invF33*mfnc.I_szx)+spatial.invF22*(spatial.invF13*mfnc.I_sxy+spatial.invF23*mfnc.I_syy+spatial.invF33*mfnc.I_szy)+spatial.invF32*(spatial.invF13*mfnc.I_sxz+spatial.invF23*mfnc.I_syz+spatial.invF33*mfnc.I_szz))*spatial.detF | 1 | Spatial identity matrix, material frame, ZY component | Domains 1–5 |
| mfnc.I_sXZ | (spatial.invF13*(spatial.invF11*mfnc.I_sxx+spatial.invF21*mfnc.I_syx+spatial.invF31*mfnc.I_szx)+spatial.invF23*(spatial.invF11*mfnc.I_sxy+spatial.invF21*mfnc.I_syy+spatial.invF31*mfnc.I_szy)+spatial.invF33*(spatial.invF11*mfnc.I_sxz+spatial.invF21*mfnc.I_syz+spatial.invF31*mfnc.I_szz))*spatial.detF | 1 | Spatial identity matrix, material frame, XZ component | Domains 1–5 |
| mfnc.I_sYZ | (spatial.invF13*(spatial.invF12*mfnc.I_sxx+spatial.invF22*mfnc.I_syx+spatial.invF32*mfnc.I_szx)+spatial.invF23*(spatial.invF12*mfnc.I_sxy+spatial.invF22*mfnc.I_syy+spatial.invF32*mfnc.I_szy)+spatial.invF33*(spatial.invF12*mfnc.I_sxz+spatial.invF22*mfnc.I_syz+spatial.invF32*mfnc.I_szz))*spatial.detF | 1 | Spatial identity matrix, material frame, YZ component | Domains 1–5 |
| mfnc.I_sZZ | (spatial.invF13*(spatial.invF13*mf | 1 | Spatial identity matrix, | Domains 1–5 |

| Name | Expression | Unit | Description | Selection |
|---|---|---|---|---|
| | nc.I_sxx+spatial.invF23*mfnc.I_syx+spatial.invF33*mfnc.I_szx)+spatial.invF23*(spatial.invF13*mfnc.I_sxy+spatial.invF23*mfnc.I_syy+spatial.invF33*mfnc.I_szy)+spatial.invF33*(spatial.invF13*mfnc.I_sxz+spatial.invF23*mfnc.I_syz+spatial.invF33*mfnc.I_szz))*spatial.detF | | material frame, ZZ component | |
| mfnc.I_sxx | 1 | 1 | Spatial identity matrix, xx component | Domains 1–5 |
| mfnc.I_syx | 0 | 1 | Spatial identity matrix, yx component | Domains 1–5 |
| mfnc.I_szx | 0 | 1 | Spatial identity matrix, zx component | Domains 1–5 |
| mfnc.I_sxy | 0 | 1 | Spatial identity matrix, xy component | Domains 1–5 |
| mfnc.I_syy | 1 | 1 | Spatial identity matrix, yy component | Domains 1–5 |
| mfnc.I_szy | 0 | 1 | Spatial identity matrix, zy component | Domains 1–5 |
| mfnc.I_sxz | 0 | 1 | Spatial identity matrix, xz component | Domains 1–5 |
| mfnc.I_syz | 0 | 1 | Spatial identity matrix, yz component | Domains 1–5 |
| mfnc.I_szz | 1 | 1 | Spatial identity matrix, zz component | Domains 1–5 |
| mfnc.intWm | mfnc.int_Wm(mfnc.d*mfnc.dWm) | J | Total magnetic energy | Global |
| mfnc.d | 1 | 1 | Contribution | Domains 1–5 |
| mfnc.unTx | mfnc.unTmx | Pa | Maxwell upward surface stress tensor, x component | Boundaries 1–32 |
| mfnc.unTy | mfnc.unTmy | Pa | Maxwell upward surface stress tensor, y component | Boundaries 1–32 |
| mfnc.unTz | mfnc.unTmz | Pa | Maxwell upward surface stress tensor, z component | Boundaries 1–32 |
| mfnc.dnTx | mfnc.dnTmx | Pa | Maxwell downward surface stress tensor, x component | Boundaries 1–32 |

| Name | Expression | Unit | Description | Selection |
|---|---|---|---|---|
| mfnc.dnTy | mfnc.dnTmy | Pa | Maxwell downward surface stress tensor, y component | Boundaries 1–32 |
| mfnc.dnTz | mfnc.dnTmz | Pa | Maxwell downward surface stress tensor, z component | Boundaries 1–32 |
| mfnc.unx | unx | | Normal vector up direction, x component | Boundaries 1–32 |
| mfnc.uny | uny | | Normal vector up direction, y component | Boundaries 1–32 |
| mfnc.unz | unz | | Normal vector up direction, z component | Boundaries 1–32 |
| mfnc.dnx | dnx | | Normal vector down direction, x component | Boundaries 1–32 |
| mfnc.dny | dny | | Normal vector down direction, y component | Boundaries 1–32 |
| mfnc.dnz | dnz | | Normal vector down direction, z component | Boundaries 1–32 |
| mfnc.unTmx | -0.5*mfnc.dnx*(real(up(mfnc.Bx))*real(up(mfnc.Hx))+real(up(mfnc.By))*real(up(mfnc.Hy))+real(up(mfnc.Bz))*real(up(mfnc.Hz)))+real(up(mfnc.Bx))*(real(up(mfnc.Hx))*mfnc.dnx+real(up(mfnc.Hy))*mfnc.dny+real(up(mfnc.Hz))*mfnc.dnz) | Pa | Maxwell upward magnetic surface stress tensor, x component | Boundaries 5–18, 21–22, 25–32 |
| mfnc.unTmy | -0.5*mfnc.dny*(real(up(mfnc.Bx))*real(up(mfnc.Hx))+real(up(mfnc.By))*real(up(mfnc.Hy))+real(up(mfnc.Bz))*real(up(mfnc.Hz)))+real(up(mfnc.By))*(real(up(mfnc.Hx))*mfnc.dnx+real(up(mfnc.Hy))*mfnc.dny+real(up(mfnc.Hz))*mfnc.dnz) | Pa | Maxwell upward magnetic surface stress tensor, y component | Boundaries 5–18, 21–22, 25–32 |
| mfnc.unTmz | -0.5*mfnc.dnz*(real(up(mfnc.Bx))*real(up(mfnc.Hx))+real(up(mfnc.By))*real(up(mfnc.Hy))+real(up(mfnc.Bz))*real(up(mfnc.Hz)))+real(up(mfnc.Bz))*(real(up(mfnc.Hx)) | Pa | Maxwell upward magnetic surface stress tensor, z component | Boundaries 5–18, 21–22, 25–32 |

| Name | Expression | Unit | Description | Selection |
|---|---|---|---|---|
| | *mfnc.dnx+real(up(mfnc.Hy))*mfnc.dny+real(up(mfnc.Hz))*mfnc.dnz) | | | |
| mfnc.unTmx | 0 | Pa | Maxwell upward magnetic surface stress tensor, x component | Boundaries 1–4, 19–20, 23–24 |
| mfnc.unTmy | 0 | Pa | Maxwell upward magnetic surface stress tensor, y component | Boundaries 1–4, 19–20, 23–24 |
| mfnc.unTmz | 0 | Pa | Maxwell upward magnetic surface stress tensor, z component | Boundaries 1–4, 19–20, 23–24 |
| mfnc.dnTmx | -0.5*mfnc.unx*(real(down(mfnc.Bx))*real(down(mfnc.Hx))+real(down(mfnc.By))*real(down(mfnc.Hy))+real(down(mfnc.Bz))*real(down(mfnc.Hz)))+real(down(mfnc.Bx))*(real(down(mfnc.Hx))*mfnc.unx+real(down(mfnc.Hy))*mfnc.uny+real(down(mfnc.Hz))*mfnc.unz) | Pa | Maxwell downward magnetic surface stress tensor, x component | Boundaries 1–32 |
| mfnc.dnTmy | -0.5*mfnc.uny*(real(down(mfnc.Bx))*real(down(mfnc.Hx))+real(down(mfnc.By))*real(down(mfnc.Hy))+real(down(mfnc.Bz))*real(down(mfnc.Hz)))+real(down(mfnc.By))*(real(down(mfnc.Hx))*mfnc.unx+real(down(mfnc.Hy))*mfnc.uny+real(down(mfnc.Hz))*mfnc.unz) | Pa | Maxwell downward magnetic surface stress tensor, y component | Boundaries 1–32 |
| mfnc.dnTmz | -0.5*mfnc.unz*(real(down(mfnc.Bx))*real(down(mfnc.Hx))+real(down(mfnc.By))*real(down(mfnc.Hy))+real(down(mfnc.Bz))*real(down(mfnc.Hz)))+real(down(mfnc.Bz))*(real(down(mfnc.Hx))*mfnc.unx+real(down(mfnc.Hy))*mfnc.uny+real(down(mfnc.Hz))*mfnc.unz) | Pa | Maxwell downward magnetic surface stress tensor, z component | Boundaries 1–32 |
| mfnc.Qh | 0 | W/m$^3$ | Volumetric loss density, electromagnetic | Domains 1–5 |

| **Name** | **Expression** | **Unit** | **Description** | **Selection** |
|---|---|---|---|---|
| mfnc.Qsh | 0 | W/m$^2$ | Surface loss density, electromagnetic | Boundaries 1–32 |
| mfnc.Qlh | 0 | W/m | Line loss density, electromagnetic | Edges 1–58 |

### 2.4.3 Magnetic Flux Conservation 1

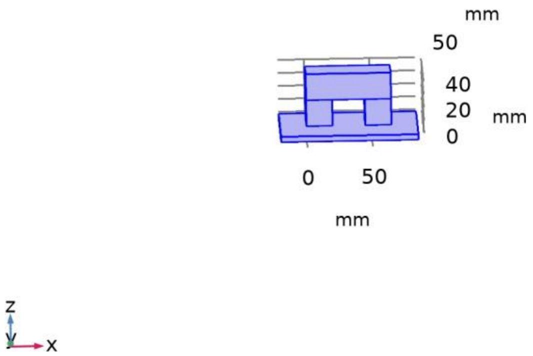

*Magnetic Flux Conservation 1*

SELECTION

| | |
|---|---|
| Geometric entity level | Domain |
| Selection | Geometry geom1: Dimension 3: All domains |

EQUATIONS

$$\nabla \cdot \mathbf{B} = 0, \quad \mathbf{B} = \mu_0 \mu_r \mathbf{H}$$

$$\mathbf{H} = -\nabla V_m$$

**Constitutive relation B-H**

SETTINGS

| **Description** | **Value** |
|---|---|
| Magnetization model | Relative permeability |
| Relative permeability | From material |

**Coordinate system selection**

SETTINGS

| **Description** | **Value** |
|---|---|

| Description | Value |
|---|---|
| Coordinate system | Global coordinate system |

PROPERTIES FROM MATERIAL

| Property | Material | Property group |
|---|---|---|
| Relative permeability | Air | Basic |
| Relative permeability | Iron 1 | Basic |
| Relative permeability | Low Carbon Steel 1002 | Basic |

### Variables

| Name | Expression | Unit | Description | Selection | Details |
|---|---|---|---|---|---|
| mfnc.Qh | mfnc.Qrh | $W/m^3$ | Volumetric loss density, electromagnetic | Domains 1–2, 4 | |
| mfnc.Hx | -Vmx | A/m | Magnetic field, x component | Domains 1–2, 4 | |
| mfnc.Hy | -Vmy | A/m | Magnetic field, y component | Domains 1–2, 4 | |
| mfnc.Hz | -Vmz | A/m | Magnetic field, z component | Domains 1–2, 4 | |
| mfnc.normH | sqrt(realdot(mfnc.Hx,mfnc.Hx)+realdot(mfnc.Hy,mfnc.Hy)+realdot(mfnc.Hz,mfnc.Hz)) | A/m | Magnetic field norm | Domains 1–2, 4 | |
| mfnc.Bx | mu0_const*(mfnc.I_sxx*mfnc.Hx+mfnc.I_sxy*mfnc.Hy+mfnc.I_sxz*mfnc.Hz+mfnc.Mx) | T | Magnetic flux density, x component | Domains 1–2, 4 | |
| mfnc.By | mu0_const*(mfnc.I_syx*mfnc.Hx+mfnc.I_syy*mfnc.Hy+mfnc.I_syz*mfnc.Hz+mfnc.My) | T | Magnetic flux density, y component | Domains 1–2, 4 | |
| mfnc.Bz | mu0_const*(mfnc.I_szx*mfnc.Hx+mfnc.I_szy*mfnc.Hy+mfnc.I_szz*mfnc.Hz+mfnc.Mz) | T | Magnetic flux density, z component | Domains 1–2, 4 | |
| mfnc.normB | sqrt(realdot(mfnc.Bx,mfnc.Bx)+realdot(mfnc.By,mfnc.By)+r | T | Magnetic flux density norm | Domains 1–2, 4 | |

| Name | Expression | Unit | Description | Selection | Details |
|---|---|---|---|---|---|
| | ealdot(mfnc.Bz,mfnc.Bz)) | | | | |
| mfnc.Mx | mfnc.chimxx*mfnc.Hx+mfnc.chimxy*mfnc.Hy+mfnc.chimxz*mfnc.Hz | A/m | Magnetization, x component | Domains 1–2, 4 | |
| mfnc.My | mfnc.chimyx*mfnc.Hx+mfnc.chimyy*mfnc.Hy+mfnc.chimyz*mfnc.Hz | A/m | Magnetization, y component | Domains 1–2, 4 | |
| mfnc.Mz | mfnc.chimzx*mfnc.Hx+mfnc.chimzy*mfnc.Hy+mfnc.chimzz*mfnc.Hz | A/m | Magnetization, z component | Domains 1–2, 4 | |
| mfnc.normM | sqrt(realdot(mfnc.Mx,mfnc.Mx)+realdot(mfnc.My,mfnc.My)+realdot(mfnc.Mz,mfnc.Mz)) | A/m | Magnetization norm | Domains 1–2, 4 | |
| mfnc.W | mfnc.Wm | J/m$^3$ | Energy density | Domains 1–2, 4 | + operation |
| mfnc.dWm | mfnc.Wm | J/m$^3$ | Integrand for total magnetic energy | Domains 1–2, 4 | Meta |
| mfnc.Wm | 0.5*(mfnc.Bx*mfnc.Hx+mfnc.By*mfnc.Hy+mfnc.Bz*mfnc.Hz) | J/m$^3$ | Magnetic energy density | Domains 1–2, 4 | |
| mfnc.Wpm | mfnc.Wm | J/m$^3$ | Magnetic coenergy density | Domains 1–2, 4 | |
| mfnc.Qrh | 0 | W/m$^3$ | Volumetric loss density, electric | Domains 1–2, 4 | + operation |
| mfnc.mfc1.eBrx | 1/sqrt(1+eps) | 1 | Remanent flux direction, x component | Domains 1–2, 4 | |
| mfnc.mfc1.eBry | 0 | 1 | Remanent flux direction, y component | Domains 1–2, 4 | |
| mfnc.mfc1.eBrz | 0 | 1 | Remanent flux direction, z component | Domains 1–2, 4 | |
| mfnc.murxx | material.mur11 | 1 | Relative permeability, xx component | Domains 1–2, 4 | Meta |

| Name | Expression | Unit | Description | Selection | Details |
|---|---|---|---|---|---|
| mfnc.muryx | material.mur21 | 1 | Relative permeability, yx component | Domains 1–2, 4 | Meta |
| mfnc.murzx | material.mur31 | 1 | Relative permeability, zx component | Domains 1–2, 4 | Meta |
| mfnc.murxy | material.mur12 | 1 | Relative permeability, xy component | Domains 1–2, 4 | Meta |
| mfnc.muryy | material.mur22 | 1 | Relative permeability, yy component | Domains 1–2, 4 | Meta |
| mfnc.murzy | material.mur32 | 1 | Relative permeability, zy component | Domains 1–2, 4 | Meta |
| mfnc.murxz | material.mur13 | 1 | Relative permeability, xz component | Domains 1–2, 4 | Meta |
| mfnc.muryz | material.mur23 | 1 | Relative permeability, yz component | Domains 1–2, 4 | Meta |
| mfnc.murzz | material.mur33 | 1 | Relative permeability, zz component | Domains 1–2, 4 | Meta |
| mfnc.chimxx | -1+mfnc.murxx | 1 | Magnetic susceptibility, xx component | Domains 1–2, 4 | |
| mfnc.chimyx | mfnc.muryx | 1 | Magnetic susceptibility, yx component | Domains 1–2, 4 | |
| mfnc.chimzx | mfnc.murzx | 1 | Magnetic susceptibility, zx component | Domains 1–2, 4 | |
| mfnc.chimxy | mfnc.murxy | 1 | Magnetic susceptibility, xy component | Domains 1–2, 4 | |
| mfnc.chimyy | -1+mfnc.muryy | 1 | Magnetic susceptibility, yy component | Domains 1–2, 4 | |
| mfnc.chimzy | mfnc.murzy | 1 | Magnetic susceptibility, zy component | Domains 1–2, 4 | |

| Name | Expression | Unit | Description | Selection | Details |
|---|---|---|---|---|---|
| mfnc.chimxz | mfnc.murxz | 1 | Magnetic susceptibility, xz component | Domains 1–2, 4 | |
| mfnc.chimyz | mfnc.muryz | 1 | Magnetic susceptibility, yz component | Domains 1–2, 4 | |
| mfnc.chimzz | -1+mfnc.murzz | 1 | Magnetic susceptibility, zz component | Domains 1–2, 4 | |

### Shape functions

| Name | Shape function | Unit | Description | Shape frame | Selection |
|---|---|---|---|---|---|
| Vm | Lagrange (Quadratic) | A | Magnetic scalar potential | Spatial | Domains 1–2, 4 |
| Vm | Lagrange (Quadratic) | A | Magnetic scalar potential | Material | Domains 1–2, 4 |
| Vm | Lagrange (Quadratic) | A | Magnetic scalar potential | Geometry | Domains 1–2, 4 |
| Vm | Lagrange (Quadratic) | A | Magnetic scalar potential | Mesh | Domains 1–2, 4 |

### Weak expressions

| Weak expression | Integration order | Integration frame | Selection |
|---|---|---|---|
| mfnc.d*(-mfnc.Bx*test(Vmx)-mfnc.By*test(Vmy)-mfnc.Bz*test(Vmz)) | 4 | Spatial | Domains 1–2, 4 |

### 2.4.4 Magnetic Insulation 1

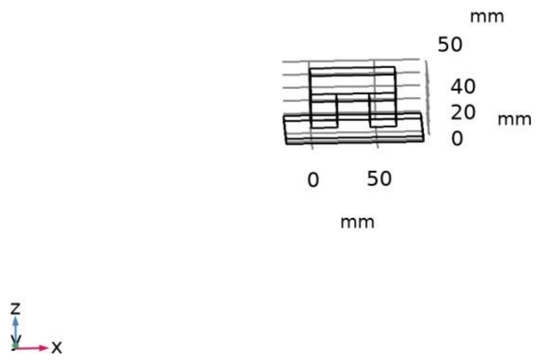

*Magnetic Insulation 1*

SELECTION

| | |
|---|---|
| Geometric entity level | Boundary |
| Selection | Geometry geom1: Dimension 2: All boundaries |

EQUATIONS

$$\mathbf{n} \cdot \mathbf{B} = 0$$

**Shape functions**

| Name | Shape function | Unit | Description | Shape frame | Selection | Details |
|---|---|---|---|---|---|---|
| Vm | Lagrange (Quadratic) | A | Magnetic scalar potential | Spatial | No boundaries | Slit |
| Vm | Lagrange (Quadratic) | A | Magnetic scalar potential | Material | No boundaries | Slit |
| Vm | Lagrange (Quadratic) | A | Magnetic scalar potential | Geometry | No boundaries | Slit |
| Vm | Lagrange (Quadratic) | A | Magnetic scalar potential | Mesh | No boundaries | Slit |

### 2.4.5 Initial Values 1

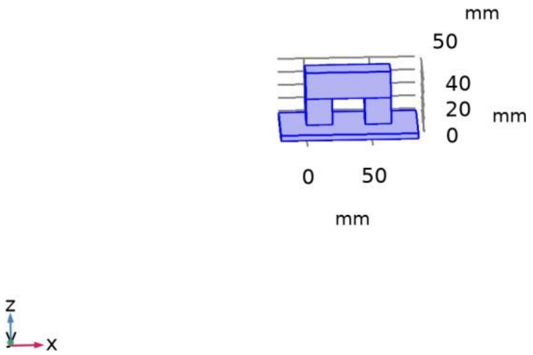

*Initial Values 1*

SELECTION

| | |
|---|---|
| Geometric entity level | Domain |
| Selection | Geometry geom1: Dimension 3: All domains |

SETTINGS

| **Description** | **Value** |
|---|---|
| Magnetic scalar potential | 0 |

### 2.4.6 Magnetic Flux Conservation 2

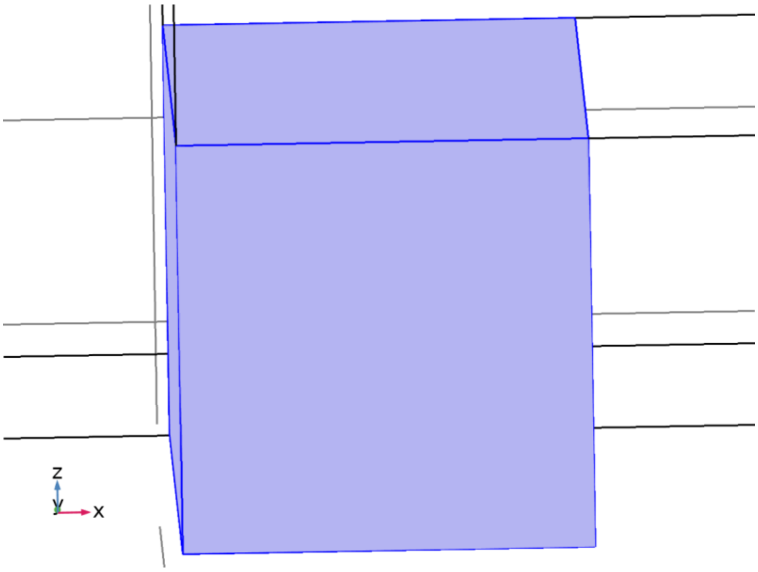

*Magnetic Flux Conservation 2*

SELECTION

| | |
|---|---|
| Geometric entity level | Domain |
| Selection | Geometry geom1: Dimension 3: Domain 3 |

EQUATIONS

$$\nabla \cdot \mathbf{B} = 0, \quad \mathbf{B} = \mu_0(\mathbf{H} + \mathbf{M})$$

$$\mathbf{H} = -\nabla V_{\mathrm{m}}$$

**Constitutive relation B-H**

SETTINGS

| Description | Value |
|---|---|
| Magnetization model | Magnetization |
| Magnetization, x component | 0 |
| Magnetization, y component | 0 |
| Magnetization, z component | 835 [kA/m] |

**Coordinate system selection**

SETTINGS

| Description | Value |
|---|---|
| Coordinate system | Global coordinate system |

**Variables**

| Name | Expression | Unit | Description | Selection | Details |
|---|---|---|---|---|---|

| **Name** | **Expression** | **Unit** | **Description** | **Selection** | **Details** |
|---|---|---|---|---|---|
| mfnc.Qh | mfnc.Qrh | W/m³ | Volumetric loss density, electromagnetic | Domain 3 | |
| mfnc.Hx | -Vmx | A/m | Magnetic field, x component | Domain 3 | |
| mfnc.Hy | -Vmy | A/m | Magnetic field, y component | Domain 3 | |
| mfnc.Hz | -Vmz | A/m | Magnetic field, z component | Domain 3 | |
| mfnc.normH | sqrt(realdot(mfnc.Hx,mfnc.Hx)+realdot(mfnc.Hy,mfnc.Hy)+realdot(mfnc.Hz,mfnc.Hz)) | A/m | Magnetic field norm | Domain 3 | |
| mfnc.Bx | mu0_const*(mfnc.I_sxx*mfnc.Hx+mfnc.I_sxy*mfnc.Hy+mfnc.I_sxz*mfnc.Hz+mfnc.Mx) | T | Magnetic flux density, x component | Domain 3 | |
| mfnc.By | mu0_const*(mfnc.I_syx*mfnc.Hx+mfnc.I_syy*mfnc.Hy+mfnc.I_syz*mfnc.Hz+mfnc.My) | T | Magnetic flux density, y component | Domain 3 | |
| mfnc.Bz | mu0_const*(mfnc.I_szx*mfnc.Hx+mfnc.I_szy*mfnc.Hy+mfnc.I_szz*mfnc.Hz+mfnc.Mz) | T | Magnetic flux density, z component | Domain 3 | |
| mfnc.normB | sqrt(realdot(mfnc.Bx,mfnc.Bx)+realdot(mfnc.By,mfnc.By)+realdot(mfnc.Bz,mfnc.Bz)) | T | Magnetic flux density norm | Domain 3 | |
| mfnc.Mx | 0 | A/m | Magnetization, x component | Domain 3 | |
| mfnc.My | 0 | A/m | Magnetization, y component | Domain 3 | |
| mfnc.Mz | 835[kA/m] | A/m | Magnetization, z component | Domain 3 | |
| mfnc.normM | sqrt(realdot(mfnc.Mx,mfnc.Mx)+realdot(mfnc.My,mfnc.My)+ | A/m | Magnetization norm | Domain 3 | |

| Name | Expression | Unit | Description | Selection | Details |
|---|---|---|---|---|---|
| | realdot(mfnc.Mz,mfnc.Mz)) | | | | |
| mfnc.W | mfnc.Wm | J/m³ | Energy density | Domain 3 | + operation |
| mfnc.dWm | mfnc.Wm | J/m³ | Integrand for total magnetic energy | Domain 3 | Meta |
| mfnc.Wm | 0.5*((mfnc.Bx-mu0_const*mfnc.Mx)*mfnc.Hx+(mfnc.By-mu0_const*mfnc.My)*mfnc.Hy+(mfnc.Bz-mu0_const*mfnc.Mz)*mfnc.Hz) | J/m³ | Magnetic energy density | Domain 3 | |
| mfnc.Wpm | mfnc.Bx*mfnc.Hx+mfnc.By*mfnc.Hy+mfnc.Bz*mfnc.Hz-mfnc.Wm | J/m³ | Magnetic coenergy density | Domain 3 | |
| mfnc.Qrh | 0 | W/m³ | Volumetric loss density, electric | Domain 3 | + operation |
| mfnc.mfc2.eBrx | 1/sqrt(1+eps) | 1 | Remanent flux direction, x component | Domain 3 | |
| mfnc.mfc2.eBry | 0 | 1 | Remanent flux direction, y component | Domain 3 | |
| mfnc.mfc2.eBrz | 0 | 1 | Remanent flux direction, z component | Domain 3 | |

### Shape functions

| Name | Shape function | Unit | Description | Shape frame | Selection |
|---|---|---|---|---|---|
| Vm | Lagrange (Quadratic) | A | Magnetic scalar potential | Spatial | Domain 3 |
| Vm | Lagrange (Quadratic) | A | Magnetic scalar potential | Material | Domain 3 |
| Vm | Lagrange (Quadratic) | A | Magnetic scalar potential | Geometry | Domain 3 |
| Vm | Lagrange (Quadratic) | A | Magnetic scalar potential | Mesh | Domain 3 |

#### Weak expressions

| Weak expression | Integration order | Integration frame | Selection |
|---|---|---|---|
| mfnc.d*(-mfnc.Bx*test(Vmx)-mfnc.By*test(Vmy)-mfnc.Bz*test(Vmz)) | 4 | Spatial | Domain 3 |

### 2.4.7 Magnetic Flux Conservation 3

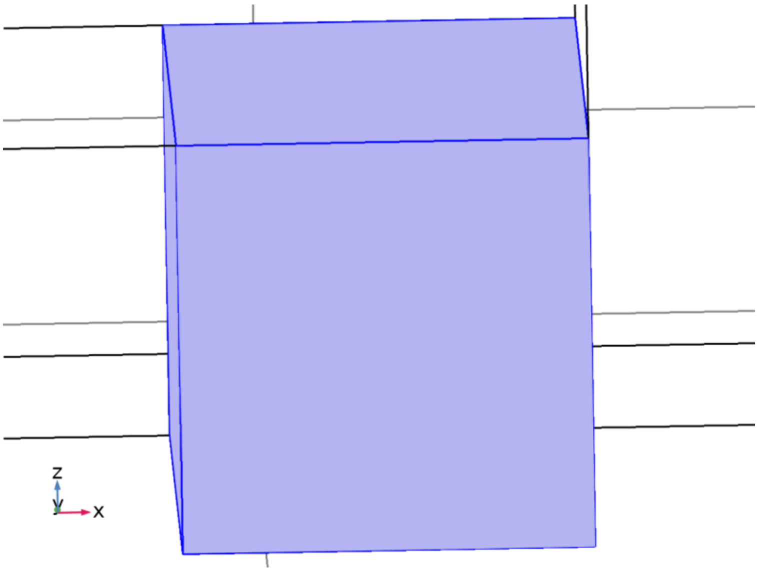

*Magnetic Flux Conservation 3*

SELECTION

| | |
|---|---|
| Geometric entity level | Domain |
| Selection | Geometry geom1: Dimension 3: Domain 5 |

EQUATIONS

$$\nabla\cdot\mathbf{B}=0,\quad \mathbf{B}=\mu_0(\mathbf{H}+\mathbf{M})$$
$$\mathbf{H}=-\nabla V_{\mathrm{m}}$$

#### Constitutive relation B-H

SETTINGS

| Description | Value |
|---|---|
| Magnetization model | Magnetization |
| Magnetization, x component | 0 |
| Magnetization, y component | 0 |
| Magnetization, z component | -835 [kA/m] |

#### Coordinate system selection

SETTINGS

| Description | Value |
|---|---|
| Coordinate system | Global coordinate system |

### Variables

| Name | Expression | Unit | Description | Selection | Details |
|---|---|---|---|---|---|
| mfnc.Qh | mfnc.Qrh | W/m³ | Volumetric loss density, electromagnetic | Domain 5 | |
| mfnc.Hx | -Vmx | A/m | Magnetic field, x component | Domain 5 | |
| mfnc.Hy | -Vmy | A/m | Magnetic field, y component | Domain 5 | |
| mfnc.Hz | -Vmz | A/m | Magnetic field, z component | Domain 5 | |
| mfnc.normH | sqrt(realdot(mfnc.Hx,mfnc.Hx)+realdot(mfnc.Hy,mfnc.Hy)+realdot(mfnc.Hz,mfnc.Hz)) | A/m | Magnetic field norm | Domain 5 | |
| mfnc.Bx | mu0_const*(mfnc.I_sxx*mfnc.Hx+mfnc.I_sxy*mfnc.Hy+mfnc.I_sxz*mfnc.Hz+mfnc.Mx) | T | Magnetic flux density, x component | Domain 5 | |
| mfnc.By | mu0_const*(mfnc.I_syx*mfnc.Hx+mfnc.I_syy*mfnc.Hy+mfnc.I_syz*mfnc.Hz+mfnc.My) | T | Magnetic flux density, y component | Domain 5 | |
| mfnc.Bz | mu0_const*(mfnc.I_szx*mfnc.Hx+mfnc.I_szy*mfnc.Hy+mfnc.I_szz*mfnc.Hz+mfnc.Mz) | T | Magnetic flux density, z component | Domain 5 | |
| mfnc.normB | sqrt(realdot(mfnc.Bx,mfnc.Bx)+realdot(mfnc.By,mfnc.By)+realdot(mfnc.Bz,mfnc.Bz)) | T | Magnetic flux density norm | Domain 5 | |
| mfnc.Mx | 0 | A/m | Magnetization, x component | Domain 5 | |
| mfnc.My | 0 | A/m | Magnetization, y component | Domain 5 | |
| mfnc.Mz | (-835)[kA/m] | A/m | Magnetization, z | Domain 5 | |

| Name | Expression | Unit | Description | Selection | Details |
|---|---|---|---|---|---|
| | | | component | | |
| mfnc.normM | sqrt(realdot(mfnc.Mx,mfnc.Mx)+realdot(mfnc.My,mfnc.My)+realdot(mfnc.Mz,mfnc.Mz)) | A/m | Magnetization norm | Domain 5 | |
| mfnc.W | mfnc.Wm | J/m³ | Energy density | Domain 5 | + operation |
| mfnc.dWm | mfnc.Wm | J/m³ | Integrand for total magnetic energy | Domain 5 | Meta |
| mfnc.Wm | 0.5*((mfnc.Bx-mu0_const*mfnc.Mx)*mfnc.Hx+(mfnc.By-mu0_const*mfnc.My)*mfnc.Hy+(mfnc.Bz-mu0_const*mfnc.Mz)*mfnc.Hz) | J/m³ | Magnetic energy density | Domain 5 | |
| mfnc.Wpm | mfnc.Bx*mfnc.Hx+mfnc.By*mfnc.Hy+mfnc.Bz*mfnc.Hz-mfnc.Wm | J/m³ | Magnetic coenergy density | Domain 5 | |
| mfnc.Qrh | 0 | W/m³ | Volumetric loss density, electric | Domain 5 | + operation |
| mfnc.mfc3.eBrx | 1/sqrt(1+eps) | 1 | Remanent flux direction, x component | Domain 5 | |
| mfnc.mfc3.eBry | 0 | 1 | Remanent flux direction, y component | Domain 5 | |
| mfnc.mfc3.eBrz | 0 | 1 | Remanent flux direction, z component | Domain 5 | |

### Shape functions

| Name | Shape function | Unit | Description | Shape frame | Selection |
|---|---|---|---|---|---|
| Vm | Lagrange (Quadratic) | A | Magnetic scalar potential | Spatial | Domain 5 |
| Vm | Lagrange (Quadratic) | A | Magnetic scalar potential | Material | Domain 5 |
| Vm | Lagrange (Quadratic) | A | Magnetic scalar potential | Geometry | Domain 5 |

| Name | Shape function | Unit | Description | Shape frame | Selection |
|---|---|---|---|---|---|
| Vm | Lagrange (Quadratic) | A | Magnetic scalar potential | Mesh | Domain 5 |

**Weak expressions**

| Weak expression | Integration order | Integration frame | Selection |
|---|---|---|---|
| mfnc.d*(-mfnc.Bx*test(Vmx)-mfnc.By*test(Vmy)-mfnc.Bz*test(Vmz)) | 4 | Spatial | Domain 5 |

### A.2.5 MESH 1

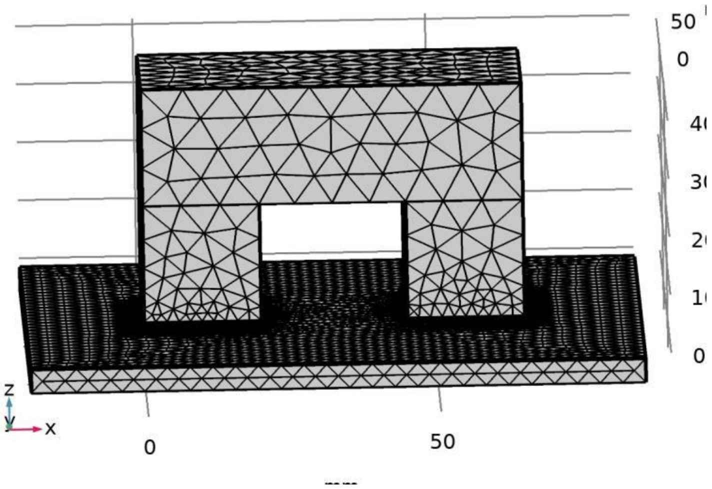

*Mesh 1*

### 2.5.1 Size (size)

SETTINGS

| Description | Value |
|---|---|
| Maximum element size | 7.2 |
| Minimum element size | 0.072 |
| Curvature factor | 0.2 |
| Maximum element growth rate | 1.3 |
| Predefined size | Extremely fine |

### 2.5.2 Free Tetrahedral 1 (ftet1)

SELECTION

| | |
|---|---|
| Geometric entity level | Remaining |

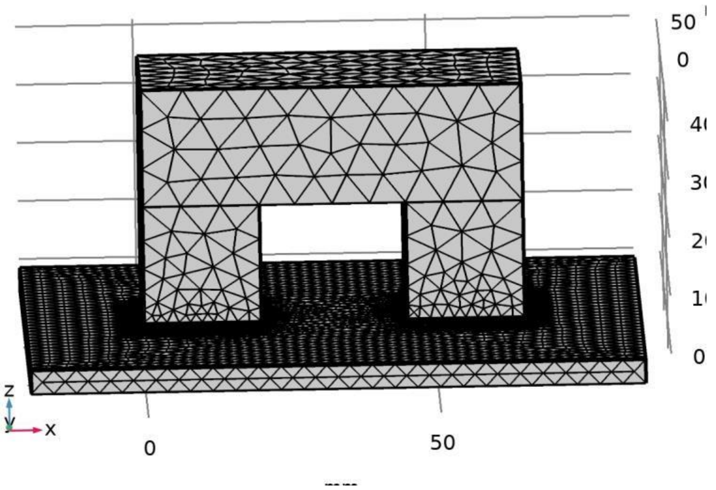

*Free Tetrahedral 1*

## A.3 Study 1

COMPUTATION INFORMATION

| | |
|---|---|
| Computation time | 5 min 4 s |
| CPU | Intel64 Family 6 Model 142 Stepping 9, 2 cores |
| Operating system | Windows 10 |

### A.3.1 PARAMETRIC SWEEP

| Parameter name | Parameter value list | Parameter unit |
|---|---|---|
| ML | 5 range(5,10,50) | mm |

STUDY SETTINGS

| Description | Value |
|---|---|
| Sweep type | Specified combinations |
| Parameter name | ML |
| Unit | mm |

PARAMETERS

| Parameter name | Parameter value list | Parameter unit |
|---|---|---|
| ML | 5 range(5,10,50) | mm |

### A.3.2 STATIONARY

STUDY SETTINGS

| Description | Value |
|---|---|
| Include geometric nonlinearity | Off |

PHYSICS AND VARIABLES SELECTION

| Physics interface | Discretization |
|---|---|
| Magnetic Fields, No Currents (mfnc) | physics |

MESH SELECTION

| Geometry | Mesh |
|---|---|
| Matlab Optimisation (geom1) | mesh1 |

### A.3.3 SOLVER CONFIGURATIONS

### 3.3.1 Solution 1

**Compile Equations: Stationary (st1)**

STUDY AND STEP

| Description | Value |
|---|---|
| Use study | Study 1 |
| Use study step | Stationary |

### Dependent Variables 1 (v1)

#### GENERAL

| Description | Value |
|---|---|
| Defined by study step | Stationary |

### Magnetic scalar potential (comp1.Vm) (comp1_Vm)

#### GENERAL

| Description | Value |
|---|---|
| Field components | comp1.Vm |

### Stationary Solver 1 (s1)

#### GENERAL

| Description | Value |
|---|---|
| Defined by study step | Stationary |

#### RESULTS WHILE SOLVING

| Description | Value |
|---|---|
| Probes | None |

### Fully Coupled 1 (fc1)

#### GENERAL

| Description | Value |
|---|---|
| Linear solver | Iterative 1 |

### Iterative 1 (i1)

#### GENERAL

| Description | Value |
|---|---|
| Solver | Conjugate gradients |

### Multigrid 1 (mg1)

#### GENERAL

| Description | Value |
|---|---|
| Solver | Algebraic multigrid |

### 3.3.2 Parametric Solutions 1

**PH=10 (su1)**

GENERAL

| Description | Value |
|---|---|
| Solution | PH=10 |

**PH=9 (su2)**

GENERAL

| Description | Value |
|---|---|
| Solution | PH=9 |

**PH=8 (su3)**

GENERAL

| Description | Value |
|---|---|
| Solution | PH=8 |

**PH=7 (su4)**

GENERAL

| Description | Value |
|---|---|
| Solution | PH=7 |

**PH=6 (su5)**

GENERAL

| Description | Value |
|---|---|
| Solution | PH=6 |

**PH=5 (su6)**

GENERAL

| Description | Value |
|---|---|
| Solution | PH=5 |

**PH=4 (su7)**

GENERAL

| Description | Value |
|---|---|
| Solution | PH=4 |

### 3.3.3 Parametric Solutions 2

#### ML=5 (su1)

GENERAL

| Description | Value |
|---|---|
| Solution | ML=5 |

#### ML=5 (2) (su2)

GENERAL

| Description | Value |
|---|---|
| Solution | ML=5 (2) |

#### ML=15 (su3)

GENERAL

| Description | Value |
|---|---|
| Solution | ML=15 |

#### ML=25 (su4)

GENERAL

| Description | Value |
|---|---|
| Solution | ML=25 |

#### ML=35 (su5)

GENERAL

| Description | Value |
|---|---|
| Solution | ML=35 |

#### ML=45 (su6)

GENERAL

| Description | Value |
|---|---|
| Solution | ML=45 |

# A.4 Results

## A.4.1 DATA SETS

### 4.1.1 Study 1/Solution 1

SOLUTION

| Description | Value |
|---|---|
| Solution | Solution 1 |
| Component | Save Point Geometry 1 |

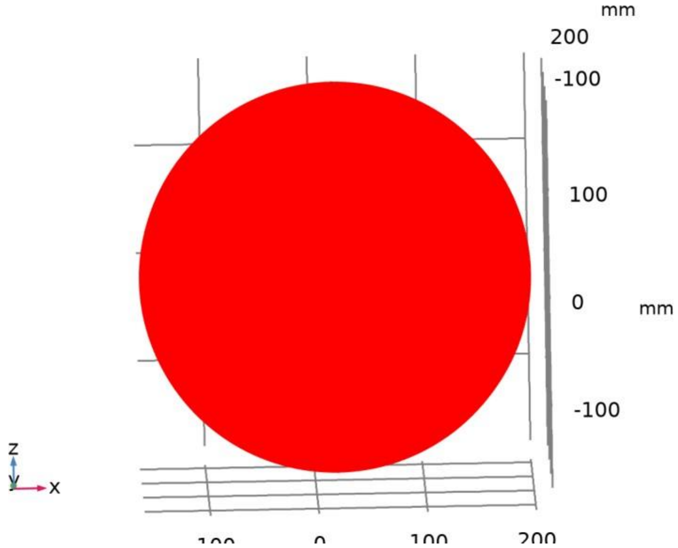

*Dataset: Study 1/Solution 1*

### 4.1.2 Flux

DATA

| Description | Value |
|---|---|
| Dataset | Study 1/Solution 1 |

LINE DATA

| Description | Value |
|---|---|
| Line entry method | Two points |
| Points | {{PW + (SD/2), ML/2, -LOff}, {PW + (SD/2), ML/2, -PH}} |

ADVANCED

| Description | Value |
|---|---|
| Space variable | cln1x |

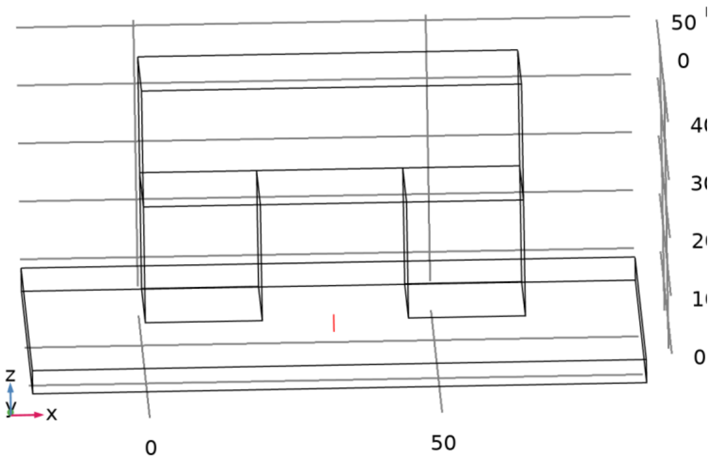

*Dataset: Flux*

### 4.1.3 Cut Point 3D 1

DATA

| Description | Value |
|---|---|
| Dataset | Study 1/Solution 1 |

POINT DATA

| Description | Value |
|---|---|
| Entry method | Coordinates |
| X | PW + (SD/2) |
| Y | ML/2 |
| Z | 1 |

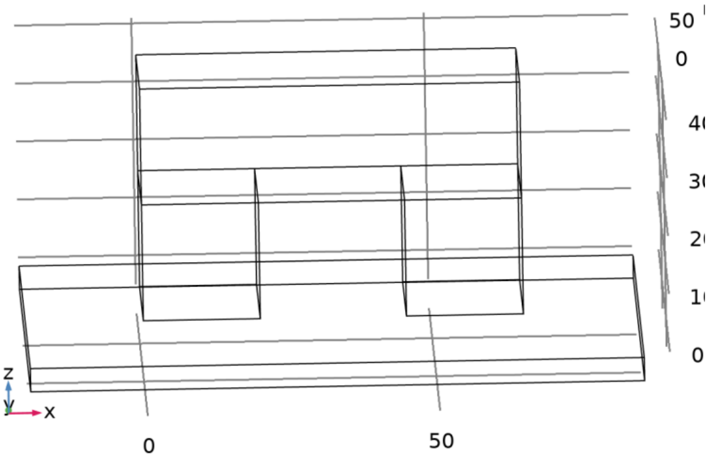

*Dataset: Cut Point 3D 1*

### 4.1.4 Study 1/Parametric Solutions 1

SOLUTION

| Description | Value |
|---|---|
| Solution | Parametric Solutions 1 |
| Component | Matlab Optimisation |

### 4.1.5 Study 1/Parametric Solutions 2

SOLUTION

| Description | Value |
|---|---|
| Solution | Parametric Solutions 2 |
| Component | Save Point Geometry 1 |

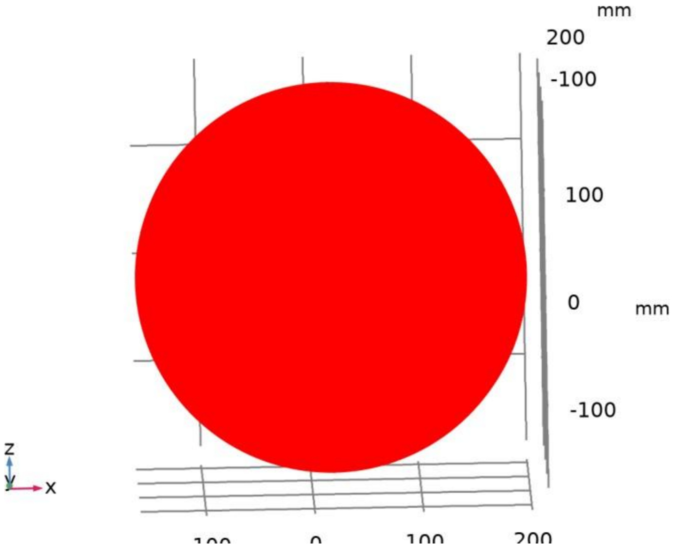

*Dataset: Study 1/Parametric Solutions 2*

## A.4.2 DERIVED VALUES

### 4.2.1 PSO

OUTPUT

| | |
|---|---|
| Evaluated in | Table 1 |

DATA

| Description | Value |
|---|---|
| Dataset | Cut Point 3D 1 |

EXPRESSIONS

| Expression | Unit | Description |
|---|---|---|
| mfnc.normB | T | Magnetic flux density norm |

## A.4.3 TABLES

### 4.3.1 Table 1

PSO

| Magnetic flux density norm (T), Point: (32.5, 20, 1) | Magnetic flux density norm (T), Point: (32.5, 20, 1) | Magnetic flux density norm (T), Point: (32.5, 20, 1) | Magnetic flux density norm (T), Point: (32.5, 20, 1) | Magnetic flux density norm (T), Point: (32.5, 20, 1) | Magnetic flux density norm (T), Point: (32.5, 20, 1) |
|---|---|---|---|---|---|
| 0.018762 | 0.019219 | 0.020463 | 0.022604 | 0.024964 | 0.028394 |

### 4.3.2 Evaluation 3D

Interactive 3D values

| x | y | z | Value |
|---|---|---|---|
| 63.331 | 186.19 | 48.410 | 3.1018 |
| 71.802 | -45.000 | -1.9690 | 0.18502 |

## A.4.4 PLOT GROUPS

### 4.4.1 Magnetic Flux Density Norm (mfnc)

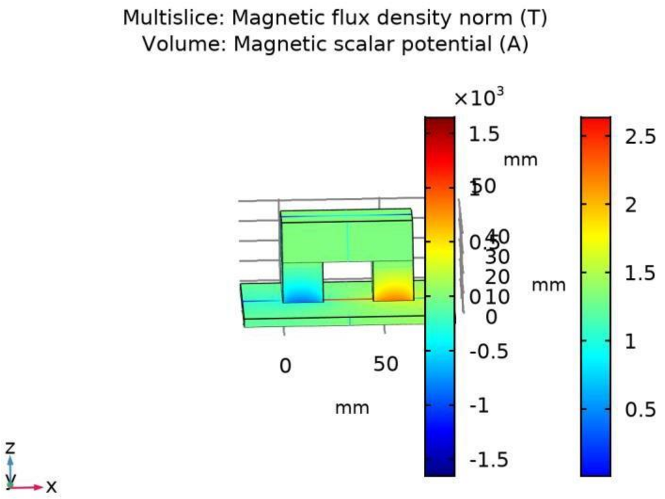

*Multislice: Magnetic flux density norm (T) Volume: Magnetic scalar potential (A)*

### 4.4.2 1D Plot Group 2

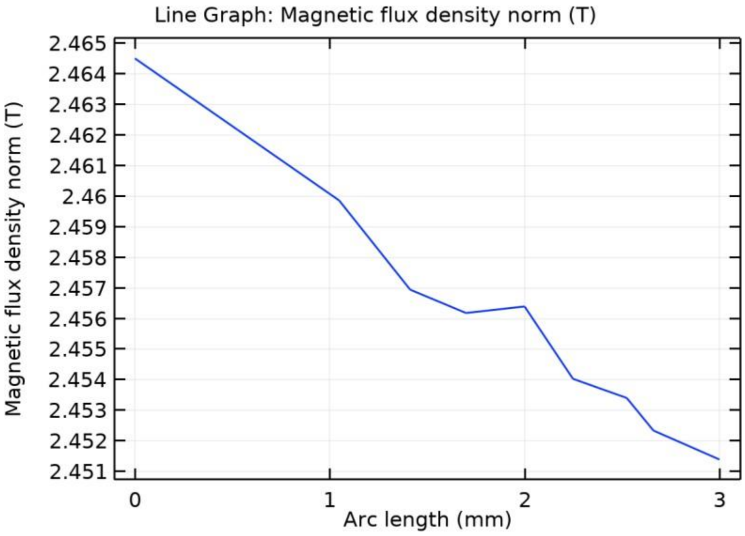

*Line Graph: Magnetic flux density norm (T)*

### 4.4.3 3D Plot Group 3

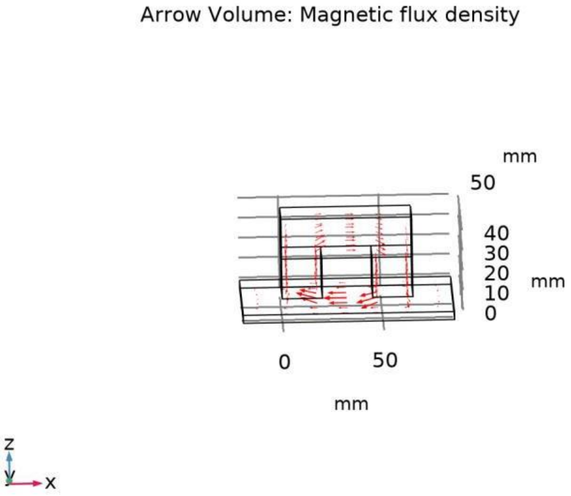

*Arrow Volume: Magnetic flux density*

### 4.4.4 3D Plot Group 7

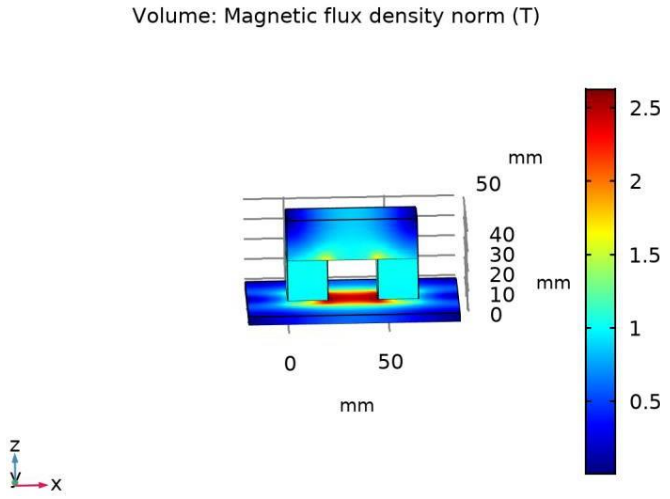

*Volume: Magnetic flux density norm (T)*

### 4.4.5 Magnetic Flux Density Norm (mfnc) 2

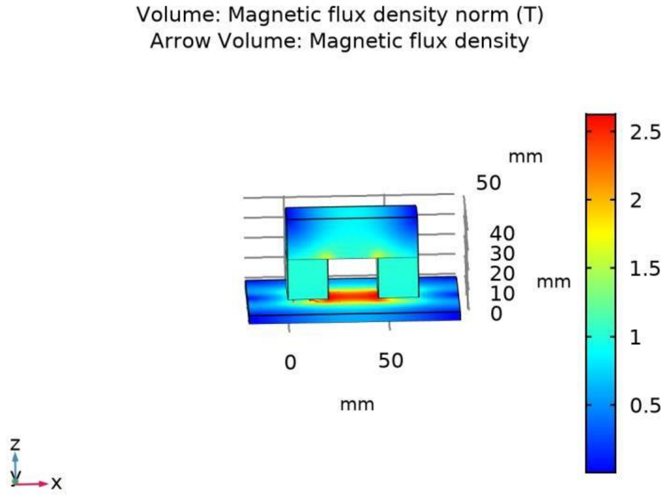

*Volume: Magnetic flux density norm (T) Arrow Volume: Magnetic flux density*

### 4.4.6 Magnetic Flux Density Norm (mfnc) 3

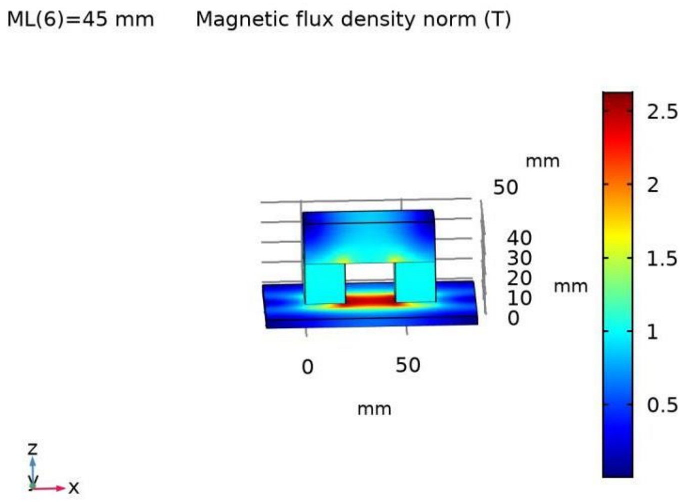

*Magnetic flux density norm (T)*

from https://www.zhaw.ch/en/lsfm/study/studiweb/master-ls/masters-thesis/

## Appendix B

# Arduino IDE code for ESP8266

```
#include "ThingSpeak.h"
//
#include <ESP8266WiFi.h>
// replace with your wifi ssid and wpa2 key
const char *ssid = "Galaxy S21 FE 5Gf8f8";
const char *pass = "wwyf1107";
WiFiClient client;
unsigned long myChannelNumber = 14741831;
const char * myWriteAPIKey = "9W7R18WSF31JGMM51";
/*
ad5933-test
Reads impedance values frothe AD5933 over I2C and
prints them serially.
*/
#include <Wire.h>
#include "AD5933.h"
#define START_FREQ (100000)
#define FREQ_INCR (1)
#define NUM_INCR (1)
#define REF_RESIST (20000)
const int analogInPin = A0;
int sensorValue = 0;
int imag1 = 0;
int impedance=0;
double gain[NUM_INCR + 1];
int phase[NUM_INCR + 1];
void setup(void)
{
// Begin I2C
Wire.begin();
// Begin serial at 9600 baud for output
Serial.begin(115200);
// Serial.setTimeout(2000);
WiFi.begin(ssid, pass);
while (WiFi.status() != WL_CONNECTED)
{
delay(500);
Serial.print("..");
}
Serial.println();
Serial.println("WiFi connected");
// dht.begin();
Wire.begin();
ThingSpeak.begin(client); // Initialize ThingSpeak
//Serial.println("AD5933 Test Started!");
// Perform initial configuration. Fail if any one of
these fail.
if (!(AD5933::reset() &&
AD5933::setInternalClock(true) &&
AD5933::setStartFrequency(START_FREQ) &&
AD5933::setIncrementFrequency(FREQ_INCR) &&
AD5933::setNumberIncrements(NUM_INCR) &&
AD5933::setPGAGain(PGA_GAIN_X1)))
{
Serial.println("FAILED in initialization!");
while (true) ;
}
// Perform calibration sweep
if (AD5933::calibrate(gain, phase, REF_RESIST,
NUM_INCR + 1))
Serial.println("Calibrated!");
```

```
else
Serial.println("Calibration failed...");
}
void loop(void)
{
frequencySweepRaw();
// Delay
delay(5000);
}
// Removes the frequencySweep abstraction from above.
This saves memory and
// allows for data to be processed in real time.
However, it's more complex.
void frequencySweepRaw() {
// Create variables to hold the impedance data and
track frequency
int real, imag, i = 0, cfreq = START_FREQ / 1000;
// Initialize the frequency sweep
if (!(AD5933::setPowerMode(POWER_STANDBY)
&& // place in standby
AD5933::setControlMode(CTRL_INIT_START_FREQ)
&& // init start freq
AD5933::setControlMode(CTRL_START_FREQ_SWEEP))) //
begin frequency sweep
{
Serial.println("Could not initialize frequency
sweep...");
}
// Perform the actual sweep
while ((AD5933::readStatusRegister() &
STATUS_SWEEP_DONE) != STATUS_SWEEP_DONE) {
// Get the frequency data for this frequency point
if (!AD5933::getComplexData(&real, &imag)) {
Serial.println("Could not get raw frequency
data...");
}
// Print out the frequency data
Serial.print(cfreq);
Serial.print(": R=");
Serial.print(real);
Serial.print("/I=");
Serial.print(imag);
// Compute impedance
double magnitude = sqrt(pow(real, 2) + pow(imag,
2));
double impedance = 1/(magnitude*gain[i]);
Serial.print(" |Z|=");
Serial.println(impedance);
// Increment the frequency
i++;
cfreq += FREQ_INCR / 1000;
AD5933::setControlMode(CTRL_INCREMENT_FREQ);
delay (3000);
sensorValue = analogRead(analogInPin);
Serial.println("sensor:" + (String) sensorValue);
delay (2000);
ThingSpeak.setField(1, String(imag));
ThingSpeak.setField(2, String(real));
ThingSpeak.setField(3, String(impedance));
ThingSpeak.setField(4, String(sensorValue));
int x = ThingSpeak.writeFields(myChannelNumber,
```

```
myWriteAPIKey);
if (x == 200) {
Serial.println("Channel update successful.");
}
else {
Serial.println("Problem updating channel. HTTP
error code " + String(x));
}
}
Serial.println("Frequency sweep complete!");
delay(5000);
// Set AD5933 power mode to standby when finished
if (!AD5933::setPowerMode(POWER_STANDBY))
Serial.println("Could not set to standby...");
delay(1000);
ESP.deepSleep(600e6);
}
```

## Appendix C

# PSO code

## PSO

```
clear all
close all
%% Problem
nVar = 1;                     % number of variables
VarMin = [10 10 10];              % lower bound of
variable
VarMax = [200 150 200];              % upper bound of
varible
%% PSO parameters
MaxIter= 50; % max number of iterations
nPop =12; % population size
wmax=0.9;
wmin=0.4; % inertia

d = 0.99; % damping ratio of the inertia
c1 = 2; % acceleration 1
c2 = 2; % acceleration 2
c3= c1+c2;
t=2/(abs(2-c3+sqrt(c3.^2-(4*c3))));
%% Initial
x0.position = [];
x0.velocity = [];
x0.fitness = [];
x0.best.position =[];
x0.best.fitness =[];
x = repmat(x0,nPop,1); % Make a population
global_best.fitness = inf;
%Velocity limits
VelMax=0.1*(VarMax-VarMin);
VelMin=-VelMax;

% Generate initial population
for i = 1: nPop
    % generate random solutions
     for k = 1:nVar
        x(i).position(k)  = unifrnd(VarMin (k),VarMax
(k));
%
%        plot(P); hold on

     end
```

```
    x(i).velocity = zeros([1 nVar]); % initial velocity
    x(i).fitness = Optimisation(x(i).position);
    x(i).best.position = x(i).position; % update the
local best
    x(i).best.fitness = x(i).fitness;   % update the
local best

        if x(i).best.fitness< global_best.fitness
            global_best=x(i).best;
        end
end


%
     B=zeros(MaxIter,1);
     C=zeros(MaxIter,nVar);
     for j=1:MaxIter
        for i=1:nPop
              w=wmax-(j/MaxIter).*(wmax-wmin);

            x(i).velocity=w*x(i).velocity+c1*rand([1
nVar]).*(x(i).best.position-x(i).position)...
                +c2*rand([1
nVar]).*(global_best.position-x(i).position);
          %+ c3*rand([1 nVar]).*(mean(x(i).position)-
x(i).position);
%
%            % Apply Velocity Limits
       x(i).velocity = max(x(i).velocity,VelMin);
        x(i).velocity = min(x(i).velocity,VelMax);

        % Update Position
        x(i).position = x(i).position + x(i).velocity;
%                      b = cat(1, x.position);
%
% a=b(:,1);
% c=b(:,2);
% d=b(:,3);
% figure(2)
%
% plot3(a,c,d,'X'); hold on
% grid on
%
%         % Velocity Mirror Effect
        IsOutside=(x(i).position<VarMin
|x(i).position>VarMax);
```

```
        x(i).velocity(IsOutside)=-
x(i).velocity(IsOutside);

        % Apply Position Limits
       x(i).position = max(x(i).position,VarMin);
       x(i).position = min(x(i).position,VarMax);



            x(i).fitness= ZCF(x(i).position);
%             e=cat(1, x.fitness);
% f=e(:,1);
%             figure(3)
%             plot3(c,a,f,'.');
%             set(gca, 'ZScale', 'log'); hold on; grid
on; drawnow
%


            if x(i).fitness< x(i).best.fitness
                x(i).best.position=x(i).position;
                x(i).best.fitness=x(i).fitness;
                if x(i).best.fitness< global_best.fitness
                    global_best=x(i).best;
                end

            end
        end



%         B(j)=global_best.fitness;
%         C(j,:)=global_best.position;
%         disp(['iteration' num2str(j) ':Best fitness='
num2str(B(j)) ':Optimal solution(L,W,H)='
num2str(C(j,:))]);
%        fprintf('%.4f', B(j))
%
       figure(1)
       plot(B(1:j,1));
        set(gca, 'YScale', 'log');drawnow
        title ('PSO Convergence Graph');
        xlabel('Iterations');
        ylabel('Objective function');

%%
       W=(C(1:j,1));
```

## Appendix D

# Coil model code

```
function z = Coil(x)
%
% Coil.m
% Model exported on Jun 6 2022, 13:06 by COMSOL 5.5.0.359.
Permeability=x(:,1);
PER=(Permeability);
import com.comsol.model.*
import com.comsol.model.util.*

model = ModelUtil.create('Model');

model.modelPath('C:\Users\wasifr\Documents\Comsol files');

model.label('Coil.mph');

model.param.set('t', '1 [s]');
model.param.set('f', '1 [Hz]');
model.param.set('m',PER);

model.component.create('comp1', true);

model.component('comp1').geom.create('geom1', 2);

model.result.table.create('tbl1', 'Table');
model.result.table.create('tbl2', 'Table');

model.component('comp1').func.create('an1', 'Analytic');
model.component('comp1').func('an1').set('expr',
'sin(2*pi*f*t)');
model.component('comp1').func('an1').set('args', {'t'});
model.component('comp1').func('an1').set('argunit', 's');
model.component('comp1').func('an1').set('fununit', 'V');
model.component('comp1').func('an1').set('plotargs', {'t'
'0' '1'});

model.component('comp1').geom('geom1').axisymmetric(true);

model.component('comp1').mesh.create('mesh1');

model.component('comp1').geom('geom1').lengthUnit('mm');
model.component('comp1').geom('geom1').create('r1',
'Rectangle');
model.component('comp1').geom('geom1').feature('r1').label(
'Air core');
```

```
model.component('comp1').geom('geom1').feature('r1').set('size', [3 18]);
model.component('comp1').geom('geom1').create('r2', 'Rectangle');
model.component('comp1').geom('geom1').feature('r2').label('Coil');
model.component('comp1').geom('geom1').feature('r2').set('pos', [3 0]);
model.component('comp1').geom('geom1').feature('r2').set('size', [5 18]);
model.component('comp1').geom('geom1').create('r3', 'Rectangle');
model.component('comp1').geom('geom1').feature('r3').label('Plate');
model.component('comp1').geom('geom1').feature('r3').set('pos', [0 -5]);
model.component('comp1').geom('geom1').feature('r3').set('size', [30 4]);
model.component('comp1').geom('geom1').create('c1', 'Circle');
model.component('comp1').geom('geom1').feature('c1').label('Air');
model.component('comp1').geom('geom1').feature('c1').set('rot', -90);
model.component('comp1').geom('geom1').feature('c1').set('r', 30);
model.component('comp1').geom('geom1').feature('c1').set('angle', 180);
model.component('comp1').geom('geom1').run;
model.component('comp1').geom('geom1').run('fin');

model.view.create('view2', 3);

model.component('comp1').material.create('mat1',  'Common');
model.component('comp1').material.create('mat2',  'Common');
model.component('comp1').material.create('mat3',  'Common');
model.component('comp1').material('mat1').selection.set([4]);
model.component('comp1').material('mat1').propertyGroup.create('Enu', 'Young''s modulus and Poisson''s ratio');
model.component('comp1').material('mat1').propertyGroup.create('linzRes', 'Linearized resistivity');
model.component('comp1').material('mat2').selection.set([1 3]);
```

```
model.component('comp1').material('mat2').propertyGroup('def').func.create('eta', 'Piecewise');
model.component('comp1').material('mat2').propertyGroup('def').func.create('Cp', 'Piecewise');
model.component('comp1').material('mat2').propertyGroup('def').func.create('rho', 'Analytic');
model.component('comp1').material('mat2').propertyGroup('def').func.create('k', 'Piecewise');
model.component('comp1').material('mat2').propertyGroup('def').func.create('cs', 'Analytic');
model.component('comp1').material('mat2').propertyGroup('def').func.create('an1', 'Analytic');
model.component('comp1').material('mat2').propertyGroup('def').func.create('an2', 'Analytic');
model.component('comp1').material('mat2').propertyGroup.create('RefractiveIndex', 'Refractive index');
model.component('comp1').material('mat2').propertyGroup.create('NonlinearModel', 'Nonlinear model');
model.component('comp1').material('mat3').selection.set([2]);
model.component('comp1').material('mat3').propertyGroup.create('BHCurve', 'B-H Curve');
model.component('comp1').material('mat3').propertyGroup('BHCurve').func.create('BH', 'Interpolation');

model.component('comp1').physics.create('mf', 'InductionCurrents', 'geom1');
model.component('comp1').physics('mf').create('coil1', 'Coil', 2);
model.component('comp1').physics('mf').feature('coil1').selection.set([4]);

model.component('comp1').mesh('mesh1').create('ftri1', 'FreeTri');

model.result.table('tbl1').comments('Global Evaluation 1');
model.result.table('tbl2').comments('Point Evaluation 1');

model.component('comp1').view('view1').axis.set('xmin', -64.556884765625);
model.component('comp1').view('view1').axis.set('xmax', 87.77389526367188);
model.component('comp1').view('view1').axis.set('ymin', -54.62464904785156);
```

```
model.component('comp1').view('view1').axis.set('ymax',
42.49330139160156);

model.component('comp1').material('mat1').label('Copper');
model.component('comp1').material('mat1').set('family',
'copper');
model.component('comp1').material('mat1').propertyGroup('de
f').set('relpermeability', {'1' '0' '0' '0' '1' '0' '0' '0'
'1'});
model.component('comp1').material('mat1').propertyGroup('de
f').descr('relpermeability_symmetry', '');
model.component('comp1').material('mat1').propertyGroup('de
f').set('electricconductivity', {'5.998e7[S/m]' '0' '0' '0'
'5.998e7[S/m]' '0' '0' '0' '5.998e7[S/m]'});
model.component('comp1').material('mat1').propertyGroup('de
f').descr('electricconductivity_symmetry', '');
model.component('comp1').material('mat1').propertyGroup('de
f').set('heatcapacity', '385[J/(kg*K)]');
model.component('comp1').material('mat1').propertyGroup('de
f').descr('heatcapacity_symmetry', '');
model.component('comp1').material('mat1').propertyGroup('de
f').set('relpermittivity', {'1' '0' '0' '0' '1' '0' '0' '0'
'1'});
model.component('comp1').material('mat1').propertyGroup('de
f').descr('relpermittivity_symmetry', '');
model.component('comp1').material('mat1').propertyGroup('de
f').set('emissivity', '0.5');
model.component('comp1').material('mat1').propertyGroup('de
f').descr('emissivity_symmetry', '');
model.component('comp1').material('mat1').propertyGroup('de
f').set('density', '8940[kg/m^3]');
model.component('comp1').material('mat1').propertyGroup('de
f').descr('density_symmetry', '');
model.component('comp1').material('mat1').propertyGroup('de
f').set('thermalconductivity', {'400[W/(m*K)]' '0' '0' '0'
'400[W/(m*K)]' '0' '0' '0' '400[W/(m*K)]'});
model.component('comp1').material('mat1').propertyGroup('de
f').descr('thermalconductivity_symmetry', '');
model.component('comp1').material('mat1').propertyGroup('En
u').set('youngsmodulus', '126e9[Pa]');
model.component('comp1').material('mat1').propertyGroup('En
u').descr('youngsmodulus_symmetry', '');
model.component('comp1').material('mat1').propertyGroup('En
u').set('poissonsratio', '0.34');
```

```
model.component('comp1').material('mat1').propertyGroup('En
u').descr('poissonsratio_symmetry', '');
model.component('comp1').material('mat1').propertyGroup('li
nzRes').set('rho0', '');
model.component('comp1').material('mat1').propertyGroup('li
nzRes').set('alpha', '');
model.component('comp1').material('mat1').propertyGroup('li
nzRes').set('Tref', '');
model.component('comp1').material('mat1').propertyGroup('li
nzRes').set('rho0', '');
model.component('comp1').material('mat1').propertyGroup('li
nzRes').set('alpha', '');
model.component('comp1').material('mat1').propertyGroup('li
nzRes').set('Tref', '');
model.component('comp1').material('mat1').propertyGroup('li
nzRes').set('rho0', '');
model.component('comp1').material('mat1').propertyGroup('li
nzRes').set('alpha', '');
model.component('comp1').material('mat1').propertyGroup('li
nzRes').set('Tref', '');
model.component('comp1').material('mat1').propertyGroup('li
nzRes').set('rho0', '1.667e-8[ohm*m]');
model.component('comp1').material('mat1').propertyGroup('li
nzRes').set('alpha', '3.862e-3[1/K]');
model.component('comp1').material('mat1').propertyGroup('li
nzRes').set('Tref', '293.15[K]');
model.component('comp1').material('mat1').propertyGroup('li
nzRes').descr('rho0_symmetry', '');
model.component('comp1').material('mat1').propertyGroup('li
nzRes').descr('alpha_symmetry', '');
model.component('comp1').material('mat1').propertyGroup('li
nzRes').descr('Tref_symmetry', '');
model.component('comp1').material('mat1').propertyGroup('li
nzRes').addInput('temperature');
model.component('comp1').material('mat2').label('Air');
model.component('comp1').material('mat2').set('family',
'air');
model.component('comp1').material('mat2').propertyGroup('de
f').func('eta').set('arg', 'T');
model.component('comp1').material('mat2').propertyGroup('de
f').func('eta').set('pieces', {'200.0' '1600.0' '-8.38278E-
7+8.35717342E-8*T^1-7.69429583E-11*T^2+4.6437266E-14*T^3-
1.06585607E-17*T^4'});
```

```
model.component('comp1').material('mat2').propertyGroup('def').func('eta').set('argunit', 'K');
model.component('comp1').material('mat2').propertyGroup('def').func('eta').set('fununit', 'Pa*s');
model.component('comp1').material('mat2').propertyGroup('def').func('Cp').set('arg', 'T');
model.component('comp1').material('mat2').propertyGroup('def').func('Cp').set('pieces', {'200.0' '1600.0' '1047.63657-0.372589265*T^1+9.45304214E-4*T^2-6.02409443E-7*T^3+1.2858961E-10*T^4'});
model.component('comp1').material('mat2').propertyGroup('def').func('Cp').set('argunit', 'K');
model.component('comp1').material('mat2').propertyGroup('def').func('Cp').set('fununit', 'J/(kg*K)');
model.component('comp1').material('mat2').propertyGroup('def').func('rho').set('expr', 'pA*0.02897/R_const[K*mol/J]/T');
model.component('comp1').material('mat2').propertyGroup('def').func('rho').set('args', {'pA' 'T'});
model.component('comp1').material('mat2').propertyGroup('def').func('rho').set('dermethod', 'manual');
model.component('comp1').material('mat2').propertyGroup('def').func('rho').set('argders', {'pA' 'd(pA*0.02897/R_const/T,pA)'; 'T' 'd(pA*0.02897/R_const/T,T)'});
model.component('comp1').material('mat2').propertyGroup('def').func('rho').set('argunit', 'Pa,K');
model.component('comp1').material('mat2').propertyGroup('def').func('rho').set('fununit', 'kg/m^3');
model.component('comp1').material('mat2').propertyGroup('def').func('rho').set('plotargs', {'pA' '0' '1'; 'T' '0' '1'});
model.component('comp1').material('mat2').propertyGroup('def').func('k').set('arg', 'T');
model.component('comp1').material('mat2').propertyGroup('def').func('k').set('pieces', {'200.0' '1600.0' '-0.00227583562+1.15480022E-4*T^1-7.90252856E-8*T^2+4.11702505E-11*T^3-7.43864331E-15*T^4'});
model.component('comp1').material('mat2').propertyGroup('def').func('k').set('argunit', 'K');
model.component('comp1').material('mat2').propertyGroup('def').func('k').set('fununit', 'W/(m*K)');
```

```
model.component('comp1').material('mat2').propertyGroup('de
f').func('cs').set('expr',
'sqrt(1.4*R_const[K*mol/J]/0.02897*T)');
model.component('comp1').material('mat2').propertyGroup('de
f').func('cs').set('args', {'T'});
model.component('comp1').material('mat2').propertyGroup('de
f').func('cs').set('dermethod', 'manual');
model.component('comp1').material('mat2').propertyGroup('de
f').func('cs').set('argunit', 'K');
model.component('comp1').material('mat2').propertyGroup('de
f').func('cs').set('fununit', 'm/s');
model.component('comp1').material('mat2').propertyGroup('de
f').func('cs').set('plotargs', {'T' '273.15' '373.15'});
model.component('comp1').material('mat2').propertyGroup('de
f').func('an1').set('funcname', 'alpha_p');
model.component('comp1').material('mat2').propertyGroup('de
f').func('an1').set('expr', '-1/rho(pA,T)*d(rho(pA,T),T)');
model.component('comp1').material('mat2').propertyGroup('de
f').func('an1').set('args', {'pA' 'T'});
model.component('comp1').material('mat2').propertyGroup('de
f').func('an1').set('argunit', 'Pa,K');
model.component('comp1').material('mat2').propertyGroup('de
f').func('an1').set('fununit', '1/K');
model.component('comp1').material('mat2').propertyGroup('de
f').func('an1').set('plotargs', {'pA' '101325' '101325';
'T' '273.15' '373.15'});
model.component('comp1').material('mat2').propertyGroup('de
f').func('an2').set('funcname', 'muB');
model.component('comp1').material('mat2').propertyGroup('de
f').func('an2').set('expr', '0.6*eta(T)');
model.component('comp1').material('mat2').propertyGroup('de
f').func('an2').set('args', {'T'});
model.component('comp1').material('mat2').propertyGroup('de
f').func('an2').set('argunit', 'K');
model.component('comp1').material('mat2').propertyGroup('de
f').func('an2').set('fununit', 'Pa*s');
model.component('comp1').material('mat2').propertyGroup('de
f').func('an2').set('plotargs', {'T' '200' '1600'});
model.component('comp1').material('mat2').propertyGroup('de
f').set('thermalexpansioncoefficient', '');
model.component('comp1').material('mat2').propertyGroup('de
f').set('molarmass', '');
model.component('comp1').material('mat2').propertyGroup('de
f').set('bulkviscosity', '');
```

```
model.component('comp1').material('mat2').propertyGroup('de
f').set('thermalexpansioncoefficient', {'alpha_p(pA,T)' '0'
'0' '0' 'alpha_p(pA,T)' '0' '0' '0' 'alpha_p(pA,T)'});
model.component('comp1').material('mat2').propertyGroup('de
f').set('molarmass', '0.02897[kg/mol]');
model.component('comp1').material('mat2').propertyGroup('de
f').set('bulkviscosity', 'muB(T)');
model.component('comp1').material('mat2').propertyGroup('de
f').descr('thermalexpansioncoefficient_symmetry', '');
model.component('comp1').material('mat2').propertyGroup('de
f').descr('molarmass_symmetry', '');
model.component('comp1').material('mat2').propertyGroup('de
f').descr('bulkviscosity_symmetry', '');
model.component('comp1').material('mat2').propertyGroup('de
f').set('relpermeability', {'1' '0' '0' '0' '1' '0' '0' '0'
'1'});
model.component('comp1').material('mat2').propertyGroup('de
f').descr('relpermeability_symmetry', '');
model.component('comp1').material('mat2').propertyGroup('de
f').set('relpermittivity', {'1' '0' '0' '0' '1' '0' '0' '0'
'1'});
model.component('comp1').material('mat2').propertyGroup('de
f').descr('relpermittivity_symmetry', '');
model.component('comp1').material('mat2').propertyGroup('de
f').set('dynamicviscosity', 'eta(T)');
model.component('comp1').material('mat2').propertyGroup('de
f').descr('dynamicviscosity_symmetry', '');
model.component('comp1').material('mat2').propertyGroup('de
f').set('ratioofspecificheat', '1.4');
model.component('comp1').material('mat2').propertyGroup('de
f').descr('ratioofspecificheat_symmetry', '');
model.component('comp1').material('mat2').propertyGroup('de
f').set('electricconductivity', {'0[S/m]' '0' '0' '0'
'0[S/m]' '0' '0' '0' '0[S/m]'});
model.component('comp1').material('mat2').propertyGroup('de
f').descr('electricconductivity_symmetry', '');
model.component('comp1').material('mat2').propertyGroup('de
f').set('heatcapacity', 'Cp(T)');
model.component('comp1').material('mat2').propertyGroup('de
f').descr('heatcapacity_symmetry', '');
model.component('comp1').material('mat2').propertyGroup('de
f').set('density', 'rho(pA,T)');
model.component('comp1').material('mat2').propertyGroup('de
f').descr('density_symmetry', '');
```

```
model.component('comp1').material('mat2').propertyGroup('def').set('thermalconductivity', {'k(T)' '0' '0' '0' 'k(T)' '0' '0' '0' 'k(T)'});
model.component('comp1').material('mat2').propertyGroup('def').descr('thermalconductivity_symmetry', '');
model.component('comp1').material('mat2').propertyGroup('def').set('soundspeed', 'cs(T)');
model.component('comp1').material('mat2').propertyGroup('def').descr('soundspeed_symmetry', '');
model.component('comp1').material('mat2').propertyGroup('def').addInput('temperature');
model.component('comp1').material('mat2').propertyGroup('def').addInput('pressure');
model.component('comp1').material('mat2').propertyGroup('RefractiveIndex').set('n', '');
model.component('comp1').material('mat2').propertyGroup('RefractiveIndex').set('ki', '');
model.component('comp1').material('mat2').propertyGroup('RefractiveIndex').set('n', '');
model.component('comp1').material('mat2').propertyGroup('RefractiveIndex').set('ki', '');
model.component('comp1').material('mat2').propertyGroup('RefractiveIndex').set('n', '');
model.component('comp1').material('mat2').propertyGroup('RefractiveIndex').set('ki', '');
model.component('comp1').material('mat2').propertyGroup('RefractiveIndex').set('n', {'1' '0' '0' '0' '1' '0' '0' '0' '1'});
model.component('comp1').material('mat2').propertyGroup('RefractiveIndex').set('ki', {'0' '0' '0' '0' '0' '0' '0' '0' '0'});
model.component('comp1').material('mat2').propertyGroup('RefractiveIndex').descr('n_symmetry', '');
model.component('comp1').material('mat2').propertyGroup('RefractiveIndex').descr('ki_symmetry', '');
model.component('comp1').material('mat2').propertyGroup('NonlinearModel').set('BA', '(def.gamma+1)/2');
model.component('comp1').material('mat2').propertyGroup('NonlinearModel').descr('BA_symmetry', '');
model.component('comp1').material('mat3').label('Low Carbon Steel 1002');
model.component('comp1').material('mat3').propertyGroup('def').set('electricconductivity', {'8.41[MS/m]' '0' '0' '0' '8.41[MS/m]' '0' '0' '0' '8.41[MS/m]'});
```

```
model.component('comp1').material('mat3').propertyGroup('de
f').descr('electricconductivity_symmetry', '');
model.component('comp1').material('mat3').propertyGroup('de
f').set('relpermittivity', {'1[1]' '0' '0' '0' '1[1]' '0'
'0' '0' '1[1]'});
model.component('comp1').material('mat3').propertyGroup('de
f').descr('relpermittivity_symmetry', '');
model.component('comp1').material('mat3').propertyGroup('de
f').set('relpermeability', {'m' '0' '0' '0' 'm' '0' '0' '0'
'm'});
model.component('comp1').material('mat3').propertyGroup('de
f').set('relpermeability_symmetry', '0');
model.component('comp1').material('mat3').propertyGroup('BH
Curve').label('B-H Curve');
model.component('comp1').material('mat3').propertyGroup('BH
Curve').func('BH').label('Interpolation 1');
model.component('comp1').material('mat3').propertyGroup('BH
Curve').func('BH').set('table', {'0' '0';  ...
'13.2474828317901' '0.0250771604938272';  ...
'26.402862654321' '0.0506172839506173';  ...
'39.3740364583333' '0.0770833333333333';  ...
'52.0689012345679' '0.104938271604938';  ...
'64.3953539737654' '0.134645061728395';  ...
'76.2612916666667' '0.166666666666667';  ...
'87.5746113040123' '0.201427469135802';  ...
'98.2432098765432' '0.239197530864198';  ...
'108.174984375' '0.280208333333333';  ...
'117.277831790123' '0.324691358024691';  ...
'125.459649112654' '0.372878086419753';  ...
'132.628333333333' '0.425';  ...
'138.78388445216' '0.481134259259259';  ...
'144.294714506173' '0.540740740740741';  ...
'149.621338541667' '0.603125';  ...
'155.224271604938' '0.667592592592592';  ...
'161.564028742284' '0.733449074074074';  ...
'169.101125' '0.8';  ...
'178.179411612654' '0.866512345679012';  ...
'188.676084567901' '0.932098765432098';  ...
'200.351676041667' '0.995833333333333';  ...
'212.966718209876' '1.05679012345679';  ...
'226.281743248457' '1.11404320987654';  ...
'240.057283333333' '1.16666666666667';  ...
'254.247286959876' '1.21404320987654';  ...
'269.579367901234' '1.25679012345679';  ...
```

```
'286.97455625' '1.29583333333333';  ...
'307.353882098765' '1.3320987654321';  ...
'331.638375540123' '1.36651234567901';  ...
'360.749066666667' '1.4';  ...
'395.938556404321' '1.43333333333333';  ...
'439.785729012346' '1.46666666666667';  ...
'495.201039583334' '1.5';  ...
'565.094943209877' '1.53333333333333';  ...
'652.377894984569' '1.56666666666667';  ...
'759.960350000001' '1.6';  ...
'893.540414429014' '1.63333333333333';  ...
'1069.96679876544' '1.66666666666667';  ...
'1308.87586458334' '1.7';  ...
'1629.9039734568' '1.73333333333333';  ...
'2052.68748695989' '1.76666666666667';  ...
'2596.86276666668' '1.8';  ...
'3270.70066280866' '1.83317978394605';  ...
'4037.00998024693' '1.86543827156836';  ...
'4847.23401250002' '1.89585416654322';  ...
'5652.81605308644' '1.92350617254688';  ...
'6405.19939552471' '1.94747299325563';  ...
'7055.82733333335' '1.96683333234573';  ...
'7579.46364197532' '1.98098688107462';  ...
'8044.15402469137' '1.99061728102439';  ...
'8541.26466666668' '1.9967291613583';  ...
'9162.16175308643' '2.00032715123962';  ...
'9998.21146913582' '2.00241587983161';  ...
'11140.78' '2.00399997629753';  ...
'12654.9534722222' '2.00590274280017';  ...
'14500.6977777778' '2.00822217350047';  ...
'16611.69875' '2.01087493555891';  ...
'18921.6422222222' '2.01377769613593';  ...
'21364.2140277778' '2.01684712239202';  ...
'23873.1' '2.01999988148764'});
model.component('comp1').material('mat3').propertyGroup('BH
Curve').func('BH').set('extrap', 'linear');
model.component('comp1').material('mat3').propertyGroup('BH
Curve').func('BH').set('argunit', 'A/m');
model.component('comp1').material('mat3').propertyGroup('BH
Curve').func('BH').set('fununit', 'T');
model.component('comp1').material('mat3').propertyGroup('BH
Curve').func('BH').set('defineinv', true);
model.component('comp1').material('mat3').propertyGroup('BH
Curve').func('BH').set('defineprimfun', true);
```

```
model.component('comp1').material('mat3').propertyGroup('BH
Curve').set('normB', '');
model.component('comp1').material('mat3').propertyGroup('BH
Curve').set('normH', '');
model.component('comp1').material('mat3').propertyGroup('BH
Curve').set('Wpm', '');
model.component('comp1').material('mat3').propertyGroup('BH
Curve').set('normB', '');
model.component('comp1').material('mat3').propertyGroup('BH
Curve').set('normH', '');
model.component('comp1').material('mat3').propertyGroup('BH
Curve').set('Wpm', '');
model.component('comp1').material('mat3').propertyGroup('BH
Curve').set('normB', '');
model.component('comp1').material('mat3').propertyGroup('BH
Curve').set('normH', '');
model.component('comp1').material('mat3').propertyGroup('BH
Curve').set('Wpm', '');
model.component('comp1').material('mat3').propertyGroup('BH
Curve').set('normB', 'BH(normHin)');
model.component('comp1').material('mat3').propertyGroup('BH
Curve').set('normH', 'BH_inv(normBin)');
model.component('comp1').material('mat3').propertyGroup('BH
Curve').set('Wpm', 'BH_prim(normHin)');
model.component('comp1').material('mat3').propertyGroup('BH
Curve').descr('normB_symmetry', '');
model.component('comp1').material('mat3').propertyGroup('BH
Curve').descr('normH_symmetry', '');
model.component('comp1').material('mat3').propertyGroup('BH
Curve').descr('Wpm_symmetry', '');
model.component('comp1').material('mat3').propertyGroup('BH
Curve').descr('normHin', 'Magnetic field norm');
model.component('comp1').material('mat3').propertyGroup('BH
Curve').descr('normHin_symmetry', '0');
model.component('comp1').material('mat3').propertyGroup('BH
Curve').descr('normBin', 'Magnetic flux density norm');
model.component('comp1').material('mat3').propertyGroup('BH
Curve').descr('normBin_symmetry', '0');
model.component('comp1').material('mat3').propertyGroup('BH
Curve').addInput('magneticfield');
model.component('comp1').material('mat3').propertyGroup('BH
Curve').addInput('magneticfluxdensity');
```

```
model.component('comp1').physics('mf').feature('coil1').set
('ConductorModel', 'Multi');
model.component('comp1').physics('mf').feature('coil1').set
('CoilExcitation', 'Voltage');
model.component('comp1').physics('mf').feature('coil1').set
('VCoil', 'an1(t)*1.98');
model.component('comp1').physics('mf').feature('coil1').set
('N', 350);

model.component('comp1').mesh('mesh1').feature('size').set(
'hauto', 1);
model.component('comp1').mesh('mesh1').feature('size').set(
'custom', 'on');
model.component('comp1').mesh('mesh1').feature('size').set(
'hmax', 0.6);
model.component('comp1').mesh('mesh1').feature('size').set(
'hnarrow', 20);
model.component('comp1').mesh('mesh1').run;

model.study.create('std1');
model.study('std1').create('param', 'Parametric');
model.study('std1').create('freq', 'Frequency');

model.sol.create('sol1');
model.sol('sol1').study('std1');
model.sol('sol1').attach('std1');
model.sol('sol1').create('st1', 'StudyStep');
model.sol('sol1').create('v1', 'Variables');
model.sol('sol1').create('s1', 'Stationary');
model.sol('sol1').feature('s1').create('p1', 'Parametric');
model.sol('sol1').feature('s1').create('fc1',
'FullyCoupled');
model.sol('sol1').feature('s1').feature.remove('fcDef');
model.sol.create('sol2');
model.sol('sol2').study('std1');
model.sol('sol2').label('Parametric Solutions 1');

model.batch.create('p1', 'Parametric');
model.batch('p1').create('so1', 'Solutionseq');
model.batch('p1').study('std1');

model.result.dataset.create('rev1', 'Revolve2D');
model.result.dataset.create('rev2', 'Revolve2D');
model.result.dataset.create('cpt1', 'CutPoint3D');
```

```
model.result.dataset('rev2').set('data', 'dset2');
model.result.numerical.create('gev1', 'EvalGlobal');
model.result.numerical.create('pev1', 'EvalPoint');
model.result.numerical('gev1').set('data', 'dset2');
model.result.numerical('gev1').set('probetag', 'none');
model.result.numerical('pev1').set('probetag', 'none');
model.result.create('pg5', 'PlotGroup1D');
model.result.create('pg1', 'PlotGroup2D');
model.result.create('pg2', 'PlotGroup3D');
model.result.create('pg3', 'PlotGroup2D');
model.result.create('pg4', 'PlotGroup3D');
model.result('pg5').create('ptgr1', 'PointGraph');
model.result('pg5').feature('ptgr1').set('data', 'dset2');
model.result('pg5').feature('ptgr1').selection.set([9]);
model.result('pg5').feature('ptgr1').set('expr',
'mf.XCoil_1');
model.result('pg1').create('surf1', 'Surface');
model.result('pg1').create('con1', 'Contour');
model.result('pg1').feature('con1').set('expr',
'mf.Aphi*r');
model.result('pg2').create('surf1', 'Surface');
model.result('pg2').create('con1', 'Contour');
model.result('pg2').feature('con1').set('expr',
'mf.Aphi*r');
model.result('pg3').set('data', 'dset2');
model.result('pg3').create('surf1', 'Surface');
model.result('pg3').create('con1', 'Contour');
model.result('pg3').feature('con1').set('expr',
'mf.Aphi*r');
model.result('pg4').create('surf1', 'Surface');
model.result('pg4').create('con1', 'Contour');
model.result('pg4').feature('con1').set('expr',
'mf.Aphi*r');

model.study('std1').feature('param').set('pname', {'f'});
model.study('std1').feature('param').set('plistarr', {'10
20 30 40 50 60 70 80 90 100'});
    % 110 120 130 140 150 160 170 180 190 200 210 220 230
240 250 260 270 280 290 300'});
model.study('std1').feature('param').set('punit', {'kHz'});
model.study('std1').feature('freq').set('punit', 'kHz');
model.study('std1').feature('freq').set('plist', 'f');

model.sol('sol1').attach('std1');
```

```
model.sol('sol1').feature('v1').set('clistctrl', {'p1'});
model.sol('sol1').feature('v1').set('cname', {'freq'});
model.sol('sol1').feature('v1').set('clist', {'f'});
model.sol('sol1').feature('s1').set('probesel', 'none');
model.sol('sol1').feature('s1').feature('p1').set('pname',
{'freq'});
model.sol('sol1').feature('s1').feature('p1').set('plistarr
', {'f'});
model.sol('sol1').feature('s1').feature('p1').set('punit',
{'kHz'});
model.sol('sol1').feature('s1').feature('p1').set('pcontinu
ationmode', 'no');
model.sol('sol1').feature('s1').feature('p1').set('preuseso
l', 'auto');
model.sol('sol1').runAll;

model.batch('p1').set('control', 'param');
model.batch('p1').set('pname', {'f'});
model.batch('p1').set('plistarr', {'10 20 30 40 50 60 70 80
90 100'});
model.batch('p1').set('punit', {'kHz'});
model.batch('p1').set('err', true);
model.batch('p1').feature('so1').set('seq', 'sol1');
model.batch('p1').feature('so1').set('psol', 'sol2');
model.batch('p1').feature('so1').set('param',
{'"f","10000"' '"f","20000"' '"f","30000"' '"f","40000"'
'"f","50000"' '"f","60000"' '"f","70000"' '"f","80000"'
'"f","90000"' '"f","100000"'});
model.batch('p1').attach('std1');
model.batch('p1').run;

model.result.dataset('rev1').set('startangle', -90);
model.result.dataset('rev1').set('revangle', 225);
model.result.dataset('rev2').set('startangle', -90);
model.result.dataset('rev2').set('revangle', 225);
model.result.dataset('cpt1').set('pointx', 0);
model.result.dataset('cpt1').set('pointy', 0);
model.result.dataset('cpt1').set('pointz', 0);
model.result.numerical('gev1').set('table', 'tbl1');
model.result.numerical('gev1').set('expr', {'mf.XCoil_1'});
model.result.numerical('gev1').set('unit', {['ohm' ]});
model.result.numerical('gev1').set('descr', {'Coil
reactance'});
model.result.numerical('pev1').set('data', 'cpt1');
```

```
model.result.numerical('pev1').set('table', 'tbl2');
model.result.numerical('pev1').set('expr', {'mf.XCoil_1'});
model.result.numerical('pev1').set('unit', {['ohm' ]});
model.result.numerical('pev1').set('descr', {'Coil
reactance'});
model.result.numerical('gev1').setResult;
model.result.numerical('pev1').setResult;
model.result('pg5').set('data', 'cpt1');
model.result('pg5').set('xlabel', 'freq (kHz)');
model.result('pg5').set('ylabel', ['Coil reactance (' 'ohm'
')']);
model.result('pg5').set('xlabelactive', false);
model.result('pg5').set('ylabelactive', false);
model.result('pg1').label('Magnetic Flux Density Norm
(mf)');
model.result('pg1').feature('surf1').set('colortable',
'RainbowLight');
model.result('pg1').feature('surf1').set('resolution',
'normal');
model.result('pg1').feature('con1').set('titletype',
'none');
model.result('pg1').feature('con1').set('number', 15);
model.result('pg1').feature('con1').set('levelrounding',
false);
model.result('pg1').feature('con1').set('coloring',
'uniform');
model.result('pg1').feature('con1').set('colorlegend',
false);
model.result('pg1').feature('con1').set('color', 'gray');
model.result('pg1').feature('con1').set('resolution',
'normal');
model.result('pg2').label('Magnetic Flux Density Norm,
Revolved Geometry (mf)');
model.result('pg2').feature('surf1').set('colortable',
'RainbowLight');
model.result('pg2').feature('surf1').set('resolution',
'normal');
model.result('pg2').feature('con1').set('titletype',
'none');
model.result('pg2').feature('con1').set('number', 15);
model.result('pg2').feature('con1').set('levelrounding',
false);
model.result('pg2').feature('con1').set('coloring',
'uniform');
```

```
model.result('pg2').feature('con1').set('colorlegend',
false);
model.result('pg2').feature('con1').set('color', 'gray');
model.result('pg2').feature('con1').set('resolution',
'normal');
model.result('pg3').label('Magnetic Flux Density Norm (mf)
1');
model.result('pg3').feature('surf1').set('colortable',
'RainbowLight');
model.result('pg3').feature('surf1').set('resolution',
'normal');
model.result('pg3').feature('con1').set('titletype',
'none');
model.result('pg3').feature('con1').set('number', 15);
model.result('pg3').feature('con1').set('levelrounding',
false);
model.result('pg3').feature('con1').set('coloring',
'uniform');
model.result('pg3').feature('con1').set('colorlegend',
false);
model.result('pg3').feature('con1').set('color', 'gray');
model.result('pg3').feature('con1').set('resolution',
'normal');
model.result('pg4').label('Magnetic Flux Density Norm,
Revolved Geometry (mf) 1');
model.result('pg4').set('data', 'rev2');
model.result('pg4').set('looplevel', [1 10]);
model.result('pg4').feature('surf1').set('colortable',
'RainbowLight');
model.result('pg4').feature('surf1').set('resolution',
'normal');
model.result('pg4').feature('con1').set('titletype',
'none');
model.result('pg4').feature('con1').set('number', 15);
model.result('pg4').feature('con1').set('levelrounding',
false);
model.result('pg4').feature('con1').set('coloring',
'uniform');
model.result('pg4').feature('con1').set('colorlegend',
false);
model.result('pg4').feature('con1').set('color', 'gray');
model.result('pg4').feature('con1').set('resolution',
'normal');
data =mphplot(model,'pg5');
```

```
str_1 = mphtable(model,'tbl1') ;
    tbl_1 = str_1.data;
    x=tbl_1(:,3);
    A=max(x);
    y_x=600-A;
a=[28.461  ; 56.922; 85.383;113.84; 142.31; 170.77;
199.23;227.69; 256.15;284.61];
f=[10;20;30;40;50;60;70;80;90;100];
Z= x(:,1)-a(:,1);

plot(f,Z)
Z1=0;
Z2=max(Z);
f1=interp1(Z,f,Z1,'linear')
% f2=interp1(Z,f,Z2,'linear')
 x=tbl_1(:,3);
%  z2=min(abs(f2-25));
z1=min(abs(f1-65));
% z=[z1 z2]';
out = model;
```

## Appendix E

# DE algorithm

```
clc;
clear;
close all;

%% Problem Definition

CostFunction = @(x) ZCF(x);     % Cost Function

nVar = 1;             % Number of Decision Variables

VarSize = [1 nVar];    % Decision Variables Matrix Size

VarMin = 250;           % Lower Bound of Decision Variables
VarMax = 550;           % Upper Bound of Decision Variables

%% DE Parameters

MaxIt =50;       % Maximum Number of Iterations

nPop = 10;         % Population Size

beta_min = 0.2;    % Lower Bound of Scaling Factor
beta_max = 0.8;    % Upper Bound of Scaling Factor

pCR = 0.5;         % Crossover Probability

%% Initialization

empty_individual.Position = [];
empty_individual.Cost = [];

BestSol.Cost = inf;

pop = repmat(empty_individual, nPop, 1);

for i = 1:nPop

    pop(i).Position = unifrnd(VarMin, VarMax, VarSize);

    pop(i).Cost = CostFunction(pop(i).Position);

    if pop(i).Cost<BestSol.Cost
        BestSol = pop(i);
    end
```

```
end

BestCost = zeros(MaxIt, 1);

%% DE Main Loop

for it = 1:MaxIt

    for i = 1:nPop

        x = pop(i).Position

        A = randperm(nPop);

        A(A == i) = [];

        a = A(1);
        b = A(2);
        c = A(3);

        % Mutation
        %beta = unifrnd(beta_min, beta_max);
        beta = unifrnd(beta_min, beta_max, VarSize);
        y = pop(a).Position+beta.*(pop(b).Position-
pop(c).Position);
        y = max(y, VarMin);
        y = min(y, VarMax);

        % Crossover
        z = zeros(size(x));
        j0 = randi([1 numel(x)]);
        for j = 1:numel(x)
            if j == j0 || rand <= pCR
                z(j) = y(j);
            else
                z(j) = x(j);
            end
        end

        NewSol.Position = z;
        NewSol.Cost = CostFunction(NewSol.Position);

        if NewSol.Cost<pop(i).Cost
            pop(i) = NewSol;
```

```
            if pop(i).Cost<BestSol.Cost
               BestSol = pop(i);
            end
        end

    end

    % Update Best Cost
    BestCost(it) = BestSol.Cost;

    % Show Iteration Information
    disp(['Iteration ' num2str(it) ': Best Cost = '
num2str(BestCost(it))]);

end

%% Show Results

figure;
plot(BestCost);
semilogy(BestCost, 'LineWidth', 2);
xlabel('Iteration');
ylabel('Best Cost');
grid on;
```